A comprehensive approach for achieving real-world driving maneuvers on complete vehicle test benches: Model-based simulation, robust control design, and deep-learning identification

Zur Erlangung des akademischen Grades eines

DOKTORS DER INGENIEURWISSENSCHAFTEN (Dr.-Ing.)

von der KIT-Fakultät für Maschinenbau des
Karlsruher Instituts für Technologie (KIT)

angenommene

Dissertation

von

M. Sc. Muhammed Alhanouti

Tag der mündlichen Prüfung: 16.04.2026
Hauptreferent: Prof. Dr. rer. nat. Frank Gauterin
Korreferent: Prof. Dr. Lutz Gröll

Kurzfassung

In dieser Dissertation wird ein systematisches Verfahren zur Simulation des Energiebedarfs bei dynamischen Fahrmanövern auf Gesamtfahrzeugprüfständen mit hoher Realitätsnähe vorgestellt. Verschiedene Prüfstandskonzepte werden verglichen und durch modellbasierte Simulation und Messungen bei realen Fahrmanövern auf ihre Tauglichkeit zur Durchführung dynamischer Fahrmanöver untersucht. Die entwickelten Methoden zur Reproduktion dynamischer Fahrmanöver werden erfolgreich mit den vorgesehenen Anwendungen validiert. Ausgehend von der Zielsetzung einer realitätsnahen Fahrversuchsdurchführung werden wesentliche Anforderungen an ein für dynamische Fahrmanöver geeignetes Prüfstandkonzept ermittelt. Der Schwerpunkt dieser Arbeit liegt auf der Simulation des Energieverbrauchs eines Elektrofahrzeugs im Straßenverkehr und bei der Durchführung von Fahrversuchen auf Gesamtfahrzeugprüfständen.

Viele Forschungsarbeiten betonen wichtige Faktoren für eine genaue Schätzung des Energieverbrauchs von Elektrofahrzeugen, wie die Entwicklung detaillierter Fahrzeugdynamikmodelle, die Schätzung der Effizienz des Antriebsstrangs in hoher Auflösung und die Berücksichtigung von Umweltauswirkungen entlang einer bestimmten Route. Allgemein, betrachteten diese Arbeiten Verfahren, die sehr komplex sind und es daher sehr aufwendig ist, validierte Modelle für den Energieverbrauch von Elektrofahrzeugen zu erhalten, oder es wurden einfachere Methoden entwickelt, die jedoch weniger genaue Ergebnisse lieferten. Diese Arbeit schlägt dagegen einen unkomplizierten Ansatz vor, der einfach zu implementieren ist und genaue Simulationsergebnisse liefert. Nachdem die genaue Modellierung für Elektrofahrzeuge erreicht wurde, besteht der nächste Schritt darin, das Fahrzeugsystemmodell in verschiedene Arten von Prüfständen für Gesamtfahrzeuge zu integrieren.

In dieser Arbeit werden vier Hauptschwerpunkte untersucht, um genaue virtuelle Simulationsergebnisse sowohl für Straßenfahrten als auch die experimentelle Simulation für Prüfstandstests zu erzielen: Erstens die Entwicklung eines adaptierbaren Modells zur Schätzung des Energieverbrauchs in Elektrofahrzeugen. Zweitens soll eine Vorhersagemethode für den Schlupf zwischen den Reifen des zu prüfenden Fahrzeugs und den Rollen eines Rollenprüfstands vorgeschlagen werden. Drittens ermöglicht der Entwurf eines Regelalgorithmus eine realitätsnahe Umsetzung der referenzierten realen Fahrmanöver auf den Gesamtfahrzeugprüfständen. Viertens die Entwicklung einer Lösung zur Ermittlung der physikalischen Ausgangsgrößen des Antriebsstrangsteuergeräts bei fehlendem Wissen zu den technischen Daten.

Viele Studien konzentrierten sich auf die Erstellung experimenteller Modelle zur Schätzung des Energieverbrauchs von Elektrofahrzeugen. Diese Art der Modellierung ist mit mehreren Anforderungen verbunden: lange Strecken fahren, geeignete Umgebungsbedingungen sicherstellen und spezielle Messinstrumente vorbereiten. Darüber hinaus gelten die Ergebnisse für die jeweiligen Testfahrzeuge; die entwickelten Modelle sind möglicherweise nicht für andere Fahrzeuge mit anderen Spezifikationen geeignet. In anderen Arbeiten wurden physikalische Modelle des gesamten Fahrzeugs erstellt, die Modelle müssen jedoch detaillierter sein, um die gewünschte Genauigkeit beim Energieverbrauch zu erzielen. In dieser Arbeit wird ein detailliertes Simulationsmodell des Energieverbrauchs im Antriebsstrang erstellt, der sich aus dem geschätzten dynamischen Verhalten des Testfahrzeugs ergibt. Darüber hinaus wird das Modell mit experimentellen Daten aus einem dynamischen realen Straßenfahrversuch validiert. Das in diesem Rahmen vorgeschlagene Batteriemodell zeigte in verschiedenen experimentellen Tests eine hohe Präzision. Verschiedene mechanische und elektrische physikalische Größen werden genau geschätzt, so dass nur die Fahrzeuggeschwindigkeit und die Verluste der Nebenaggregate als Eingaben für das Simulationsmodell dienen. Das Modell ist unter bestimmten Bedingungen gültig, nämlich beim Fahren auf ebenem Untergrund, ohne Berücksichtigung der Straßenoberflächenrauheit und bei konstanter Umgebungstemperatur. Diese modellbasierte Simulation diente

als Referenz für die Genauigkeit der Schätzung des Energieverbrauchs des Fahrzeugs auf dem Rollenprüfstands und als Referenzmodell für einen noch in der Entwicklung befindlichen Vehicle-in-the-loop-Prüfstand.

Der Energieverbrauch des elektrischen Versuchsfahrzeugs auf dem Rollenprüfstand wird eingehend untersucht. Die experimentellen Daten wurden für die Standardfahrzyklustests NEFZ- und WLTP-Klasse-2 erfasst. Die Ergebnisse zeigen, dass bei der Schätzung des mit diesen Standardtests verbundenen Energiebedarfs auf dem Prüfstand Abweichungen zum Referenzsimulationsmodells auftreten. Diese Ergebnisse sprechen dafür, dass die Ursache in der Dynamik des Reifen-Rollen-Kontakts zu suchen ist.

Mehrere Einschränkungen des Rollenprüfstands machten die Durchführung hochdynamischer Fahrmanöver zu einer anspruchsvollen Aufgabe. Aus diesem Grund wurde ein weiterer Typ von Gesamtfahrzeugprüfständen untersucht, ein sogenannter Vehicle-in-the-Loop-Prüfstand. Bei diesem Prüfstandstyp werden die gewünschten Fahrwiderstände durch Belastungsmaschinen bei abgenommenen Rädern direkt auf die Radnaben des Prüffahrzeugs aufgebracht. Diese Architektur vermeidet die unerwünschten Einflüsse des Rollen- und Reifenkontakts, wie dies bei Rollenprüfständen der Fall ist. Um das dynamische Verhaltendes Vehicle-in-the-loop-Prüfstands zu verbessern und seine mechanischen Leistungsverluste zu berücksichtigen, wurde ein robuster Regelungsalgorithmus entwickelt. Die Übertragungsfunktion für das Gesamtsystem aus Prüfstand und Testfahrzeug wird erstellt, um die Stabilität verschiedener Reglertypen im Frequenzbereich umfassend zu analysieren und die Qualität der Rauschunterdrückung zu bewerten. Darüber hinaus wurden die Erwartungen aus der Frequenzanalyse im Zeitbereich bestätigt. Außerdem wurden Empfindlichkeitsanalysetests durchgeführt, um die Robustheit jedes Reglers gegenüber der Unbestimmtheit der Modellierungsparameter zu bewerten. Basierend auf den Analyseergebnissen wurde schließlich ein Regelalgorithmus entwickelt, der einen LQI-Zustandsraumregler mit einem PI-Momentregler integriert. Der vorgeschlagene Regelalgorithmus soll die Kraftübertragung zwischen den Belastungsmaschinen und den

Radträgern des Testfahrzeugs regeln, indem sowohl die Drehzahlen als auch die Drehmomente der Räder gesteuert werden. Der vorgeschlagene Regler wird in das Vehicle-in-the-loop-Prüfstandsmodell integriert und anschließend werden die virtuellen Prüfstandssimulationsergebnisse mit den Simulationsergebnissen des Testfahrzeugmodells beim Straßenfahren verglichen. Der vorgeschlagene Regelungsalgorithmus ermöglicht eine genaue Schätzung des Energieverbrauchs für ein bestimmtes Manöver. Mithilfe des validierten Modells des Testfahrzeugs wird die Leistung des entsprechenden Antriebsstrangs im Fahrzyklus der WLTP-Klasse 3 simuliert.

Der letzte Schritt der Verbindung des Testfahrzeugs mit der Prüfstandstestumgebung besteht darin, das Antriebsdrehmoment des Fahrzeugs auf dem Vehicle-in-the-loop Prüfstand zu reproduzieren, um den gleichen Lastfall wie beim realen Fahrmanöver zu erreichen. Es wird eine Identifikationstechnik vorgeschlagen, um einen Zusammenhang zwischen der Fahrpedalstellung und dem entsprechenden Antriebsmoment herzustellen. Dieser Schritt ist von Vorteil, um das komplexe physikalische Modell des Fahrzeugsteuergeräts zu ersetzen, das möglicherweise mit weiteren Informationen zur Modellierung versorgt werden muss. Das nichtlineare autoregressive exogene (NARX)-Netzwerk erwies sich als fähiger, langfristige Abhängigkeiten zu lernen als das statische neuronale Netzwerk. Darüber hinaus erwies es sich als vielversprechende Technik für die Online-Erkennung in verschiedenen Automobilanwendungen unter realen Fahrbedingungen. Das NARX-Netzwerk in dieser Dissertation als dynamisches neuronales Netzwerk mit Feedback- und Speicherfunktionen dient der Vorhersage des Elektromotormoments des Fahrzeugs unter Berücksichtigung der Fahrpedalstellung, der Winkelgeschwindigkeit des Motors und der Fahrzeuggeschwindigkeit. Das Modell ist jedoch auf Fahrten in der Ebene eingeschränkt, ohne Berücksichtigung der Straßenoberflächenrauheit und bei konstanter Umgebungstemperatur. Dieses Modell erwies sich als äußerst effizient bei der Abbildung dieses hochkomplexen Zusammenhangs. Die für den Identifikationsprozess verwendeten Daten stammen aus einer realen dreidimensionalen Route mit dynamischen Eigenschaften wie abrupten Änderungen des Fahrmodus, unterschiedlichen

Geschwindigkeitsbegrenzungen und Höhenunterschieden. Damit soll der Wertebereich des Drehmoments durch variierende Fahrereingaben möglichst umfassend abgedeckt werden. Das Modell wird dann mit Messungen aus einem tatsächlichen Feldtestmanöver validiert. Abschließend wird das identifizierte Modell in ein größeres Fahrzeugmodell und einen Prüfstand integriert. Die Ausgabe des identifizierten Antriebsmoments wird einem Momentregler zugeführt, der das Antriebsmoment des Antriebsstrangs des auf dem Prüfstand montierten Fahrzeugs steuert.

Der vorgeschlagene Rahmen ermöglicht eine präzise Abschätzung des Energieverbrauchs, während die Abhängigkeit von kostenintensiven und nicht reproduzierbaren Straßentests reduziert wird. Sowohl Rollenprüfstände als auch Vehicle-in-the-loop -Prüfstände weisen spezifische Vor- und Nachteile auf, bilden jedoch gemeinsam ein komplementäres Instrumentarium für eine effiziente Fahrzeugentwicklung. Die Beiträge dieser Arbeit liegen in der Entwicklung validierter Simulationsmodelle, der fortschrittlichen Modellierung von Reibungs- und Reifenverhalten, der Ausarbeitung robuster Regelungsalgorithmen sowie in datengetriebenen Methoden zur Identifikation nichtlinearer Systeme. All dies ist in eine kohärente Methodik integriert, die den dringenden Bedarf an reproduzierbaren, genauen und effizienten prüfstandsbasierten Fahrzeugtests adressiert.

Abstract

This dissertation presents a systematic procedure to simulate the energy consumption during dynamic driving maneuvers on complete vehicle test benches with high realism. Different test bench concepts are compared and examined for their suitability for carrying out dynamic driving maneuvers through model-based simulation and measurements recorded during real environment driving maneuvers. The developed methods for reproducing dynamic driving maneuvers are successfully validated with the designated applications. Based on the objective of realistic driving test implementation, essential requirements for a test bench concept suitable for dynamic driving maneuvers are identified. This work focuses on simulating the energy consumption of an electric vehicle in case of street driving, and while conducting driving tests on complete vehicle test benches.

Many researches emphasize significant factors for accurately estimating the energy consumption in electric vehicles, such as developing detailed vehicle dynamic models, estimating high-resolution powertrain efficiency, and considering environmental effects along a specific route. Generally, those works consider procedures are very complex and therefore very time-consuming to obtain validated models for the energy consumption of electric vehicles or more straightforward methods but with less accurate results. In contrast, this work proposes an uncomplicated approach that is easy to implement and creates accurate simulation results. As a reliable modeling for the electric vehicle is achieved, the next step will be integrating the vehicle system model with different types of complete vehicle test benches.

Four main focus topics are investigated in this work, to achieve accurate virtual simulation results for the street driving and the experimental simulation for the test bench testing: First, developing an adaptable model to estimate the energy consumption in electric vehicles. Second, proposing a prediction

method for the slip between the vehicle's tires under test and rollers of a chassis dynamometer test bench. Third, designing a control algorithm that enables realistic implementation of the referenced real driving maneuvers on the complete vehicle test benches. Fourth, finding a solution to identify the physical output quantities from the powertrain control unit without knowledge of technical data.

Many studies focused on creating experimental models to estimate energy consumption for EVs. Several requirements accompany this type of modeling: driving long routes, assuring suitable environmental conditions, and preparing specific measurement instruments. Moreover, the results would be valid for the particular test vehicles; the developed models might not be valid for vehicles with different specifications. Other works built physical models of the complete vehicle, but the models must be more detailed to produce the desired energy consumption accuracy. A thorough energy consumption simulation model in the powertrain is created in this work, which results from the estimated dynamic behavior of the test vehicle. Moreover, the model is validated with experimental data from a dynamic real road test. The battery model, proposed in this context, proved high precision for different experimental tests. Various mechanical and electrical physical quantities are estimated accurately, giving only the vehicle speed, the road and driving environment conditions, and auxiliary power losses as inputs for the simulation model. The model is valid under certain conditions, which are driving on a level ground, without taking road surface roughness into account, and at a constant ambient temperature. This model-based simulation served as a reference for the accuracy of estimating energy consumption using the chassis dynamometer test bench and as a reference model for a Vehicle-in-the-loop test bench that is still under development. The energy consumption of the electric test vehicle on the roller dynamometer test bench is thoroughly investigated. The experimental data were recorded for the NEDC and the WLTP-class 2 standard driving cycle tests. The results show that the energy consumption associated with these tests could be estimated using the measured

values of the chassis dynamometer. These findings suggest that the cause lies in the dynamics of the tire and roller contact.

Several limitations of the roller dynamometer test bench made highly dynamic driving maneuvers a challenging task. Consequently, another type of complete vehicle test bench is investigated, which is called the Vehicle-in-the-loop test bench. In this type of test bench, the desired driving resistances are directly applied to the wheel hubs, with wheels removed, of the test vehicle by loading machines. This architecture avoids the undesirable influences of roller and tire contact, as in the case of roller test benches. In order to improve the Vehicle-in-the-loop test bench dynamic response and to appropriately take into account its mechanical power losses, a robust control algorithm is developed. The transfer function for the entire system that combines the test bench and the test vehicle is created to extensively analyze the stability of different types of controllers in the frequency domain and evaluate the noise rejection quality. Moreover, the expectations from the frequency analysis were approved in the time domain. Furthermore, sensitivity analysis tests were made to evaluate each controller's robustness against the modeling parameters' uncertainty. Finally, a control algorithm that integrates a LQI state space feedback controller with a PI moment controller was developed based on the analysis results. The proposed control algorithm is designed to regulate power transmission between the loading machines to the test vehicle wheels by controlling both rotational speeds and moments of the wheels. The proposed controller is integrated with the Vehicle-in-the-loop test bench model. Then the simulation results are compared with the test vehicle model on street driving. The proposed controller enables accurate estimation of energy consumption for a specified maneuver. The validated model of the test vehicle is used to simulate the corresponding powertrain's power during the WLTP-class 3 driving cycle.

The last step of interfacing the test vehicle with the test bench testing environments is to reproduce the powertrain torque on the Vehicle-in-the-loop test bench to achieve the same load case as in the real-world driving

maneuvers. An identification technique is proposed to create a relation between the accelerator pedal position and the corresponding driving moment. This step is beneficial to replace the complex physical model of the vehicle control unit, which maybe needs to be provided with more information to model it. The nonlinear autoregressive exogenous (NARX) network was proven to be more capable of learning long-term dependencies than the static neural network. Moreover, it proved to be a promising technique for the online recognition of different automotive applications under real driving conditions. The NARX network is utilized in this dissertation as a dynamic neural network with feedback and memory functions to predict the electric motor moment of the electric vehicle, given the accelerator pedal position, the motor's angular speed, and the vehicle's speed. However, the model is limited to driving on flat surfaces, without taking into account road surface roughness and at constant ambient temperature. This model proved to be extremely efficient in resembling this highly complex relationship. The data used for the identification process is chosen from a real-world three-dimensional route with dynamic characteristics of sudden changes in the driving mode, different speed limits, and elevations. The aim is to cover the range of torque values as comprehensively as possible through varying driver inputs. The model is then validated with measurements from an actual field test maneuver. Finally, the identified model is integrated into a larger-scale vehicle model and a test bench. The output of the identified driving moment is fed to a moment controller, which controls the powertrain driving moment of the vehicle mounted on the test bench.

The proposed framework provides accurate energy consumption estimation while reducing reliance on costly and irreproducible road tests. Both, roller dynamometer and vehicle-in-the-loop test benches are shown to have specific advantages and limitations, but together they form a complementary set of tools for efficient vehicle development. The contributions of this work lie in the development of validated simulation models, advanced friction and tire behavior modeling, robust control algorithms, and data-driven methods for nonlinear system identification. All integrated into a coherent methodology

that addresses the pressing need for reproducible, accurate, and efficient test bench-based vehicle testing.

Table of Contents

List of Figures

List of Tables

Abbreviations

ABS	Anti-lock braking system
AC	Alternating current
ACoRTA	Advanced co-simulation methods for real-time applications
ANN	Artificial neural networks
ARX	Autoregressive exogenous model
BEV	Battery electric vehicle
BMS	Battery management system
CG	Center of gravity
C-rate	Battery capacity rate
CV	Constant velocity joints
DC	Direct current
ECM	Equivalent circuit model
ECU	Engine control unit
ETRTO	European tire and rim technical organization
EV	Electric vehicle
FCEV	Fuel cell electric vehicle
FL	Front left wheel
FMI	Functional mock-up interface
FOC	Field-oriented control
FR	Front right wheel
GUI	Graphical user interface

HEV	Hybrid electric vehicle
HiL	Hardware-in-the-loop
HMI	Human-machine interface
hp	Horsepower
ICE	Internal combustion engine
ICOS	Independent co-simulation platform
IGBT	Insulated-gate bipolar transistor
I-SS	State space with integral action
LiB	Lithium-ion battery
$LiFePO_4$	Lithium iron phosphate
LQ	Linear-quadratic
LQI	Linear-quadratic with integral action
MPC	Model predictive control
NARX	Nonlinear autoregressive exogenous model
NEDC	New European driving cycle
nonRT	Non-real-time system
NRMSE	Normalized root mean square error
NVH	Noise, vibration, and harshness
OCV	Open circuit voltage
PDF	Probability density function
PHEV	Plug-in hybrid electric vehicle
RDE	Real driving emissions
RL	Rear left wheel
RLS	Road load simulation
RMSE	Root mean square error

RR	Rear right wheel
RT	Real-time systems
RWD	Real-world driving
SOC	State of charge
SPARC	Secure propulsion using advanced redundant control
UUT	Unit under test
VCU	Vehicle control unit
VEL	Vehicle-in-the-loop test bench
ViL	Vehicle-in-the-loop
VLAN	Virtual local area network
VUT	Vehicle under test
WLTP	Worldwide harmonized light vehicles test procedure

Nomenclature

Symbol	Unit	Description
A	V	Exponential zone amplitude
A	-	Scaling factor for the slip value at the peak longitudinal force
$\boldsymbol{A}$	-	System's state space matrix
A_{batt}	m^2	Battery-block surface area
A_F	m^2	Front surface area of the vehicle
A_{tire}	m^2	Outside tire surface area
$A_{V,max}$	N	Maximum traction force on the front axle
a_x	m/s^2	Vehicle longitudinal acceleration
a_y	m/s^2	Vehicle lateral acceleration
B	Ah^{-1}	Exponential zone time constant inverse
b	-	Constant property of the electrolyte
$\boldsymbol{B_1}$	-	State space input vector of the electric machine moment
$\boldsymbol{B_2}$	-	State space input vector of the differential gearbox output moment
$\boldsymbol{d_i}$	-	Dilation coefficients vector for the sigmoid-network
b_s	s	Normalized internal damping of the shaft
$b_{St,f}$	m	Width of the front anti-roll bar
$b_{St,r}$	m	Width of the rear anti-roll bar

B_x	-	Longitudinal force initial slope in Pacejka formula
B_y	-	Lateral force initial slope in Pacejka formula
B_z	-	Aligning torque initial slope in Pacejka formula
$\boldsymbol{b_z}$	-	State space input vector for the disturbance
$\boldsymbol{C}$	-	State space output matrix
C_d	-	Air resistance coefficient with frontal flow wind
$c_{F,f}$	N/m	Spring stiffness front
$c_{F,r}$	N/m	Spring stiffness rear
C_{Fx}	kN/m	Tire longitudinal stiffness coefficient
$C_{F\alpha}$	kN/rad	Tire cornering stiffness factor
$C_{F\kappa}$	kN	Tire longitudinal slip stiffness
c_i	-	Translations scalars for the sigmoid-network
C_L	F	Battery internal resistance capacitor for long-time transient response
C_p	J/(kg·K)	Specific heat capacity
C_S	F	Battery internal resistance capacitor for short-time transient response
$c_{St,f}$	Nm/rad	Stiffness of the front anti-roll bar
$c_{St,r}$	Nm/rad	Stiffness of the rear anti-roll bar
C_{usable}	Ah	Usable battery capacity
C_x	-	Longitudinal force shape factor in Pacejka formula
C_y	-	Lateral force shape factor in Pacejka formula
C_z	-	Aligning torque shape factor in Pacejka formula
D_{Ax}	Nm·s/rad	Axle equivalent rotational damping
$d_{D,f}$	N·s/m	Damping coefficient front

$d_{D,r}$	N·s/m	Damping coefficient rear
D_s	Nm·s/rad	Shaft equivalent rotational damping
D_x	kN	Longitudinal force peak factor in Pacejka magic formula
D_y	kN	Lateral force peak factor in Pacejka magic formula
D_z	kN	Aligning torque peak factor in Pacejka magic formula
E	kWh	Total cumulative vehicle energy consumption
$\boldsymbol{e}$	-	Error dynamics vector
e	-	Immeasurable noise
$e_{C\alpha}$	-	Correction factor for the contact patch length between the tire and the dynamometer roller
e_{FR}	-	Correction factor rolling resistance on the dynamometer roller
E_x	-	Longitudinal force curvature factor in Pacejka formula
E_y	-	Lateral force curvature factor in Pacejka formula
E_z	-	Aligning torque curvature factor in Pacejka formula
$\boldsymbol{F}$	-	Precompensation gain vector
F_A	N	Air resistance
F_{acc}	N	Acceleration resistance
F_b	N	Friction force in LuGre model in braking mode
F_{BooIn}	N	Brake booster input force
F_{BooOut}	N	Brake booster output force

F_C	N	Climbing resistance
F_{curve}	N	Resistance from curvature driving
F_d	N	Total driving force
$F_{D,W}$	N	Vertical forces of the corresponding damper
$F_{F,W}$	N	Vertical forces of the corresponding spring
F_G	N	Vehicle weight
f_{norm}	-	Normalization factor for electric motors
F_R	N	Rolling resistance force of the tire on the road
F_R*	N	Steady-state rolling resistance force
f_{regen}	-	Normalization factor for regenerative braking
F_{rest}	N	Force at the restraint
F_{RR}	N	Effective rolling resistance on the dynamometer roller
f_{RR}	-	Rolling resistance coefficient
$F_{St,W}$	N	Vertical forces of the corresponding anti-roll bar
F_x	N	Driving force
$F_{x,f}$	N	Front axle traction force
F_{xW}	N	Tire traction force
F_{yW}	N	Tire cornering force
$F_{z,f}$	N	Front axle normal force
$F_{z,r}$	N	Rear axle normal force
F_{Zp}	-	Normalized tire load (i.e compared to the full tire load) according to the ETRTO load standard
F_{zW}	N	Tire normal force
g	m/s^2	Acceleration of the gravity

$G(s)$	-	Transfer function
$G_d(s)$	-	Time delay transfer function
$G_\Delta(s)$	-	Total delay transfer function
H	-	Loop transfer function
h	m	Hight of the vehicle center of gravity
h	W/m²/°K	Heat transfer coefficient
h_0	W/m²/°K	Reference heat exchange coefficient for rubber and air
h_{CR}	m	Hight of the vehicle rolling center
h_{rest}	m	Restraint height
I^*_{batt}	A	Filtered battery current
I_{batt}	A	Battery current
i_D	-	Differential gear ratio
i_g	-	Transmission gear ratio
It	Ah	Integration of the battery current over time
$J_{a,f}$	kg·m^2	Front axle inertia
$J_{a,r}$	kg·m^2	Rear axle inertia
J_{Ax}	kg·m^2	Axle inertia parameter
J_E	kg·m^2	Vehicle motor inertia
J_g	kg·m^2	Gearbox inertia
J_M	kg·m^2	Motor inertia
J_{Pt2W}	kg·m^2	Front axle inertia plus half of the powertrain equivalent inertia
J_S	kg·m^2	Constant velocity shaft inertia around its longitudinal axis

J_t	kg·m^2	Tire inertia
J_T	kg·m^2	Equivalent inertia of the electrical loading machine and the continuous velocity shaft
J_W	kg·m^2	Wheel inertia
J_{WH}	kg·m^2	Wheel hub inertia
J_{xx}	kg·m^2	Moment of inertia around the longitudinal axis
J_{zz}	kg·m^2	Moment of inertia around the vertical axis
k	-	Sensibility exponent factor of the tire
$k_{\Delta\omega}$	Nm/rad	Viscous friction factor
K_{Ax}	Nm/rad	Axle stiffness
k_{FF}	-	Feedforward gain
k_i	-	Integral gain
$k_{I,M}$	-	Integral gain for the moment controller
$\boldsymbol{K_{LQ}}$	-	Full-state feedback gain matrix for the LQ controller
$\boldsymbol{K_{LQI}}$	-	Full-state feedback gain matrix for the LQI controller
$\boldsymbol{K_x}$	-	Full-state feedback gain matrix for the LQI controller without the additional integral gain
K_ξ	-	State feedback gain for the additional integral gain in the LQI controller
k_M	-	Friction moment factor
k_p	-	Proportional gain
K_{pc}	V/(Ah)	Polarization constant
K_{pr}	Ω	Polarization resistance

K_s	Nm/rad	Shaft equivalent rotational stiffness
$k_{V,low}$	N·s/m	Tire damping coefficient
$k_{V,low0}$	N·s/m	Tire damping coefficient at low speed
L	m	Contact patch length
$\boldsymbol{l}$	-	Weights vector for the sigmoid-network
L_{LE}	m	Tire contact patch length on the flat surface
$\boldsymbol{L_{LQ}}$	-	Luenberger observer gain matrix for LQ controller
$\boldsymbol{L_{LQI}}$	-	Luenberger observer gain matrix for LQI controller
L_{LT}	m	Tire contact patch length on the roller contact
$l_{St,f}$	m	Length of the front anti-roll bar
$l_{St,r}$	m	Length of the rear anti-roll bar
l_w	m	Wheelbase
m	kg	Vehicle mass
$M(s)$	-	Measurement time delay transfer function
$M_{A,f}$	Nm	Moment at the front axle
$M_{A,r}$	Nm	Moment at the rear axle
M_{batt}	kg	Battery module mass
$M_{brake,ref}$	Nm	Total reference braking moment
$M_{brake,VEL}$	Nm	Total braking moment from the VEL model
M_{drive}	Nm	Total powertrain driving moment
$M_{drive}*$	Nm	Total controlled powertrain driving moment
$M_{drive,i}$	Nm	Driving moment on the corresponding wheel
$M_{drive,ref}$	Nm	Total powertrain reference driving moment
M_e	Nm	Electric motor moment

M_F	Nm	Coulomb friction moment
M_{F0}	Nm	Coulomb friction moment constant
M_M	Nm	Electrical loading machine moment
M_S	-	Maximum sensitivity
M_{sum}	Nm	Sum of measured moments on the driven wheels
M_{Sx}	Nm	Final output moment at one side of the differential gear
m_{tire}	kg	Mass of tire
M_{zW}	Nm	Tire self-aligning torque
n_{cyc}	-	Number of charging and discharging cycles
$N(s)$	-	Noise transfer function
p	bar	Tire pressure
$\boldsymbol{P}$	-	Solution matrix for the Riccati equation
$\boldsymbol{P}$	-	Projection matrix for the sigmoid-network
P_{aux}	W	Auxiliary load power
$P_{Battery}$	W	Measured electrical power from the VUT battery
P_d	W	Total driving resistance power
P_{ins}	W	Powertrain instantaneous power
P_{loss}	W	Power losses
P_{LuGre}	W	Estimated power consumption using LuGre model
p_{MC}	bar	Hydraulic braking pressure of the master cylinder
P_{mech}	W	Mechanical power of the vehicle
$P_{Mech,Street}$	W	Street driving estimated mechanical power at the wheels
P_{mo}	W	Mechanical output power of the motor

P_{mr}	W	Motor power
P_{Street}	W	Simulated total power in the street driving
$P_{Total,Dyno}$	W	Estimated total power from the roller dynamometer test bench
$P_{Trac,Dyno}$	W	Mechanical power measured from the test bench system
q	-	Backward shift operator in the ARX model
Q	Ah	Battery capacity
$\boldsymbol{Q}$	-	Weighting matrix for the state vector of the LQ controller
$\boldsymbol{Q}$	-	Projection matrix for the sigmoid-network
$\tilde{\boldsymbol{Q}}$	-	Weighting matrix for the state vector of the LQI controller
$\boldsymbol{R}$	-	Weighting matrix for the state vector of the LQ controller
$\tilde{\boldsymbol{R}}$	-	Weighting matrix for the state vector of the LQI controller
R_{cyc}	Ω	Equivalent resistance for the battery capacity fading effect
r_e	m	Tire effective dynamic rolling radius
r_f	m	Unloaded tire radius
R_i	m	Inner radius of brake pad
R_L	Ω	Battery internal resistance for long-time transient response
R_m	m	Mean radius of brake pad force

R_o	m	Outer radius of brake pad
R_O	Ω	Ohmic resistance
R_r	m	Chassis dynamometer roller radius
R_S	Ω	Battery internal resistance for short-time transient response
s	-	Tire longitudinal slip in LuGre model
S	-	Wheel slip point
$S(j\omega)$	-	Sensitivity transfer function
$S(X)$	-	Sum of dilated and translated sigmoid functions
S'	-	Contact point of the deflected part of the tire
S_D	%	Digitized accelerator pedal percentage value
$S_{D,f}$	m	Distances of the front damper
$S_{D,r}$	m	Distances of the rear damper
S_f	m	Distance between center of gravity—front axle
$S_{F,f}$	m	Distances of the front suspension
$S_{F,r}$	m	Distances of the rear suspension
s_i	-	Output coefficients scalar weights for the sigmoid-network
S_r	m	Distance between center of gravity—rear axle
$S_{St,f}$	m	Distances of the acting point of the front anti-roll beam
$S_{St,r}$	m	Distances of the acting point of the rear anti-roll beam
S_W	m	Half-track width between front wheels or rear wheels

T	°C	Instantaneous operating temperature
T^*	°C	Steady-state operating temperature
T_{amb}	°C	Ambient temperature
T_{batt}	°C	Temperature of the battery
T_{cell}	°C	Temperature of the battery cell
T_d	s	Time delay in the moment control loop
T_m	s	Measurement time delay
$U(s)$	-	Input of the system's transfer function
u	-	Input of the system
u	m	Tire deflection in axial directions
u_1	-	State space input of the electric machine moment
u_2	-	State space input of the differential gearbox output moment
V	m/s	Relative tangential velocity between surfaces in contact
v	m/s	Vehicle speed
V_{batt}	V	Estimated battery output voltage
V_L	V	Voltage of the slow transient response battery equivalent RC-circuit
V_{low}	m/s	Low-speed threshold
V_{OC}	V	Open circuit voltage
$V_{OC,ch}$	V	Open circuit voltage in case of charging
$V_{OC,dis}$	V	Open circuit voltage in case of discharging
v_r	m/s	Tire relative speed
v_{rel}	m/s	Air relative speed

v_s	m/s	Stribeck relative velocity
V_s	V	Voltage of the fast transient response battery equivalent RC-circuit
V_{sx}	m/s	Tire slip longitude velocity
v_w	m/s	Tire velocity
v_{w0}	m/s	Reference tire velocity
V_x	m/s	Longitudinal speed of the wheel center
V_x	m/s	Vehicle desired longitudinal velocity
w	-	Constant property of the electrolyte
W	-	Wheel position
x	-	Fraction of the electric motor mechanical power
$\boldsymbol{x}$	-	State variables vector
$\boldsymbol{X}$	-	Vector of regressors
$\hat{\boldsymbol{x}}$	-	Estimated state variables vector
$Y(s)$	-	Output of the system's transfer function
y	-	Output of the system
$\boldsymbol{y}$	-	Reference data for system identification
$\hat{\boldsymbol{y}}$	-	Estimated output vector
$\hat{\boldsymbol{y}}$	-	Identified model output
y_0	-	Scalar output offset
z	-	State space disturbance
α	rad	Tire slip angle
α'	rad	Transient lateral slip
α_f	rad	Slip angle of the front axle wheels
α_{In}	rad	Inclination angle of the road

α_r	rad	Slip-angle rear axle wheels
α_t	-	Bandwidth of the electrical part of the VEL test bench
β	rad	Vehicle sideslip angle
δ	rad	Equivalent steering angle calculated from the inner and outer steering angles
δ_i	rad	Steering angle of the inner wheel
δ_o	rad	Steering angle of the outer wheel
ε	1/K	Sensitivity of rolling resistance to temperature
ε	-	Emissivity of heat
η_g	%	Total gear transmission efficiency
η_{gen}	%	Generator efficiency
η_{mot}	%	Motor efficiency
η_{pe}	%	Efficiency of the power electronics
ϑ	°K	Battery cell temperature
θ_M	rad	The loading machine angular position
θ_{sx}	rad	The differential gear output angular position
θ_W	rad	The wheel hub angular position
κ	-	Tire longitudinal slip
κ^*	-	Tire transient longitudinal slip on the roller
κ'	-	Tire transient longitudinal slip
λ^*	-	Vehicle equivalent rotational mass factor
μ_c	-	Coulomb friction coefficient
μ_h	-	Static friction coefficient
v	m	Tire deflection in lateral directions

ξ	-	State variable for the additional integral controller of the LQI controller
ρ	kg/m^3	Air density
ρ_k	m	Vehicle instantaneous turning radius
$\rho_{X,Y}$	-	Pearson correlation coefficient
σ	$W \cdot m^{-2} \cdot K^4$	Stefan-Boltzmann constant
σ_0	m^{-1}	Tire longitudinal lumped stiffness factor
σ_2	s/m	Tire viscous damping factor
σ_{min}	m	Tire minimum relaxation length
σ_α	m	Tire lateral relaxation length
$\sigma_{\alpha 0}$	m	Tire lateral nominal relaxation length
σ_κ	m	Tire longitudinal relaxation length
$\sigma_{\kappa 0}$	m	Tire longitudinal nominal relaxation length
φ	rad	Vehicle rolling angle
ψ	rad	Vehicle yawing angle
ω	rad/s	Wheel angular speed
ω	rad/s	Average angular speed of the driving wheels
ω_i	rad/s	Angular speed for the corresponding wheel
ω_M	rad/s	Angular speed of the electrical loading machine
ω_{ref}	rad/s	Reference angular speed
ω_{Sx}	rad/s	Angular speed of the differential gear output
$\Delta\omega_D$	rad/s	Angular speed difference between the differential gear outputs

1 Introduction

Tests on the road are sometimes limited by legislation. Developers and application engineers have the major disadvantage of these tests being irreproducible and expensive. Moreover, they must always include factors that cannot be fully controlled, such as the driving style, the traffic, and environmental conditions. Therefore, road testing is a challenging development environment. Indeed, it will be more efficient to reproduce the driving conditions for development on test benches (Maschmeyer et al., 2016). Driving tests using test benches are reproducible, and the influences of many factors can be controlled. In addition, bench tests facilitate various measurement technologies, leading to more meaningful measurement results (S. Bauer et al., 2018). Nevertheless, an automation platform is necessitated to achieve reproducible and reliable results approved for certification testing on test benches and promote data acquisition accuracy (Maschmeyer et al., 2016; Paulweber & Lebert, 2016).

Due to the growing emphasis on innovation, there is a rising need for shorter development cycles and more efficient testing and development methodologies (R. Pfeffer & Leichsenring, 2016). However, this also leads to change requirements for the test bench systems. The desire for less development time and the increasing complexity of fulfilling the requirements are acting adversely (Paulweber & Lebert, 2016; Vögl et al., 2009), as shown in Figure 1.1. Despite the increasing computing capacity and the advanced simulation tools, the generation of realistic driving maneuvers tests will always be a crucial part of the development process

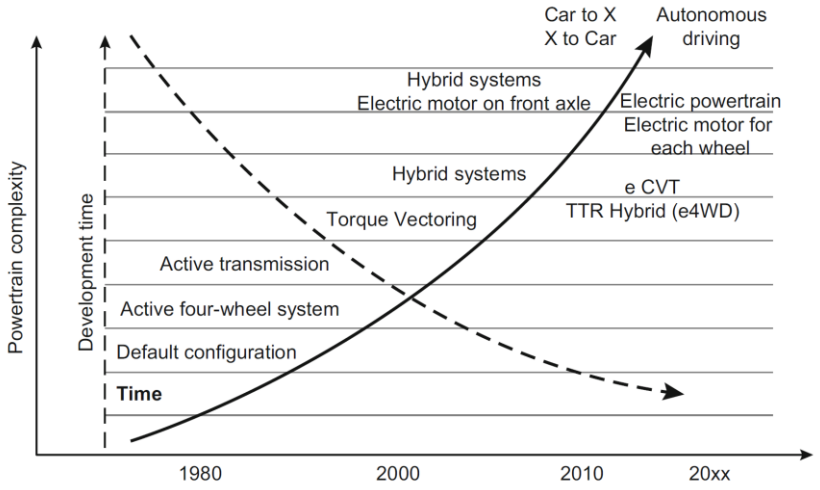

Figure 1.1: Relation between the growing complexity and the development time of vehicular systems (Paulweber & Lebert, 2016).

This growing complexity can be justified by the following aspects, among other things (R. Pfeffer & Leichsenring, 2016):

- Greater diversity of vehicle alternatives,
- Shorter development cycles,
- Increasing interlinking of systems (interlinking of sensors, electronic control units, operator controls, and actuators),
- Road environment data from several sensors provide the basis for information used by a single system (sensor data fusion),
- Greater variety of driving scenarios.

Developing vehicles with new, highly complex driving concepts requires new methods and approaches to enable an efficient testing environment. The

complexity of these systems makes the development process a challenging task (Paulweber & Lebert, 2016). The topics of energy consumption (customer-driven) and emission reduction (politics-driven) are two essential goals for automotive development (Düser, 2010). Energy consumption estimation as a topic for energy management in electric vehicles (EVs) was thoroughly investigated in numerous researches (Adaikkappan & Sathiyamoorthy, 2022; Asamer et al., 2016; De Cauwer et al., 2015; Manoharan et al., 2022; Shrivastava et al., 2022; Smuts et al., 2017; Younes et al., 2013; Y. Zhang et al., 2012; Zheng et al., 2018). In addition, practical solutions for major challenges of trip-level management were also provided. Thus, the electrification of commercial, public, and freight delivery vehicles became essential (IEA, 2017; Kohrs, 2017).

The development and validation of modern vehicles are increasingly challenged by the limitations of on-road testing. Such tests are often costly, time-consuming, and influenced by factors that cannot be fully controlled, such as traffic, environmental conditions, and driver behavior. Moreover, the growing demands for reduced emissions and improved energy efficiency place additional pressure on developers to shorten development cycles while ensuring accuracy and reproducibility. Against this backdrop, test benches emerge as indispensable tools, providing controlled environments that enable repeatable experiments, precise measurements, and the opportunity to explore various driving scenarios.

1.1 Motivation

In the process, existing development methods are reaching their limits, and the measurement effort and development costs increase significantly without developing new methods. In order to increase the efficiency in the development process by shortening the development time and saving costs accordingly, it is vital to generate reliable test results for realistic driving scenarios (S. Bauer et al., 2018). Although the road as a test environment, with its

multitude of influences, provides the necessary miscellaneous basis to ensure that vehicles fulfill the technical requirements and customer desires, it is nearly impossible to carry out two measurements under the same conditions in actual road tests due to many factors and influences, which are challenging to control and compare explicitly with the reference state (S. Bauer et al., 2018), thus, adapting or extending the existing testing platforms to more realistic driving testing becomes necessary.

More actual components or assemblies can be integrated into the development and validation process up to entire vehicles in the development process. Consequently, real road drives are shifted from the road to the test bench for development and application activities, enabling carrying them out automatically and independently of weather-related or daytime-dependent influences (Lensch-Franzen et al., 2017). Doing so can realize various actual effects and makes random test conditions possible. These advantages emphasize the need to employ test benches as a vehicle development platform (S. Bauer et al., 2018). It is, therefore, most important to interface the tools used in the testing process, from the conceptual design to the multi systems simulation, then through to the complete vehicle testing application, and finally to the street driving test (Düser, 2010).

Many researches are dedicated to enhancing complete vehicle test benches, focusing on various key areas. Concept development for highly dynamic driving maneuvers (Pillas, 2017) and in-depth analysis of dynamic characteristics in the integration of the test bench and vehicle (Fietzek, 2014) are among the highlighted research topics. Another crucial yet overlooked aspect is the necessity for a robust control algorithm for the combined system of the test bench and the test vehicle's powertrain (Forstinger, 2017). This area deserves increased attention from researchers to further develop and optimize performance in this field. Still, research work must investigate, more deeply, the test benches' accuracy and reliability extent for real environment driving maneuvers. Based upon that, this dissertation aims to develop a comprehensive method to accurately execute dynamic driving maneuvers on test benches

through model-based simulation. The basis of the model-based simulation should enable the reproduction of real-world driving maneuvers applicable to different test benches. A major challenge is developing trustworthy procedure to evaluate test benches' test results. This task is initially achieved by creating a precise test vehicle simulation model. Then, the vehicle model will be validated with actual results from field driving tests, i.e., physical driving tests with a real vehicle on a real road. After that, the test vehicle model will be integrated with different test platforms to enable examining the system as a whole. The evaluation criterion will compare the mechanical and electrical power consumed during reference driving tests between the test vehicle model and the results for the developed models of the complete vehicle test benches. Test benches have some undesired influences on the measurements dictating the implementation of a suitable control algorithm for the complete test bench platform. So, several control algorithms will be thoroughly investigated to find the most fitting among them.

1.2 Outline of the dissertation

The present work is structured as follows:

In **Chapter 2**, a detailed dynamic model for the electric test vehicle is developed to simulate the mechanical power, which comprises the wheel's rotational speed and moments on the wheels. The model includes body dynamics, driving resistance, and tire slip modeling. In addition, energy consumption is estimated using a battery model, a power losses model, and the mechanical power estimated from the dynamic model. Then, the chassis roller dynamometer is thoroughly investigated in **Chapter 3**. First, the limitations of testing on this type of test bench are defined from the literature, then approved by the experimental results. Moreover, a new tire model for the interaction between the tire and the roller is proposed to better anticipate the actual dynamic influences on the test vehicle during the test maneuver. Finally, the proposed model is adapted to the vehicle model developed in Chapter 2.

Chapter 4 presents the model development and control algorithm design for the Vehicle-in-the-loop test bench. First, the most appropriate control system is acquired by performing frequency, time-domain, and sensitivity analyses. Next, the complete system of the controlled VEL test bench with the test vehicle underwent different test maneuvers to approve the performance of the developed control algorithm.

The models in Chapter 2 and Chapter 4 are combined with the proposed controller. Building on these foundations, **Chapter 5** addresses the implementation of real-world driving maneuvers on complete vehicle test benches. Beginning with platform configuration and automation, the chapter discusses the integration of virtual vehicle components through the Functional Mock-Up approach, maneuver-based simulation strategies, and the application of steerable test benches to expand the range of permissible operating conditions. The integration of the VEL controller with a simulation environment such as CarMaker[1] enables the execution of realistic test scenarios. This is followed by methods for generating representative driving maneuvers on the bench platform, supported by empirical and data-driven techniques for nonlinear system identification. In particular, the nonlinear autoregressive exogenous (NARX) model, trained on real-world route data, is employed to establish a robust link between accelerator pedal inputs and vehicle control unit behavior. Finally, the performance of the integrated VEL simulation model is evaluated, confirming its ability to reproduce dynamic driving maneuvers with high fidelity. The dissertation concludes, in **Chapter 6**, by synthesizing the findings into a comprehensive methodology for reproducing real-world maneuvers on test benches through simulation-driven approaches.

[1] CarMaker is a software that is primarily used in vehicle and system development in the automotive industry. In addition, it provides a development environment and corresponding models to simulate real road test scenarios in the virtual world., retrieved 22.10.2021

2 Modeling and simulation of street driving with electric vehicles

To establish a reliable automated testing platform for vehicles, the development of a simulation environment is a prerequisite. This environment guarantees the consistent replication of driving maneuvers on test benches while accurately capturing the essential dynamics of the physical vehicle. This chapter fulfills this requirement through a systematic introduction to the main components of the vehicle dynamics and energy consumption models.

Various models for estimating electric vehicles (EVs) energy consumption concentrate on key parameters, including detailed vehicle dynamics, high-resolution powertrain efficiency, and route-specific environmental effects. Existing methodologies typically entail either complex procedures for enhanced accuracy or simplified approaches that compromise precision. A review of the literature on EV energy consumption modeling is provided in Section 2.2. This chapter presents an adaptable simulation model, whose principal advantage is its simplified design, which still yields highly accurate results. Furthermore, the simulation results are validated against empirical measurements obtained from the test vehicle. The battery model in Section 2.2.2 was first introduced in (Alhanouti et al., 2016). Sections 2.3 and 2.4 are based on material originally published in (Alhanouti & Gauterin, 2024a).

The vehicle model incorporates driving resistance, tire dynamics, battery characteristics, and EV power loss. Moreover, the model is parameterized using available technical data and empirical testing conducted on the vehicle. It is specifically designed to evaluate energy consumption for urban, suburban, and highway driving cycles. It's crucial to highlight that the model isn't ideal for simulating high lateral slip as it utilizes a linear lateral slip model. The modeling purpose would be to accurately simulate real dynamic driving

maneuvers, including estimating the corresponding vehicle's powertrain driving moment, rotational speeds, and total energy consumption in electric cars. The vehicle dynamics model is based on a backward calculation approach, wherein the driving resistance is computed from a predefined vehicle speed and without a driver model. To accurately capture tire-road interaction, the Pacejka tire slip model is implemented. A single-track vehicle model is employed and extended with vertical load transfer and rolling motion models, allowing for additional degrees of freedom in simulating vehicle body dynamics. Based on the resulting driving power demand and considering power losses within the powertrain, the net power requirement is estimated and used as an input for a forward calculation battery simulation model. By combining the mechanical dynamics with the electrical and thermal submodels, an adaptable energy consumption model is formulated to assess how different driving conditions impact the overall efficiency of the electric powertrain. The integration of these submodels into a complete vehicle model allows for the simulation of complex driving maneuvers with minimal input requirements, thus providing an effective reference framework for test bench automation. The validation process, based on direct comparison with experimental data from the vehicle under test, ensures that the model is not only theoretically consistent but also practically reliable. Through this layered approach, the dissertation demonstrates how the interplay between each submodel supports the development of a high performing test bench automation platform.

As the simulation model is validated, the estimated physical quantities from it can be employed as reference tracking signals for the test bench control algorithms; the estimated rotational speed of the tires would be the reference signals that the speed controllers should track, and the powertrain model would generate the reference signal for the moment controller. Since the validated simulation model enables predicting the behavior of the simulated vehicle, it will also be employed to assess the testing accuracy on the designated test benches by comparing the expected results from the

simulation model with the results from the same maneuver tests performed on the designated test benches.

2.1 Vehicle dynamics model

The electric vehicle, displayed in Figure 2.1, is employed for research in different projects. In addition to the vehicle's technical specifications, empirical maneuver test data will be employed to validate the developed simulation model

Figure 2.1: Vehicle under test (Alhanouti & Gauterin, 2023a).

2.1.1 Driving resistance model

Different test benches aim to simulate real-world driving resistances by applying the corresponding resistance moment at the vehicle's driven wheels under specific operating conditions (Heißing & Ersoy, 2007).

Figure 2.2 summarizes the major driving resistances (Gauterin, 2017; Haken, 2018). Equation (2.1) describes curve resistance (Haken, 2018). F_{curve} is a function of the geometrical distance dimensions from the vehicle's center of gravity (CG) to the front axle (S_f), the distance to the rear axle (S_r), the wheelbase

length (l_W), the lateral acceleration (a_y), and the slip angles of the front axle wheels and rear axle wheels (α_f) and (α_r), respectively

$$F_{curve} = m\, a_y \left(\frac{S_f}{l_W}\sin(\alpha_r) + \frac{S_r}{l_W}\sin(\alpha_f)\right) \tag{2.1}$$

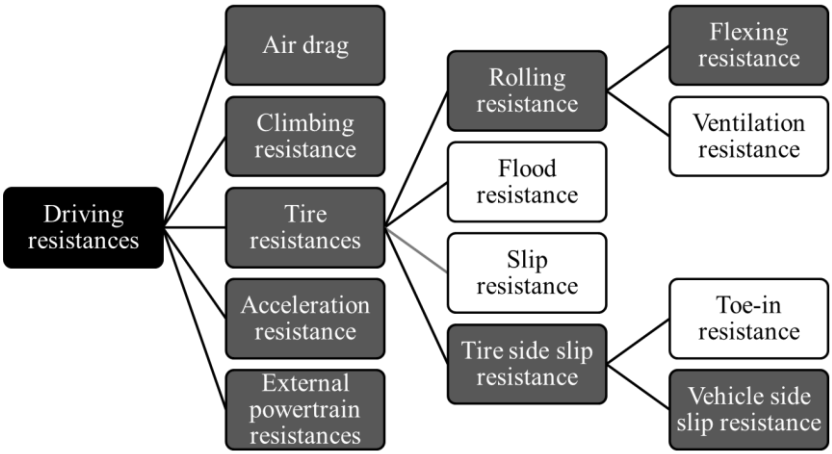

Figure 2.2: Driving resistances diagram (The quantities in white boxes are not considered in this work).

According to (R. Bauer, 2011a), the driving force calculation for a powertrain test bench is known as the road load simulation. Then, by assuming driving on a dry surface and ignoring the toe-in resistance, slip resistance, and the tire rolling resistance (F_R) part from air ventilation, the total driving force (F_d) is expressed by equation (2.2).

$$F_d = F_A + F_R + F_C + F_{acc} + F_{curve} \tag{2.2}$$

where

F_A Air resistance
F_R Rolling resistance
F_{acc} Acceleration resistance

F_C Climbing resistance
F_{curve} Curvature driving resistance.

The air resistance (F_A) acting in the longitudinal direction is dependent upon the vehicle's frontal cross-section area of the vehicle (A_F), the air density (ρ), air resistance coefficient with frontal flow wind (C_d), and the relative air speed in the direction of travel (v_{rel}). These terms are combined in equation (2.3)

$$F_A = \frac{1}{2}\rho\, A_F C_d v_{rel}^2 \,. \tag{2.3}$$

Acceleration resistance (F_{acc}) arises during variations in velocity, whereby the inertia of the vehicle opposes the direction of motion. The rotational mass factor (λ^*) is critical for considering the additional mass influence contributed by the rotating components of the vehicle. Consequently, the acceleration resistance is determined as a function of the longitudinal acceleration (a_x), as given by the equation (2.4)

$$F_{acc} = m\, \lambda^* a_x. \tag{2.4}$$

During acceleration, the engine, i.e., or the electric motor within an electric powertrain, along with other rotating powertrain components such as the wheels, must be angularly accelerated. This process generates a reaction torque that opposes the motive force, an effect which can be represented as an augmentation to the vehicle's actual mass (m). According to (Meywerk, 2015), λ^* is obtained as in equation (2.5). J_E, $J_{a,f}$, $J_{a,r}$ are the inertias of the engine/motor, front axle, and rear axles. i_D, i_g are the gear ratios of the differential gear and the gearbox, respectively, r_e is the effective dynamic rolling radius.

$$\lambda^* = 1 + \frac{\left(J_{a,f} + J_{a,r} + {i_D}^2 {i_g}^2 J_E\right)}{m\, {r_e}^2} \tag{2.5}$$

The climbing resistance (F_C) occurs if the roadway is inclined by an angle (α_{In}).

Therefore, equation (2.6) represents F_C as a function of the sine of α_{In}, and vehicle weight (F_G)

$$F_C = F_G \sin \alpha_{In}. \tag{2.6}$$

Considering the approximately linear relationship of rolling resistance with the wheel normal load (F_{zW}), a load-dependent characteristic can be established using the dimensionless rolling resistance coefficient (f_{RR}). Typical values for the rolling resistance coefficient f_{RR} are shown in Figure 2.3

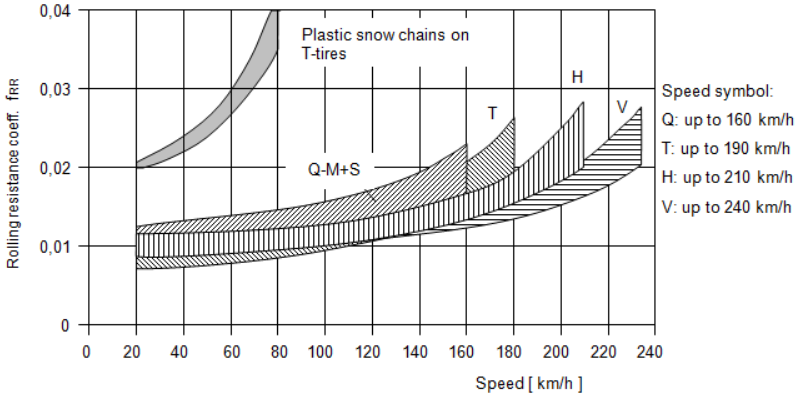

Figure 2.3: Rolling resistance coefficient as a function of the vehicle speed for different wheel constructions (Mitschke & Wallentowitz, 2004).

The study by (Ficht & Lienkamp, 2015) indicates that rolling resistance varies considerably under dynamic driving conditions, with potential increases of approximately 20% above steady-state estimations. Therefore, the tire model developed by (Ficht & Lienkamp, 2015), which accounts for the influences of temperature and velocity, will be utilized to precisely estimate the tire's rolling resistance on the roller. The model defines the steady-state rolling resistance (F_R*) in equation (2.7). The tire's steady-state temperature (T*) is given by equation (2.8), while the transient temperature $T(t)$ is derived from

solving equation (2.9). The rolling resistance force is subsequently expressed in equation (2.10) as a function of speed, temperature, and vertical load

$$F_R{}^* = f_{RR}\, F_{z,W} \tag{2.7}$$

$$T^* = \frac{F_R{}^*\, v_{w0}^k\, v_w^{1-k}}{A_{tire}\, h_0} + T_{amb} \tag{2.8}$$

$$v_w F_R{}^* \left[1 + \varepsilon\left(T^* - T(t)\right)\right] - h_0 \left(\frac{v_w}{v_{w0}}\right)^k A_{tire}\left((T(t) - T_{amb})\right) = m_{tire} c_{p,tire} \frac{dT}{dt} \tag{2.9}$$

$$F_R(t) = F_R{}^* \left[1 + \varepsilon\left(T^* - T(t)\right)\right] \tag{2.10}$$

where

f_{RR}	Rolling resistance coefficient
F_{zW}	Normal force on the tire [N]
A_{tire}	Outer tire surface area [m²]
k	Sensibility exponent factor
h_0	Reference heat exchange coefficient for rubber and air [W/m²/K]
ε	Sensitivity of rolling resistance to temperature [1/K]
C_p	Specific heat transfer factor [J/kg/K]
$F_R(t)$	Instantaneous rolling resistance force [N]
$F_R{}^*$	Steady-state rolling resistance force [N]
m_{tire}	Mass of tire [kg]
T_{amb}	Ambient temperature [°C]
T^*	Steady-state operating temperature [°C]
$T(t)$	Instantaneous operating temperature [°C]
v_{w0}	Reference tire speed [m/s]
v_w	Tire speed [m/s].

The parameters k and h_0 were empirically determined through curve fitting (Ficht & Lienkamp, 2015). The tests, conducted at various reference speeds, yielded optimal results at v_{w0} = 80 km/h (22.22 m/s). The total driving resistance is a composite of multiple factors, extending beyond those previously

mentioned (Gauterin, 2017; Haken, 2018; Mitschke & Wallentowitz, 2004; Haken, 2018).

2.1.2 Tire slip model

The tire constitutes a critical element in vehicular dynamic modeling, serving as the principal medium of interaction between the automobile and the roadway. Consequently, it is fundamental to vehicle handling and performance. The inherent flexibility and pneumatic properties of tires result in strongly nonlinear behavior, complicating their analysis. To characterize the various properties of the vehicle under test (VUT) tires, an empirical equation with fitted coefficients, known as Pacejka's Magic Formula, is employed. All subsequent equations in this section are sourced from (Pacejka, 2006).

The contact patch forces acting on the wheel comprise the traction force (F_{xW}), i.e., *W* denotes wheel's position; front left (FL), front right (FR), rear left (RL), or rear right (RR)), the cornering force (F_{yW}), the normal force (F_{zW}), and the self-aligning torque (M_{zW}). The traction force is a function of slip and the normal force, whereas the cornering force and self-aligning torque are functions of slip angle and normal force. These forces exhibit nonlinear relationships with the normal force. Influenced by rolling resistance and camber parameters, the tread patch forces are utilized to compute the resulting tread patch motions (Pacejka, 2006). The camber steer effect is not considered in this analysis. Derivations for all equations in this section are provided by (Pacejka, 2006).

The Magic Formula is an empirical equation frequently employed to model contact patch forces, also referred as fore and aft forces, within the tire model. The general form of the magic formula is given by

$$Y = D\sin(C\arctan(B\emptyset)), \qquad \emptyset = (1-E)\,X + \left(\frac{E}{B}\right)\arctan(BX). \tag{2.11}$$

The coefficient *D* is the maximum peak value of the curve, *C* determines the

shape of the curve, *B* determines the initial slope of the curve when it is multiplied by the factors *C* and *D*, and *E* is the curvature factor that modifies the location of the peak and the curve curvature. *Y* stands for traction force, cornering force, or self-aligning torque. The variable *X* means the slip (κ) for traction force or slip angle (α) for cornering and self-aligning torque. Coefficients *D, C, B*, and *E* are functions of more than 20
empirical constants specific to individual tires. These constants are derived from extensive experimental data characterizing tire response to varying vertical loads, slip, slip angles, and camber angles. The friction effect is inherently captured within these coefficients through the experimental measurements. Therefore, the model utilizes pre-existing estimates for parameters *D*, *C*, *B*, and *E* (Bakker et al., 1987; Pacejka, 2006). When torque is applied to the wheel's axis of rotation, the longitudinal slip κ occurs, which can be defined by the equation (2.12).

The rolling radius facilitates the calculation of the loaded tire's translational velocity. Under free-rolling conditions with no longitudinal forces, it can be estimated by dividing the tire's travel distance by its angular displacement. Consequently, the effective dynamic rolling radius (r_e) assumes a value bounded by the free unloaded tire radius (r_f) and the distance from the wheel center to the road surface. The sign convention is such that slip is positive when F_{xw} is a driving force and negative during braking. When the angular speed (ω) is zero, indicating a locked wheel, the slip (κ) equals -1. Longitudinal slip is further defined by the ratio of the circumferential slip velocity (V_{sx}) to the longitudinal speed of the wheel center (V_x), as given in equation (2.13)

$$\kappa = -\frac{V_x - r_e\,\omega}{V_x} \tag{2.12}$$

$$\kappa = -\frac{V_{sx}}{V_x}. \tag{2.13}$$

Figure 2.4 depicts the wheel slip point *S* fixed to the wheel rim. Point *S'* represents the tire contact point, situated at the intersection of the plane

through the wheel axis and the road plane. The velocity differential between these points induces a deflection in the carcass equivalent springs. Consequently, the rate of change of this spring deflection in the longitudinal tire direction (*u*) is given by the equation (2.14)

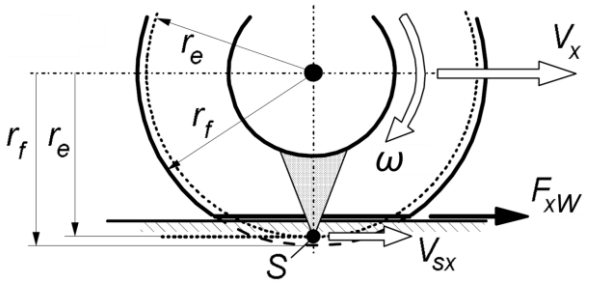

(a) Side view showing the effective dynamic rolling radius

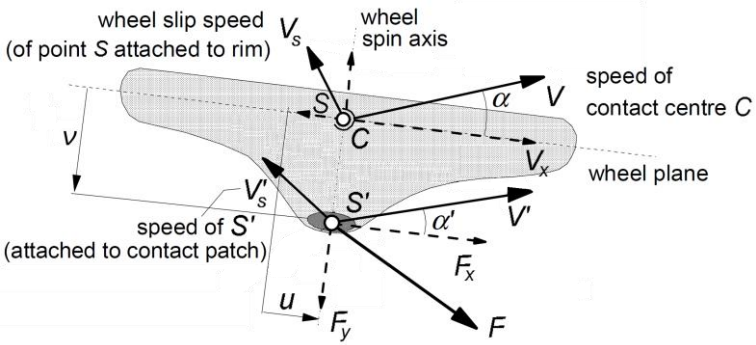

(b) Top view showing the longitudinal and lateral components

Figure 2.4: Single contact point tire model (Pacejka, 2006)

$$\frac{du}{dt} = -(V_{sx} - V'_{sx}) \cdot \tag{2.14}$$

The internal elastic force generates a tire stiffness coefficient at the road level, which equilibrates the slip forces. Under small slip conditions, the longitudinal tire stiffness at the road level is denoted by (C_{Fx}), and the longitudinal slip stiffness by ($C_{F\kappa}$). According to equation (2.15), $C_{F\kappa}$ corresponds to the slope of the longitudinal force (F_{xW}) versus slip (κ) curve at low slip values, as presented in (Schramm et al., 2014).

$$C_{F\kappa} = \left(\frac{\partial F_{xW}}{\partial \kappa}\right)_{\kappa=0} \cdot \tag{2.15}$$

As in equation (2.16), $C_{F\kappa}$ can be approximated from the multiplication of the longitudinal Pacejka's coefficients B_x, C_x, and D_x

$$C_{F\kappa} = B_x C_x D_x \cdot \tag{2.16}$$

The relaxation length is a key parameter governing the lag in slip force response to the input slip. Under low slip conditions, the longitudinal relaxation length (σ_κ) is given by equation (2.17)

$$\sigma_\kappa = \frac{C_{F\kappa}}{C_{Fx}} \cdot \tag{2.17}$$

From equation (2.14), the differential equation for the deflection u is derived. The relationship between u and σ_κ is defined by the differential equation (2.18)

$$\frac{du}{dt} + \frac{1}{\sigma_\kappa} |V_x|\, u = |V_x|\, \kappa = -V_{sx} \,. \tag{2.18}$$

For linear and small slip conditions, the transient longitudinal slip (κ') and the correspondence F_{xW} are determined using equation (2.19)

$$\kappa' = \frac{u}{\sigma_\kappa}\,, \qquad F_{xW} = C_{F\kappa}\,\kappa'. \tag{2.19}$$

A similar formulation applies to the lateral force response. The lateral relaxation length (σ_α) is defined in equation (2.20) as the ratio of tire lateral stiffness at the road level (C_{Fy}) to the cornering stiffness as ($C_{F\alpha}$). The differential equation for lateral deflection (v) is derived from equation (2.21), where the wheel slip angle (α) is approximated as $\alpha \approx -V_{sy}/|V_x|$, with V_{sy} representing the tire lateral slip velocity. Under linear and small slip conditions, the transient lateral slip (α') and the corresponding F_{yW} are given by equation (2.22). The value of $C_{F\alpha}$ is obtained from the slope of the lateral force (F_{yW}) versus α' curve at low slip values, as expressed in equation (2.23). Alternatively, it is approximated by the product of the lateral Pacejka's coefficients B_y, C_y, and D_y, according to equation (2.24)

$$\sigma_\alpha = \frac{C_{F\alpha}}{C_{Fy}} \tag{2.20}$$

$$\frac{dv}{dt} = -\left(V_{sy} - V'_{sy}\right) \tag{2.21}$$

$$\alpha' \approx \tan\alpha' = \frac{v}{\sigma_\alpha}\,, \qquad F_{yw} = C_{F\alpha}\,\alpha' \tag{2.22}$$

$$C_{F\alpha} = \left(\frac{\partial F_{yW}}{\partial \alpha}\right)_{\alpha=0} \tag{2.23}$$

$$C_{F\alpha} = B_y C_y D_y\,. \tag{2.24}$$

Under conditions where the longitudinal velocity V_x approaches zero, equation (2.18) exhibits integrator behavior, which can produce excessive deflection. To maintain physical plausibility and ensure numerical stability, constraints on the longitudinal deflection u are necessary when $V_x < V_{low}$ and the deflection from (2.18) exceeds realistic limits. An approximate value for the

slip at peak longitudinal force, derived from equation (2.25), can be utilized to mitigate simulation instabilities

$$\kappa'_{F_{xW,max}} = A\left(\frac{3D_x}{C_{F\kappa}}\right). \tag{2.25}$$

Employing a scaling factor *A* with a default value of 1, an increased value may enhance performance (Pacejka, 2006). Consequently, the formulation for identifying σ_κ presented in the linear equation (2.17) can be augmented with the nonlinear equation (2.26). Here, $\sigma_{\kappa 0}$ and σ_{min} represent the nominal longitudinal relaxation length and the minimum relaxation length, respectively. σ_{min} is introduced to prevent instability and excessive computational demand. Substituting equation (2.19) into (2.18) yields the differential equation (2.27)

$$\sigma_\kappa = \max\left[\sigma_{\kappa 0}\left(1 - \frac{C_{F\kappa}}{3D_x}\,|\kappa'|\right), \sigma_{min}\right] \tag{2.26}$$

$$\sigma_\kappa \frac{d\kappa'}{dt} + |V_x|\kappa' = -V_{sx}\,. \tag{2.27}$$

At a standstill, the tire operates as a spring (Pacejka, 2006). This is verified from equation (2.14) at $V_x = 0$, where the longitudinal deflection u functions as an integrator $u = -\int V_{sx}\,dt$, provided the lateral deflection is disregarded, i.e., $V'_{sy} = 0$. The longitudinal force is expressed as $F_{xW} = C_{F\kappa}\,\kappa' = C_{F\kappa}\,u/\sigma_\kappa$, which equals to $C_{Fx}\,u$. These relationships indicate that a tire initiating motion from the standstill, it acts like a longitudinal or tangential spring, which transforms into an artificial damper with a rate of $C_{F\kappa}/|V_x|$ as rolling begins. Consequently, the tire's damping characteristic exhibits high stiffness at low velocities. At higher speeds, the tire primarily functions as a damper, whereas at low speeds, particularly during initial acceleration or final deceleration, its behavior is more akin to a deformable spring. This transient spring-damper dynamic is illustrated in Figure 2.5. The damping diminishes as speed increases from zero. The damping coefficient $k_{V,low}$, defined in equation (2.28), is

progressively suppressed to zero as the travel speed V_x approaches a specified low-speed threshold V_{low} from a standstill, according to the formula (2.29)

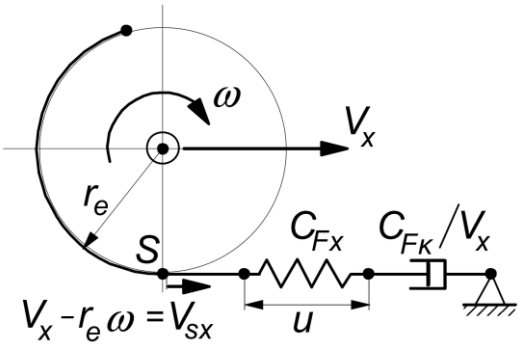

Figure 2.5: A mechanical model of transient tangential tire behavior (Pacejka, 2006)

$$\kappa' = \left(\frac{u}{\sigma_k} - \frac{k_{Vlow}}{C_{F\kappa}}\, V_{sx}\right) \tag{2.28}$$

$$k_{V,low} = \begin{cases} \frac{1}{2} k_{V,low0} \left(1 + \cos\left(\pi \frac{|V_x|}{V_{low}}\right)\right) & if\ |V_x| \le V_{low} \\ 0 \quad if\ |V_x| > V_{low}\ . \end{cases} \tag{2.29}$$

2.1.3 Vertical load distribution and rolling model

The wheel load (F_{zw}) is a critical parameter for the determination of contact patch forces. The longitudinal distribution of the total vehicle weight F_G is predominantly governed by the position of the center of gravity (CG). Key geometric parameters, including the longitudinal distances from the CG to the front (S_f) and rear (S_r) axles, as well as the CG height (h), are illustrated in Figure 2.6. The air drag lift forces are neglected in this model. The front axle wheel loads are derived from the moment equilibrium about the rear tire contact patch, while an analogous procedure, establishing torque balance about

the front tire contact point, yields the rear axle wheel loads (Gauterin, 2017; Haken, 2018). Furthermore, road inclination and vehicular acceleration induce dynamic shifts in axle load distribution, resulting in static and dynamic load components. The static load component for the front and rear axles is computed via the following equations (2.30) and (2.31)

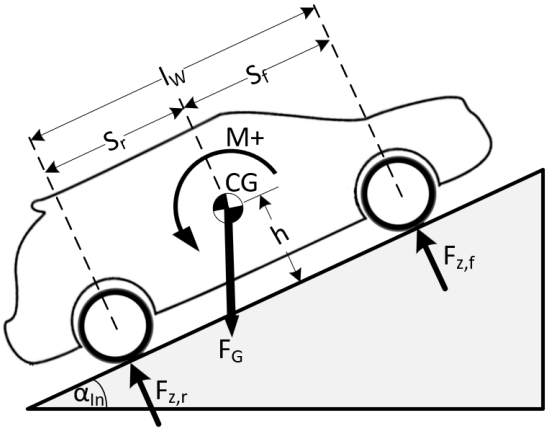

Figure 2.6: Determination of axle load for the typical case of an accelerated up-hill drive (Alhanouti & Gauterin, 2023a)

$$F_{z,f/static} = \frac{S_r}{l_w} F_G \cos\alpha_{In} - \frac{F_G}{l_w} h \sin\alpha_{In} \tag{2.30}$$

$$F_{z,r/static} = \frac{S_f}{l_w} F_G \cos\alpha_{In} + \frac{F_G}{l_w} h \sin\alpha_{In}. \tag{2.31}$$

Acceleration influences wheel load, as the inertial force generated during acceleration acts upon the vehicle's center of gravity in opposition to the acceleration vector. Consequently, the dynamic component of the vertical load on the axles is quantified by equations (2.32) and (2.33) (Gauterin, 2017; Meywerk, 2015)

$$F_{z,f/acceleration} = -m\ a_x\ \frac{h}{l_w} \tag{2.32}$$

$$F_{z,r/acceleration} = m\ a_x\ \frac{h}{l_w}. \tag{2.33}$$

The total axle loads for the front ($F_{z,f/total}$) and rear ($F_{z,r/total}$) axles are subsequently derived by summing the static terms from equations (2.30) and (2.31) with the dynamic terms in equations (2.32) and (2.33), respectively, resulting in equations (2.34) and (2.35), which are applicable to straight driving

$$F_{z,f/total} = \frac{S_r}{l_w} F_G \cos\alpha_{In} - \frac{F_G}{l_w} h \sin\alpha_{In} - m\ a_x\ \frac{h}{l_w} \tag{2.34}$$

$$F_{z,r/total} = \frac{S_f}{l_w} F_G \cos\alpha_{In} + \frac{F_G}{l_w} h \sin\alpha_{In} + m\ a_x\ \frac{h}{l_w}. \tag{2.35}$$

During curve driving, lateral load transfer induces variations in individual wheel loads ($\Delta F_{z,FL}$, $\Delta F_{z,FR}$, $\Delta F_{z,RL}$, $\Delta F_{z,RR}$). This transfer is a consequence of suspension system reaction forces and the centrifugal force (Haken, 2018; Jazar, 2008; Schramm et al., 2014), with the resultant axle loads described by equations (2.36) and (2.37)

$$F_{z,f} = F_{z,f/total} + \Delta F_{z,FL} + \Delta F_{z,FR} \tag{2.36}$$

$$F_{z,r} = F_{z,r/total} + \Delta F_{z,RL} + \Delta F_{z,RR}. \tag{2.37}$$

A linear rolling model, which is valid for small roll angles (φ) and assuming the lateral inertial force acts perpendicular to the direction of motion through the center of mass, can be employed to determine the load distribution across all four wheels during cornering (Schramm et al., 2014). Figure 2.7 demonstrates the forces acting on the vehicle's chassis during corning. The rolling dynamics about the roll center (CR) are governed by several quantities, including the chassis inertia about the x-axis, the heights of the roll center (h_{CR}) and center of gravity (h), and the forces from springs ($F_{F,W}$), dampers ($F_{D,W}$), and anti-roll bars ($F_{St,W}$) at each wheel's position (W). W is specified for each quantity, as

front left (FL), front right (FR), rear left (RL), or rear right (RR)). The distances of the action points of the front and rear springs ($S_{F,f}$), ($S_{F,r}$) are measured from the middle plane of the symmetrically assumed vehicle's body. Likewise, the distances of the front and rear dampers ($S_{D,f}$), ($S_{D,r}$), also the distances of the front and rear anti-roll bars ($S_{St,f}$), ($S_{St,r}$).

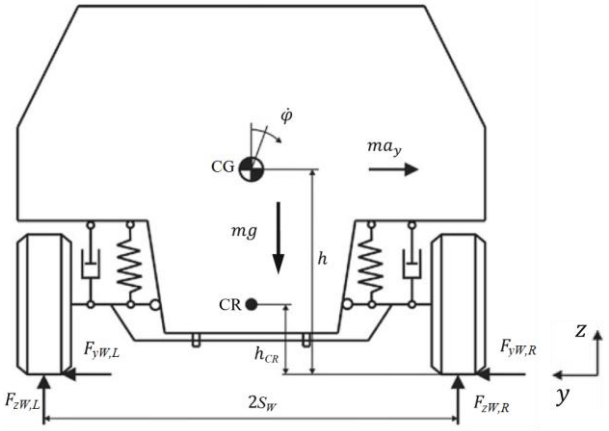

(a) Linear rolling model with front and rear forces

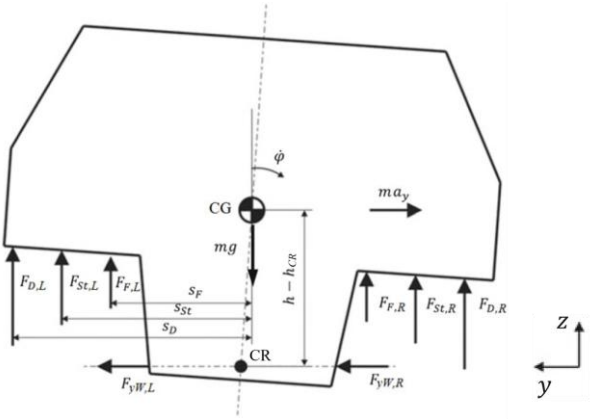

(b) Free body diagram for the rolling model

Figure 2.7: Illustration of the roll dynamics according to (Schramm et al., 2014).

Equation (2.38) expresses the moments' equilibrium of the vehicle around CR in the x-axis direction, where the positive direction is considered, as shown in Figure 2.8 (Schramm et al., 2014)

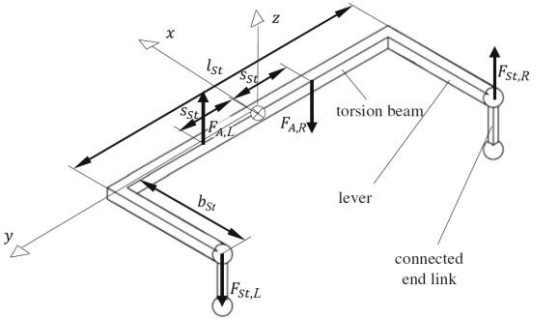

Figure 2.8: Passive anti-roll bar mechanism (Schramm et al., 2014)

$$
\begin{aligned}
I_x\ddot{\varphi} = {} & m\, a_y\, (h - h_{CR}) \cos\varphi + m\, g\, (h - h_{CR}) \sin\varphi \\
& + S_{F,f}\left(F_{F,FL} - F_{F,FR}\right) + S_{F,r}\left(F_{F,RL} - F_{F,RR}\right) \\
& + S_{D,f}\left(F_{D,FL} - F_{D,FR}\right) + S_{D,r}\left(F_{D,RL} - F_{D,RR}\right) \\
& + S_{St,f}\left(F_{St,FL} - F_{St,FR}\right) + S_{St,r}\left(F_{St,RL} - F_{St,RR}\right).
\end{aligned}
\tag{2.38}
$$

The forces exerted by the spring-damper systems are a function of their coefficients (c_F, d_D), the rolling angle (φ), and the rolling rate ($\dot{\varphi}$). The forces for the front suspension, which are given by equations (2.39) – (2.42), have analogous equations that are applicable to the rear (Schramm et al., 2014). Similarly, the forces from the front anti-roll bar, dependent on torsional stiffness (c_{St}) and beam geometry of length, and width (l_{St}, b_{St}), are stated in equations (2.43) and (2.44). By substituting equations (2.39) – (2.44) along with their rear counterpart equations into the general dynamic equation (2.45), φ is determined by solving the differential equation (2.45)

$$F_{F,FL} = -c_{F,f}\, S_{F,f} \sin\varphi \approx -c_{F,f}\, S_{F,f}\, \varphi \tag{2.39}$$

$$F_{F,FR} = c_{F,f}\, S_{F,f} \sin\varphi \approx c_{F,f}\, S_{F,f}\, \varphi \tag{2.40}$$

$$F_{D,FL} = -d_{D,f}\, S_{D,f} \cos\varphi\, \dot{\varphi} \approx -d_{D,f}\, S_{D,f} \dot{\varphi} \tag{2.41}$$

$$F_{D,FR} = d_{D,f}\, S_{D,f} \cos\varphi\, \dot{\varphi} \approx d_{D,f}\, S_{D,f} \dot{\varphi} \tag{2.42}$$

$$F_{St,FL} = -\frac{c_{St,f}}{b_{St,f}} \arcsin\left(\frac{l_{St,f}}{2b_{St,f}} \sin\varphi\right) \approx -\frac{1}{2}\frac{c_{St,f}\, l_{St,f}}{{b_{St,f}}^2}\varphi \tag{2.43}$$

$$F_{St,FR} = \frac{c_{St,f}}{b_{St,f}} \arcsin\left(\frac{l_{St,f}}{2b_{St,f}} \sin\varphi\right) \approx \frac{1}{2}\frac{c_{St,f}\, l_{St,f}}{{b_{St,f}}^2}\varphi \tag{2.44}$$

$$\begin{aligned} &I_x\ddot{\varphi} + 2\left(S_{D,f}^2\, d_{D,f} + S_{D,r}^2\, d_{D,r}\right)\dot{\varphi} \\ &+2\left(S_{F,f}^2\, c_{F,f} + S_{F,r}^2\, c_{F,r} + \frac{S_{St,f}\, c_{St,f}\, l_{St,f}}{2b_{St,f}^2} + \frac{S_{St,r}\, c_{St,r}\, l_{St,r}}{2b_{St,r}^2}\right)\varphi \\ &= m\, a_y\, (h - h_{CR}) + m\, g\, (h - h_{CR}) \sin\varphi. \end{aligned} \tag{2.45}$$

The lateral load transfer for the front and rear axles is derived from equilibrium conditions in the lateral and vertical directions, as well as the moments' equilibrium around CR (Schramm et al., 2014). The summation of vertical forces transmitted to the chassis by the suspension is provided for the front and rear axles in equations (2.46) and (2.47), respectively. Under steady-state cornering, the lateral tire forces per axle would be equivalent to the centrifugal force, as expressed in equations (2.48) and (2.49). On the other hand, the torque equilibrium around CR for each axle is given by equations (2.50) and (2.51), with the resulting moments at the front ($M_{A,f}$) and the rear axles ($M_{A,r}$) are defined by equations (2.52) and (2.53)

$$\Delta F_{z,f} = \Delta F_{z,FL} + \Delta F_{z,FR} = F_{F,FL} - F_{F,FR} + F_{D,FL} - F_{D,FR} + F_{St,FL} - F_{St,FR} \tag{2.46}$$

$$\Delta F_{z,r} = \Delta F_{z,RL} + \Delta F_{z,RR} = F_{F,RL} - F_{F,RR} + F_{D,RL} - F_{D,RR} + F_{St,RL} - F_{St,RR} \tag{2.47}$$

$$F_{y,FL} + F_{y,FR} = \frac{S_r}{l_w} m\, a_y \tag{2.48}$$

$$F_{y,RL} + F_{y,RR} = \frac{S_f}{l_w} m\, a_y \tag{2.49}$$

$$\left(\Delta F_{z,FR} - \Delta F_{z,FL}\right) S_W - \left(F_{y,FL} + F_{y,FR}\right) h_{CR} = M_{A,f} \tag{2.50}$$

$$\left(\Delta F_{z,RR} - \Delta F_{z,RL}\right) S_W - \left(F_{y,RL} + F_{y,RR}\right) h_{CR} = M_{A,r} \tag{2.51}$$

$$M_{A,f} = -S_{F,f}\left(F_{F,FR} - F_{F,FL}\right) - S_{D,f}\left(F_{D,FR} - F_{D,FL}\right) - S_{St,f}\left(F_{St,FR} - F_{St,FL}\right) \tag{2.52}$$

$$M_{A,r} = -S_{F,r}\left(F_{F,RR} - F_{F,RL}\right) - S_{D,r}\left(F_{D,RR} - F_{D,RL}\right) - S_{St,r}\left(F_{St,RR} - F_{St,RL}\right). \tag{2.53}$$

By solving equations (2.46) – (2.53), the solution for the load change distribution of each tire is obtained as in equations (2.54) – (2.57)

$$\Delta F_{z,FL} = -\frac{M_{A,f}}{2S_W} + \frac{S_r}{2l_w}\frac{h_{CR}}{S_W} m\, a_y \tag{2.54}$$

$$\Delta F_{z,FR} = \frac{M_{A,f}}{2S_W} - \frac{S_r}{2l_w}\frac{h_{CR}}{S_W} m\, a_y \tag{2.55}$$

$$\Delta F_{z,RL} = -\frac{M_{A,r}}{2S_W} + \frac{S_f}{2l_w}\frac{h_{CR}}{S_W} m\, a_y \tag{2.56}$$

$$\Delta F_{z,RR} = \frac{M_{A,R}}{2S_W} - \frac{S_f}{2l_w}\frac{h_{CR}}{S_W} m\, a_y\,. \tag{2.57}$$

2.1.4 Single-track vehicle model

The tire contact patch forces (i.e., F_{xW}, F_{yW}, and M_{zW}) contribute to the vehicle body movement since tires are interfacing elements between the vehicle and the road. As shown in Figure 2.9, the vehicle's movement results from the contact patch forces acting at the contact area between the tires and the road. In the Ackermann steering system, the front wheels have different steering angles.

The vehicle model permits the analysis of fundamental driving dynamics relationships within lateral acceleration. First, some quantities need to be defined to develop a reliable model. The equivalent steering angle (δ) is computed according to (Jazar, 2008) by averaging the cotangent of the steering angles of the outer and inner wheels δ_o, δ_i, respectively, as in equation (2.58). The instantaneous turning radius (ρ_k) of the vehicle is a function of the vehicle speed (v), yawing angle (ψ), and vehicle sideslip angle (β). ρ_k is determined using equation (2.59)

$$\cot(\delta) = \frac{\cot(\delta_o) + \cot(\delta_i)}{2} \tag{2.58}$$

$$\rho_k = \frac{v}{\dot{\psi} + \dot{\beta}} \tag{2.59}$$

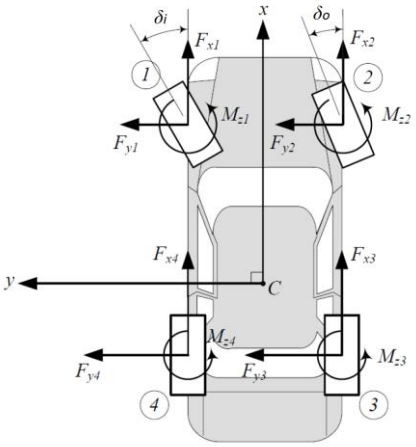

Figure 2.9: Tires forces acting in xy-plane for a vehicle with Ackermann steering system (Jazar, 2008).

The model describes the vehicle motion regarding front and rear axles, as defined in (Schramm et al., 2014). Hence summation of front tires' cornering stiffness ($C_{F\alpha,f}$), as well as rear tires' cornering stiffness ($C_{F\alpha,r}$), are introduced in equations (2.60) and (2.61), respectively. Furthermore, $C_{F\alpha}$ can be determined using equations (2.23) and (2.24)

$$\mathrm{C}_{F\alpha,f} = \mathrm{C}_{F\alpha,FL} + \mathrm{C}_{F\alpha,FR} \tag{2.60}$$

$$\mathrm{C}_{F\alpha,r} = \mathrm{C}_{F\alpha,RL} + \mathrm{C}_{F\alpha,RR}. \tag{2.61}$$

The cornering acceleration (a_y), yawing angle (ψ), and vehicle sideslip angle (β) can be determined in correspondence to a single input that is the steering angle (δ) as stated in equation (2.62) and as in the differential equations sets (2.63) (Jazar, 2008; Schramm et al., 2014), where J_{zz} is the vehicle inertia around the z-axis

$$a_y = \frac{v^2}{\rho_k}, \quad \text{for small } \beta \tag{2.62}$$

$$\begin{bmatrix} \ddot{\psi} \\ \dot{\beta} \end{bmatrix} = \begin{bmatrix} \frac{-1}{v}\left(\frac{C_{F\alpha,f}S_f{}^2 + C_{F\alpha,r}S_r{}^2}{J_{zz}}\right) & -\frac{C_{F\alpha,f}S_f - C_{F\alpha,r}S_r}{J_{zz}} \\ -1 - \frac{1}{v^2}\left(\frac{C_{F\alpha,f}S_f - C_{F\alpha,r}S_r}{m}\right) & \frac{-1}{v}\left(\frac{C_{F\alpha,f} + C_{F\alpha,r}}{m}\right) \end{bmatrix} \begin{bmatrix} \dot{\psi} \\ \beta \end{bmatrix} + \begin{bmatrix} \frac{C_{F\alpha,f}S_f}{J_{zz}} \\ \frac{1}{v}\frac{C_{F\alpha,f}}{m} \end{bmatrix} \delta(t)\,. \tag{2.63}$$

2.1.5 Hydraulic braking simulation model

The pressure distribution among the wheels is determined by CarMaker simulation model. Figure 2.10 shows the power-assisted braking system within the vehicle

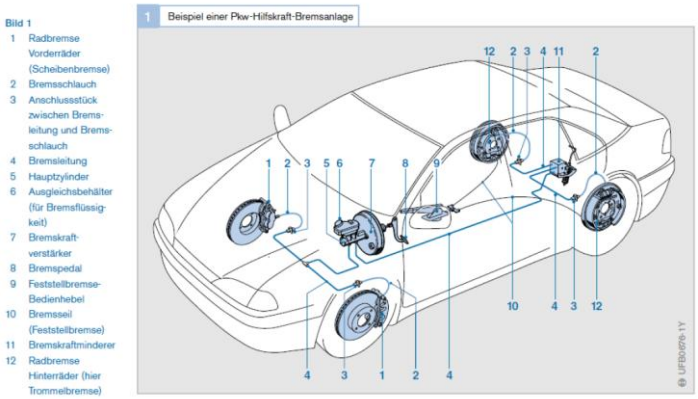

Figure 2.10: Schematic diagram of a vehicle brake system (Reif, 2010).

The braking actuation from the driver is applied to the brake pedal which is mechanically transformed into a braking input force for the brake booster (F_{BooIn}). The brake booster, in turn, amplifies the input braking force and passes its output force (F_{BooOut}) to the master brake cylinder. Then, the piston rod force is converted into the pressure of the master cylinder (p_{MC}), as shown in Figure 2.11. The master cylinder has two hydraulic ports one for the front wheels braking circuit and the other one is for the rear wheels, as illustrated in Figure 2.12

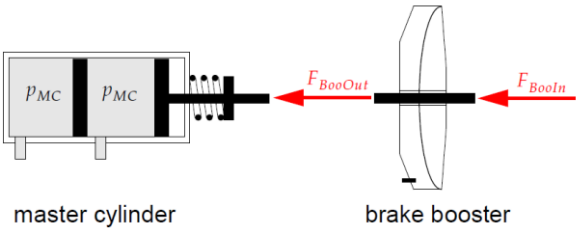

Figure 2.11: Amplification of braking actuation force by the brake booster (IPG Automotive GmbH, n.d.)

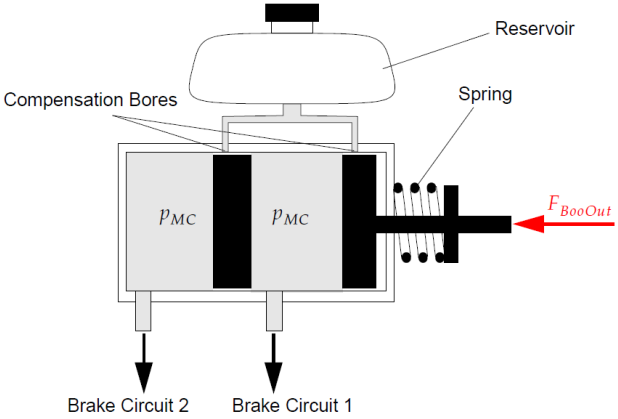

Figure 2.12: master brake cylinder (IPG Automotive GmbH, n.d.).

The brake system in this work is modeled as a conventional hydraulic brake system with disc brakes for the front wheels. Since the rear wheels of the VUT are not driven, they are not included in the powertrain model. However, their effect is considered on the vehicle dynamic model. The disc brake model is available in physical modeling toolbox in SIMULINK library. Figure 2.13 shows the side and front views of a disc brake. R_m is the mean radius of brake pad force applied on the brake disc, R_o is the outer radius of brake pad, R_i is the inner radius of brake pad

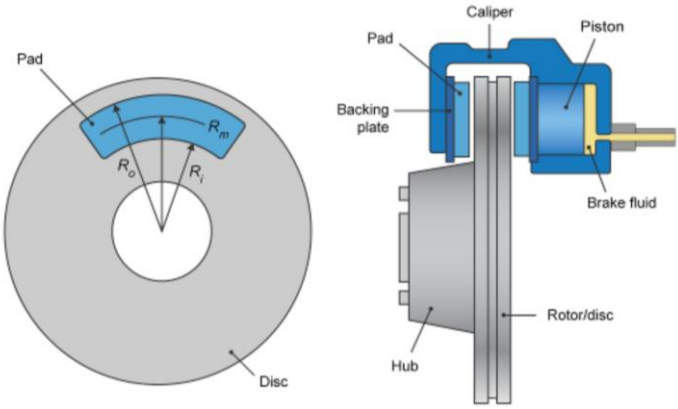

Figure 2.13: Front and side views of a disc brake system (Mathworks Inc., 2023).

The brake is performed as the master cylinder transfers the pressure to the friction pads. Then, the applied pressure causes the pads to exert friction force as they are been pressed against the brake disc.

2.2 Energy consumption estimation in electric vehicles

Over the past decade, interest in sustainable energy and conservation measures has accelerated the adoption of electric vehicles (EVs). Common powertrain configurations include hybrid (HEVs), plug-in hybrid (PHEVs), battery-electric (BEVs), and fuel-cell EVs (FCEVs) (Yao et al., 2013; Contestabile et al., 2011).

(Travesset-Baro et al., 2015). compared internal combustion engine (ICE) and electric vehicles along mountainous routes and found that although BEVs are generally heavier, regenerative braking leads to lower overall energy use. BEVs can achieve nearly double the efficiency of ICEs due to superior powertrain performance (Asamer et al., 2016; Alhanouti & Gauterin, 2024a).

Moreover, electric motors can provide a high torque for a wide-ranging rotational speed. Hence, a single-gear transmission is necessitated, which improves the powertrain's efficiency even more. Generally, a BEV contains fewer rotating parts than an ICE vehicle, causing lower maintenance costs (Prandtstetter et al., 2013). Other researchers focus on estimating the remaining driving range of EVs, and precise estimation of the battery's state of charge (SOC) are popular areas of study (Adaikkappan & Sathiyamoorthy, 2022; Asamer et al., 2016; De Cauwer et al., 2015; Manoharan et al., 2022; Shrivastava et al., 2022; Smuts et al., 2017; Younes et al., 2013; Y. Zhang et al., 2012; Zheng et al., 2018). The factors influencing the remaining range of electric vehicles were systematically investigated in (Smuts et al., 2017) The authors comprehensive survey resulted in a classification of these factors into five key categories: Route and terrain, weather and environment, driving behavior, vehicle modeling, and battery modeling. An experimental investigation of the energy consumption in electric vehicles was presented by (Younes et al., 2013) based on driving course type, driving style, and ambient temperature. The remaining driving range is a sophisticated concept affected by multiple factors complicating its estimation. The vehicle's driving conditions primarily include the reference speeds and the altitude curves. Vehicle speeds and altitude changes are determined based on information such as driving routes, driver's behavior, road traffic, environment conditions, and vehicle dynamics models (Mei et al., 2023).

Several research projects are oriented to establish accurate energy consumption estimations that achieve the optimal energy economy to drive to a particular destination by modeling the driving condition, considering driving style, and selecting the optimal driving route (Wang & Lukic, 2011). Likewise, the authors of (Ahn et al., 2002) developed a mathematical model for vehicle energy consumption based on eight different test vehicles' instantaneous speed and acceleration measurements. The authors considered different influential factors on energy consumption: The roadway grade and roughness, the vehicle interaction with the traffic, and the driver behavior. Developing energy estimation algorithms under realistic conditions became imperative. Subsequently, various concepts are adopted to calculate the accumulated

energy consumption during real driving routes. Some methods are based on sparse GPS observations (J. Wang et al., 2017), where readings from 68 EVs were used in a linear regression approach to calibrate an energy consumption prediction model. In comparison, some other approaches adapted to kinetic and potential energy changes during the trip, as in (Wu et al., 2015), in which a measured and estimated energy consumption process in a customized conversion electric vehicle was realized by collecting the data for energy consumption for different routes with alternating driving modes. Another approach for energy consumption modeling oriented toward quantifying correlations between energy consumption in electric vehicles and its kinematic parameters using real-world data has been developed (R. Zhang & Yao, 2015).

Two main approaches are used to model EVs (Mapelli & Tarsitano, 2012). The first is forward modeling, also known as the "dynamic approach." The second is the backward modeling, also known as the "quasi-static approach." The Forward approach is characterized by a causal structure that solves the differential equations governing component dynamics and their interactions. This method does not presume a driving cycle but requires a driver or controller model to manage vehicle speed. Its foundation in dynamic equations yields high precision, though this comes at the expense of significant computational resources. The Backward approach adopts an inverse simulation strategy. It begins with a predefined reference velocity trajectory and calculates the corresponding forces at the wheels. This demand is then propagated backward through the powertrain to determine the necessary motor moment and, eventually, the energy to be supplied by the battery. This method relies on analytical models of vehicle dynamics and efficiency maps for loss estimation, resulting in a computationally efficient solution that forgoes high dynamic resolution. Consequently, the choice of methodology is dictated by the study's focus—whether it prioritizes the accurate simulation of transient dynamics (favoring the forward approach) or the rapid estimation of energy consumption over a standard cycle (favoring the backward approach) (Fiori et al., 2016). In general, computational models require more processing than analytical models. However, they are more precise as they operate based on

data analysis and prediction. Besides, analytical models can only respond to changes in vehicle performance as they are vehicle dynamics-dependent and based on physical modeling. More details about the advantages and disadvantages of these approaches are available in (Horrein et al., 2012; Miri et al., 2021).

The authors of (Asamer et al., 2016) conducted a sensitivity analysis to evaluate the precision of battery electric vehicle (BEV) energy demand estimation. Their methodology employed a mechanical modeling approach, incorporating driving resistances and powertrain losses. The analysis identified the uncertainty associated with powertrain efficiency and the rolling resistance coefficient as the most influential factors on estimation accuracy. Furthermore, their findings indicated that the uncertainty in auxiliary power demand, particularly for cabin climate control systems, has a substantial impact on accuracy at lower velocities. In a subsequent study, the authors of (Miri et al., 2021) emphasized the necessity for a high-fidelity, power-based model for EV energy consumption. Their research utilized a forward-looking simulation architecture integrating a powertrain system, longitudinal vehicle dynamics, and a driver model. Efficiency maps for the electric motor and power electronics were derived from technical specifications of a specific vehicle. The model's input was a reference driving cycle, which the driver model was designed to track. Validation was performed against standard driving cycles within a simulation environment, without recourse to physical field testing. It is noted, however, that the model's applicability may be constrained by its dependency on efficiency maps unique to a particular EV and its incorporation of a simplified battery model with static parameters.

The battery system is one of the most vital components of an electric vehicle. Within the spectrum of developing technologies for energy storage, lithium-ion batteries (LiBs) are widely regarded as the most promising alternative, a status attributed to their distinctive advantages including high energy density, minimal maintenance requirements, and extended cycle life (Kohrs, 2017; Shrivastava et al., 2022). A critical parameter for battery management is the

SOC, which represents the available remaining charge. Accurate estimation of SOC is particularly vital for LiBs, as their operational integrity is compromised by both over-charging and over-discharging, thereby necessitating highly precise SOC prediction (Manoharan et al., 2022). The methodologies for SOC estimation can be categorized into five primary approaches based on battery modeling: the tank model, empirical models, lumped-parameter equivalent circuit models (ECMs), machine learning models, and electrochemical model-based estimation (Asamer et al., 2016). Among these, ECM-based estimation has become the predominant technique for online applications, such as in electric vehicles, due to its capacity to simulate the voltage response of an actual LiB to a given current excitation. However, in reality, some characteristics of the LiBs might not be adequately represented by circuit elements, such as the hysteresis effect.

The authors of (R. Zhang & Yao, 2015) developed a regression model depending on instantaneous speed, acceleration, and the SOC. The developed model encloses four driving modes: Acceleration, deceleration, cruising, and idling. Likewise, in (De Cauwer et al., 2015), the developed models have regression parameters that were attained based on the aggregated data from the real-world trips. Which is extended in (De Cauwer et al., 2017) by creating a multiple linear regression model to estimate energy consumption. Many other studies reviewed the latest SOC estimation methods to define the pros and cons of each approach, including physical modeling state estimation (Adaikkappan & Sathiyamoorthy, 2022; Shrivastava et al., 2022) or Artificial Intelligence techniques (Adaikkappan & Sathiyamoorthy, 2022; Manoharan et al., 2022). Moreover, the authors added a neural network model to predict microscopic driving parameters. In a similar context, a model to estimate the energy consumption for EVs was proposed in (Qi et al., 2018). The authors of (Younes et al., 2013) benefit from the acceleration distribution and altitude difference. They are classified as positive kinetic energy, relative positive acceleration, and the standard deviation of the variation of the battery current. In (Yi & Bauer, 2017), an adaptive multiresolution approach was proposed for real-time energy consumption estimation in electric vehicles. A two-step

nonlinear iterative algorithm was utilized to approximate three key parameters: Powertrain efficiency, wind speed, and rolling resistance. The first step involves a linear estimation with a Kalman filter, while the second step entails a nonlinear optimization search.

The precise modeling of battery dynamics across diverse operational scenarios is fundamental to the accurate forecasting of energy consumption in electric vehicles (Alhanouti et al., 2016). Within this context, the reliable estimation of the SOC is a critical parameter. Techniques such as empirical open-circuit voltage (OCV) modeling and look-up table interpolation are characterized by their low computational demands. The direct OCV-based method for SOC estimation, in particular, achieves a favorable balance between computational efficiency and estimation accuracy (Alhanouti et al., 2016). Furthermore, when integrated with an Equivalent Circuit Model (ECM), the OCV-based approach can be effectively extended to dynamic operating conditions (Asamer et al., 2016). A significant advantage of this method is the fundamental consistency of the OCV curve across LiBs, permitting the application of experimentally derived curves in online estimation systems, thereby establishing OCV-based estimation as a highly practical solution. Nevertheless, the relative stability of OCV characteristics in LiBs, they are subject to variation due to factors such as cycle life and temperature (Lavigne et al., 2016; Marongiu et al., 2016). Consequently, establishing a robust SOC-OCV correlation necessitates empirical data that quantifies the influence of these aging and environmental conditions (Adaikkappan & Sathiyamoorthy, 2022). Despite these dependencies, the methodological error associated with OCV-based SOC estimation remains comparatively lower than that of alternative approaches, as shown in Figure 2.14

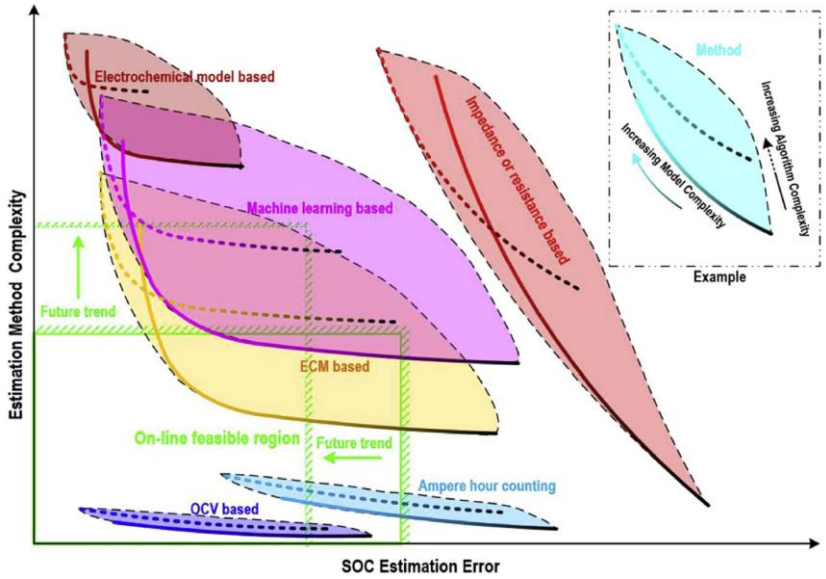

Figure 2.14: Estimation error and computational complexity for the common SOC estimation methods (Zheng et al., 2018).

Although the OCV area is located in the online feasible region, special attention should be given to the influences of temperature, aging, and hysteresis (Zheng et al., 2018). Our prior research (Alhanouti et al., 2016) successfully addressed these limitations by integrating an empirical OCV model, expressed as a function of SOC and temperature, with an ECM. Furthermore, the components of the internal resistance model were also formulated as functions of SOC and temperature. The model additionally accounts for charge-discharge hysteresis and incorporates capacity fade to represent battery aging. This integrated model has demonstrated high accuracy in simulating highly dynamic maneuvers from real-world driving profiles. Consequently, based on these established results and the supporting investigation by (Marongiu et al., 2016), the model from (Alhanouti et al., 2016) is adopted for the LiB modeling in the present work.

This study identifies critical factors influencing the accuracy of electric vehicle energy consumption estimation, such as the formulation of detailed vehicle dynamics models, high-resolution assessments of powertrain efficiency, and the effect of route-specific environmental conditions. Prior research has often utilized either methodologies of excessive complexity, which hinder generalization, or oversimplified approaches that compromise precision. To address these shortcomings, this work proposes a generalized modeling framework. This framework employs predefined efficiency maps for different electric motor sizes and delivers an approximated efficiency map for power electronics. Furthermore, it integrates a sophisticated battery model, established in earlier work by the authors, to substantially enhance estimation accuracy. Subsequently, a comprehensive vehicle model incorporating the battery system is presented. A principal feature of this model is its systematic method for forecasting both energy consumption and variations in the battery SOC. Model inputs consist of measured vehicular speed during a driving maneuver, initial SOC, and auxiliary power demand, enabling precise calculation of energy consumption. Validation is conducted using empirical data from a test vehicle, with due consideration given to auxiliary devices owing to their significant effect on estimation accuracy. The methodology is furthermore structured for compatibility with a wide array of motor and power electronic systems.

2.2.1 Adaptable energy consumption model for the electric powertrain

The authors of (Genikomsakis & Mitrentsis, 2017) proposed a computational model for energy consumption in EVs. They introduced an adaptable battery model based on technical data. The model's accuracy is promoted by incorporating the technical specifications of electric machines, which are employed to generate efficiency curves for both motor and generator operation phases. This study enhances the model established by (Genikomsakis & Mitrentsis, 2017) through the integration of more detailed models for driving resistance and the battery system. The driving resistance formulation is

detailed in Section 2.1.1. A precise battery model is necessary to accurately estimate the energy consumption associated with a maneuver test. Electric motors typically achieve optimal operational efficiency at approximately 75% of their rated load, with effective performance generally sustained between 50% and 100% of full load. Efficiency declines significantly when operating below 50% load. Figure 2.15 illustrates load-efficiency curves for standard electric motors across various rated power levels, with motor sizes indicated in horsepower (hp). These curves, developed using curve fitting methods, categorize motors with analogous efficiency characteristics; each curve thus represents all motors within the specified power range (US Department of Energy, 2014)

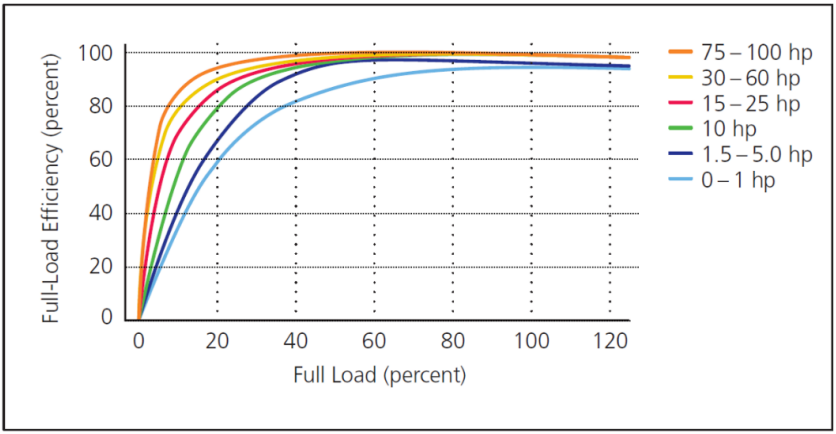

Figure 2.15: Motor load efficiencies for motors with different power (US Department of Energy, 2014).

According to (Genikomsakis & Mitrentsis, 2017), motor efficiency can be estimated as a function of the fraction (x), which is defined as the ratio of the absolute value of the mechanical output power (P_{mo}) in W to the rated motor power (P_{mr}) in kW, expressed as $x = 0.001|P_{mo}|/P_{mr}$. The generalized efficiency for an electrical machine, applicable in both motor (η_{mot}) and generator (η_{gen}) modes, is given by equation (2.64). The coefficients for this equation,

obtained through curve fitting of data from multiple motors, are provided in Table 2.1

$$\text{efficiency}(x) = \begin{cases} \dfrac{\text{cout1}\ x + \text{cout2}}{x + \text{cout3}}, & 0 \le x < 0.25 \\ \text{dout1}\ x + \text{dout2}, & 0.25 \le x < 0.75 \\ \text{eout1}\ x + \text{eout2}, & x \ge 0.75. \end{cases} \tag{2.64}$$

Table 2.1: Coefficients for determining efficiency in equation (2.64) (Genikomsakis & Mitrentsis, 2017)

	Induction electric machine		**Synchronous electric machine**	
Coefficient	**Motor mode**	**Generator mode**	**Motor mode**	**Generator mode**
cout1	0.924300	0.925473	0.942269	0.942545
cout2	0.000127	0.000148	0.000061	0.000067
cout3	0.012730	0.014849	0.006118	0.006732
dout1	0.080000	0.075312	0.060000	0.057945
dout2	0.860000	0.858605	0.905000	0.904254
eout1	−0.073600	−0.062602	−0.076000	−0.066751
eout2	0.975200	0.971034	1.007000	1.002698

A principal characteristic of electrical machines is that their efficiency increases with their physical size (McCoy & Douglass, 2014). Consequently, when determining the efficiency of an electrical machine for a given output power, the initial efficiency value obtained from equation (2.64) must be multiplied by a normalization factor (f_{norm}) a scaling coefficient derived from the motor's rated power. For operations involving regenerative braking, this efficiency must be further multiplied by a regenerative factor (f_{regen}) as detailed by (Genikomsakis & Mitrentsis, 2017). The data from this source are derived from empirical measurements on multiple engines across various power ranges. Figure 2.16 illustrates the relationship between the efficiency normalization factor and the rated output power. According to this figure, the value of f_{norm} for a 45 kW motor is 0.978 for the test vehicle

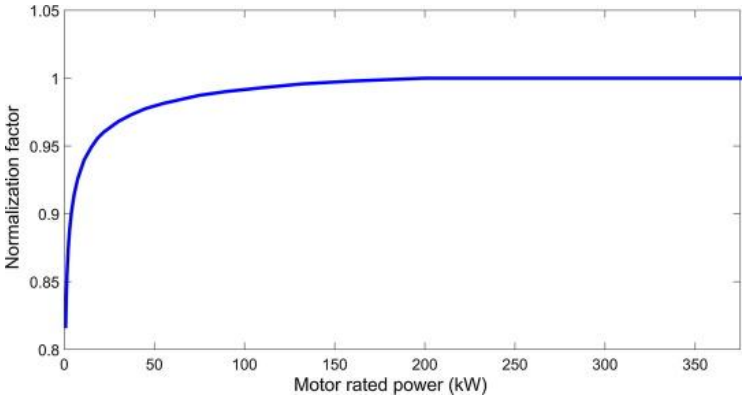

Figure 2.16: Normalization factor curve (Genikomsakis & Mitrentsis, 2017).

The total gear transmission mechanical losses are evaluated by the efficiency (η_g) (Kurczveil et al., 2014). The test vehicle model considers the losses in the transmission, differential, and shaft joints. The authors of (Fiori et al., 2016) also developed an energy consumption model for EVs with a deceleration-dependent regenerative braking efficiency model. They validated their model with different electric vehicles over several typical driving cycles. The energy consumption of EVs depends on the traction energy, as well as the auxiliary device consumption (Ramsey et al., 2022; Wang & Lukic, 2011).Therefore, the vehicle model must comprise them for more accurate energy consumption estimation (Miri et al., 2021; Ramsey et al., 2022). The authors of (De Cauwer et al., 2015) analyzed the impact of auxiliary systems load on energy consumption by performing the simulation at three different ambient temperatures. Consequently, the total power output from the battery must also supply the auxiliary load (P_{aux}) in addition to providing power to the motor or absorbing power from the generator. As energy consumption from auxiliary devices is influenced by multiple variables, certain devices are deactivated during testing to minimize uncertainty in estimating P_{aux} (Yao et al., 2013). To simplify the analysis, average power values are assigned to represent the typical consumption of each auxiliary device in an EV. The effective power

consumption during testing is subsequently calculated according to the operational duration of each active device (Miri et al., 2021). It is noted that the energy consumption for P_{aux} is measured empirically in this study, rather than being derived from a model. In the model proposed by (Genikomsakis & Mitrentsis, 2017),, a constant correction factor is applied to the power model to account for the round trip efficiency loss. Conversely, the present study utilizes a detailed physical battery model that integrates multiple variable loss factors to determine the terminal battery voltage.

Losses in the power electronics result from the conversion of direct current from the battery to a three-phase current for the motor. Motor torque is directly proportional to current. Therefore, in high-torque operating regions, typically depicted in the upper section of the efficiency map, the current passing through the power electronics rises substantially. This elevated current induces greater conduction losses, which are particularly pronounced at lower rotational speeds (RPM), where high motor moment is required to overcome inertia and load resistance. In contrast, motor speed determines the inverter switching frequency. At high RPM, especially under low torque conditions, the increased switching frequency leads to higher switching losses, despite the relatively low current. Thus, the efficiency of the power electronics (η_{pe}) can be represented using an efficiency map similar to that of the electric machine, as illustrated in Figure 2.17. The power electronics used for this efficiency map estimation are the insulated-gate bipolar transistor (IGBT), consistent with the VUT. The data presented in this figure correspond to a motor with a maximum power of 100 kW (März, 2010). The front-wheel-driven VUT powertrain topology is shown in Figure 2.18. The VUT motor is powered by alternating current (AC), delivered from the power electronics that convert the battery's direct current (DC)

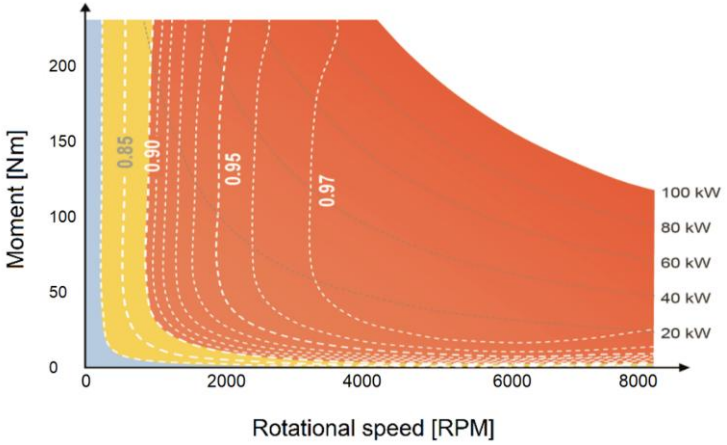

Figure 2.17: Power electronics efficiency map as a rotational speed vs moment resresentation (März, 2010)

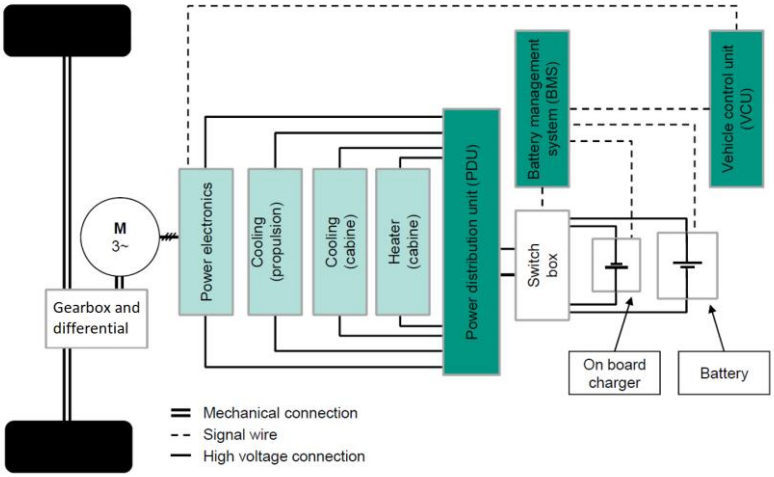

Figure 2.18: Basic drive train topology of the Mercedes A-Class research vehicle (Fritz et al., 2012).

The battery management system (BMS) regulates charging and discharging processes while monitoring the temperature of the battery pack modules. A signal indicating “torque demand”, generated by the accelerator pedal, is interpreted by the vehicle control unit (VCU) and converted into an appropriate output based on the vehicle's current driving operational state, battery condition, motor, and pedals inputs. The asynchronous machine specifications of the VUT are listed in Table 2.2.

Table 2.2: Technical data of the VUT electric motor (Alhanouti & Gauterin, 2023b)

Parameter	**Value**
Rated power	45 kW
Peak power	68 kW
Peak torque	210 Nm
Rated speed	3000 RPM
Maximum Speed	13000 RPM
Number of poles	6

2.2.2 Battery model

The battery pack of the VUT consists of 19 battery modules. Each module encompasses 300 lithium iron phosphate ($LiFePO_4$)–graphite cells (Alhanouti et al., 2016). The battery module specifications are given in Table 2.3.

Table 2.3: Technical data of $LiFePO_4$ Battery module (Valence Technology Inc., 2011)

Parameter	**Value**	**Unit**
Nominal battery module voltage	19.2	V
Nominal battery module capacity	69	Ah
Nominal battery voltage	364.8	V
Max continuous battery load current	120	A
Peak battery current for 30 s	200	A

The VUT comprises battery cell units of a $LiFePO_4$ cathode. These cells are distinguished from other battery types, such as lead-acid, Nickel Metal Hydride, and Nickel-Cadmium, by their open-circuit voltage curves that remain almost constant over the SOC range from 20% to 80%, even at different ambient temperatures (Alhanouti et al., 2016). The same model developed in (Alhanouti et al., 2016), which accurately simulates the changes in the battery during dynamic maneuvers, will also be employed in this work. The proposed battery model is capable of simulating the OCV curves of $LiFePO_4$ batteries across a range of temperatures, accounting for both charging and discharging states, in addition to the variations in the battery internal resistance. Furthermore, a lumped thermal model is incorporated to capture the temperature evolution within the battery. The battery model requires the following inputs: The battery current, the SOC signal, the corresponding capacity rates (C-rate), the ambient and battery temperatures, and the number of charging and discharging cycles the battery underwent. The battery circuit model diagram is shown in Figure 2.19

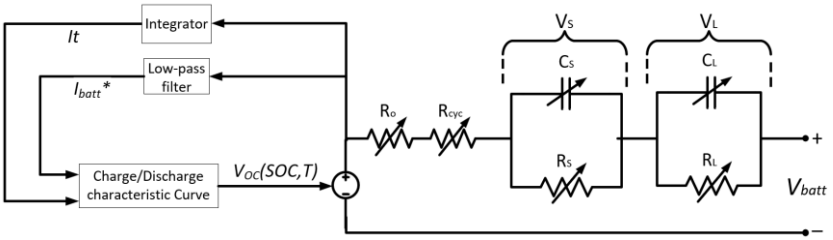

Figure 2.19: Battery circuit model (Alhanouti et al., 2016) .

The open circuit voltage (V_{OC}) is influenced by SOC and temperature. The remaining circuit part, which involves the equivalent resistances and capacitances elements, is responsible for determining the voltage drop. The battery circuit model also comprises a variable ohmic resistance (R_O), which signifies the electric conductivity of the electrolyte, anode, cathode, and separator, with the separator playing a crucial role in preventing direct contact between the anode and cathode, facilitating ion transport. The battery circuit model

considers also the capacity fading effect by adding resistance in series (R_{cyc}). Additionally, two variable RC circuits: R_SC_S that characterizes the fast transient response to voltage changes, and R_LC_L contributes to the slower time response effect. The corresponding voltage to R_SC_S is V_S. Similarly, V_L represents the voltage of the R_LC_L circuit. I_{batt} is the input current of the battery voltage model, and V_{batt} is the battery model output voltage. The filtered battery current (I_{batt}*), which is used to avoid inserting the noise of the current signal to the battery model, and the integration of the battery current over time (It) are required inputs for determining the open-circuit voltage (V_{OC}). The proposed V_{OC} model in (Alhanouti et al., 2016), as a function of the battery SOC and temperature, is represented by equations (2.65) and (2.66). According to (Alhanouti et al., 2016), the open voltage is modeled by separate equations in case of discharging, i.e., $V_{OC,dis}$ and charging, i.e., $V_{OC,ch}$. The corresponding constant values are given in Table 2.4.

Table 2.4: V_{OC} parameter values (Alhanouti et al., 2016)

Constant	Unit	Value	Constant	Value	Unit
a_1	V	−1.166	b_1	−0.9135	V
a_2	-	35	b_2	−35	-
a_3	V	3.344	b_3	3.484	V
a_4	V	0.1102	b_4	0.1102	V
a_5	V	−0.172	b_5	−0.1718	V
a_6	-	2×10^{-3}	b_6	8×10^{-3}	-
$dV_{OC,d}/dT$	V/K	0.00125	$dV_{OC,c}/dT$	0.00069	V/K

The effect of the temperature on the discharge and charge curves over SOC are taken into account through the constant gradients $dV_{OC,d}/dT$ and $dV_{OC,c}/dT$ respectively

$$V_{OC,dis}(SOC,T) = a_1\, e^{-a_2\, SOC} + a_3 + a_4\, SOC + a_5\, e^{-\frac{a_6}{1-SOC}} + T_{batt}\frac{dV_{OC,d}}{dT} \tag{2.65}$$

$$V_{OC,ch}(SOC,T) = b_1\, e^{-b_2\, SOC} + b_3 + b_4\, SOC + b_5\, e^{-\frac{b_6}{1-SOC}} + T_{batt}\frac{dV_{OC,c}}{dT}. \tag{2.66}$$

By neglecting the temperature differences between the cells in the same battery block, the temperature variations of the battery module (T_{batt}) can be described in equation (2.67) (Wijewardana et al., 2016)

$$M_{batt}\, C_p \frac{dT_{\mathrm{batt}}}{dt} = I_{batt}(V_{\mathrm{OC}} - V_{\mathrm{batt}}) - h\, A_{batt} \Delta T - \epsilon\, \sigma\, A_{batt}(T_{\mathrm{cell}}^4 - T_{\mathrm{amb}}^4) \qquad (2.67)$$

where ΔT is the temperature difference between the battery cell and the ambient ($T_{cell} - T_{amb}$). The constants of equation (2.67) are defined and evaluated in Table 2.5.

Table 2.5: Battery thermal model parameter list (Alhanouti et al., 2016)

Symbol	Description	Value	Unit
A_{batt}	Battery module surface area	0.284	m^2
M_{batt}	Battery module mass	12	kg
C_p	Specific heat capacity	1360	$J{\cdot}kg^{-1}{\cdot}K^{-1}$
σ	Stefan-Boltzmann constant	5.67×10^{-8}	$W{\cdot}m^{-2}{\cdot}K^4$
ε	Emissivity of heat	0.950	-
h	Natural heat convection constant	4	$W{\cdot}m^{-2}{\cdot}K^{-1}$

R_{cyc} is identified in (Wijewardana et al., 2016), as shown in equation (2.68), as a function of the number of charging and discharging cycles (n_{cyc}). The usable battery capacity (C_{usable}) is a function of n_{cyc} and temperature (Erdinc et al., 2009). Figure 2.20 shows the percentage of C_{usable} from the initial capacity (C_0) over the n_{cyc} and at a reference ambient temperature of 23 °C. A simple definition for the change in SOC is made by equation (2.69) (Wijewardana et al., 2016), where SOC_0 is the initial state of charge. The values of the internal resistance components of resistances and capacitors are determined through equations (2.70) – (2.74) (Lam et al., 2011). Where ϑ is the battery cell temperature [K], and the constants c_1–c_{39} values are listed in Table 2.6

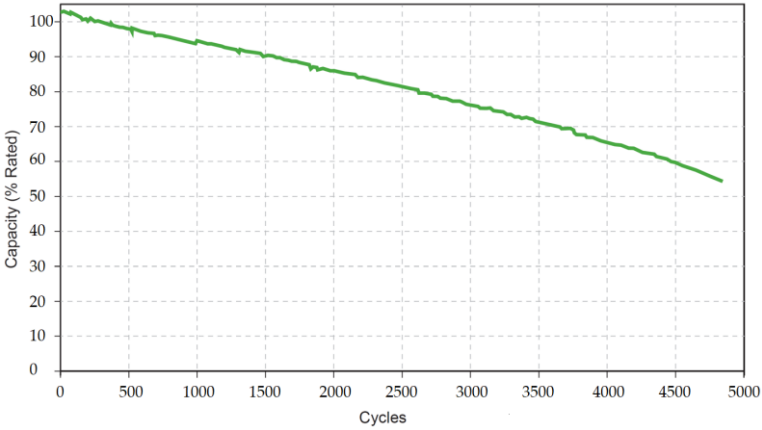

Figure 2.20: Measured discharge capacity performance for a single battery module at 23 °C (Valence Technology Inc., 2011).

The equations (2.75) and (2.76) incorporates multiple nonlinear and dynamic terms to capture the complexity of battery discharging and charging. V_{batt} is expressed as a function of OCV, which varies with the SOC and temperature, and is reduced by ohmic and cycle-induced voltage drops represented by $(R_O+R_{cyc})\cdot I_{batt}$. Additional dynamic voltage contributions VS and VL model short- and long-term effects, respectively. The nonlinear terms involving $K_{pc}Q/(Q-It)\cdot It$, $K_{pr}Q/(Q-It)\cdot I^*_{batt}$, and $K_{pr}Q/(\text{It-0.1Q})\cdot I^*_{batt}$ account for voltage losses due to charge depletion and hysteresis. An exponential decay term $Ae^{-B\cdot It}$ is included to capture short-term voltage recovery. This hybrid empirical electrical model enables accurate voltage prediction across varying load profiles by integrating electrochemical, thermal, and aging effects.

These parameters apply to the same battery cell type ($LiFePO_4$–graphite). Furthermore, the simulation results using these parameters will be validated by measurements. The total estimated battery output voltage (V_{batt}) is modeled as in equation (2.75) (Alhanouti et al., 2016). According to (Tremblay & Dessaint, 2009), the hysteresis effect between the discharge and charge behaviors is considered in V_{batt} by implementing two different equations, i.e., (2.75)

for discharging and (2.76) for charging. This work enhances the V_{batt} model proposed in (Tremblay & Dessaint, 2009) by adding variable internal resistances and open-circuit voltages. The parameters of the equations (2.75) and (2.76) are defined and evaluated in Table 2.7

$$R_{cyc} = 0.0015\left(n_{cyc}\right)^{0.5} \tag{2.68}$$

$$SOC(t) = SOC_0 - \int_0^t (I_{batt}/C_{usable})\, d\tau. \tag{2.69}$$

The battery internal resistance parameters in equation (2.77) are acquired by multiplying the corresponding battery cell internal resistance parameter, calculated by equations (2.70)–(2.74), by the total number of cells. *Q* defines the exponential part of the discharge characteristic curve, upon which the discharged voltage changes exponentially regarding to the capacity of the battery. I_{batt} is the battery current, I^*_{batt} is the filtered battery current, and *It* is the integration over time of the battery current, as shown in Figure 2.19

$$R_{s,cell}(\mathrm{SOC},\vartheta) = \left(c_1 e^{(c_2\mathrm{SOC})} + c_3 + c_4\mathrm{SOC}\right) + c_5\Delta\vartheta + c_6\ \mathrm{SOC}\ \Delta\vartheta \tag{2.70}$$

$$C_{s,cell}(\mathrm{SOC},\vartheta) = (c_7\mathrm{SOC}^3 + c_8\mathrm{SOC}^2 + c_9\mathrm{SOC} + c_{10}) + c_{11}\mathrm{SOC}\ \Delta\vartheta + c_{12}\Delta\vartheta \tag{2.71}$$

$$\begin{aligned} R_{l,cell}(\mathrm{SOC},\vartheta,I_{C-rate}) = \Big(\left(c_{13}\mathrm{e}^{(c_{14}\mathrm{SOC})} + c_{15} + c_{16}\mathrm{SOC}\right) + c_{17}\Delta\vartheta\mathrm{e}^{(c_{18}\mathrm{SOC})} \\ + c_{19}\,\Delta\vartheta\Big) \times (c_{20}\,(I_{C-rate})^{c_{21}} + c_{22}) \end{aligned} \tag{2.72}$$

$$\begin{aligned} C_{l,cell}(\mathrm{SOC},\vartheta) = (c_{23}\mathrm{SOC}^6 + c_{24}\mathrm{SOC}^5 + c_{25}\mathrm{SOC}^4 + c_{26}\mathrm{SOC}^3 + c_{27}\mathrm{SOC}^2 \\ + c_{28}\mathrm{SOC} + c_{29}) + c_{30}\mathrm{e}^{\frac{c_{31}}{\vartheta}} \end{aligned} \tag{2.73}$$

$$R_{o,cell}(\mathrm{SOC},\vartheta) = (c_{32}\mathrm{SOC}^4 + c_{33}\mathrm{SOC}^3 + c_{34}\mathrm{SOC}^2 + c_{35}\mathrm{SOC} + c_{36})\ c_{37}\ \mathrm{e}^{\frac{c_{38}}{\vartheta - c_{39}}} \tag{2.74}$$

$$\begin{aligned} V_{\mathrm{batt}} = V_{\mathrm{OC,dis}}(\mathrm{SOC},T) - \left(R_O + R_{\mathrm{cyc}}\right)\cdot I_{batt} + V_S + V_L - K_{pc}\frac{Q}{Q-It}\cdot It \\ - K_{pr}\frac{Q}{Q-It}\cdot I^*_{batt} + A\ \mathrm{e}^{-B\cdot It} \end{aligned} \tag{2.75}$$

$$V_{\text{batt}} = V_{\text{OC,ch}}(\text{SOC}, T) - \left(R_O + R_{\text{cyc}}\right) \cdot I_{batt} + V_S + V_L - K_{pr}\frac{Q}{It - 0.1Q} \cdot I^*_{batt} - K_{pc}\frac{Q}{Q - It} \cdot It + A\,\text{e}^{-B \cdot It} \tag{2.76}$$

$$\frac{dV_S}{dt} = \frac{I_{batt}}{C_S} - \frac{V_S}{R_S C_S}, \qquad \frac{dV_L}{dt} = \frac{I_{batt}}{C_L} - \frac{V_L}{R_L C_L}. \tag{2.77}$$

Table 2.6: Constants values of equations (2.70)–(2.74) (Lam et al., 2011)

Constant	Value	Constant	Value	Constant	Value	Constant	Value
c_1	1.080×10^{-2}	c_{11}	−6.580	c_{21}	-6.919×10^{-1}	c_{31}	-2.398×10^{3}
c_2	−11.03	c_{12}	12.11	c_{22}	2.902×10^{-1}	c_{32}	1.298×10^{-1}
c_3	1.827×10^{-2}	c_{13}	2.950×10^{-1}	c_{23}	2.130×10^{6}	c_{33}	-2.892×10^{-1}
c_4	-6.462×10^{-3}	c_{14}	−20.00	c_{24}	-6.007×10^{6}	c_{34}	2.273×10^{-1}
c_5	-3.697×10^{-4}	c_{15}	4.722×10^{-2}	c_{25}	6.271×10^{6}	c_{35}	-7.216×10^{-2}
c_6	2.225×10^{-4}	c_{16}	-2.420×10^{-2}	c_{26}	-2.958×10^{6}	c_{36}	8.980×10^{-2}
c_7	1.697×10^{2}	c_{17}	6.718×10^{-3}	c_{27}	5.998×10^{5}	c_{37}	7.613×10^{-1}
c_8	-1.007×10^{3}	c_{18}	−20.00	c_{28}	-3.102×10^{4}	c_{38}	10.14
c_9	1.408×10^{3}	c_{19}	-5.967×10^{-4}	c_{29}	2.232×10^{3}	c_{39}	2.608×10^{2}
c_{10}	3.897×10^{2}	c_{20}	6.993×10^{-1}	c_{30}	3.128×10^{3}		

The equations (2.75) and (2.76) incorporates multiple nonlinear and dynamic terms to capture the complexity of battery discharging and charging. V_{batt} is expressed as a function of OCV, which varies with the SOC and temperature, and is reduced by ohmic and cycle-induced voltage drops represented by $(R_O+R_{cyc})\cdot I_{batt}$. Additional dynamic voltage contributions V_S and V_L model short- and long-term effects, respectively. The nonlinear terms involving $K_{pc}Q/(Q-It)\cdot It$, $K_{pr}Q/(Q-It)\cdot I^*_{batt}$, and $K_{pr}Q/(It-0.1Q)\cdot I^*_{batt}$ account for voltage losses due to charge depletion and hysteresis. An exponential decay term A

$e^{-B.It}$ is included to capture short-term voltage recovery. This hybrid empirical electrical model enables accurate voltage prediction across varying load profiles by integrating electrochemical, thermal, and aging effects.

Table 2.7: Parameters list for the battery discharge voltage model (Tremblay & Dessaint, 2009)

Symbol	Description	Value	Unit
K_{pc}	Polarization constant	0.012	V/(Ah)
K_{pr}	Polarization resistance	0.012	Ω
Q	Battery capacity	Variable	Ah
A	Exponential zone amplitude	0.271	V
B	Exponential zone time constant inverse	152.130	$(Ah)^{-1}$

The battery voltage model is already validated in (Alhanouti et al., 2016). However, all test maneuvers are performed with relatively low speeds and short testing periods due to the size of the testing site. Therefore, the VUT underwent the Worldwide harmonized Light vehicles test procedure class two (WLTP2) driving cycle on a roller dynamometer test bench, shown in Figure 2.21, to validate the model for higher speeds and a more extended test period

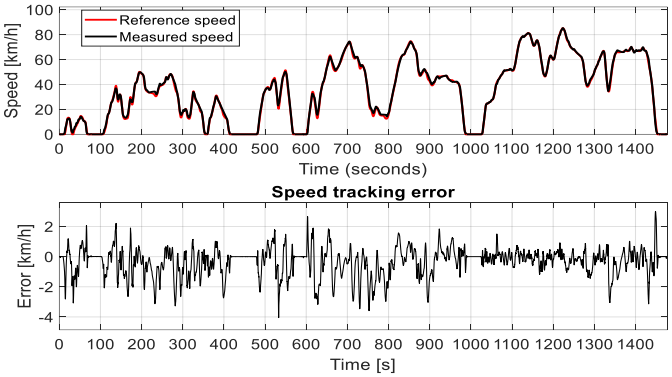

Figure 2.21: WLTP2 cycle tracking performance (Alhanouti & Gauterin, 2023b).

Figure 2.22 displays that the battery model estimated the total battery-pack output voltage, corresponding to the measured battery current, with a high Pearson correlation coefficient ($\rho_{X,Y}$) (Montgomery & Runger, 2010) of 0.981 and a root mean square error (RMSE) is equal to 0.948 V

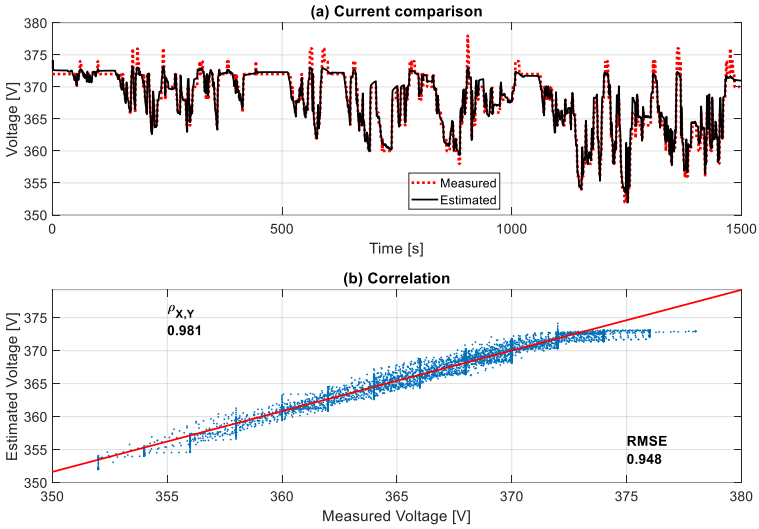

Figure 2.22: The correlation between the measured and estimated V_{batt} for the WLTP2 cycle test (Alhanouti & Gauterin, 2023b).

This high accuracy is related mainly to the variable internal resistance model, shown in Figure 2.19, and to considering the temperature influences (Alhanouti et al., 2016). The battery model must be as accurate as possible because the total energy consumption will be linked directly to the accuracy of the estimated V_{batt} and I_{batt}. Several factors are considered in the battery model to accurately estimate the output voltage using the measured battery current as an input. The most significant factors for battery modeling are charging-discharging different behaviors, changes in internal resistance, open circuit voltage, and battery temperature influences. The simulated battery

voltage was validated using measurements from real driving maneuvers. Based upon the available data shown in Figure 2.20, the battery aging factor is taken into account as the percentage change of the usable battery capacity (C_{usable}) as a function of the number of charging and discharging cycles. Nevertheless, it must be emphasized that the estimation of SOC using the ampere-hour counting method, represented by equation (2.69) is not reliable for long-time simulations without continuous regulation for the accumulated measurement error in I_{batt} and the error from estimating C_{usable}, which is affected by several factors, such as temperature (Manoharan et al., 2022; Zheng et al., 2018). Because of these reasons, the measured SOC signal is considered in this work for estimating V_{batt} and I_{batt}. Further tests are conducted in (Alhanouti & Gauterin, 2023b, 2024a) to validate the energy consumption using the estimated values of V_{batt} and I_{batt}. The I_{batt} estimation will be explained in the next section.

2.3 Creation and validation of the complete vehicle energy consumption model

The complete model of the VUT is shown in Figure 2.23. This model is integrated from the submodels developed in Sections 2.1 and 2.2. Instead of requiring multiple inputs to simulate a particular driving maneuver, the model can determine the physical quantities of the assigned maneuver. The reference speed initiates the computation process within the backward simulation model, which comprises two main submodels of the vehicle dynamics model. By entering the vehicle's desired longitudinal velocity (V_x) as an input to the simulation model, the corresponding traction force (F_{xW}), calculated from the tire slip model, will take part in estimating the angular speed for each wheel. The road gradient contributes an additional climbing force, thereby increasing the total resistance force acting on the vehicle. First, the vertical load ($F_{zW,i}$) on each tire is determined as described in Sections 2.1.3 and 2.1.4. Then it determines the contact patch forces according to the tire model in Section 2.1.2. The method used to estimate the wheel angular speed

is a further improvement to the concepts developed in (R. Bauer, 2011a, 2011b; Pillas, 2017), considering more detailed models of the driving resistance and the tire. Figure 2.24 demonstrates the relation between the driving moment on the wheel ($M_{drive,i}$), determined from equation (2.2) of the driving resistance model, and the moment from F_{xW} multiplied by r_e. As in equation (2.78), the rotational acceleration for the corresponding wheel ($\dot{\omega}_i$) is estimated by dividing the equation by the wheel inertia (J_W). Then ω_i is determined according to equation (2.79), while the tire slip is considered in the quantity F_{xW} of the corresponding tire

$$J_W \, \dot{\omega}_i = M_{drive,i} - F_{xW,i} \, r_e \tag{2.78}$$

$$\omega_i = \int_0^t \frac{1}{J_W} \left(M_{drive,i} - F_{xW,i} \, r_e \right) d\tau. \tag{2.79}$$

Then, the mechanical power at the wheels (P_{mech}) can be estimated according to equation (2.80). The P_{mech} sign indicates whether the vehicle is in driving or braking modes. In the case of driving, the battery provides an equivalent power that covers the P_{mech} demands plus the powertrain power losses (P_{loss}) and the power demand of the auxiliary systems (P_{aux}). Next, the battery current (I_{batt}) corresponds to each of the estimated mechanical power at the wheels, the powertrain power losses, and the corresponding battery voltage (V_{batt}) is estimated using equation (2.81). The total cumulative energy consumption $E(t)$ is calculated as integrating the total power over time, as shown in equation (2.82)

$$P_{mech} = \sum_{i=1}^{4} M_{drive,i} \, \omega_i \tag{2.80}$$

$$I_{batt} = \frac{P_{mech} + P_{loss} + P_{aux}}{V_{batt}} \tag{2.81}$$

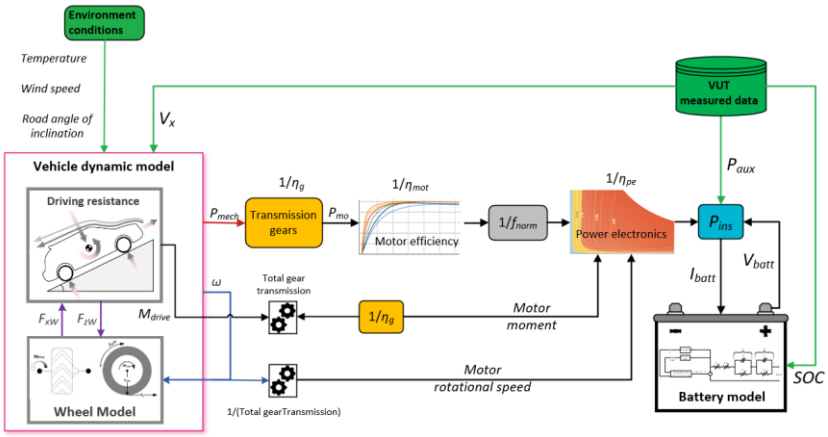

Figure 2.23: Integrated energy consumption model for electric vehicles (Alhanouti & Gauterin, 2023a).

The approach proposed in (Genikomsakis & Mitrentsis, 2017) to simplify the regenerative braking modeling is also implemented in this work. Furthermore, the combined mechanical and regenerative braking systems are complementary due to the electrical machine's physical limitations and the maximum limit of the battery SOC. Suppose the braking moment exceeds the moment limits; in that case, the rest of the braking power is dissipated as heat due to the mechanical braking (Y. Gao & Ehsani, 2009; Kubaisi, 2018). Moreover, the percentage of regenerative braking taking effect has a speed-dependent regeneration factor f_{regen}, as a function of vehicle speed V_x: below the speeds lower threshold limit, no regenerative braking is produced, and therefore, the mechanical braking system is exclusively responsible for decelerating the vehicle to a standstill. Mainly, a lower threshold speed must be surpassed so that the electrical machine regenerates energy, while it achieves its maximum regeneration capability for speeds higher than an upper threshold speed. For speeds between these two thresholds, the percentage of recoverable power follows a linear interpolation with vehicle speed. The same lower and upper threshold speeds implemented in (Genikomsakis &

Mitrentsis, 2017) are 1.39 m/s (5 km/h) and 4.72 m/s (17 km/h), which are considered for this work as well. Equation (2.83) describes the instantaneous power at the time (*t*)

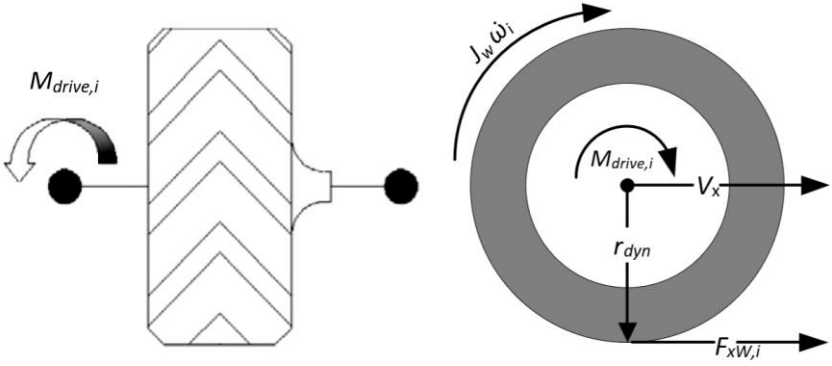

Figure 2.24: Relation between $M_{drive,i}$, $F_{xW,i}$, and ω_i (Alhanouti & Gauterin, 2023a).

$$E(t) = \int_{t_0}^{t} P_{ins}(\tau) d\tau \tag{2.82}$$

$$P_{ins}(t) = \begin{cases} \dfrac{P_{mech}(t)}{\eta_{pe}\,\eta_g\,\eta_{mot}(x)\,f_{norm}} + P_{aux}\,, & P_{mech}(t) \geq 0 \\ P_{mech}(t)\,\eta_{pe}\eta_g\eta_{gen}(x)\,f_{norm}\,f_{regen}(V_x) + P_{aux} & P_{mech}(t) < 0 \end{cases} \tag{2.83}$$

where

P_{ins}	Total powertrain's instantaneous power (electrical power at the battery)
P_{mech}	Mechanical power
η_{pe}	Power electronics efficiency
η_g	Total gear transmission efficiency
η_{mot}	Motor efficiency
η_{gen}	Generator efficiency
x	Fraction of the motor's mechanical power
f_{norm}	Normalization factor
f_{regen}	Regenerative braking factor as a function of V_x
P_{aux}	Auxiliary power.

There are several significant advantages to forming that long sequence of computations. Primarily, the power transformation in the VUT system from mechanical to electrical power can be estimated, including the different involving quantities, as elaborated in Sections 2.1 and 02.2. Moreover, the influence on the energy consumption of different factors that reform the speed profile can be investigated using this model, such as the roadway grade, roughness, and vehicle interaction with the traffic (Brundell-Freij & Ericsson, 2005).

2.4 Validation of the complete vehicle model

The developed vehicle model is validated using the measured data of the test vehicle. The validation target is to determine the estimation accuracy of the power transferred through the electric vehicle's powertrain, i.e., the electrical power consumed from the battery and then transformed into mechanical driving power and power losses. The test vehicle was driven in a circular path with a 30 m turning radius of about 385 s. The driver applied a dynamic pedal input to create a very dynamic response. The test results are displayed in Figure 2.25.

The positive battery current corresponds to the discharged current during the driving mode, whereas the negative values occur during the braking. It can be noticed that the voltage dropped drastically during the high acceleration driving, then remained around 370 V while braking. After the total gear ratio transmission, the final drive moment is produced, responding similarly to the battery current. Finally, the electric motor rotational speed along the maneuver is also shown. The parameters employed in the test vehicle dynamics model are demonstrated in Table 2.8.

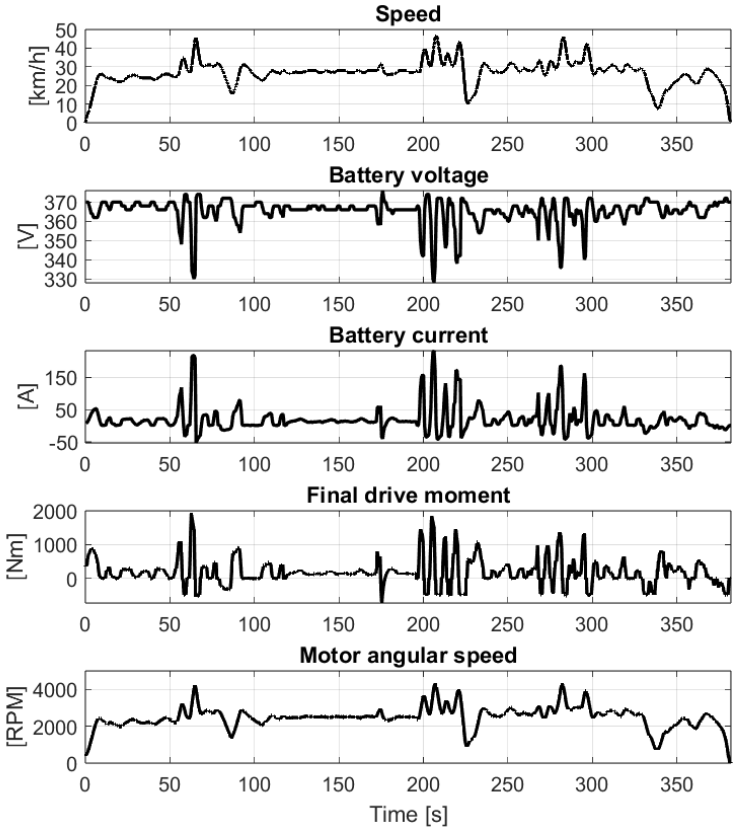

Figure 2.25: Measured data from the VUT field driving test (Alhanouti & Gauterin, 2023a)

The average rotational speed of the front axle is estimated for both wheels, then the car's motor rotational speed is calculated considering the total gear ratio. The motor's rotational speed is estimated accurately with a correlation of 0.997 to the measured rotational speed, as illustrated in Figure 2.26. The corresponding wheels' driving moment estimation is also accurate, with a correlation of 0.984 to the measured moment.

Table 2.8: Parameters list for the VUT dynamic models

Symbol	Description	Value	Unit
m	Vehicle mass	1528	kg
J_{xx}	Moment of inertia about the longitudinal axis	482	kg·m²
J_{zz}	Moment of inertia about the vertical axis	2585	kg·m²
l_w	Wheelbase	2.59	m
S_f	Distance between center of gravity and the front axle	1.47	m
S_r	Distance between center of gravity and the rear axle	1.11	m
h	Height of the vehicle's center of gravity	0.45	m
i_g	Transmission gear ratio	4	-
i_D	Differential gear ratio	2.5	-
J_E	Vehicle engine/motor inertia	0.03	kg·m²
$J_{a,f}$	Front axle inertia	$3.7x10^{-3}$	kg·m²
$J_{a,r}$	Rear axle inertia	$3.7x10^{-3}$	kg·m²
J_t	Tire inertia	0.87	kg·m²
J_W	Wheel inertia	1.33	kg·m²
f_{RR}	Rolling resistance coefficient	0.015	-
A_{tire}	Outer tire surface area	0.6	m²
k	Sensibility exponent factor	0.5	-
h_0	Reference heat exchange coefficient for rubber and air	55	W/m²/K
ε	Sensitivity of rolling resistance to temperature	0.014	1/K
C_p	Specific heat transfer factor	1670	J/kg/K
m_{tire}	Mass of tire	12	kg
T_{amb}	Ambient temperature	298.15	K
v_{w0}	Reference tire speed	22.2	m/s
h_{CR}	Height of the vehicle's rolling center	0.31	m
S_W	Half-track width between front wheels or rear wheels	0.78	m
$S_{F,f}$	Distances of the front suspension from the middle	0.78	m
$S_{D,f}$	Distances of the front damper from the middle	0.78	m
$S_{St,f}$	Distances of the acting point of the front anti-roll beam	0.78	m
$S_{F,r}$	Distances of the rear suspension from the middle	0.78	m
$S_{D,r}$	Distances of the rear damper from the middle	0.78	m
$S_{St,r}$	Distances of the acting point of the rear anti-roll beam	0.78	m
$c_{F,f}$	Spring stiffness front	21269	N/m
$d_{D,f}$	Damping coefficient front	2244	N·s/m
$c_{St,f}$	Stiffness of the front anti-roll bar	7019	Nm/rad
$c_{F,r}$	Spring stiffness rear	17374	N/m
$d_{D,r}$	Damping coefficient rear	1551	N·s/m

$c_{St,r}$	Stiffness of the rear anti-roll bar	5733	Nm/rad
$l_{St,f}$	Length of the front anti-roll bar	1.49	m
$l_{St,r}$	Length of the rear anti-roll bar	1.49	m
$b_{St,f}$	Width of the front anti-roll bar	0.37	m
$b_{St,r}$	Width of the rear anti-roll bar	0.37	m
B_x	Longitudinal force initial slope in Pacejka formula	23.64	-
C_x	Longitudinal force shape factor in Pacejka formula	1.35	-
D_x	Longitudinal force peak factor in Pacejka magic formula	6.3	kN
E_x	Longitudinal force curvature factor in Pacejka formula	1.37	-
B_y	Lateral force initial slope in Pacejka formula	18.05	-
C_y	Lateral force shape factor in Pacejka formula	2.17	-
D_y	Lateral force peak factor in Pacejka magic formula	7.83	kN
E_y	Lateral force curvature factor in Pacejka formula	0.99	-
B_z	Aligning torque initial slope in Pacejka formula	16.37	-
C_z	Aligning torque shape factor in Pacejka formula	1.13	-
D_z	Aligning torque peak factor in Pacejka magic formula	1.17	-
E_y	Aligning torque curvature factor in Pacejka formula	0.89	-
r_e	Tire-effective dynamic rolling radius	0.31	m
C_{Fx}	Tire longitudinal stiffness coefficient	134	kN/m
$C_{F\alpha}$	Tire cornering stiffness coefficient	19.53	kN/rad
$\sigma_{\kappa 0}$	Tire longitudinal nominal relaxation length	1.5	m
$\sigma_{\alpha 0}$	Tire lateral nominal relaxation length	1.35	m
σ_{min}	Tire minimum relaxation length	0.05	m
V_{low}	Low-speed threshold	2.50	m/s
$k_{V,low0}$	Tire damping coefficient at low speed	770	N·s/m
-	Tire's width	186	mm
-	Tire's ratio of height to width	65	-
-	Tire's size	R15	-
-	Tire's load Index	88	-
-	Tire's speed Index	T	-

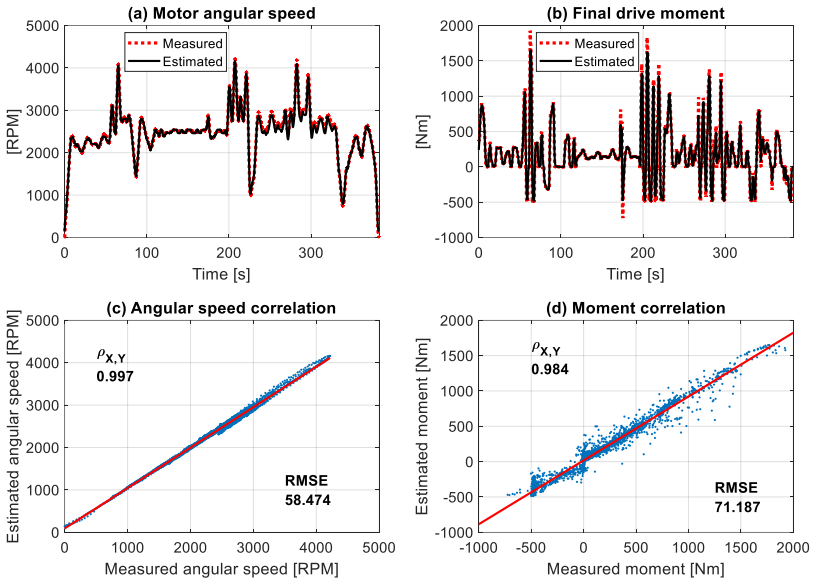

Figure 2.26: Comparison between the measured and estimated values for both the motor angular speed and the final driving moment at the wheels during the field maneuver test

The RMSE values are 58.474 RPM and 71.187 Nm for the estimated motor's rotational speed and the final driving moment on the wheels, respectively. Given the measured speed, as shown in Figure 2.23, the VUT Simulation model was able to estimate the mechanical power that needs to be delivered by the powertrain to overcome the corresponding driving resistances. The accuracy of P_{mech}, attained from the multiplication of the estimated angular speed and moment, has a correlation of 0.983 compared to the expected, as in Figure 2.27 and a RMSE value of 2.309 kW. After confirming the accuracy of P_{mech}, the power losses in the powertrain need to be taken into account to estimate the total powertrain's power (P_{ins})

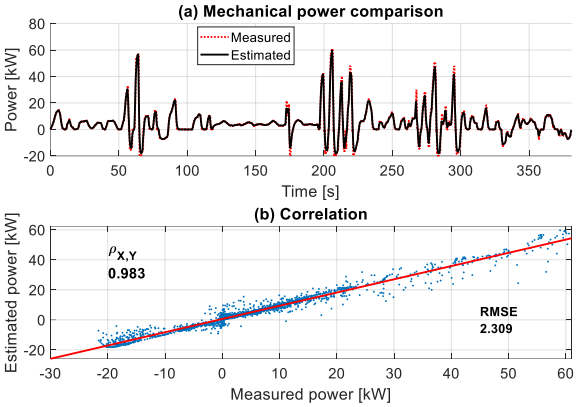

Figure 2.27: The correlation between the measured and estimated VUT powertrain's mechanical power during the field maneuver test (Alhanouti & Gauterin, 2023a).

Referring to equation (2.83), f_{norm}, η_{pe}, η_g, and P_{aux} are required to determine $P_{ins}(t)$:

- f_{norm} for the VUT electrical machine class is 0.978, according to Table 2.2 and Figure 2.16,
- η_{pe} is determined from Figure 2.17 at each motor's rotational speed,
- η_g is set to 0.97, similar to the VUT in (Genikomsakis & Mitrentsis, 2017). P_{aux} is determined based on the best match to the experimental results. The value of 300 W yielded the best match with measurements, which is also similar to the P_{aux} value in (Genikomsakis & Mitrentsis, 2017). As shown in Figure 2.28, an excellent overall match is achieved with a correlation of 0.973 and a RMSE of 3.022 kW.

P_{aux} could have a wide range of variations depending on the operation of other energy-consuming devices, such as air conditioning (De Cauwer et al., 2015, 2017). The next step is to estimate the electrical power factors, which

are the V_{batt} during the maneuver and the resulting I_{batt} from the battery pack. They are estimated using the model shown in Figure 2.23

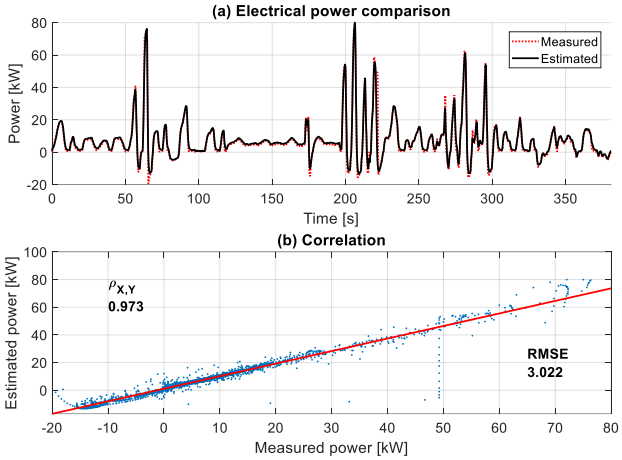

Figure 2.28: The correlation between the measured electrical power and the estimated P_{ins} during the field maneuver test (Alhanouti & Gauterin, 2023a).

Figure 2.29(a) reveals that the estimation of I_{batt} from this complex model is remarkably accurate, with a correlation of 0.973 relative to the corresponding measurements, as shown in Figure 2.29(b). Due to the low precision of the voltage measurements, as shown in Figure 2.29(c), the correlation of V_{batt} to the measured voltage has slightly diminished to 0.964, as shown in Figure 2.29(d). The battery current RMSE value is equal to 8.749 A, while the voltage RMSE reached 1.771 V. The accuracy of results is ascribed to the detailed modeling and accurate parametrization, especially for the battery model. Despite the frequent and severe fluctuations of different physical quantities along the measurements, the integrated model of several submodels did not accumulate high errors after this series of calculations

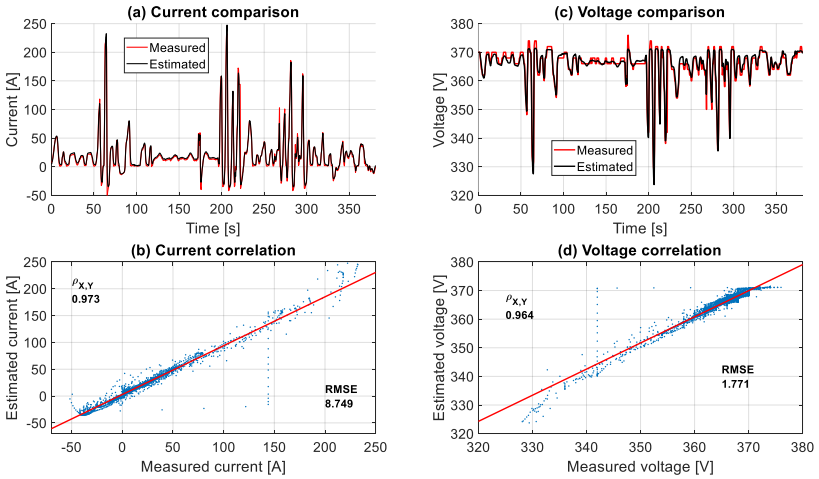

Figure 2.29: The correlation between the measured and estimated values for I_{batt} and V_{batt} during the field maneuver test (Alhanouti & Gauterin, 2023a).

2.5 Conclusion

The foundation of this work lies on the development of a reliable vehicle model that can capture the essential dynamics of driving in real-world conditions. By constructing detailed representations of resistive forces, load distributions, tire behavior, and energy consumption, it becomes possible to create virtual vehicles that serve both as predictive tools and as references for experimental validation. Such models are critical not only for simulation but also for their integration into physical test benches, where they guide the configuration of complete vehicle test benches and ensure that test accurately replicates the road conditions.

3 Chassis roller dynamometer

The chassis dynamometers are widely used in test environments in vehicle development due to their relatively simple configurations and versatility (Mayyas et al., 2013; Paulweber & Lebert, 2016). Their scope involves vehicles, from motorcycles to heavy industrial machinery. Roller test benches can be easily integrated into diverse research and development applications. In addition, they play a chef role in developing the advanced functionalities of modern mobility. A typical use for a chassis dynamometer will be to assign a standard driving cycle as a reference speed with time. Then, the performance of the test vehicle is evaluated after it undergoes the designated driving cycle. As regulatory frameworks increasingly demand precise energy consumption and emission measurements under standardized driving cycles, it becomes crucial to refine the methodologies applied to roller bench testing. This requires not only careful consideration of the mechanical setup, such as the restraining system and roller configuration, but also advanced modeling approaches to better represent real-world conditions. Central to this effort are improved models of tire–roller interaction, friction estimation techniques, and thermal influence assessments, all of which impact the credibility of test results.

This chapter therefore focuses on systematically addressing these interrelated aspects of chassis dynamometer testing. First, the fundamental principles and applications of chassis roller dynamometers are introduced, followed by a detailed analysis of the restraining point height and its effect on traction force transmission. This is complemented by experimental evaluations of energy consumption under standard driving cycles, with particular attention given to the role of restraint systems. The dissertation then proposes an approach to estimate tire–roller friction and develops an enhanced tire model to better capture dynamic behavior on the test bench. Finally, the thermal influence of rollers on tire performance and the validation of an

improved power estimation model are discussed, aiming to provide a comprehensive framework for enhancing test bench accuracy and applicability.

3.1 Introduction

The loading machines of the chassis dynamometer generate moments according to a driving resistance curve corresponding to the rollers' rotational speeds, considering the rollers inertias and the bearing friction losses. The driving resistance curve is commonly identified as an n-order polynomial whose coefficients are determined by regression methods on the results of several experiments (Düser et al., 2011). According to (Martyr & Plint, 2012), there is a noticeable difference between running a tire on a flat road and running it on rollers of different diameters. The modified rolling resistance at the roller is approximated in (Clark, 1976) as in equation (3.1)

$$F_{RR} = F_R \left(1 + \frac{r}{R_r}\right)^{\frac{1}{2}}. \tag{3.1}$$

The rolling resistance force on the road (F_R) depends on the ratio between the tire's unloaded radius (r) to the roller radius (R_r), producing an effective rolling resistance on the roller (F_{RR}). (Unrau, 2013) refined the rolling resistance model by introducing a correction factor e_{FR} to equation (3.1), which can be expressed simply as $e_{FR} = 0.195\ p/F_{Zp}$, where p denotes the tire's pressure (in bar), and F_{Zp} is the normalized tire's load, compared to the full load, according to the ETRTO[1] standard. More details are available in (Unrau, 2013). Finally, the corrected effective rolling resistance on the roller is given by equation (3.2)

$$F_{RR} = F_R \left(1 + e_{FR}\frac{r}{R_r}\right)^{\frac{1}{2}}. \tag{3.2}$$

[1] European Tire and Rim Technical Organization (ETRTO), retrieved 23.08.2018

Coast-down and acceleration behaviors are influenced not only by longitudinal dynamics but also by lateral effects, particularly during cornering where each wheel may rotate at different speeds and advanced systems like torque vectoring are active. Since a chassis dynamometer keeps the wheel axes parallel to the rollers, realistic testing requires a four-wheel, individually driven roller configuration. In this context, the 4x4 roller dynamometer provides the most accurate results (Albers et al., 2013).

The following Sections 3.2 and 3.3 are entirely adapted from our previous work (Alhanouti & Gauterin, 2023b). The study begins by conducting a detailed literature survey to identify key limitations of chassis roller dynamometer testing for electric vehicles, particularly regarding tire-roller contact, dynamometer loading, and energy-consumption measurement deviations. Next, we performed experimental tests on an electric test vehicle using two standardized cycles (NEDC and WLTP class 2) on a roller test bench, capturing vehicle speed, traction force, and battery power data. Simultaneously, we develop an integrated physical simulation model that combines a vehicle dynamics (road-load) model, an electric-powertrain loss model, and an enhanced tire-roller contact submodel, which is based on the LuGre friction model modified for roller geometry and slip behavior. Model calibration is achieved using the test bench data. Finally, we evaluate the model's accuracy in estimating total energy consumption under driving, and propose correction factors for tire friction modelling.

3.2 Limitations of chassis roller dynamometer

To address the limitations of real-world testing, the use of test benches has become an indispensable methodology in modern vehicle development. Among these, the chassis roller dynamometer stands out as one of the most versatile and widely adopted tools, enabling controlled, reproducible, and cost-effective evaluations of vehicle performance. However, the accuracy and reliability of results obtained on chassis dynamometers depend strongly on a

variety of influencing factors that are not trivial to manage. For instance, the manner in which a vehicle is restrained on the test bench can significantly affect the measured traction forces, while the rolling resistance on the dynamometer may differ considerably from that experienced on the road due to roller size, tire behavior, and thermal effects.

It was emphasized that testing on a chassis dynamometer requires additional corrections so that the results would be more relevant to the corresponding road driving tests. The chassis dynamometer itself, however, creates an "environment" that adversely influences the experimental results. Depending on the focus of the investigations in a test bench facility, there is usually a conflict of objectives.

A study was made in (Brace et al., 2009) to investigate the influence of altering some test conditions of a chassis dynamometer on fuel consumption. In the chassis dynamometer setup, some factors significantly influenced the fuel consumption measurement, such as pedal operating, speed error, vehicle alignment, tire type, tire pressure, and the simulated vehicle mass. According to (Sato et al., 2010) tire loss is the major contributor to vehicle mechanical losses in fuel economy tests on roller dynamometers. The tire losses are most significant at speeds less than 40 km/h.

Another issue is the conflict between acoustics experiments and controlling the climatic conditions of the chassis dynamometer test bench. The test concept for acoustic examinations of the test vehicle requires minimizing the noise from the test bench (Pillas, 2017). According to (Martyr & Plint, 2012), heating and distortion effects may damage tires used even for a short time on rolling roads. As a solution, some dynamometer systems would be equipped with tire-cooling systems to reduce tire damage, as investigated by (Nakajo & Tsuchiya, 2009). Nevertheless, the operating of an extensive air conditioning system would significantly impact acoustics (Pillas, 2017). It was shown in (Hendrick et al., 2003) that even different retaining methods affect the acoustic signature and the noise level of the test vehicle in various amounts.

3.2.1 Effect of the restraining point height on the maximum transmissible traction force

A fundamental component in the chassis dynamometer apparatus is the vehicle fastening system, which holds the test vehicle over the rollers. The vehicle is aligned on the rollers with a particular retention system. Moreover, restraining the test vehicle with conventional securing via straps or chains substantially affects the test results (Nehlsen et al., 2006; Pillas, 2017). Alternatively, the vehicle may be tied to the rear of the trailer hitch or a towing lug. This bondage does not establish any constraints to the vertical axis, however, it should be sufficiently stiff in dynamic operations to prevent displacements during the test course (Hendrick et al., 2003; Nehlsen et al., 2006; Pillas, 2017). Two types of retaining the test vehicle on a chassis dynamometer are examined by (Hendrick et al., 2003): The typical strap tie-down restraint and an adjustable barrier/corner restraint. The second type is shown in Figure 3.1. The advantage of employing the barrier/corner design over other types is their minimal effect on the vehicle dynamics. Moreover, they add no additional loading to the tires, from the restraint system. Also, the test vehicle may be accurately centered on the rollers

Figure 3.1: Adjustable barrier/corner restraint (Hendrick et al., 2003).

The maximum transmissible force between the driven wheels and the roller depends on many factors, such as the restraining points' heights of the vehicle

compared to the location of the vehicle's center of gravity, as proven in (Pillas, 2017). The free body diagram in Figure 3.2 demonstrates the forces acting on the test vehicle when using the rear restraint type to avoid introducing additional vertical load on the tires. For convenience, the analysis of the dynamic influences of testing on the chassis dynamometer is performed for the Mercedes A-Class test vehicle. By forces and moments equilibrium, the vertical loads on the front axle ($F_{z,f}$) and rear axle ($F_{z,r}$) are described in equation (3.3)

$$\begin{aligned} F_{z,f} &= m\,g\,\frac{S_r}{l_w} - F_{rest}\,\frac{h_{rest}}{l_w}, \qquad \text{where } F_{rest} = F_{x,f} + F_{x,r} \\ F_{z,r} &= m\,g\,\frac{S_f}{l_w} + F_{rest}\,\frac{h_{rest}}{l_w} \end{aligned} \tag{3.3}$$

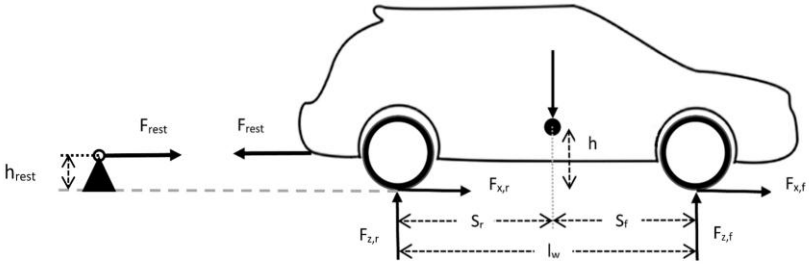

Figure 3.2: Free body diagram of a restrained vehicle (Alhanouti & Gauterin, 2023b).

The traction force on the front axle ($F_{x,f}$) is calculated by dividing the driving moment at the front axle by the effective dynamic rolling radius (r_e). The static friction coefficient (μ_h) between rollers and tires is assumed to equal 1, and the height of the vehicle's center of gravity (h) is determined experimentally equal to 0.3 m. The maximally transmissible force of the front axle ($A_{V,max}$) is achieved as in equation (3.4). By varying restraint height (h_{rest}) and F_{rest}, we get the corresponding $A_{V,max}$ values, demonstrated by a plane in Figure 3.3. On the other hand, the demanded driving force (F_x) that equals the driving moment (M_{drive}) divided by the effective rolling radius (i.e., $F_x = M_{drive}/r_e$, is a linearly increasing surface independent of h_{rest}. At the end the intersection

between the $A_{V,max}$ and F_x surfaces, identify the range of reachable traction force for a specific μ_h

$$A_{V,max} = \mu_{\mathrm{h}}\, F_{z,f} = \mu_{\mathrm{h}} \left(m\, g \frac{S_r}{l_w} - F_{rest}\, \frac{\mathrm{h}_{rest}}{l_w} \right). \tag{3.4}$$

If the driving moment exceeds the traction potential of the axle, the wheels begin to spin. Furthermore, the vertical loads of the front axle decrease with increasing either h_{rest} or F_x. While it increases for the rear axle drive, as proven in (Pillas, 2017). In addition, the driving resistance force must be accurately reproduced on the test bench to match the real environment driving

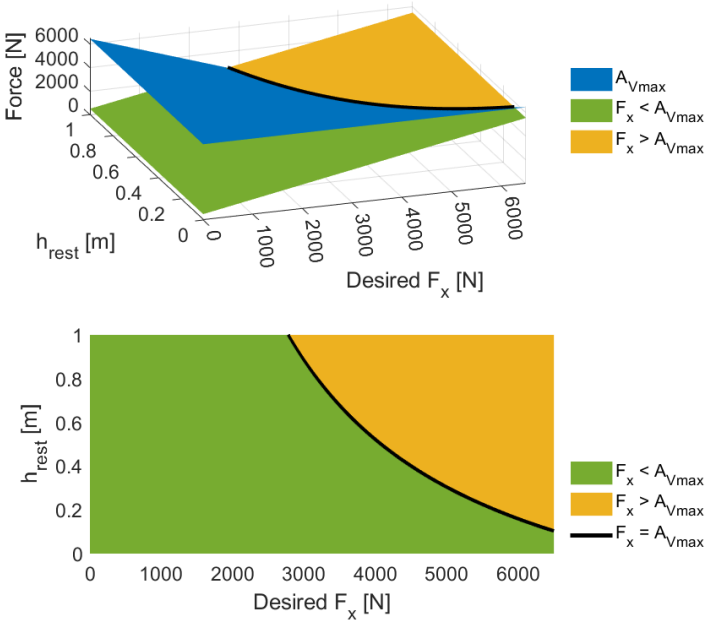

Figure 3.3: Estimating the maximum transmissible drive force corresponding to h_{res} by the front-drive wheels of Mercedes A-Class test vehicle when mounted on the chassis dynamometer, the friction coefficient between rollers and tires is assumed to be equal to 1 (Alhanouti & Gauterin, 2023b).

High slipping between the tire and roller will occur when the driving moment exceeds the traction potential. If the slip exceeds a critical slip value, the coating material of the roller and the tire surface will wear faster, so more errors will occur in the test results (Baker & Presnell, 2006; Pillas, 2017). The consequence would be decreased adhesion between the tire and the roller. Therefore, the driving moment must always be maintained at less than the maximum transmissible force depending on the normal force and the adhesion coefficient. In other words, the frictionally engaged contact between the tire and the roller can critically limit the range of mobility in dynamic driving maneuvers. Therefore, this incident must be avoided to prevent damaging the coating of the roll surface and the attached tire. Figure 3.4 shows how much friction influences the traction force capacity. For h_{rest} = 0.3 m, the maximum F_x is diminished from 5015 N to 3775 N by reducing μ_h from 1 to 0.7

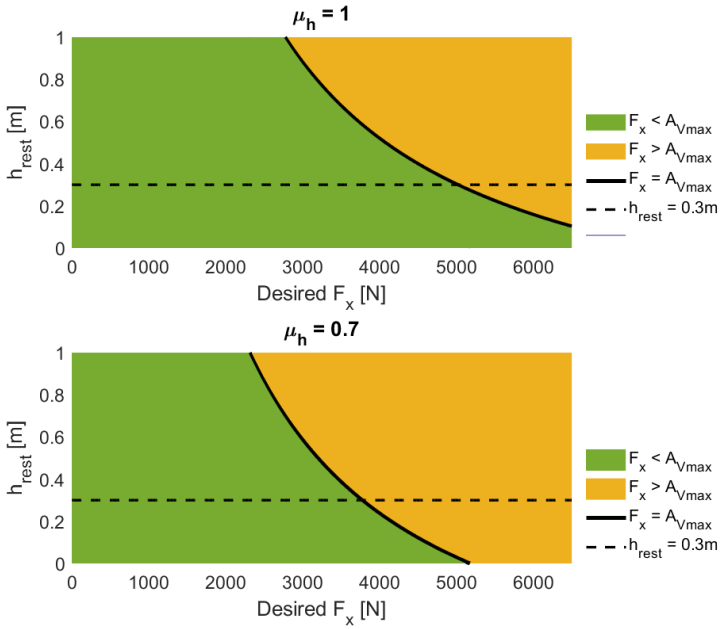

Figure 3.4: Effect of reducing μ_h on F_x (Alhanouti & Gauterin, 2023b).

3.2.2 Evaluation of the energy consumption testing on roller dynamometer test benches

The evaluation is made using the Mercedes A-Class test vehicle's experimental results from the New European driving cycle (NEDC) and WLTP2 driving cycles. The restraint used in this experiment is shown in Figure 3.5. It also does not restrict the wheels loads changes during driving and braking. This feature helps to evaluate the testing results with the influence of the restraint system. The vehicle's center of gravity height (h) is estimated at 0.3 m, while the restraint point (h_{rest}) height equals 0.3 m

Figure 3.5: Mounting the test vehicle on the roller dynamometer test bench (Alhanouti & Gauterin, 2023b).

3.2.2.1 NEDC and WLTP2 driving cycle results from the dynamometer test bench

The first performed driving cycle was the NEDC. It can be seen from Figure 3.6 that the reference speed was tracked with a good performance with a root mean square error of 1.2168 km/h. The validated model for the VUT, developed earlier in Section 2.3, would be of great advantage in assessing the plausibility of the test measurement results. It can be seen from Figure 3.7 that the total reaction forces on the rollers attached to the front tires (corresponding to $F_{x,f}$ and $F_{x,r}$ in Figure 3.2) reach comparatively lower positive values than the expected values from the VUT model during acceleration. While braking, the force behavior matches the expectations from simulated street driving of

the VUT. The divergence between the measured and the simulated forces is ascribed to the fact that the influence of the rolling resistance force of the tires is not captured in the measurements

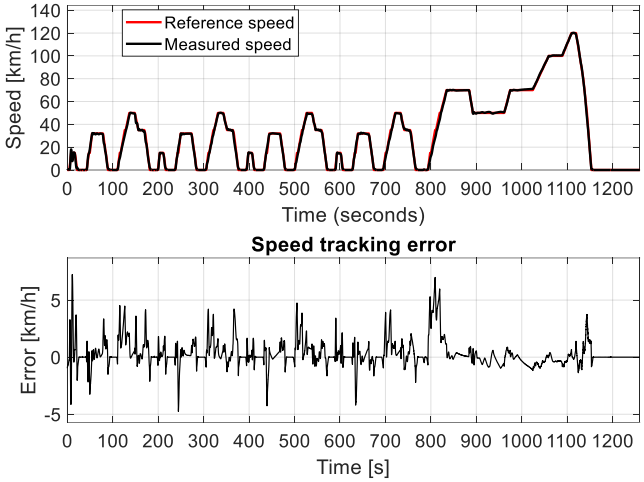

Figure 3.6: NEDC cycle tracking performance (Alhanouti & Gauterin, 2023b)

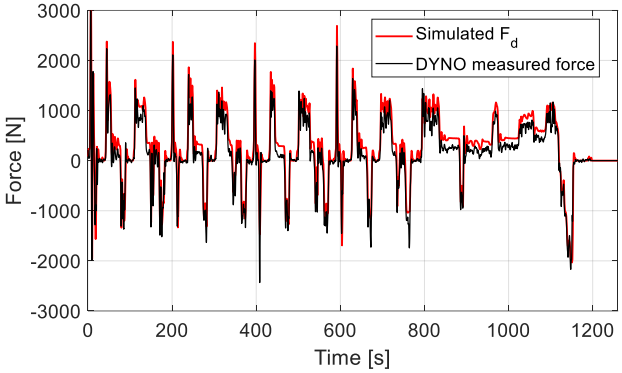

Figure 3.7: Traction force simulation of the front axle wheels of the VUT model (F_d) vs. the actual force measurements on the roller test bench for the NEDC cycle (Alhanouti & Gauterin, 2023b).

Correspondingly, the mechanical power measured from the test bench system ($P_{Trac,Dyno}$), which is determined by multiplying the measured traction force with the measured vehicle's speed, has relevant mismatches with the street driving estimated mechanical power at the wheels ($P_{Mech,Street}$) of the same driving cycle estimated by equation (2.2), as shown in Figure 3.8. The test bench automation system is calibrated by executing a group of coast-down tests on the VUT prior to the desired maneuver tests. Nevertheless, this did not change the fact that the VUT underwent different driving resistances than street driving, which dictates the need to implement specific corrections on the dynamometer test bench results to simulate the corresponding street driving maneuvers. It is worth mentioning that high slipping between the tires and rollers was observed during the experimental test period from 894 to 1160 seconds, which is expected to cause an error in power estimation for the high-speed part of the cycle

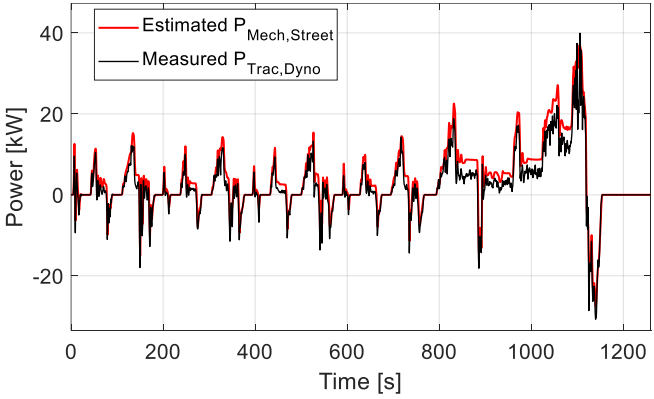

Figure 3.8: A comparison between the estimated mechanical power ($P_{Mech,Street}$) with the estimated traction power from the roller dynamometer ($P_{Trac,Dyno}$) test bench for the NEDC driving cycle test (Alhanouti & Gauterin, 2023b).

Next, the WLTP2 test is performed on the same car. This test was explicitly chosen because it has a lower maximum speed (85 km/h) than the NEDC cycle (120 km/h). Moreover, WLTP2 is more dynamic than the NEDC cycle.

Consequently, the slipping due to high speed would be reduced in this maneuver, and the acceleration influence on the slip (due to the more dynamic course at lower speeds) could be emphasized. Figure 3.9 shows the speed tracking performance accuracy for the WLTP2 reference driving cycle, which was also performed well with a root mean square error of 0.9786 km/h. Figure 3.10 illustrates the measured reaction force from the test bench and the expected traction force for the validated VUT model for street driving simulation. Since the test bench reacted the same way as it did with the NEDC cycle, the diagram for comparing the power for the WLTP2 cycle is excluded here

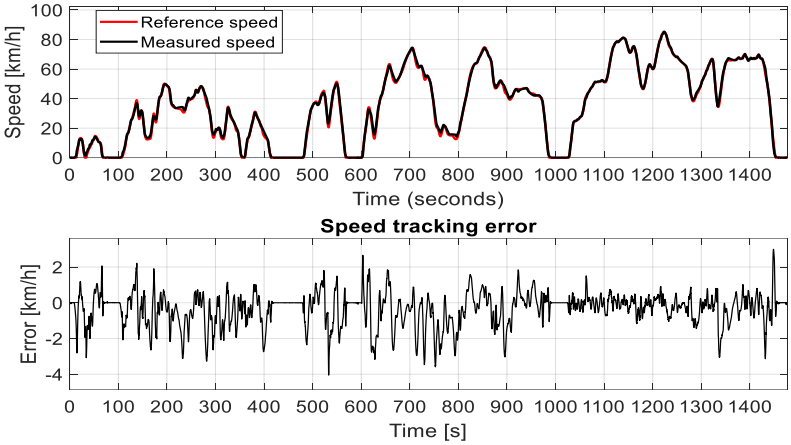

Figure 3.9: WLTP2 cycle tracking performance (Alhanouti & Gauterin, 2023b).

It was shown in (Pelkmans & Debal, 2006) that significant divergences exist between the on-road emissions and fuel consumption measurements and the driving cycles' measurements on the chassis dynamometer. It was also proven in (Baker & Presnell, 2006) that slip at the contact point between the vehicle's tires and the dynamometer's rollers leads to unmanageable inconsistency in emission measurements. While tightening the vehicle restraints may increase emissions and energy consumption. A conclusion was made in (El-Sharkawy, 2007) that the uncertainty in determining the road load coefficients, i.e.,

typically the so-called ABC factors, will significantly affect the reliability of the test measurements for the vehicle system. In addition, a comparison was made in (Duarte et al., 2016) between the on-road data and the measured fuel consumption and pollutant emission from the roller dynamometer for 16 different vehicles. The comparison criteria were based on the vehicle's specific power and portable emission measurement systems. The vehicles under test underwent the NEDC and WLTP-class three (WLTP3) driving cycles on a chassis roller dynamometer. The results show significant differences between street and driving cycle measurements, especially for internal combustion engine vehicles

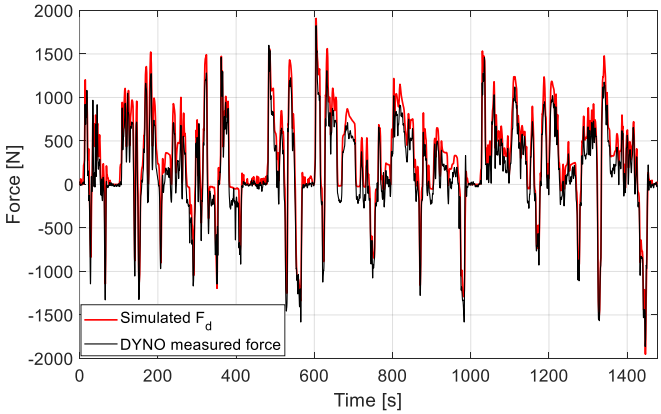

Figure 3.10: Traction force simulation of the front axle wheels of the VUT model (F_d) vs. the actual force measurements on the roller test bench for the WLTP2 cycle (Alhanouti & Gauterin, 2023b).

As a final point, it must be indicated that chassis dynamometers are continuously moving away from being employed as certification tools, development platforms for calibration, or system optimization and validation tasks (Mayyas et al., 2013; Paulweber & Lebert, 2016; Pfister et al., 2009).

3.2.2.2 Improving the results from the roller dynamometer test bench

It was previously presented that there are several limitations and sources of errors when testing with the chassis dynamometer. The slip is the major problem that caused the substantial mismatch between the expected and the measured energy consumption. Therefore, an analytical study and additional adjustments are proposed in the tire model in this section to interpret the deviation of the actual testing measurements on chassis dynamometers from the expected results from street driving. So, to compensate for this difference, the additional power calculated from the rolling resistance model in equation (2.10), i.e., $F_R V_x$ valid for the flat road surface, with the correction equation (3.2) is added to the results of the roller test bench, i.e., $P_{Mech,Dyno}$ = (DYNO Measured force + F_{RR}) V_x, valid for simulating driving resistance of the flat road surface, given the roller dynamometer test measurements. Consequently, the estimated mechanical power from the roller dynamometer leads to very well-matching results with the simulation of the VUT model, as demonstrated in Figure 3.11

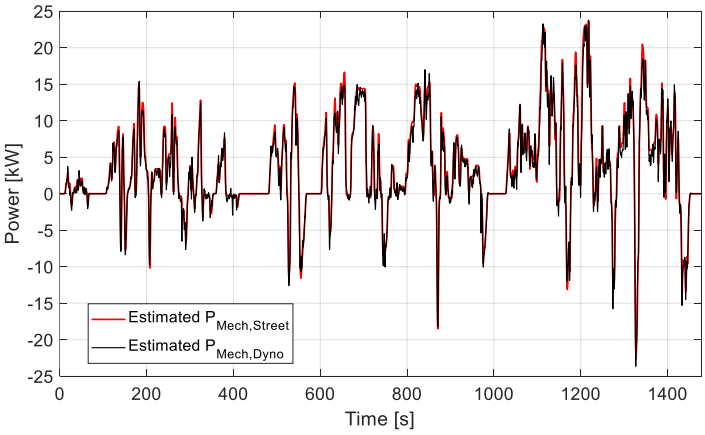

Figure 3.11: A comparison between the estimated mechanical power ($P_{Mech,Street}$) with the estimated mechanical power from the roller dynamometer ($P_{Mech,Dyno}$) test bench for the WLTP2 driving cycle test, the additional power due to rolling resistance is considered (Alhanouti & Gauterin, 2023b).

Therefore, the proposed power estimation models of the street driving and the roller dynamometer should have analogous results when estimating the total power consumption, P_{in}, determined from equation (2.83), as Figure 3.12 and Figure 3.13 show

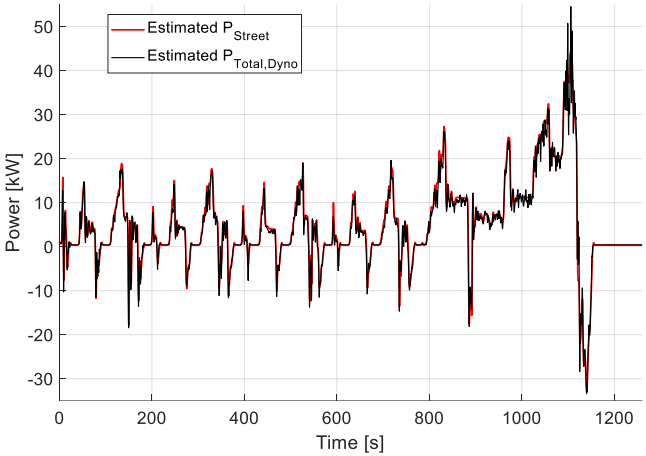

Figure 3.12: A comparison between the simulated total power in the street driving (P_{Street}) with the estimated total power from the roller dynamometer test bench ($P_{Total,Dyno}$) for the NEDC driving cycle test, the additional power due to rolling resistance is considered (Alhanouti & Gauterin, 2023b).

The root mean squared error concerning P_{ins} between the test bench with respect to the street driving estimation concerning the VUT model is determined for both NEDC and WLTP2 tests. The RMSE results for the NEDC and WLTP2 tests are 1.693 kW and 1.156 kW, respectively

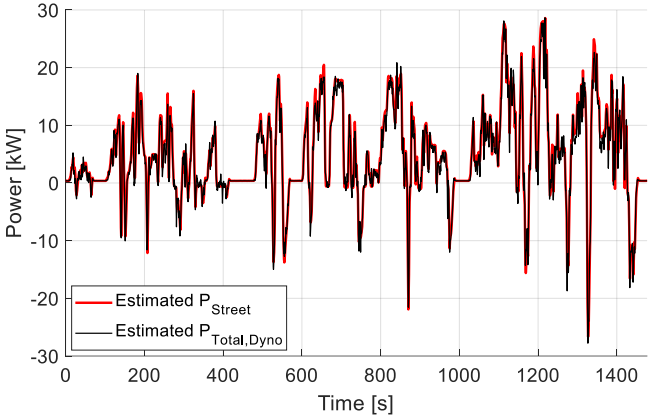

Figure 3.13: A comparison between the simulated total power in the street driving (P_{Street}) with the estimated total power from the roller dynamometer test bench ($P_{Total,Dyno}$) for the WLTP2 driving cycle test, the additional power due to rolling resistance is considered (Alhanouti & Gauterin, 2023b).

3.3 A proposed approach for estimating the friction between the tire and the roller

The classical road load simulation (RLS) is calculated with only three constant parameters: A, B, and C, attained from the test vehicle's coast-down test (R. Bauer, 2011b; Maschmeyer et al., 2016; T. Weber et al., 2014). Furthermore, the influences of road inclination, route curvature, acceleration dynamics, and ambient conditions, such as temperature and pressure, can be considered. After getting these parameters, a driving resistance force as a speed function is formulated. The attained experimental function is equivalent to the driving force F_d in equation (2.2)**.** Thus, standard driving cycles such as NEDC and WLTP can be performed using this technique. Moreover, it could be employed for evaluating the development goals, such as real driving emissions (RDE) analysis (Lensch-Franzen et al., 2018; Maschmeyer et al., 2016). Figure 3.14 demonstrates an exemplary approach for adjusting the driving

resistances model of the chassis dynamometer which was proposed in (T. Weber et al., 2014). The authors introduced some adjustment factors to reproduce the chassis dynamometer's driving resistances correctly

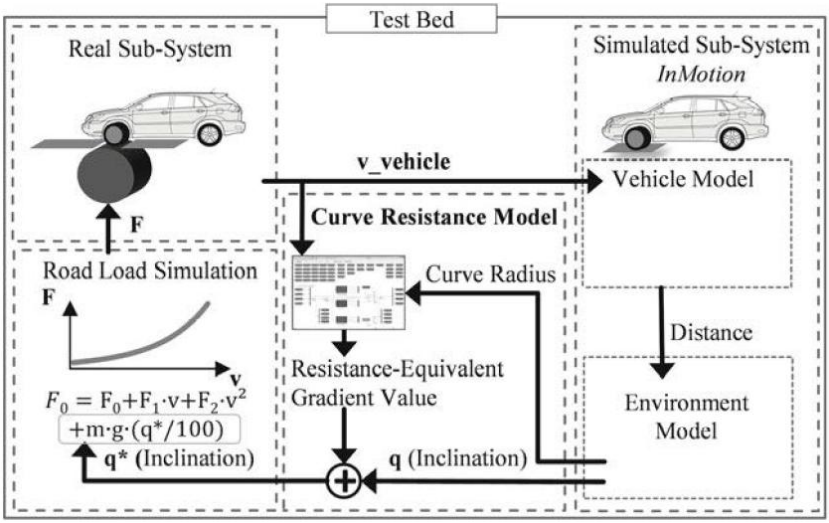

Figure 3.14: Driving resistances model parametrization approach for curve driving simulation on the chassis dynamometer (T. Weber et al., 2014).

The procedure begins with data acquisition from on-road testing. Next, an offline simulation verifies the vehicle model by comparing the coast-down test results of actual and simulated values. Finally, an online simulation is executed on the test bench. The scaling factors for the rolling resistance model are tuned by a compensation model in the final stage. The adjustment factors were verified by comparing the results of the coast-down tests between the real-world measurements, simulation results, and test bench measurements. The accuracy of the results varied with speed. The maximum error for the driving test was about 8 % at a 10 km/h velocity. Nevertheless, the RLS without tire slip considerations causes deviation between the actual driving resistance in the real driving environment and the simulated driving resistance on the test bench. For this reason, it is denoted as a non-slip model in some

researches (Pillas, 2017). Moreover, acceleration resistance is neglected in this approach. This makes it a driving resistance model only for constant or slowly changing speeds.

The authors of (Hendrick et al., 2003) developed a chassis dynamometer with a twin roller for each tire and a vehicle longitudinal dynamics model considering the contact between tire and rollers. By employing a Pacejka tire model to simulate the vehicle dynamics, they achieved accurate results compared to measured data. However, the error value was substantially higher for a slip-independent tire model. Mechanical power loss in the tire is the main contributor to vehicle losses in fuel economy tests on roller dynamometers (Sato et al., 2010). Consequently, several research works have emphasized developing detailed dynamic tire models for determining high-resolution powertrain efficiency, such as modeling the tire deformation with a flexible ring model that extended with dynamic pressure distribution as it underwent high-speed rolling conditions (X. Gao et al., 2021). In another work shown by (O'Neill et al., 2022), a brush-type tire model was proposed intending to achieve tire behavior similar to Pacejka's model results but using a more straightforward approach while considering rubber friction characteristics. A relevant work (Yamashita et al., 2015) proposes a hybrid tire model of the absolute modal coordinate formulation with the LuGre tire model. One of the recent works for a detailed physical model for the contact between the tire and a twin-roller was developed in (Lourenço et al., 2023). The creation of this model is based on substituting the normal force from the twin roller in a Pacejka tire model. However, the rolling resistance increases in case of the double contact between the two rollers and traction tire compared to the flat contact patch on the road or to a single roller dynamometer (Eckert et al., 2017; Lourenço et al., 2023). The authors of (Lourenço et al., 2023) validated their model with two coast-down tests, starting at 60 km/h and 100 km/h. Since there are insufficient thorough tire-roller analytical studies for dynamic driving maneuvers, this work investigates the adaptation of different tire models to predict the traction force behavior of the tire on the roller of the chassis dynamometer test bench. Moreover, the examination proposed in

this article concentrates on reproducing the total bench resistance forces for both driving and braking cases and modeling the slip tire-roller interactions based on different driving cycle maneuvers.

3.3.1 Friction tire model

Understandably, tire contact with the roller is an important matter when modeling the vehicle's dynamic behavior. Hence, it is highly relevant for accurate vehicle dynamic simulation models. Therefore, the tire contact on the bench must be analyzed thoroughly for chassis benches (Hendrick et al., 2003). The tires of the drive wheels are placed on the rollers and are engaged with the rollers by means of friction forces. Therefore, regarding constraints and potential sources of error, the chassis dynamometer directly influences the measurement results. These mainly concern the measurement of losses in the drive train and tires, such as the rolling resistance of the tire mounted on the roller differs significantly from its actual value on the flat road. Furthermore, there is a clear difference between running it on rollers of different diameters (Martyr & Plint, 2012), since the rollers' size affects the rolling resistance significantly (Pexa et al., 2020). Moreover, in the same study, other influential quantities on the rolling were also investigated for each roller size: vertical load, angular speed, and inflation pressure. The results showed that the smaller the roller size, the more sensitive the rolling resistance would be to changing other quantities.

Friction is a complex interaction between the surface and the near-surface regions of two bodies moving relative to each other. The tire dynamic friction model (Canudas-de-Wit et al., 2003; de Wit et al., 1995; de Wit & Tsiotras, 1999) combines the *Dahl* model (Canudas-de-Wit et al., 2003) with steady-state friction characteristics, which comprises both the tire's transient and steady-state behavior. In addition, the authors developed an ordinary differential equation called the *LuGre* model (de Wit et al., 1995), a surface- and velocity-dependent model on the contact patch length (L) between the tire and the ground to approximate the distributed friction model, as represented

in Figure 3.15. The model simulates several longitudinal tire friction phenomena, such as *the Stribeck effect, spring-like characteristics*, and *stick-slip* motion

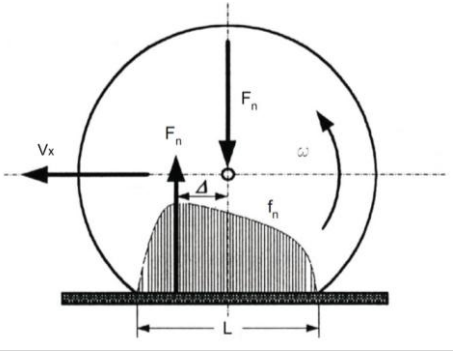

Figure 3.15: Normal load distribution along with the contact patch (Guo & Ren, 1999).

As shown in Figure 3.16, the Stribeck effect (Lantos & Márton, 2011) appears as a drop in the forces at low speeds, where V represents the relative tangential velocity between the surfaces in contact. A Stribeck relative velocity parameter shapes the Stribeck curve, i.e., the velocity of the tire surface relative to the velocity of the tire's body, as defined in equation (3.5), shapes the Stribeck curve. Moreover, it incorporates the tire's longitudinal lumped stiffness factor (σ_0) and a viscous damping factor relative to the longitudinal speed (σ_2). This tire model also includes a viscous damping term ($g(s)$) as a function of longitudinal slip (s), static friction coefficient (μ_h), Coulomb friction coefficient (μ_c), and the Stribeck relative velocity (v_s). v_s describes how the coefficient of friction between two surfaces decreases as the relative sliding speed increases. This behavior is most noticeable in low-speed or near-stiction conditions and can lead to nonlinear and hysteretic friction behavior. v_s is manually tuned in this work to enhance the fitting between the simulated and measured forces. The model proposed in (de Wit et al., 1995) distinguishes between driving and braking modes based on the relative speed (v_r). The slip (s) is defined according to (de Wit et al., 1995) as in equation (3.6).

The wheel rotational speed (ω) is evaluated by the proposed model previously in Section 2.3. After that, the driving mode, i.e., driving, braking, or standstill modes, are classified according to the test car traction force measurements. Since the slip estimation is more extensively defined in Pacejka's model (Section 2.1.2) than in equation (3.6), the slip defined in equation (2.28) will be employed instead

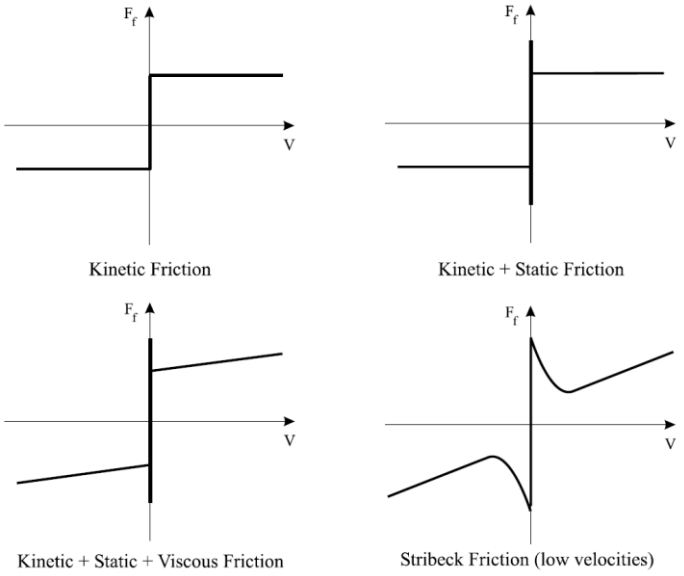

Figure 3.16: Static and kinetic friction models (Lantos & Márton, 2011).

$$v_r = r_e\omega - V_x \tag{3.5}$$

$$s = \begin{cases} s_d = 1 - \dfrac{V_x}{r_e\omega}, & for\ driving \\ s_b = \dfrac{r_e\omega}{V_x} - 1, & for\ braking\ . \end{cases} \tag{3.6}$$

The uniform load LuGre friction model is described with the equations (3.7) –

(3.8) for driving mode, and the equations (3.9) – (3.10) model the tire friction in the braking mode (Canudas-de-Wit et al., 2003)

$$F_d(s) = \left(\text{sgn}(v_r)\, g(s) \left(1 + \frac{g(s)}{\sigma_0 L |s_d|}\left(e^{-\frac{\sigma_0 L |s_d|}{g(s)}} - 1\right)\right) + \sigma_2\, r_e \omega\, s_d\right) F_z \tag{3.7}$$

$$g(s) = \mu_c + (\mu_h - \mu_c)\, e^{-\left|\frac{r_e \omega\, s_d}{v_s}\right|^{0.5}} \tag{3.8}$$

$$F_b(s) = \left(\text{sgn}(v_r)\, g(s) \left(1 + \frac{g(s)|1 + s_b|}{\sigma_0 L |s_b|}\left(e^{\frac{\sigma_0 L |s_b|}{g(s)|1+s_b|}} - 1\right)\right) + \sigma_2\, V_x\, s_b\right) F_z \tag{3.9}$$

$$g(s) = \mu_c + (\mu_h - \mu_c)\, e^{-\left|\frac{V_x\, s_b}{v_s}\right|^{0.5}} \tag{3.10}$$

The tire's contact patch differs for roller contact (L_{LT}) than for flat surface contact (L_{LE}), as shown in Figure 3.17. The ratio between the two cases is also estimated in (Unrau, 2013) with a correction factor $e_{C\alpha}$, as shown in equation (3.11). This concept is employed in this work to estimate the variable (L) in equations (3.7) and (3.9), which enables comparison between testing on-road and the dynamometer rollers

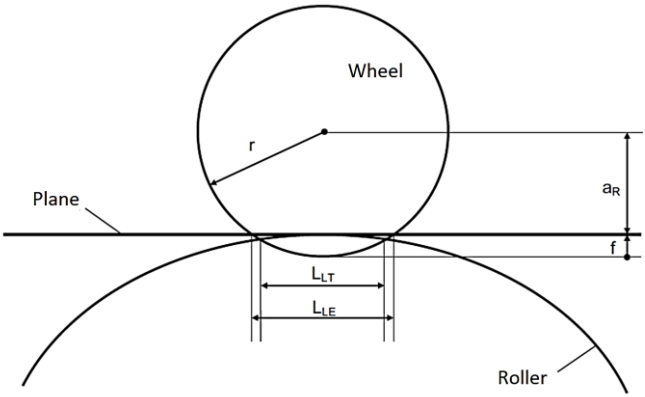

Figure 3.17: Effect of roller geometry (Unrau, 2013).

In this work, the LuGre model parameters μ_h, μ_c, v_s, and L_{LE} are set to 1.29, 0.93, 3.72 m/s, and 0.2 m, respectively, according to (Canudas-de-Wit et al., 2003). Based on (Unrau, 2013), a tire pressure of 2.2 bar and 100% load according to the ETRTO standards, the correction factors e_{FR} and $e_{C\alpha}$ are determined as 0.52 and 0.10, respectively. Then, equation (3.11) determines the L_{LT} value corresponding to the given L_{LE} value. A relevant work (Yamashita et al., 2015) proposed a hybrid tire model, which combines an absolute nodal coordinate formulation with the LuGre tire model. It was also proved that the LuGre model is very efficient in modeling braking behavior, especially in extreme maneuvers. Two tire models are employed in (Yamashita et al., 2015); one for driving and the other for braking

$$\frac{L_{LE}^2}{L_{LT}^2} = 1 + e_{C\alpha}\frac{r}{R_r}. \tag{3.11}$$

The LuGre model in this work is implemented for driving and braking but with different parameters. Then, the parameters σ_2 and σ_0 are manually tuned to 0.2 s/m and 210 m^{-1}, respectively, until the best fitting between the experimental and simulated power consumption is achieved for the driving part of the maneuver. Next, by tuning the braking part of the LuGre model, it is found that only by reducing σ_0 to 130 m^{-1} and using the same parameters as for the driving part, an accurate estimation of the braking dynamic is achieved.

3.3.2 Influence of the roller on the temperature of the tire

The tires can heat up severely during dynamic test runs, which must be monitored during the test run (Pillas, 2017). Furthermore, solving the paradox of avoiding additional vertical load by the employed restraint type and excessive slip between the tire and the roller is still a challenging issue. So, the rolling resistance model, i.e., equations (2.7) – (2.10), is employed to compare the estimated rolling resistance for street driving and the tire rotating on the roller simulation. For the dynamometer testing simulation, L_{LT} is used instead of L_{LE} in equations (3.7) and (3.9), and then correction in equation (3.2) is

applied. There is also a noticeable increase in the rolling resistance in the dynamometer simulation compared to the street driving simulation by 15%, which leads to more heating for the tires by roller dynamometer testing, as shown in Figure 3.18 and Figure 3.19

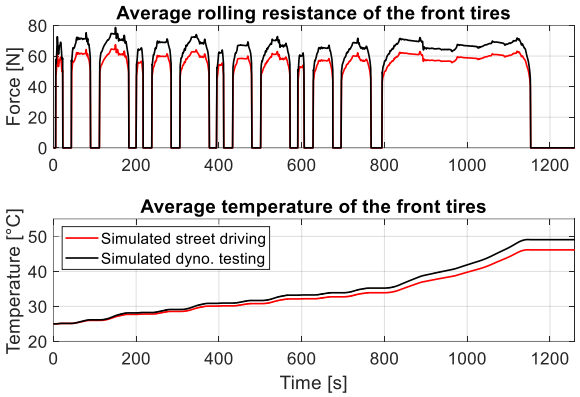

Figure 3.18: Simulated rolling resistance and its corresponding tires' temperature during the NEDC cycle (Alhanouti & Gauterin, 2023b)

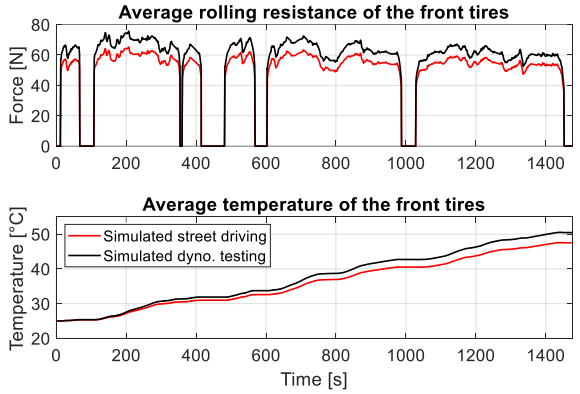

Figure 3.19: Simulated rolling resistance and its corresponding tires' temperature during the WLTP2 cycle (Alhanouti & Gauterin, 2023b).

The proposed simulation model estimates the test tire's friction forces and the slip between the tire and the roller, enabling accurate estimation of the actual energy consumption on the roller dynamometer test bench. Furthermore, it estimates some essential physical properties during the testing process, such as the tire's temperature, which can help to monitor these quantities if the relevant measurement technologies are unavailable.

3.3.3 Validation of the enhanced power estimation model for the roller dynamometer measurements

It is then desired to assess to which extent the direct measurements of the electrical power consumption from the VUT battery on the roller test bench may be estimated based on the direct force and speed measurements in combination with other simulated driving resistances and power losses. These results are shown for both NEDC and WLTP2 driving cycle tests in Figure 3.20 and Figure 3.21, respectively. The mechanical power (P_{mech}) is calculated by multiplying the vehicle's measured speed with the measured traction force. Then the total power ($P_{Total,Dyno}$) is determined using equation (2.83). Obviously, the most considerable divergence occurred in the higher-speed parts of the tests, as shown in Figure 3.20(a). At the same time, the errors are distributed along the WLTP2 test in Figure 3.21(a). On the other hand, the actual braking impact on the VUT was less than expected. These differences between the actual and the estimated results are ascribed to the excessive slipping of the tires on the rollers. As a result, Figure 3.20(b) and Figure 3.21(b) indicate that the battery power consumption during acceleration is higher than the estimated total, which is attained from the measured mechanical power then adding the power losses according to equation (2.83), as demonstrated in Section 3.2.2.2. Moreover, some measured power pinpoints in the positive range are not captured in the force measurements, which made them unpredictable for the model. These observations indicate that the testing on the roller dynamometers causes higher energy consumption than expected. This deviation is attributed to insufficient measured entries for the model. Only two actual measured quantities are provided by the test bench: The

traction force on each tire F_{xW}, and the rollers' rotational speed, which is used to estimate the vehicle's speed. So, there is no physical measurement system for the tires. These form sources of inaccuracy in the estimation results no matter how detailed and precise the model is. For instance, it is well-established that tire rolling resistance can only be adequately measured with specialized apparatus (Ejsmont & Owczarzak, 2019). It is then expected to have some errors from the rolling resistance model equation (2.10) due to inaccurate entries, such as the actual vehicle speed V_x

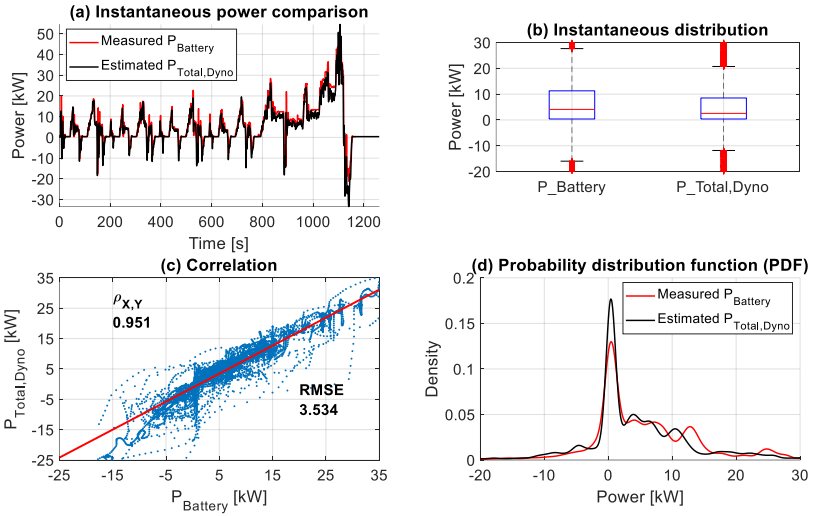

Figure 3.20: A comparison between the measured electrical power from the VUT battery ($P_{Battery}$) with the estimated total power consumption from measurements of the roller dynamometer test bench ($P_{Total,Dyno}$), corresponding to the NEDC driving cycle test.

Despite these, Figure 3.20(c) displays a very good match between the measured $P_{Battery}$ and estimated $P_{Total,Dyno}$, with $\rho_{X,Y}$ of 0.951 for the NEDC cycle, and a correlation of 0.976 for WLTP2 driving cycle, as shown in Figure 3.21(c). The error in Figure 3.20(a) is more significant at the last part of the NEDC, where the speed is higher than the rest of the test and the expected negative braking

power is, mostly, more extensive than the measured. These lead to RMSE readings of 3.534 kW for NEDC and 2.161 kW in the case of the WLTP2 test. The errors also appeared as differences in power allocations between $P_{Battery}$ and $P_{Total,Dyno}$ in Figure 3.20(b) and Figure 3.21(b). Consequently, there are unsymmetric error distributions that are shifted more to the positive error portion, as illustrated in the probability density function (PDF) (Montgomery & Runger, 2010) analyses of the measured and simulated signals for the NEDC cycle in Figure 3.20(d). The PDF exhibits a distribution with its peak located near zero. The relatively narrow spread of the distribution reflects low inconsistency in the residuals, suggesting that the model maintains consistent accuracy throughout most of the driving cycle

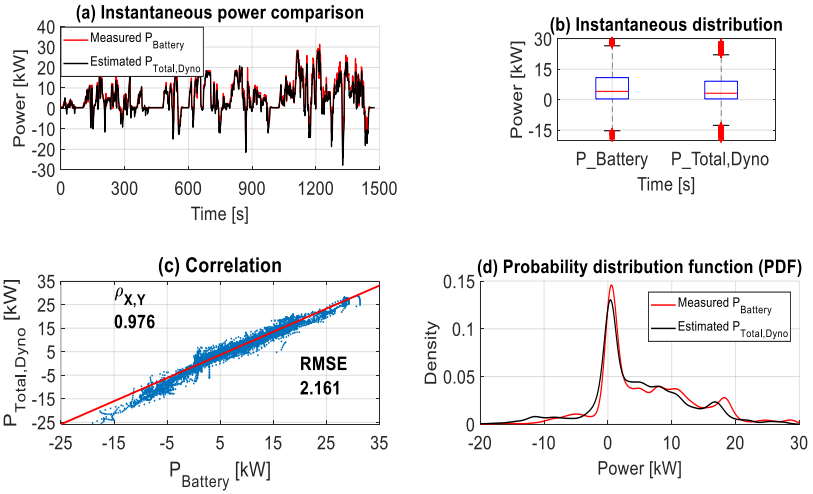

Figure 3.21: A comparison between the measured electrical power from the VUT battery ($P_{Battery}$) with the estimated total power consumption from measurements of the roller dynamometer test bench (*c*), corresponding to the WLTP2 driving cycle test.

However, a clear difference in peaks between the measured and simulated power curves is ascribed to the difference between the simulation and the measurements, especially at the last part of the NEDC cycle. The limited

presence of extreme deviations, indicated as the short tails of both curves, further confirms that large errors occur infrequently, emphasizing the overall reliability of the simulation.

In summary, the PDF analysis demonstrates that the simulated NEDC signal reproduces the measured data with high fidelity, capturing the primary trends and magnitudes effectively. Nonetheless, further development of the model is still necessary to improve the matching with the expected results. In comparison, the PDF in the case of the WLTP2 test, shown in Figure 3.21(d), demonstrates a better fitting between the simulated and measured signals. The distributions are also placed near zero and show that the simulation closely replicates the measured behavior. The PDF of the estimated power is relatively narrow spread, reflecting consistent performance, while the absence of significant tails suggests few large deviations.

3.3.4 Validation of the proposed power consumption model

Figure 3.22 shows that employing the LuGre model with the proposed adjustments accurately predicts the instantaneous power for the NEDC cycle test. The matching between the proposed model and the measured data is evident in Figure 3.22(a)-(d). Moreover, the errors from the high slipping period from 894 to 1160 seconds (see Figure 3.8) are reduced significantly compared to the results from the street model, as shown by the reduced difference in power distribution in Figure 3.22(b) and the correlation in Figure 3.22(c) that reached about 0.99 and RMSE of 1.454 kW. The difference between the measurements and the estimated signals is shown in Figure 3.22(d). The PDF distribution is concentrated around its peak, which lies close to zero, indicating that the simulation results align closely with experimental observations and exhibit minor errors on the positive side. The narrow width of the curve reflects low variability in the error magnitude, confirming that the simulation maintains high precision and stability across different operating conditions within the NEDC cycle. Furthermore, the short and well contained tails demonstrate that large discrepancies between the simulated and measured

signals are infrequent. Nonetheless, slight deviations are observed between the peaks of the measured and estimated power profiles, as well as noticeable differences in the positive range

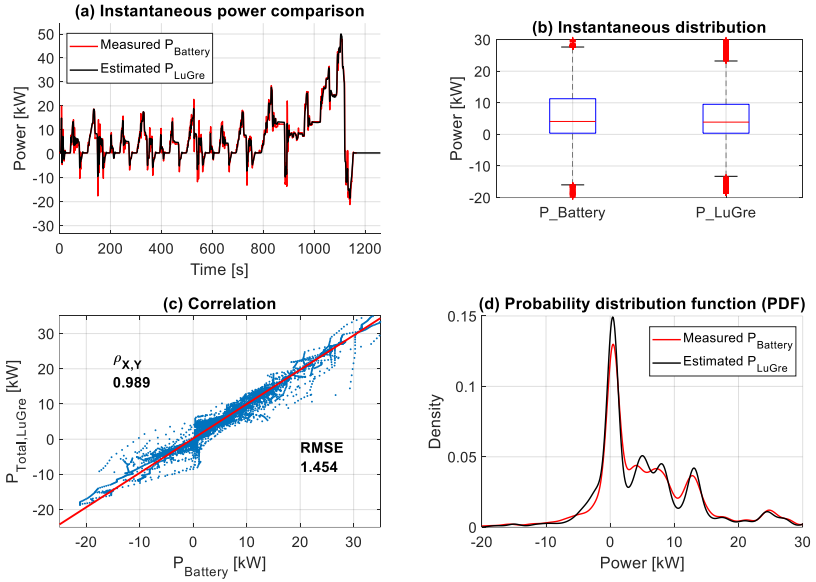

Figure 3.22: A comparison between the measured electrical power from the VUT battery ($P_{Battery}$) with the estimated total power consumption using the proposed LuGre model (P_{LuGre}) using the speed measurement, corresponding to the NEDC driving cycle test.

In addition, the negative power part, representing the braking mode, is better matching the measured values. Subsequently, the overall results in Figure 3.22 demonstrate a substantial improvement compared to the performance in Figure 3.20. Likewise, Figure 3.23 illustrates the similarity between the actual measurements from the WLTP2 test and the simulated results from the proposed model. The correlation in Figure 3.23(c) is about 0.984, and the RMSE reached about 1.393 kW. The estimated PDF in Figure 3.23(d) displays a sharp and symmetrical peak located near to zero and shows that the

simulated data is closely match the measured with some difference between the peaks

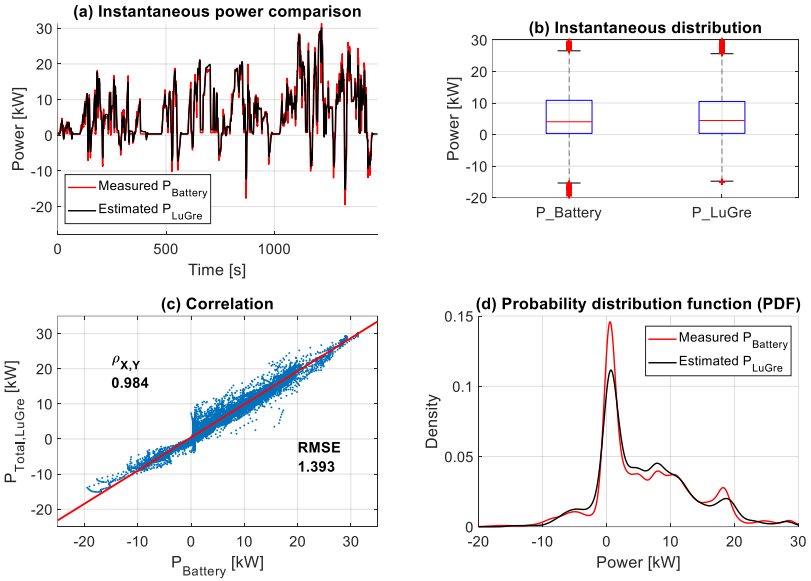

Figure 3.23: A comparison between the measured electrical power from the VUT battery ($P_{Battery}$) with the estimated total power consumption using the proposed LuGre model (P_{LuGre}) using the speed measurement, corresponding to the WLTP2 driving cycle test.

The narrow spread of the PDF indicates that the majority of errors are small in magnitude, reflecting a high degree of consistency and stability across the entire driving cycle. Nonetheless, slight divergences are still present due to the uncertainty of the slip quantity between the tires and the rollers. These values confirm the significant improvement in power estimation accuracy, which complies with the observations in Figure 3.20 – Figure 3.23. Figure 3.24 demonstrates the proposed model for the total power estimation process of the VUT under the chassis dynamometer testing conditions. The road inclination and the cornering resistance forces are not taken into account in this

model, since the focus is on estimating energy consumption during standard driving cycles.

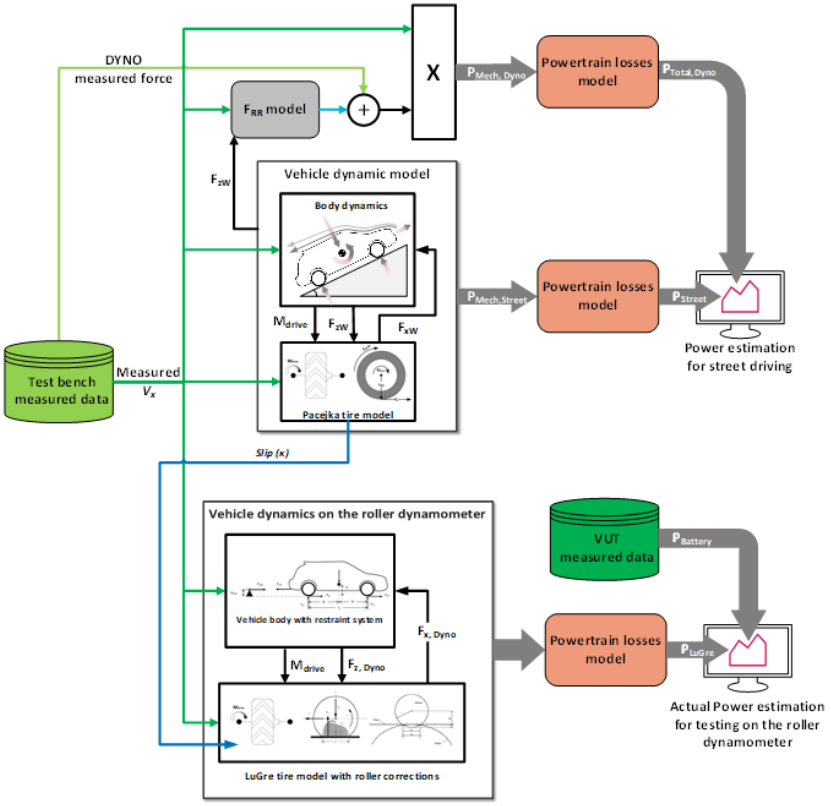

Figure 3.24: Integrated full vehicle model in the roller dynamometer (Alhanouti & Gauterin, 2023b)

3.4 Conclusion

Chassis roller dynamometers, which are still widely used in industry, provide an accessible and versatile platform for vehicle testing. Yet their limitations,

such as the influence of restraint systems on measured traction forces, discrepancies in rolling resistance compared to flat-road driving, and thermal effects on tire-roller interactions, must be carefully understood and addressed. Developing improved methods for quantifying these effects and refining power estimation models ensures that roller-based testing delivers results that are both reliable and transferable to real-world conditions.

4 Vehicle-in-the-loop test bench (VEL)

In order to obtain meaningful test results on the roller test bench, specific arrangements and corrections are to be made, as elaborated in Chapter 3. However, applying the simulated driving resistance directly to the wheel hub is a more suitable solution to avoid the dynamometer dynamic effects on the test vehicle. So, the loading machines will be directly connected by side shafts to the vehicle's powertrain (R. Bauer, 2011a, 2011b). This configuration connects the vehicle's powertrain to the loading machines through side shafts, enhancing test stability and allowing the powertrain to operate independently while interfacing with electrical load units (Nehlsen et al., 2006). Such powertrain test benches are effective in reproducing dynamic driving scenarios and serve as valuable tools for developing and evaluating advanced driver assistance systems. For example, (R. Bauer, 2011a, 2011b) proposed a control concept capable of simulating varying road surface conditions, including dry, wet, and icy surfaces, with successful validation through anti-lock braking system (ABS) testing on mixed-friction patches. However, realistic tire modeling remains essential to represent tire-road interactions accurately. To address this, (S. Weber et al., 2017) introduced an empirical method optimizing Pacejka tire parameters to correlate test bench outcomes with real-road behavior.

4.1 VEL test bench

Figure 4.1 depicts the Vehicle-in-the-loop (VEL) testing system, designed to reproduce the effects of real-world driving environments by reproducing tire driving resistances. The configuration allows for a direct mechanical connection between the VEL setup and the vehicle's wheel hubs, ensuring high-fidelity interaction between simulated and physical dynamics

Figure 4.1: Vehicle-in-the-loop[1] (Alhanouti & Gauterin, 2023a).

The VEL platform integrates two primary actuator types. The first consists of four electrical loading machines labeled as (1) in Figure 4.1, responsible for applying resistance moments corresponding to the desired driving maneuver around each wheel's rotational axis. The second set includes two servo motors, labeled as (2) in Figure 4.1, which simulate the self-aligning torque on the front wheels. Additionally, an airstream simulator, marked as (3), reproduces environment wind speed effects, providing both thermal cooling. This configuration allows for both straight-line and cornering tests to be conducted in controlled laboratory settings. Adjustable track width and wheelbase accommodate diverse vehicle geometries (El-Haji, 2016). The technical data of the VEL test bench are listed in Table 4.1. As shown in Figure 4.2, the front-left wheel carrier assembly features two movable support plates and a shaft with constant-velocity (CV) joints at both ends, allowing steering motion under power transmission. In addition, real-time self-aligning torque M_{zW} generation enhances dynamic accuracy in curve simulations (Diewald et al., 2021)

[1] https://www.fast.kit.edu/lff/4667.php, retrieved 01.11.2021

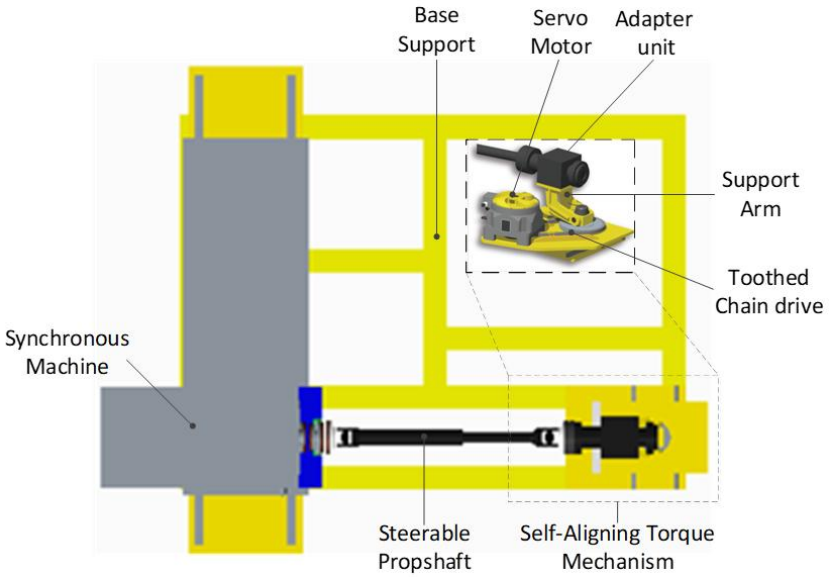

Figure 4.2: Vehicle-in-the-loop, Front-left part schematic.

Table 4.1: Technical specification data of VEL test rig (Alhanouti & Gauterin, 2023a)

Element	**Value**	**Unit**
Maximum allowable vehicle mass	12000	kg
Maximum allowable wheel load	3000	kg
Wheelbase range	1.8 – 4.9	m
Vehicle's track width range	1.2 – 3.9	m
Maximum speed of the loading machine motor	2000	RPM
Nominal loading machine torque	2500	Nm
Nominal loading machine power	209	kW
Steering angle range at the front wheels	± 20	degree
Maximum steering load torque at the front wheels	1000	Nm
Maximum air speed of the portable airstream simulator	135	km/h

In this chapter, a multi mass model for the integrated system from the power-train of the test vehicle and the mechanical part of the VEL test bench is

derived. Moreover, the developed model will be employed in designing different angular speed control algorithms. Then, all control alternatives will be thoroughly investigated in both frequency and time domains. The evaluation criteria of the different controllers will be mainly based on performance, robustness, and reference signal tracking. This part of the chapter, includes in Section 4.2, and Sections 4.3.1 – 4.3.6 reproduces the material from (Alhanouti & Gauterin, 2023a), with minor modifications for clarity. After that, a moment controller will also be employed with the best control algorithm. Finally, the completed system of the powertrain system with the coupled parts from the VEL test bench and the selected controllers will enable realistic driving maneuvers on the VEL test bench.

4.2 Modeling of VEL test bench

The overall system model integrates the powertrain of the VUT with the mechanical subsystems of the VEL test bench. In this configuration, the VUT is a front wheel drive electric vehicle, accompanied by a physical model of its braking system. Each loading machine is linked to the respective axle and wheel hub via a CV shaft, with sensors measuring angular velocity at the machine and moment at the wheel hub. The electric loading machines generate resistance moments transmitted through the VEL drivetrain, as shown in Figure 4.3. Given the symmetry between left and right front-drive assemblies, the model is simplified by analyzing one half of the system for controller design, later mirrored for both sides. This reduction technique aligns with prior modeling methodologies (Fietzek, 2014; Forstinger, 2017). As illustrated in Figure 4.4, the plant can be represented as three mass models interconnected by two torsional spring-damper systems. The inertial components include the combined mass of the loading machine and the CV shaft inertia (J_S), the wheel hub inertia (J_{WH}), and the axle with half of the equivalent powertrain inertia (J_{Pt2W}). The elastic couplings, i.e., the CV shaft and the axle, are modeled using equivalent stiffness and damping coefficients to reflect shaft flexibility and torsional oscillations

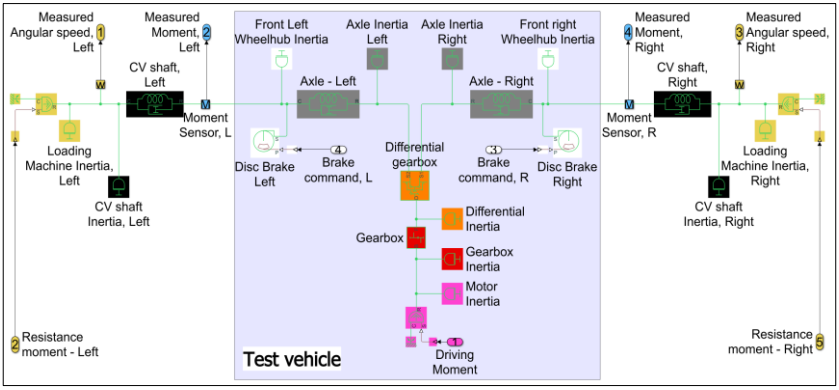

Figure 4.3: A complete simulation model of the VEL mechanical power transmission system and a front-wheel-drive (Alhanouti & Gauterin, 2023a)

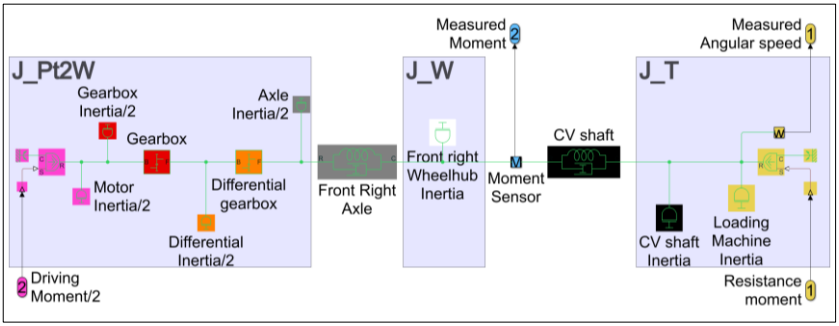

Figure 4.4: Three-mass model (Alhanouti & Gauterin, 2023a).

The system's inputs comprise the loading machine's applied resistance moment (M_M) for speed control and half of the torque at the differential output (M_{Sx}), where *x* indicates the left or right side. The angular velocity of the loading machine serves as the system's primary measured output. Since modern gearboxes exhibit high efficiency, backlash losses are considered negligible (Forstinger, 2017; Forstinger et al., 2016). However, gear friction, which is modeled through combined Coulomb and viscous components, introduces nonlinear dynamics and slip effects, necessitating its inclusion in the model

and causing a limited-slip behavior (Forstinger, 2017; Forstinger et al., 2016). The friction in the differential gearbox combines Coulomb and viscous friction (Fietzek, 2014; Forstinger, 2017; Forstinger et al., 2016).

The Coulomb friction moment has a constant value (M_{F0}) and a moment-dependent part. The total output moment from the differential equals the vehicle's motor moment (M_e) multiplied by the total gear's transmission ratio, i.e., gearbox transmission ratio (i_g) multiplied by the differential transmission ratio (i_D). This multiplication of quantities, i.e. $M_e\, i_g\, i_D$, is specified by the factor (k_M). The factor ($k_{\Delta\omega}$) and the angular speed difference between the differential outputs ($\Delta\omega_D$) determine the viscous friction moment portion. Therefore, the total gear friction moment (M_F), which can be considered a disturbance, is described in equation (4.1)

$$M_F = \left(M_{F0} i_D + k_M \left| M_e i_g i_D \right|\right) \operatorname{sgn}(\Delta\omega_D) + k_{\Delta\omega} \Delta\omega_D \,. \tag{4.1}$$

M_F will be distributed equally between the left and right sides of the total system model (Forstinger, 2017; Forstinger et al., 2016). Parameter values for the front wheel mechanical subsystem of the VEL are summarized in Table 4.2. In order to create the state space model, the state variables have to be specified as follows:

- The angular speed of the electrical loading machine (ω_M),
- The difference between the loading machine angular position (θ_M) and the wheel hub angular position (θ_W),
- The angular speed of the wheel hub (ω),
- The difference between the wheel hub angular position (θ_W) and the differential gear output angular position (θ_{Sx}),
- The angular speed of the differential gear output (ω_{Sx}).

Consequently, the states vector is expressed in equation (4.2)

$$\boldsymbol{x}^T = [\omega_M \quad (\theta_M - \theta_W) \quad \omega \quad (\theta_W - \theta_{Sx}) \quad \omega_{Sx}] \,. \tag{4.2}$$

Table 4.2: Parameters of the VEL mechanical parts associated with front wheels (Alhanouti & Gauterin, 2023a)

Element	**Value**	**Unit**	**Reference**
Powertrain motor inertia (J_E)	0.03	kg·m^2	(Z. Gao et al., 2019)
Wheel hub inertia (J_{WH})	0.464	kg·m^2	(Petersen & Starkey, 1996)
Axle inertia (J_{Ax})	3.7x10^{-4}	kg·m^2	(Petersen & Starkey, 1996)
Differential inertia (J_D)	1x10^{-2}	kg.m^2	(Z. Gao et al., 2019; Hu et al., 2019; Petersen & Starkey, 1996)
Gearbox inertia (J_g)	0.0524	kg·m^2	(Petersen et al., 1996)
Gearbox transmission ratio (i_g)	4	—	Technical datasheet
Differential transmission ratio (i_D)	2.5	—	Technical datasheet
Loading machine inertia (J_M)	0.6	kg·m^2	Technical datasheet
CV shaft inertia (J_S)	0.0243	kg·m^2	Technical datasheet
CV shaft stiffness (K_S)	171450	Nm/rad	Technical datasheet
CV shaft internal damping (D_S)	5.99	Nm.s/rad	Technical datasheet
Axle stiffness (K_{Ax})	7700	Nm/rad	(Scamarcio et al., 2020)
Axle internal damping (D_{Ax})	3.57	Nm.s/rad	(Ineichen, 2013)
Coulomb friction constant (M_{F0})	0.5	Nm	(Forstinger, 2017)
Friction moment factor (k_M)	0.06	—	(Petersen & Starkey, 1996)
Viscous friction factor ($k_{\Delta\omega}$)	0.06	—	(Petersen & Starkey, 1996)

ω_M is the reference variable, ω and ω_{Sx} are estimated quantities, and ($\theta_M - \theta_W$) and ($\theta_W - \theta_{Sx}$) are correspond to the estimated angular differences between the loading machine and the wheel hub, and between the wheel hub and the differential gearbox, respectively. The controlled plant and the controller in the state space model can be expressed in differential equations and in form of matrices. Hence, the model of the system in Figure 4.4 reads as in equations (4.3) and (4.4)

$$J_T \frac{d\omega_M}{dt} = M_M - D_S(\omega_M - \omega) - K_S(\theta_M - \theta_W)$$

$$J_W \frac{d\omega}{dt} = D_S(\omega_M - \omega) + K_S(\theta_M - \theta_W) - D_{Ax}(\omega - \omega_{Sx}) - K_{Ax}(\theta_W - \theta_{Sx})$$

$$J_{Pt2W} \frac{d\omega_{Sx}}{dt} = D_{Ax}(\omega - \omega_{Sx}) + K_{Ax}(\theta_W - \theta_{Sx}) - M_{Sx} - \frac{M_F}{2} \tag{4.3}$$

where

$$J_{Pt2W} = J_{Ax} + \frac{J_D i_D^2 + \left(J_E + J_g\right) i_D^2 i_g^2}{2}$$

$$\dot{\boldsymbol{x}} = \underbrace{\begin{bmatrix} -\frac{D_S}{J_T} & -\frac{K_S}{J_T} & \frac{D_S}{J_T} & 0 & 0 \\ 1 & 0 & -1 & 0 & 0 \\ \frac{D_S}{J_W} & \frac{K_S}{J_W} & \frac{-(D_S + D_{Ax})}{J_W} & -\frac{K_{Ax}}{J_W} & \frac{D_{Ax}}{J_W} \\ 0 & 0 & 1 & 0 & -1 \\ 0 & 0 & \frac{D_{Ax}}{J_{Pt2W}} & \frac{K_{Ax}}{J_{Pt2W}} & -\frac{D_{Ax}}{J_{Pt2W}} \end{bmatrix}}_{\boldsymbol{A}} \boldsymbol{x} + \underbrace{\begin{bmatrix} \frac{1}{J_T} \\ 0 \\ 0 \\ 0 \\ 0 \end{bmatrix}}_{\boldsymbol{B_1}} u_1 + \underbrace{\begin{bmatrix} 0 \\ 0 \\ 0 \\ 0 \\ -\frac{1}{J_{Pt2W}} \end{bmatrix}}_{\boldsymbol{B_2}} u_2 + \underbrace{\begin{bmatrix} 0 \\ 0 \\ 0 \\ 0 \\ -\frac{1}{2\,J_{Pt2W}} \end{bmatrix}}_{\boldsymbol{B_z}} z \tag{4.4}$$

$$y = \underbrace{\begin{bmatrix} 1 & 0 & 0 & 0 & 0 \end{bmatrix}}_{\boldsymbol{C}} \boldsymbol{x}\,.$$

A is the system's state space matrix, ***B₁*** is the input vector of moment M_M, which is denoted by u_1. ***B₂*** is the input vector of moment M_{Sx}, represented by u_2. ***B_z*** is the input vector for the disturbance moment M_F, denoted by z. and ***C*** is the output matrix. The electric loading machines are voltage-driven by inverters employing field-oriented control (FOC), which allows precise moment manipulation (Forstinger, 2017). The response is described by a transfer

function from the reference signal to the motor moment (Harnefors & Nee, 1998; Saarakkala & Hinkkanen, 2014). According to (Forstinger, 2017; Harnefors & Nee, 1998), the electrical components add a time delay, which is modeled in equation (4.5) as the transfer function $G_d(s)$

$$G_d(s) = \frac{\alpha_t}{s + \alpha_t} \mathrm{e}^{-s\,T_d}\,, \tag{4.5}$$

where T_d is the time delay, and α_t is the bandwidth of the electrical components of the VEL test bench. Excessive T_d can destabilize the speed control loop, particularly when high-frequency dynamics are significant (Forstinger, 2017; Saarakkala & Hinkkanen, 2014). Therefore, the hardware setup of the electrical components should be optimized for small time delays and sudden changes in moment dynamics. Measurement delays originating from the incremental encoders further compound the total delay, as indicated in (Saarakkala & Hinkkanen, 2014). The working principle of the incremental encoder is based on calculating the difference in the measured rotational angle within a specific sampling time interval. Thus, significant quantization noise and time delay in the measurements are produced from the sampling scheme (Muszynski & Deskur, 2010). Hence, the measurement time delay is modeled in (Saarakkala & Hinkkanen, 2014) as a transfer function $M(s)$ with the measurement time delay (T_m). $M(s)$ is modeled in equation (4.6)

$$M(s) = \mathrm{e}^{-s\,T_m}. \tag{4.6}$$

As discussed in(Saarakkala & Hinkkanen, 2014), the total delay transfer function $G_\Delta(s)$ that captures the combined effect of T_d and T_m is modeled in equation (4.7)

$$G_\Delta(s) = G_d(s)\,M(s) = \frac{\alpha_t}{s + \alpha_t} \mathrm{e}^{-s\,(T_d + T_m)}. \tag{4.7}$$

4.3 Control algorithm

The detailed nonlinear drivetrain system shown in Figure 4.4 is simplified for controller design purposes to a three-mass model represented by a fifth-order linear continuous-time state space formulation. This reduced model captures the essential torsional dynamics between the motor, shaft, axle, and wheel sides and exhibits five poles at 0, -2.65 ± j108, and -41.2 ± j1310, as shown in Figure 4.5

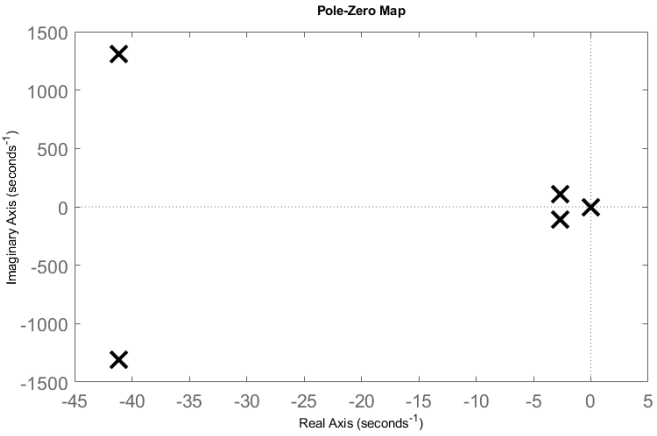

Figure 4.5: Poles of the plant (Alhanouti & Gauterin, 2023a).

The pole at the origin reflects marginal stability, while the complex conjugate poles correspond to dominant torsional resonance modes at 108 rad/s and 1310 rad/s with low damping ratios of 0.0244 and 0.0315, respectively. For operating-point analysis, steady-state conditions are defined by zero state derivatives, implying constant rotational speeds and moments with no angular acceleration, i.e., the operating point satisfies $\dot{\boldsymbol{x}} = \mathbf{0}$. Under these conditions, the couplings enforce equal steady-state angular speeds across all inertias, and constant torsional deflections arise in the shaft and axle, proportional to the applied motor moment and inversely proportional to their stiffness

coefficients. At equilibrium, the motor moment exactly balances the external load moment at the wheel side, yielding a unique operating point characterized by uniform rotational speed, static elastic deformation, and zero net acceleration. Although this linearized model is suitable for controller synthesis and stability analysis, the simulation models should retain the system's nonlinearities to accurately capture real-world behavior (Fietzek, 2014; Forstinger, 2017; Forstinger et al., 2016). Effective control design must therefore stabilize the marginally stable mode and significantly increase damping of the dominant low-frequency resonance.

A control algorithm is required to compensate for the mechanical losses and suppress the torsional vibrations in the system with flexible couplings (R. Bauer, 2011a). Speed control algorithms manipulate the angular speeds to compensate for mechanical losses and suppress torsional vibrations in the system (Fietzek, 2014; Saarakkala et al., 2012; Saarakkala & Hinkkanen, 2014; Szabat & Orlowska-Kowalska, 2007, 2012). The vibrations arise mainly from shaft elasticity, gear backlash, and torque harmonics from the electric drives (Fietzek & Rinderknecht, 2013; Forstinger, 2017; Nordin & Gutman, 2002; Thomsen & Fuchs, 2009).

4.3.1 Literature review and control algorithms evaluation

Proportional integral (PI) controllers are commonly applied in torsional vibration mitigation due to their simplicity, robustness, and ease of tuning (Fietzek & Rinderknecht, 2015; Nordin & Gutman, 2002). However, PI controllers inherently offer a trade-off between robustness and tracking performance and are less effective in damping high-order torsional dynamics (Fietzek, 2014; Saarakkala & Hinkkanen, 2014). In addition, many studies verified that PI control performed poorly in damping the torsional vibrations (Saarakkala & Hinkkanen, 2014; Szabat & Orlowska-Kowalska, 2007; Thomsen et al., 2011). Moreover, due to its limited tunable parameters, i.e., proportional gain (k_P) and integral gain (k_I), it has a low performance with complex systems (Saarakkala & Hinkkanen, 2014).

To extend control bandwidth, additional internal feedback paths can be introduced. For instance, (G. Zhang & Furusho, 2000) proposed a dual feedback configuration for improved pole placement. While, (Szabat & Orlowska-Kowalska, 2012) introduced feedback gains based on shaft torque and motor's wheel speed differences.

State feedback control (SFC) provides an alternative by employing full-state feedback of all system variables, i.e., rotational speeds and torsional moments, to achieve superior damping and dynamic performance (Beineke et al., 1997; Ji & Sul, 1995; Szabat & Orlowska-Kowalska, 2006). It offers systematic pole placement, strong transient response, and improved handling of nonlinearities. However, its implementation requires full system modeling and accurate parameterization (Thomsen et al., 2011). Moreover, the parameters are uncertain affects the steady-state results. Lastly, and most importantly, it is unable to regulate the output error.

To eliminate steady-state error, an integral term can be incorporated into the state space feedback controller, forming an integral state space (I-SS) control structure (Saarakkala & Hinkkanen, 2014; R. Zhang & Tong, 2006). It was also confirmed in (Saarakkala & Hinkkanen, 2014) that the I-SS is a much better alternative compared to the PI controller with additional feedbacks. However, the downside of the I-SS control compared to the state space feedback is the increment in the settling time and decrease in the phase margin.

A comparative analysis of various control algorithms, including conventional PI control, I-SS control, and model predictive control (MPC), was conducted by (Thomsen et al., 2011). The findings indicated that PI control exhibited the poorest performance in terms of dynamic characteristics. Conversely, both I-SS and MPC delivered superior performance, albeit at the cost of increased implementation and tuning complexity. Concerning stability and robustness, I-SS was ranked highest, followed by PI control, with MPC performing least effectively in this regard. Additionally, MPC required the greatest computational effort, as measured by processing time. The study concludes that the

selection of an optimal speed control strategy is contingent upon user-specific requirements and the particular application.

In order to systematically evaluate the suitability of different control strategies for vehicle test bench applications, it is essential to compare them across a set of consistent performance and implementation criteria. Each algorithm embodies specific strengths and weaknesses, which become particularly evident when applied to highly dynamic, nonlinear multi mass systems. For clarity, the comparison is structured along several key categories:

- **Approach**, describing the fundamental principle of the control method.
- **Main merits and downsides**, summarizing its primary advantages and limitations.
- **Speed tracking performance**, assessing its ability to follow rapid reference changes.
- **Robustness and steady-state error**, evaluating sensitivity to uncertainties and ability to eliminate long-term offsets.
- **Vibration suppression**, reflecting performance in attenuating torsional oscillations.
- **Modeling and implementation effort**, estimating the resources required for modeling, design, and deployment.
- **Applicability to multi mass test bench system**, highlighting its practical relevance for complex drivetrain configurations.

This structured framework ensures that the algorithms are not only contrasted in terms of theoretical capability but also judged against the practical demands of real-world test benches. The following comparative overview is intended to guide the selection of the most appropriate control method under specific development and testing conditions.

Approach: PI

- **Main merits**: **Very simple** design and tuning; widely used; does not require full state space model,
- **Main downsides**: Only two tuning parameters (K_p, K_i); limited closed-loop pole placement; trade-off between robustness and tracking; poor at damping torsional vibrations in many studies,
- **Speed tracking performance**: **Good** for basic control performance if tuned for one objective, but cannot optimize multiple objectives simultaneously,
- **Robustness and steady-state error**: **Moderate** robustness if conservatively tuned; steady-state error for constant references is removable by integral action, however the dynamics tradeoffs remain,
- **Vibration suppression**: **Poor** because it is not effective for torsional vibration damping in general,
- **Modeling and implementation effort**: **Low** because it is easy to implement on the test bench controller,
- **Applicability to multi mass test benches**: **Good** baseline; often used for two-mass systems.

Approach: PI with additional feedback gains

- **Main merits**: Maintains PI simplicity but adds more closed-loop poles via extra feedback loops; better of regulating speed and torque differences,
- **Main downsides**: More tuning variables than the PI controller; restricted compared to full state feedback; design is not systematic,
- **Speed tracking performance**: **Better** than plain PI for multi objective tuning (vibration + tracking) if gains chosen well,
- **Robustness and steady-state error**: **Improved** robustness compared to plain PI is possible, but depends on tuning strategy; still limited interpretability,
- **Vibration suppression**: **Improved** relative to plain PI; can actively damp torsional modes by adding moment and relative-speed feedback,
- **Modeling and implementation effort**: **Moderate** because it needs measurement for extra feedbacks,

- **Applicability to multi mass test benches**: **Good** compromise when model data are limited, but additional sensors are available.

Approach: PI with decoupling control

- **Main merits**: Decouples between subsystems, so PI loops can act more independently; can improve the performance without full state feedback,
- **Main downsides**: Requires a model for decoupling blocks; decoupling degrades with model mismatch; added design complexity vs plain PI,
- **Speed tracking performance**: **Better** tracking of coupled multi mass dynamics compared to plain PI,
- **Robustness and steady-state error**: **Good**. Decoupling can improve robustness but adds sensitivity to model errors,
- **Vibration suppression**: **Good** if the decoupling is applicable and the model mismatch is small,
- **Modeling and implementation effort**: **Moderate** because it needs a decoupling modeling; implementation still simpler than full state space,
- **Applicability to multi mass test benches**: Suitable when coupling is the dominant issue and a reasonable plant model is available but full state space feedback is too costly.

Approach: SFC

- **Main merits**: Uses feedback from all relevant state variables: can place closed-loop poles arbitrarily; fast detection of internal deviations; structured design; handling of nonlinearities in model,
- **Main downsides**: Requires accurate state space model and state measurement or observers; higher design and tuning effort; steady-state error not guaranteed to be zero,
- **Speed tracking performance**: **Excellent**. Able to trade tracking speed vs damping by pole placement,
- **Robustness and steady-state error**: Robustness **depends** on model accuracy; without an integral action steady-state error may persist,

- **Vibration suppression**: **Very good**. Can damp high torsional modes via state feedback,
- **Modeling and implementation effort**: **High** due to the need of the modelling, observer design, and complex tuning and implementation,
- **Applicability to multi mass test benches**: Very appropriate for multi mass design where internal states are measurable or estimable.

Approach: I-SS

- **Main merits**: Adds integral action to state feedback; enforces zero steady-state error for constant references; retains multi state damping capability; top ranked for stability and robustness in some studies,
- **Main downsides**: Requires accurate state space model and state measurement or observers; higher design and tuning effort; steady-state error not guaranteed to be zero,
- **Speed tracking**: Combines pole placement for dynamics with integral corrector for steady-state,
- **Robustness and steady-state error**: **Excellent** due to its robustness and zero steady-state error for constant references. However, careful tuning required to avoid sluggishness,
- **Vibration suppression**: **Excellent** due to the full-state feedbacks with the integral makes it effective at damping and eliminating offset,
- **Modeling and implementation effort**: **High** due to the need of the modeling, integral augmentation tuning; implementation effort is substantial,
- **Applicability to multi mass test benches**: Recommended when multi mass dynamics and vibration suppression are critical and modelling resources exist.

Approach: MPC

- **Main merits**: Can optimize the objective cost subject to constraints; excellent transient performance in many cases; flexible to include constraints explicitly,

- **Main downsides**: **Highest** computational load; longest calculation time; tuning and implementation is complex,
- **Speed tracking performance**: **Very good** for constrained optimal tracking, but performance depends on model fidelity and prediction horizon,
- **Robustness and steady-state error**: **Good**. Can be tuned for robustness, but less robust than I-SS and PI in at least one comparative study; highest processing/real-time requirements,
- **Vibration suppression**: **Very good** if vibration modes are included in prediction model and cost is formulated accordingly,
- **Modeling and implementation effort**: **Very high**. Needs accurate predictive model and real-time optimization tools,

Applicability to multi mass test benches: Best when constraint handling and optimal performance are applicable; and when sufficient real-time compute and a validated model are available; may be too much for simple test benches.

The evaluation Table 4.3 provides a qualitative assessment of the control algorithms, which mentioned in the literature review, against four equally weighted performance criteria: tracking capability, robustness, vibration suppression, implementation complexity, and suitability for multi mass systems. Using a symbolic scale of "+" for favorable and "-" for less favorable, the table reveals clear trade-offs among the control strategies. Controllers with strong tracking performance often exhibit reduced robustness or higher vibration sensitivity, while those with superior robustness may involve greater implementation complexity. Vibration suppression emerges as a differentiating factor, with some designs providing notable attenuation while others offer only marginal improvement. By applying equal weighting across criteria, the Table 4.3 facilitates an unbiased, high-level comparison that highlights the relative strengths and weaknesses of each approach, thereby informing subsequent selection for detailed frequency domain, time domain, and sensitivity analyses. The entries are: ++++ (excellent), +++ (very good), ++ (good), + (moderate), - (poor), -- (very poor). Accordingly, the control algorithms are sorted form the best to worst for this application: I-SS, SFC, PI + additional feedback, MPC, PI with decoupling, and the PI control is the least.

Table 4.3: Equal weight decision matrix for the control algorithms

Controller	Tracking	Robustness and steady-state error	Vibration suppression	Complexity	Applicability to multi mass test benches	Overall ranking
PI	++	++	--	++++	+	6
PI with additional feedbacks	+++	+++	++	+++	++	3
PI with decoupling	+++	++	++	++	+++	4
SFC	++++	+++	+++	+	++++	2
I-SS	++++	++++	++++	-	++++	1
MPC	+++	++	+++	--	+++	5

The ranking derived from the equal-weight decision matrix reflects the multi-dimensional trade-offs inherent in selecting a speed and moment control strategy for a powertrain test bench. The state space feedback controller with additional integral action (I-SS) occupies the top position due to its balanced strengths across all evaluated criteria—tracking, robustness, and vibration suppression—while its increased complexity is regarded acceptable in view of its superior closed-loop performance. This aligns with findings by (Saarakkala & Hinkkanen, 2014; R. Zhang & Tong, 2006), which demonstrated that integral augmentation effectively eliminates steady-state error and enhances disturbance rejection compared to pure state space feedback.

The pure state space feedback controller ranks second, offering high tracking accuracy and strong vibration suppression due to its full-state feedback structure, but lacking the integral action that secures steady-state error elimination. The PI controller with additional feedback gains follows closely, representing a pragmatic enhancement of a conventional PI loop. This structure benefits from improved dynamic shaping through added feedback channels, but its vibration suppression remains limited compared to full-state approaches, as also observed by (Szabat & Orlowska-Kowalska, 2012).

MPC ranks lower despite excellent tracking and vibration suppression capabilities, primarily due to its high implementation complexity and tuning demands. In real-time applications such as VEL test benches, computational burden and robustness under uncertainty are decisive factors, and MPC's lower robustness rating here reflects those constraints. The PI controller with decoupling performs similarly to PI with additional feedback in certain scenarios, but its reliance on accurate coupling models reduces robustness when plant uncertainties are significant.

The conventional PI controller predictably ranks lowest, confirming the consensus in (Fietzek, 2014; Thomsen et al., 2011) that while it remains the simplest and most easily tuned approach, it offers limited multi objective optimisation capacity, particularly in vibration suppression and high-order system control.

Overall, the ranking suggests that for a multi mass powertrain test bench, in the I-SS or SFC controllers are the most promising candidates for further detailed analysis. Among all the previously mentioned references (Fietzek, 2014; Fietzek & Rinderknecht, 2015) have developed a state space feedback controller for a multi mass system, while the rest had applications with a two-mass system at the most. Thus, a I-SS controller for a multi mass system will be proposed. Furthermore, a state space feedback controller, similar to the control algorithm in (Fietzek, 2014), will be further investigated. An optimized PI controller will also be tested to evaluate how well could the simplest approach perform.

The evaluation of control strategies for the powertrain test bench is conducted using a structured, sequential workflow designed to ensure that each algorithm is examined comprehensively in terms of stability, robustness, tracking accuracy, and vibration suppression. The process commences with controller design, in which a state feedback control simulation is developed based on a rigorously modelled state space representation of the system. This stage aims to regulate the plant to satisfy desired performance criteria,

including adequate stability margins, robustness against external disturbances, elimination of steady-state error, and desirable transient characteristics.

Following the design phase, frequency domain analysis is employed to characterise the closed-loop behavior of each controller. Within this stage, the sensitivity function serves as a quantitative measure of disturbance attenuation, indicating the extent to which output variations are mitigated by feedback. A detailed stability analysis is performed using the Nyquist criterion, explicitly accounting for delays originating in both the electrical actuation subsystem and the angular speed measurement chain. The insights obtained from the frequency domain investigations are subsequently validated through time-domain analysis. Here, both transient and steady-state responses are examined under representative dynamic reference profiles. These tests are repeated with and without the measurement noise to assess the stability of each control strategy under none ideal conditions. Next, a sensitivity analysis with respect to parameter uncertainty is undertaken to evaluate robustness when deviations from nominal model parameters occur. This includes systematic testing for the effects of time delay variations, disturbance torque injections, single-parameter deviations, and simultaneous multi parameter perturbations.

Once the baseline evaluations are complete, dynamic driving maneuvers are simulated on the VEL test bench model. Unlike earlier tests, which employ a fixed speed reference, these maneuvers simulate actual driving condition, ensuring that both steady-state and transient dynamics are implemented under high dynamic loading. In these experiments, two controllers—one per wheel—are operated concurrently, allowing verification of stable, coordinated behavior in a multi actuator configuration.

Finally, the driving moment controller is designed and integrated. This stage, is following the successful validation of the speed control loop, enables precise moment regulation in accordance with desired moment profiles. By progressing through these six methodological stages in sequence, the evaluation

framework ensures that each control strategy undergoes rigorous and systematic validation prior to practical implementation.

4.3.2 Controller design

A state feedback control simulation can be effectively carried out with an accurately identified plant model and a properly synthesized state feedback controller that ensures closed-loop stability as a requirement, while achieving specified performance objectives such as robustness to model uncertainties and disturbances, steady-state accuracy, and desired transient and dynamic response characteristics (Fietzek, 2014; Fietzek & Rinderknecht, 2015; Thomsen et al., 2011).

4.3.2.1 LQ controller

The primary objective of the linear-quadratic (LQ) optimization approach is to minimize a quadratic cost functional (4.8), in which the matrices $\boldsymbol{Q}$ and $\boldsymbol{R}$ as the weighting factors for the state vector ($\boldsymbol{x}$) and the input vector ($\boldsymbol{u}$), respectively. The minimization of the cost functional (J) is achieved by the state feedback law given in Equation (4.9), constrained by the system's dynamic equations. Unlike the pole-placement approach, which arbitrarily assign closed-loop poles without directly optimizing performance, this method formulates the control problem as an optimization of a specified performance output, which is derived from equation (4.10) based on the Riccati equation solution ($\boldsymbol{P}$) described in equation (4.11) (Astrom & Murray, 2010; Ogata, 2009)

$$\min_{u(t)} J(x,u) = \min_{u(t)} \int_0^{\infty} \left(\boldsymbol{x}^T(t)\, \boldsymbol{Q}\, \boldsymbol{x}(t) + \boldsymbol{u}^T(t)\, \boldsymbol{R}\, \boldsymbol{u}(t) \right) dt \tag{4.8}$$

$$\boldsymbol{u}(t) = -\boldsymbol{K_{LQ}}\, \boldsymbol{x}(t) \tag{4.9}$$

$$\boldsymbol{K_{LQ}} = \boldsymbol{R^{-1}}\, \boldsymbol{B_M^T}\, \boldsymbol{P} \tag{4.10}$$

$$\boldsymbol{A^T P + PA - PB_M R^{-1} B_M^T P + Q = 0}\,. \tag{4.11}$$

The resulting state feedback gain matrix ($\boldsymbol{K_{LQ}}$) is obtained implicitly as the solution to this optimization problem and corresponds to a globally optimal closed-loop response.

While the optimal LQ regulator ensures that the closed-loop system achieves the desired balance between control effort and state performance, its effectiveness fundamentally relies on the availability of accurate and complete state information. In theoretical formulations, it is generally assumed that all state variables are directly accessible for feedback, enabling the controller to apply the computed optimal gain matrix without restrictions. However, this assumption rarely holds true in real-world implementations, where measurement constraints, sensor noise, and physical inaccessibility of certain variables limit the ability to obtain full-state data. As a result, even an optimally designed LQ controller cannot be fully realized unless the system incorporates a technique to reconstruct or infer the unmeasured states. This necessity naturally leads to the incorporation of state observers or estimators, which complement the feedback design by providing reliable approximations of the internal system dynamics when direct measurements are insufficient or unavailable (Astrom & Murray, 2010; Ogata, 2009).

In practical applications, achieving a high-performing state space feedback controller becomes challenging when all required system states are not directly measurable, which is a common situation in industrial systems (Fietzek, 2014; Fietzek & Rinderknecht, 2015; Thomsen et al., 2011). Direct measurement of each mechanical state is often infeasible, costly, or detrimental to system reliability. To address this limitation, estimators are introduced to reconstruct the unmeasured variables (Beineke et al., 1997; Ji & Sul, 1995; Orlowska-Kowalska & Szabat, 2007). Estimation algorithms such as the Luenberger observer, neural networks, or Kalman filters (Astrom & Murray, 2010; Ogata, 2009) provide solutions to the non-measurable state problem (Beineke et al., 1997; Ji & Sul, 1995; Orlowska-Kowalska & Szabat, 2007). The

deviation between the model output and the measured system output is fed back to correct the model's state until convergence with the actual system states is achieved. The observer gain matrix ($\boldsymbol{L_{LQ}}$) is parameterized so that this deviation tends toward zero (Astrom & Murray, 2010; Ogata, 2009). To achieve high estimation accuracy, the gains of $\boldsymbol{L_{LQ}}$ are determined from the desired eigenvalues of the closed-loop characteristic matrix (4.12) of the full-state feedback controller using the same design principles (Fietzek, 2014). Consequently, the dynamics of the estimated state vector ($\hat{\boldsymbol{x}}$) are formulated in equation (4.13). By continuously comparing the measured output (y) with the estimated output ($\hat{\boldsymbol{y}}$), the estimated states are adjusted to asymptotically converge to the real states, yielding the observer error dynamics ($\boldsymbol{e}$) expressed in equation (4.14)

$$(\boldsymbol{A_{cl}})_{LQ} = \begin{bmatrix} \boldsymbol{A} - \boldsymbol{B_1 K_{LQ}} & \boldsymbol{B_1} \\ \boldsymbol{C} & \boldsymbol{0} \end{bmatrix} \tag{4.12}$$

$$\dot{\hat{\boldsymbol{x}}} = \boldsymbol{A}\hat{\boldsymbol{x}} + \boldsymbol{B_1 u} + \boldsymbol{L_{LQ}}(\boldsymbol{y} - \hat{\boldsymbol{y}}) \tag{4.13}$$

$$\dot{\boldsymbol{e}} = \dot{\boldsymbol{x}} - \dot{\hat{\boldsymbol{x}}} = \big(\boldsymbol{A} - \boldsymbol{L_{LQ}}\boldsymbol{C}\big)\boldsymbol{e}\,. \tag{4.14}$$

At this stage, the steady-state error has not yet been incorporated into the control structure. Unlike conventional controllers, the LQ method multiplies all states by the designed $\boldsymbol{K_{LQ}}$ and compares the result with the reference input. A precompensation gain ($\boldsymbol{F}$) is introduced to the reference signal to correct steady-state deviations. The precompensator gain $\boldsymbol{F}$ is determined as in equation (4.15) (Astrom & Murray, 2010; Ogata, 2009)

$$\boldsymbol{F} = \Big(\boldsymbol{C}\big(-\boldsymbol{A} + \boldsymbol{B_1 K_{LQ}}\big)^{-1}\boldsymbol{B_1}\Big)^{-1}. \tag{4.15}$$

The complete LQ controller combines the full-state feedback component with the linear section of the state estimator. The overall closed-loop dynamics of

the system are represented by equation (4.16), where ω_{ref} denotes the reference angular velocity (Ogata, 2009). The corresponding block diagram of this configuration is illustrated in Figure 4.6

$$\dot{\hat{\boldsymbol{x}}} = \left(\boldsymbol{A} - \boldsymbol{L_{LQ}C} - \boldsymbol{B_1 K_{LQ}}\right)\hat{\boldsymbol{x}} + \left[\boldsymbol{F B_1}\ \boldsymbol{L_{LQ}}\right]\begin{bmatrix}\omega_{ref}\\ \boldsymbol{y}\end{bmatrix}$$
$$\boldsymbol{u} = -\boldsymbol{K_{LQ}}\hat{\boldsymbol{x}} + \boldsymbol{F}\omega_{ref} \tag{4.16}$$

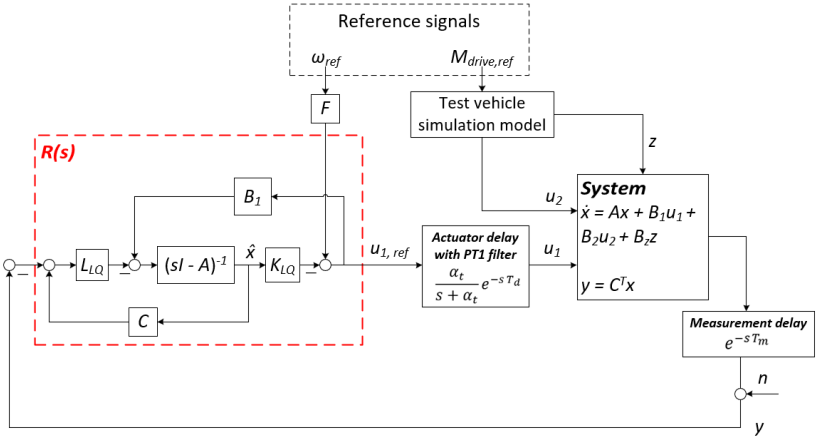

Figure 4.6: Block diagram of the plant system and the full-state feedback controller.

In this system, $G(s)$ represents the transfer function defined in equation (4.17), while the controller transfer function $R(s)$ consists of the state feedback and observer elements. The poles of the closed-loop LQ-system in Figure 4.6 cannot be directly specified; however, when $\boldsymbol{Q}$ and $\boldsymbol{R}$ are defined as diagonal matrices, each feedback gain within $\boldsymbol{K_{LQ}}$ can be individually adjusted (Fietzek, 2014)

$$G(s) = \frac{Y(s)}{U_{1,ref}(s)} = \boldsymbol{C}(s\boldsymbol{I} - \boldsymbol{A})^{-1}\boldsymbol{B_1}\, G_{\Delta}(s)\,. \tag{4.17}$$

The iterative tuning of $\boldsymbol{Q}$ and $\boldsymbol{R}$ is documented in equation (4.18), with tuning criteria focusing on three main objectives: (1) minimizing the deviation between the estimated values of ($\theta_M - \theta_W$) and ($\theta_W - \theta_{Sx}$) to reduce system vibration and fluctuation, (2) reducing the steady-state error of y (Fietzek, 2014), and (3) minimizing controller effort by reducing the manipulated variable M_M, thereby mitigating mechanical stress and preventing electrical overload (Fietzek, 2014; Forstinger, 2017; Pillas, 2017)

$$\boldsymbol{Q} = \begin{bmatrix} 1 \times 10^8 & 0 & 0 & 0 & 0 \\ 0 & 1 & 0 & 0 & 0 \\ 0 & 0 & 5 \times 10^6 & 0 & 0 \\ 0 & 0 & 0 & 1 & 0 \\ 0 & 0 & 0 & 0 & 1 \times 10^7 \end{bmatrix}, \qquad \boldsymbol{R} = 1500\,. \tag{4.18}$$

Following the optimization of $\boldsymbol{Q}$ and $\boldsymbol{R}$, the gain matrices $\boldsymbol{K_{LQ}}$ and $\boldsymbol{L_{LQ}}$ are computed as in equation (4.19), with the precompensator gain $\boldsymbol{F}$ equals to 277

$$\boldsymbol{K_{LQ}} = [250.75 \quad -1211.20 \quad 12.07 \quad 612.79 \quad 14.07]$$

$$\boldsymbol{L_{LQ}} = \begin{bmatrix} 401.65 \\ 0.01 \\ 97.35 \\ -0.08 \\ 3.38 \end{bmatrix}. \tag{4.19}$$

4.3.2.2 LQI controller

Figure 4.7 illustrates the extension of the LQ-controlled system, shown in Figure 4.6, into a linear-quadratic-integral (LQI) control scheme, designed as outlined in (Saarakkala & Hinkkanen, 2014; R. Zhang & Tong, 2006). The design procedure starts by augmenting the system with an additional integrator state variable (ξ) to capture the steady-state error, forming the extended system described by equation (4.20). Feedback is then included in the control law to regulate the output variable through integration. Subsequently, the LQ design principles are applied to LQI extended system

$$\dot{\xi} = \boldsymbol{C}\boldsymbol{x} - \omega_{ref}$$
$$u = -\boldsymbol{K_x}\,\boldsymbol{x} - K_\xi\,\xi - \boldsymbol{F}\,\omega_{ref}$$
$$\begin{bmatrix}\dot{\boldsymbol{x}}\\ \dot{\xi}\end{bmatrix} = \begin{bmatrix}\boldsymbol{A} & \boldsymbol{0}\\ \boldsymbol{C} & \boldsymbol{0}\end{bmatrix}\begin{bmatrix}\boldsymbol{x}\\ \xi\end{bmatrix} + \begin{bmatrix}\boldsymbol{B_1}\\ \boldsymbol{0}\end{bmatrix}u + \begin{bmatrix}\boldsymbol{0}\\ -1\end{bmatrix}\omega_{ref} \tag{4.20}$$
$$y = [\boldsymbol{C} \quad \boldsymbol{0}]\begin{bmatrix}\boldsymbol{x}\\ \xi\end{bmatrix}$$

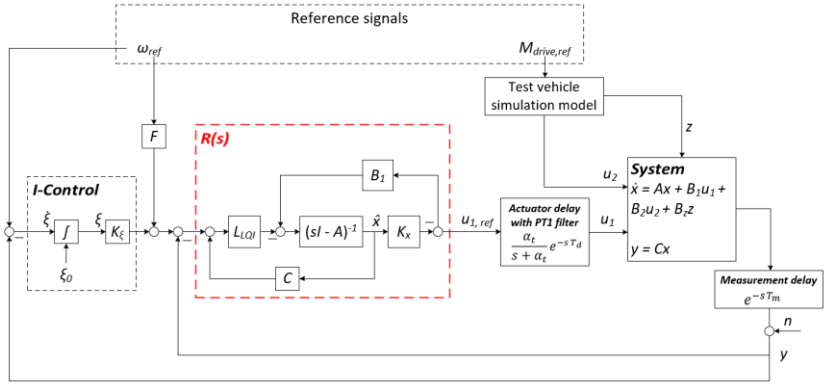

Figure 4.7: Block diagram representation of the plant system and the LQI controller.

It was determined that maintaining the same weighting matrix structures for $\boldsymbol{Q}$ and $\boldsymbol{R}$ in the LQI case, denoted $\tilde{\boldsymbol{Q}}$ and $\tilde{\boldsymbol{R}}$, yields comparable robustness and control effort to the LQ configuration, provided that the additional $\tilde{\boldsymbol{Q}}$ parameter corresponding to the new state variable (ξ) is appropriately tuned. The tuning was conducted to ensure both LQ and LQI share nearly identical closed-loop pole locations, facilitating a fair comparison. The final tuned $\tilde{\boldsymbol{Q}}$ and $\tilde{\boldsymbol{R}}$ values are shown in equation (4.21)

$$\widetilde{\boldsymbol{Q}} = \begin{bmatrix} 1\times10^{8} & 0 & 0 & 0 & 0 & 0 \\ 0 & 1 & 0 & 0 & 0 & 0 \\ 0 & 0 & 5\times10^{6} & 0 & 0 & 0 \\ 0 & 0 & 0 & 1 & 0 & 0 \\ 0 & 0 & 0 & 0 & 1\times10^{7} & 0 \\ 0 & 0 & 0 & 0 & 0 & 1\times10^{10} \end{bmatrix}, \widetilde{\boldsymbol{R}} = 1500\,. \qquad (4.21)$$

The corresponding gain matrices for the LQI controller ($\boldsymbol{K_{LQI}}$) and its observer ($\boldsymbol{L_{LQI}}$) are derived analogously to K_{LQ} and $\boldsymbol{L_{LQ}}$, as expressed in equation (4.22), with the LQI precompensator gain $\boldsymbol{F}$ determined to be 320.5

$$\boldsymbol{K_{LQI}} = [\boldsymbol{K_x} \quad K_\xi] = [256.1 \quad -1602.7 \quad 13.1 \quad 328.9 \quad 51.3 \quad 2582]\,,\ \boldsymbol{L_{LQI}} = \begin{bmatrix} 410.29 \\ 0.01 \\ 105.91 \\ -0.04 \\ 12.31 \end{bmatrix}. \qquad (4.22)$$

4.3.2.3 PI controller

To facilitate a fair comparison, the PI controller gains are tuned manually so that its dominant poles closely match those of the LQI system, resulting in k_p = 260, and k_i = 2050. As a result, the PI and LQI systems are expected to exhibit similar time-domain behaviors. Figure 4.8 presents the closed-loop pole distributions for all controllers. For the LQ controller, the optimal state feedback gain $\boldsymbol{K_{LQ}}$ and observer gain $\boldsymbol{L_{LQ}}$ were calculated and substituted into the closed-loop system matrix $(\boldsymbol{A_{cl}})_{LQ}$. This yields the final closed-loop poles, which define the system's stability and dynamics. The LQ-controlled system exhibits ten stable poles, while the inclusion of integral action in LQI introduces an eleventh. In contrast, the PI-controlled system features only six stable poles. Remarkably, all controllers successfully shifted the zero pole and the low-frequency resonant poles at -2.65 ± j108 further to the left side, ensuring system stability. Figure 4.9 highlights the dominant poles among the controllers

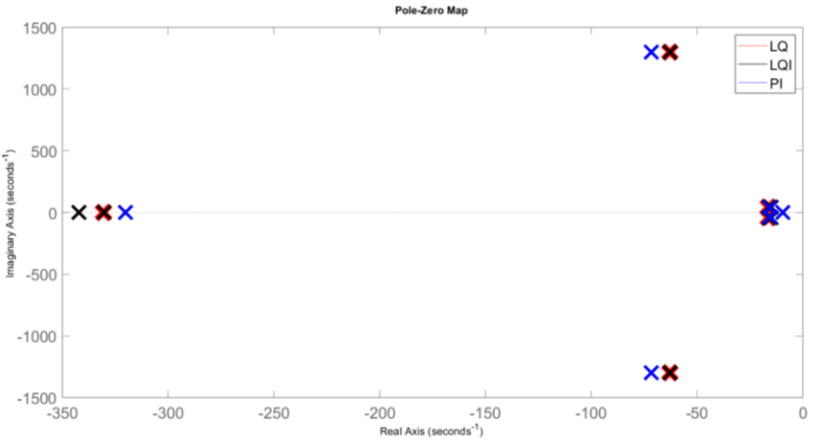

Figure 4.8: Closed-loop poles associated with each control system (Alhanouti & Gauterin, 2023a)

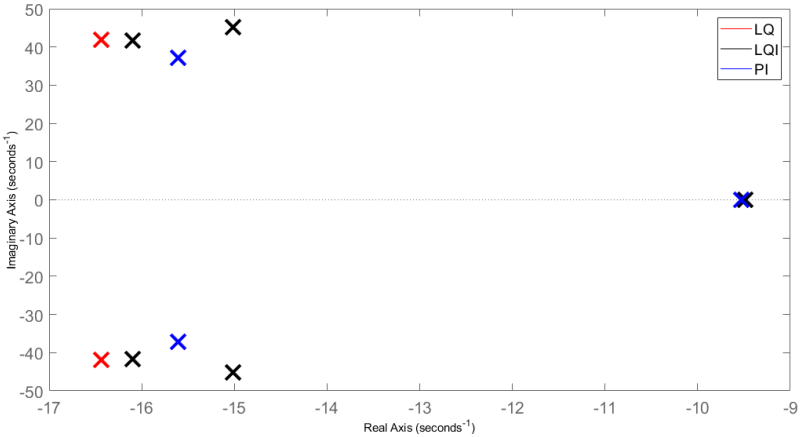

Figure 4.9: Closed-loop dominant poles associated with each control system (Alhanouti & Gauterin, 2023a).

The poles attributed to the integrator action of the PI and LQI controllers are positioned similarly, and the underdamped poles of the PI system were tuned

to closely align with those of the LQ and LQI systems to achieve comparable dynamic responses. However, the PI controller's poles could not be freely placed, confirming the observations in (Saarakkala et al., 2012; Saarakkala & Hinkkanen, 2014) that PI controllers are inherently more limited than state space feedback strategies.

Table 4.4 summarizes each control system's closed-loop poles, damping ratios, and natural frequencies. Although LQ and LQI share similar $\boldsymbol{Q}$ and $\boldsymbol{R}$ values, the slight variations in LQI poles arise from the additional tuning of the diagonal $\tilde{\boldsymbol{Q}}$ matrix. The presence of an extra real pole in LQI results directly from incorporating the integral action.

Table 4.4: Closed-loop poles and dynamic characteristics for each control system

LQ poles	LQ (ξ, ω_n) pairs	LQI poles	LQI (ξ, ω_n) pairs	PI poles	PI (ξ, ω_n) pairs
		-9.49	1, 9.49 rad/s	-9.53	1, 9.53 rad/s
-16.4 ± j41.9	0.37, 45 rad/s	-16.1 ± j41.6	0.36, 44.6 rad/s	-15.6 ± j37.2	0.38, 40.3 rad/s
-16.4 ± j41.9	0.37, 45 rad/s	-15 ± j45.1	0.32, 47.6 rad/s		
-62.9 ± j1300	0.05, 1300 rad/s	-62.9 ± j1300	0.048, 1300 rad/s	-71.7 ± j1300	0.06, 1300 rad/s
-62.9 ± j1300	0.05, 1300 rad/s	-62.8 ± j1300	0.048, 1300 rad/s		
-331	1, 33 rad/s	-330	1, 33 rad/s	-320	1, 320 rad/s
-331	1, 33 rad/s	-342	1, 34 rad/s		

4.3.3 Frequency analysis

In this section, the complete closed-loop system is analyzed in the frequency domain to assess its dynamic characteristics and control performance. Multiple closed-loop configurations, formed by the same plant in combination with different candidate controllers, are systematically compared. This section is organized as follows:

- Sensitivity function definition
- Nyquist stability analysis of proportional-integral control, optimal linear quadratic regulator, and optimal linear quadratic regulator with integral
- Measurement noise amplification for all controllers

The robustness of the closed speed-control loop will be evaluated by applying the maximum *peak criteria for the sensitivity function*.

4.3.3.1 Sensitivity function

The sensitivity function provides a quantitative measure of disturbance attenuation in feedback systems. It describes how output variations are influenced by disturbances. When the magnitude of the sensitivity function satisfies $|S(j\omega)| < 1$, disturbances at the corresponding frequencies are attenuated, whereas those at frequencies where $|S(j\omega)| > 1$ are amplified by the closed-loop. The maximum sensitivity, denoted as (M_S) in equation (4.23), represents the largest amplification of disturbances and typically occurs near the crossover frequency. It is expressed as a function of the open-loop transfer function $L(s)$ in equation (4.23). According to robustness criteria (Astrom & Murray, 2010; Saarakkala & Hinkkanen, 2014), a closed-loop system exhibits good robustness when $M_S < 2$, while $M_S > 4$ indicates poor performance and reduced stability margins

$$M_S = \max_{0\leq\omega<\infty} \left|\frac{1}{1+H(j\omega)}\right| = \max_{0\leq\omega<\infty} |S(j\omega)| \,. \tag{4.23}$$

4.3.3.2 Stability analysis

The sensitivity of the closed-loop systems is evaluated under ideal and delayed conditions. Two primary delay sources are considered: Electrical delay of the VEL system, represented by G_d(s), and 1.Electrical delay of the VEL system, represented by M(s). Then, the stability will be evaluated using *Nyquist criteria* (Astrom & Murray, 2010; Ogata, 2009). The total delay transfer function ($G_\Delta(s)$) is parameterized according to (Saarakkala & Hinkkanen, 2014), with α_t is 1800 rad/s, and T_d = 0.2 ms. The measurement delay T_m, which depends on the sensor sampling time (Muszynski & Deskur, 2010; Saarakkala &

Hinkkanen, 2014), is fixed to 0.7 ms in this analysis, resulting in a total delay, G_Δ, of approximately 0.9 ms. Consequently, $G_\Delta(s)$ can be approximated as a first-order delay function. The open-loop transfer functions of the PI, LQ, and LQI controllers are defined in equations (4.24) – (4.26), respectively

$$H_{PI}(s) = G(s)\left[k_p + \frac{k_i}{s}\right] \tag{4.24}$$

$$H_{LQ}(s) = \boldsymbol{K_{LQ}}\left(s\boldsymbol{I} - \boldsymbol{A} + \boldsymbol{L_{LQ}C}\right)^{-1} + \left[\boldsymbol{L_{LQ}}G(s) + \boldsymbol{B_1}\right] \tag{4.25}$$

$$H_{LQI}(s) = \boldsymbol{K_x}\left(s\boldsymbol{I} - \boldsymbol{A} + \boldsymbol{L_{LQI}C}\right)^{-1} + \left[\boldsymbol{L_{LQI}}G(s) + \boldsymbol{B_1}\right] + \frac{K_\xi}{s}G(s)\,. \tag{4.26}$$

The Nyquist plot in Figure 4.10 provides that the PI closed-loop control system exhibits high robustness in the ideal case with $M_S = 1$, i.e., $G_\Delta(s) = 1$. However, introducing a 0.9 ms delay reduces robustness with $M_S > 2$, as evidenced by the Nyquist contour approaching the critical (-1) point. Despite this, the closed-loop remains stable according to the Nyquist criterion. The LQ-controlled system maintains stability and robustness, with only a minor increase in M_S under delay conditions, as illustrated in Figure 4.11. In Figure 4.12, the LQI-controlled system demonstrates identical robustness to the LQ controller, with similar Nyquist plots in both ideal and delayed cases. In the presence of delay, the LQI contour exhibits a slight spiral pattern, indicating minimal phase sensitivity but preserved stability

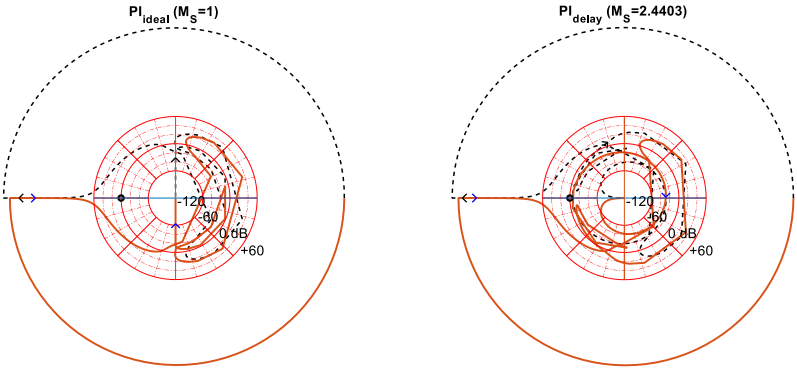

Figure 4.10: Nyquist plot in logarithmic scale[2]for PI-controlled system (Alhanouti & Gauterin, 2023a)

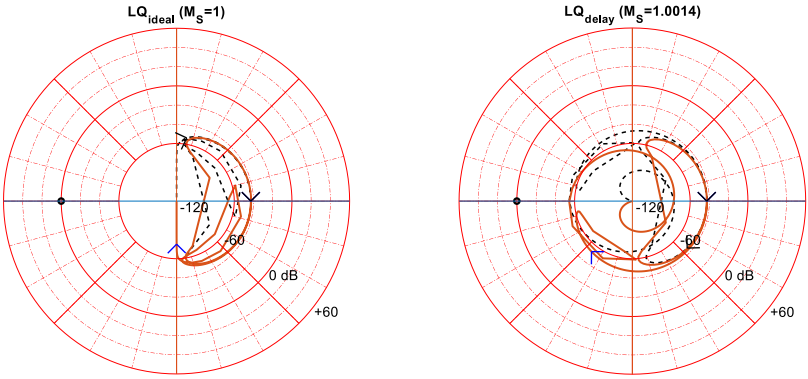

[2] Luca Ballotta (2021). Complete Nyquist plot on logarithmic scale https://github.com/lucaballotta/NyquistLog/releases/tag/1.0.1), GitHub. Retrieved December, 12, 2024.

Figure 4.11: Nyquist plot in logarithmic scale for LQ-controlled system (Alhanouti & Gauterin, 2023a)

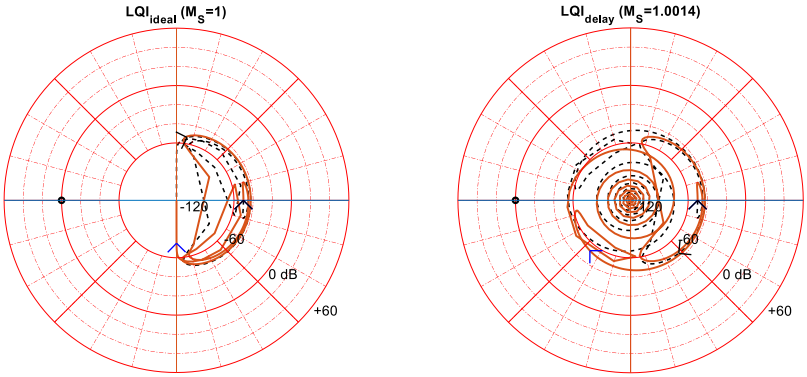

Figure 4.12: Nyquist plot in logarithmic scale for LQI-controlled system (Alhanouti & Gauterin, 2023a).

4.3.3.3 Measurement noise amplification

The influence of measurement noise in the closed-loop system is analyzed using the noise transfer function from the noise input *n* to the electromagnetic motor moment M_M (Saarakkala & Hinkkanen, 2014), as presented in Figure 4.6 and Figure 4.7. The noise transfer functions for the PI, LQ, and LQI controllers are derived in equations (4.27) – (4.29), respectively. Figure 4.13 illustrates that noise rejection capability increases with frequency for all control loops

$$N_{PI}(s) = -G_d(s)\left[k_p + \frac{k_i}{s}\right] \tag{4.27}$$

$$N_{LQ}(s) = -G_d(s)\left[\boldsymbol{K_{LQ}}(s\boldsymbol{I} - \boldsymbol{A})^{-1}\boldsymbol{L_{LQ}}\right] \tag{4.28}$$

$$N_{LQI}(s) = -G_d(s)\left[\boldsymbol{K_x}(s\boldsymbol{I} - \boldsymbol{A})^{-1}\boldsymbol{L_{LQI}} + \frac{K_\xi}{s}\right] \tag{4.29}$$

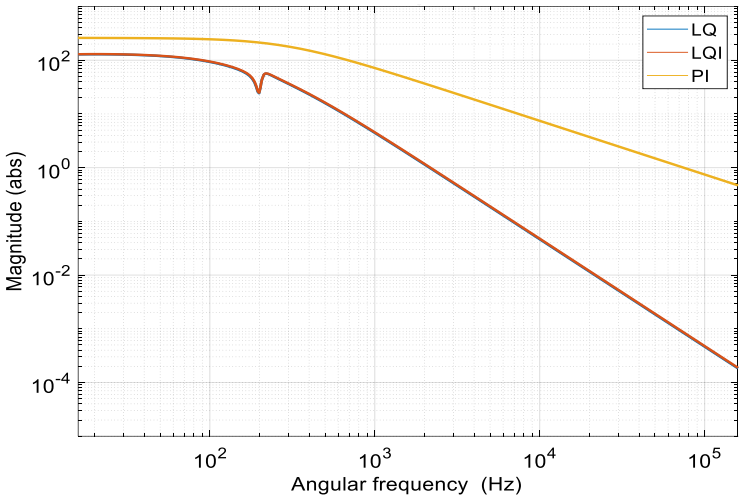

Figure 4.13: Measurement noise amplification magnitude of all types of controllers with time delay (Alhanouti & Gauterin, 2023a).

Both LQ and LQI controllers exhibit excellent noise rejection characteristics, while the PI controller performs the worst in this regard. The spiral Nyquist contour observed under internal delay reflects high phase offset at high frequencies (Segovia et al., 2014), further confirming that the LQ system's phase is least sensitive to delay. This observation means the LQ-controlled system's phase is the least sensitive to time delay.

4.3.4 Time domain analysis

In the previous section, each controller was assessed using frequency response analysis. Here the conclusions made earlier will be approved with the time response. In this section, the time response of all controllers will be examined through a dynamic test case. Next, the same test will be repeated with measurement noise. In Figure 4.14, the central figure shows the desired angular speed, as achieved by integrating the angular acceleration (Saarakkala & Hinkkanen, 2014)

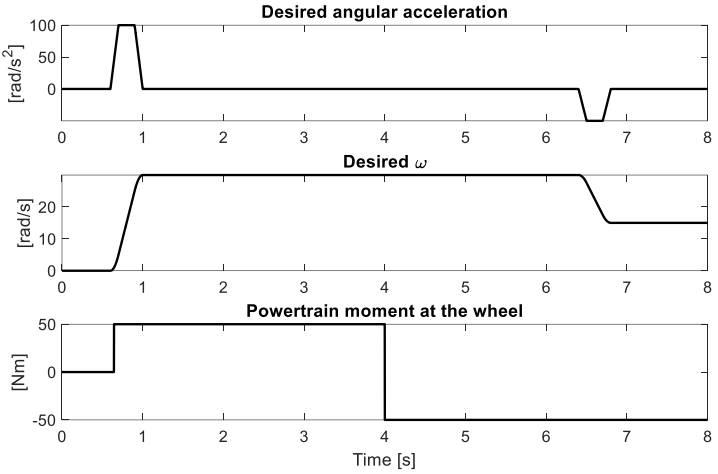

Figure 4.14: Desired reference signal and powertrain moment (Alhanouti & Gauterin, 2023a).

Using this approach smoothen the abrupt transition angles in the speed profile. So, it eliminates high peaks in the acceleration that may create high moment impulses. A highly dynamic test maneuver is applied, characterized by an angular acceleration transition from 0 to 1000 rpm (104.7 rad/s) within 0.4 s, which is equivalent to an acceleration of approximately m/s^2, followed by a powertrain torque inversion from 500 Nm to –500 Nm after 4 s. This test assesses each controller's ability to maintain target speed under rapid acceleration and torque disturbance conditions. In Figure 4.15, the PI-controlled system shows high robustness and good tracking performance under ideal conditions, i.e., $G_{\Delta}(s) = 1$ in the ideal case. However, its performance deteriorates significantly in the presence of a 0.9 ms delay, after the inversion of the powertrain moment, as shown in the figures at the right. This outcome validates the accuracy of the frequency analysis (Alhanouti & Gauterin, 2023a)

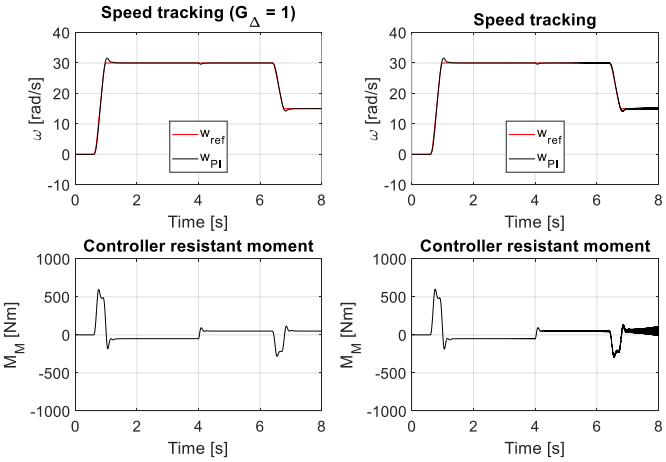

Figure 4.15: Time response of the PI-controlled system: (Left) without time delay, (Right) with time delay (Alhanouti & Gauterin, 2023a).

The LQ controller remains robust even with delay, though it exhibits a small steady-state error, as shown in Figure 4.16. The LQI controller, on the other hand, achieves excellent tracking performance with zero steady-state error and negligible influence from delay; as illustrated in Figure 4.17. Figure 4.18 presents the controllers angular speed tracking errors under delay. While PI and LQI share similar dominant pole locations, their robustness differs considerably. The LQ system retains good robustness but presents a steady-state deviation of approximately 0.37 rad/s, whereas the LQI controller eliminates steady-state error entirely within a short settling time

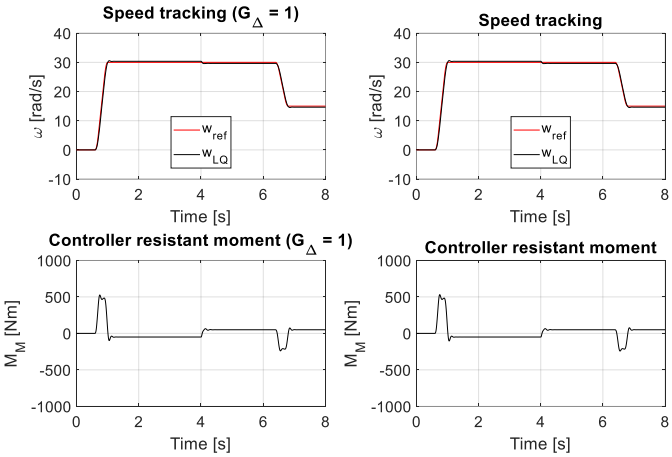

Figure 4.16: Time response of the optimal LQ-controlled system: (Left) without time delay, (Right) with time delay (Alhanouti & Gauterin, 2023a)

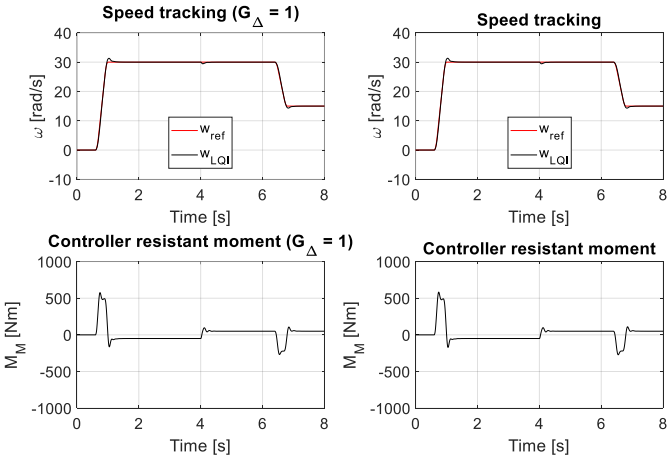

Figure 4.17: Time response of the optimal LQI-controlled system: (Left) without time delay, (Right) with time delay (Alhanouti & Gauterin, 2023a)

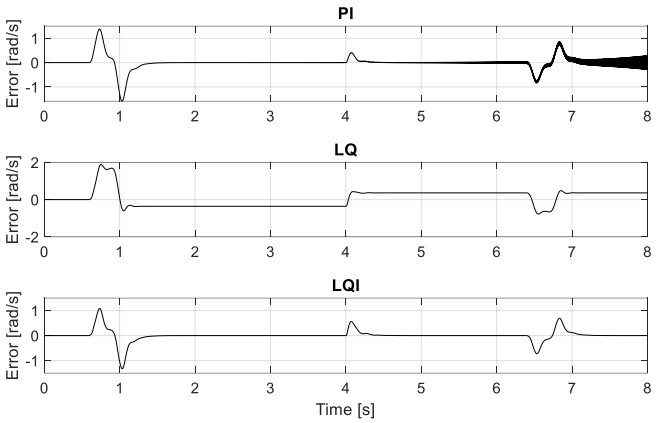

Figure 4.18: Angular speed error comparison: (Top) PI-controlled, (Middle) LQ-controlled, (Bottom) LQI-controlled (Alhanouti & Gauterin, 2023a).

To validate the noise rejection performance shown in Figure 4.13, the simulation was repeated with white noise introduced into the angular speed feedback signal. When white measurement noise with an amplitude of ±0.5 rad/s and a sampling time of $1x10^{-5}$ s, is introduced, the noise amplification magnitudes are found to be 4.678, 0.019, and 0.018 for the PI, LQ, and LQI controllers, respectively. As predicted, the PI controller amplifies noise significantly, leading to moment oscillations exceeding ±1000 Nm, despite the filtering effect of $G_d(s)$ on the controller moment compared to the ideal case. In contrast, both LQ and LQI controllers limit noise induced moment fluctuations to approximately ±3 Nm. These expectations are confirmed in Figure 4.19 – Figure 4.21. Overall, the PI controller is less capable of managing complex dynamic interactions. Both LQ and LQI controllers demonstrate high robustness against time delay and measurement noise. However, the PI controller fails under highly dynamic reference conditions and exhibits poor noise rejection. Based on these outcomes, the PI controller is excluded from further analyses in this study

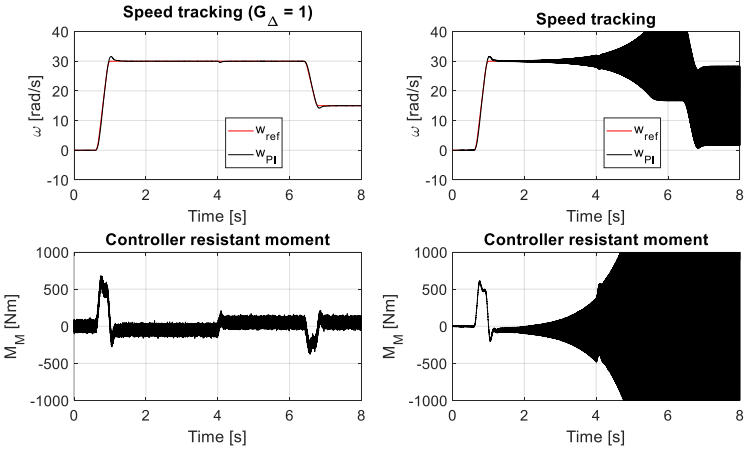

Figure 4.19: Measurement noise amplification of PI controller: (Left) without time delay, (Right) with time delay (Alhanouti & Gauterin, 2023a)

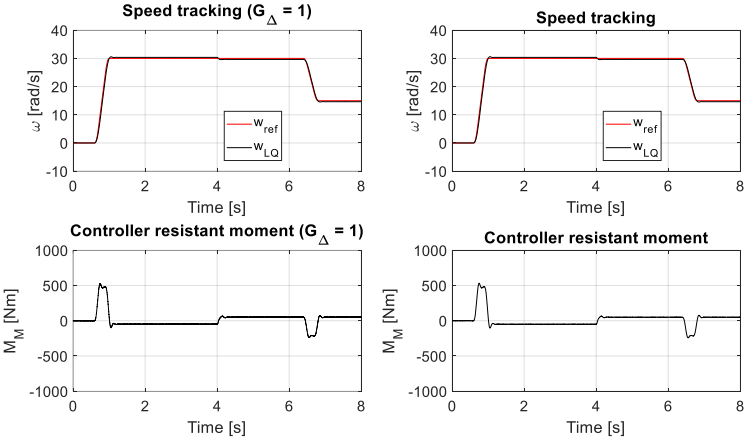

Figure 4.20: Measurement noise amplification of LQ controller: (Left) without time delay, (Right) with time delay (Alhanouti & Gauterin, 2023a)

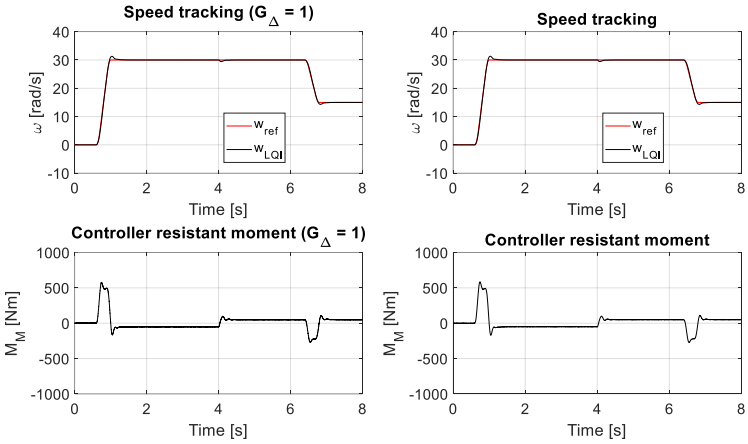

Figure 4.21: Measurement noise amplification of LQI controller: (Left) without time delay, (Right) with time delay (Alhanouti & Gauterin, 2023a).

4.3.5 Sensitivity analysis for a single parameter uncertainty

The selected controllers are created using prior knowledge of system model equations and the estimated values of their parameters. To assess the influence of model uncertainty on control performance, the same test procedures are repeated multiple times, each with a variation in one or more parameters (Alhanouti & Gauterin, 2023a). In this analysis, only the LQ and LQI controllers are investigated, since the PI controller was excluded from further evaluation due to its insufficient performance in the basic robustness and noise tests. The sensitivity of each closed-loop system is examined with respect to four factors: time-delay sensitivity, disturbance moment effect, single-parameter uncertainty, and multi parameter uncertainty. As discussed previously in Section 4.2, two primary time delays exist in the system: The electrical component delay of the test bench, modeled by $G_d(s)$ function in equation (4.5), and the measurement delay of the angular speed sensor, modeled by equation (4.6). For the present study, the electrical delay is fixed at T_d at 0.2 s, while

the measurement delay T_m varies randomly between 0.5 ms and 5 ms to simulate samplingtime variations. The results indicate that the LQ controller maintains high robustness against measurement delay variations, although a slight degradation in speed-tracking performance can be observed in Figure 4.22. The LQI controller, as anticipated from the frequency domain analysis, exhibits higher sensitivity to time delay. However, it remains stable and effective up to a measurement delay of 5 ms, as demonstrated in Figure 4.23

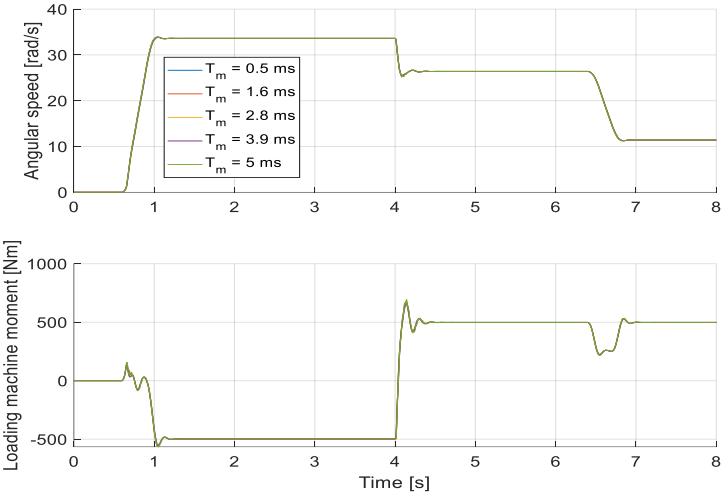

Figure 4.22: Time response of LQ controlled system at different T_m values (Alhanouti & Gauterin, 2023a)

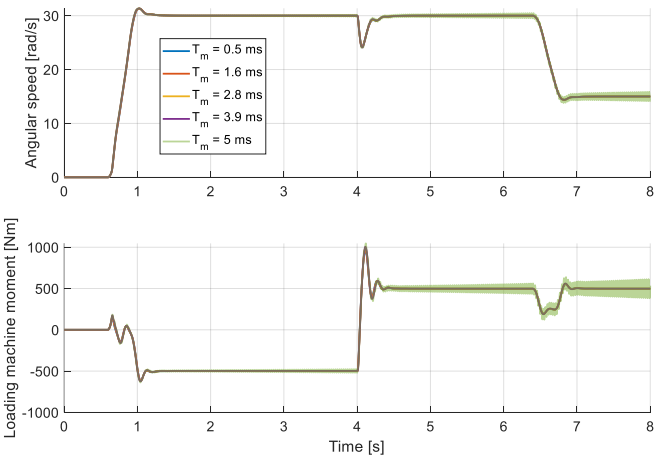

Figure 4.23: Time response of LQI controlled system at different T_m values (Alhanouti & Gauterin, 2023a).

The applied powertrain driving moment (M_{drive}) is perceived by the electrical loading machine as a disturbance acting on the speed control loop. Accordingly, it must generate a compensating resistive moment that preserves the desired rotational speed. Figure 4.24 and Figure 4.25 illustrate the influence of varying the driving moment on the performance of the LQ and LQI-controlled systems, respectively. Under no load conditions, i.e., M_{drive} = 0 Nm, LQ controller accurately follows the reference speed profile. However, the presence of external torque leads to a proportional shift in the steady-state response: positive moment, i.e., driving produces an upward offset, while negative moment, i.e., braking, causes a downward offset in speed. In contrast, the LQI controller maintains consistent speed-tracking performance across all disturbance torque levels, successfully compensating for even extreme moment changes. For instance, when the driving moment varies from +500 Nm to –500 Nm, the LQI controller experiences a temporary speed error of approximately 5 rad/s, which is fully corrected within 0.5 s

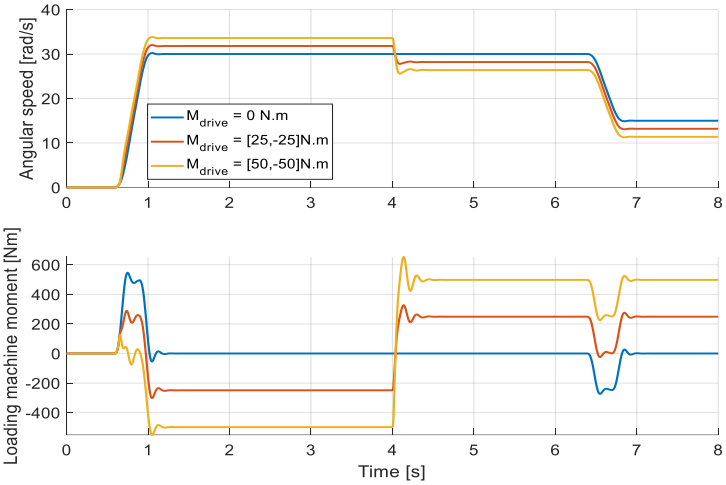

Figure 4.24: Time response of LQ-controlled system at different M_{drive} values (Alhanouti & Gauterin, 2023a)

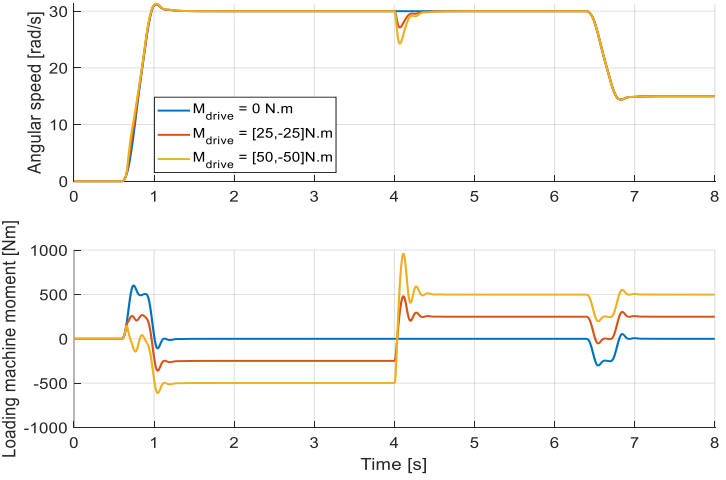

Figure 4.25: Time response of LQI-controlled system at different M_{drive} values (Alhanouti & Gauterin, 2023a).

To further analyze robustness, the same controller tuning parameters for both LQ and LQI are retained across all tests, while parameter uncertainties are introduced to evaluate their effect on system behavior. A large disturbance moment (from +500 Nm to –500 Nm) is also applied to create extreme conditions. The first case investigates the uncertainty in J_{Pt2W}, the equivalent inertia from the powertrain to the wheel hub. Monte Carlo simulations are employed to generate random deviations in this parameter. As illustrated in Figure 4.26, the LQ controller exhibits strong robustness to changes in J_{Pt2W}, with negligible variations in both angular speed tracking and controller moment response

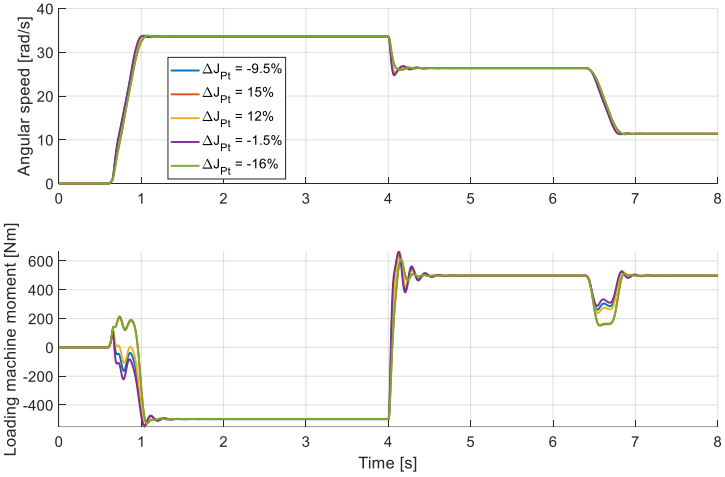

Figure 4.26: Time response of LQ-controlled system at different J_{Pt2W} values (Alhanouti & Gauterin, 2023a).

Similarly, the LQI controller preserves its high tracking accuracy and exhibits minimal sensitivity to this parameter variation, as shown in Figure 4.27 Next, the effect of uncertainty in K_{Ax}, the axle stiffness coefficient, is examined. As presented in Figure 4.28, variations in K_{Ax} do not significantly affect the LQ controller's dynamic behavior, although slight differences in steady-state

angular speed and moment response are observed. The LQI controller again demonstrates strong robustness to stiffness uncertainty, shown in Figure 4.29, maintaining nearly identical tracking performance and control-moment characteristics despite substantial parameter deviations. In summary, both LQ and LQI controllers exhibit high resilience to individual parameter uncertainties and external disturbance moments. The LQI controller, however, provides improved steady-state tracking and faster error correction under transient and uncertain conditions

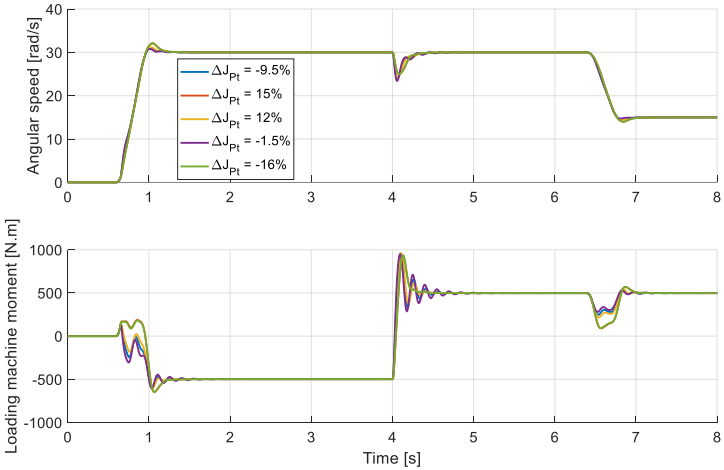

Figure 4.27: Time response of LQI-controlled system at different J_{Pt2W} values (Alhanouti & Gauterin, 2023a)

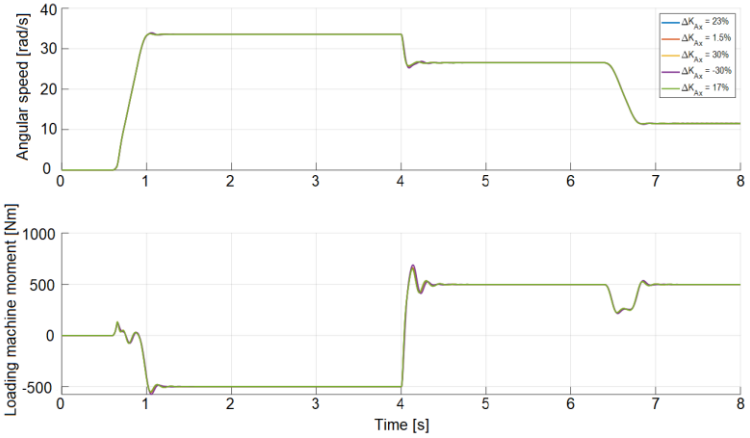

Figure 4.28: Time response of LQ-controlled system at different K_{Ax} values (Alhanouti & Gauterin, 2023a)

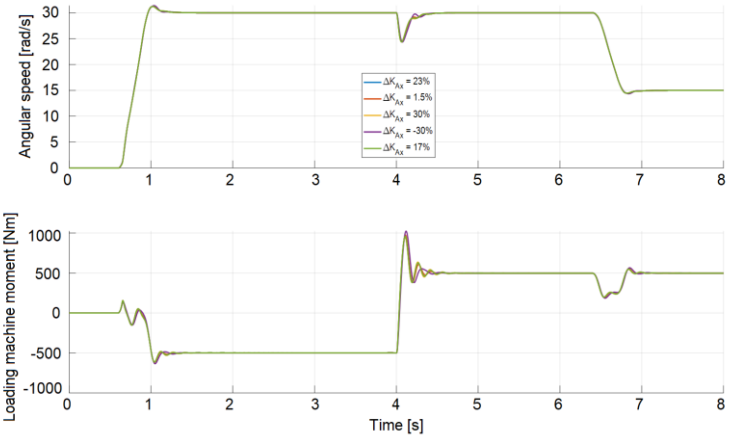

Figure 4.29: Time response of LQI-controlled system at different K_{Ax} values (Alhanouti & Gauterin, 2023a).

4.3.6 Sensitivity analysis for multiple parameter uncertainties

The same sets of uncertain variations for J_{Pt2W} and K_{Ax} are applied in paired combinations. The performance of the LQ and LQI-controlled systems under these conditions is illustrated in Figure 4.30 and Figure 4.31, respectively. The results demonstrate that the presence of two inaccurate parameter estimations induces a substantial degradation in the speed response of the LQ controller. In contrast, the LQI controller maintains a consistent tracking performance, exhibiting only minor deviations. It is noteworthy, however, that the moment control command differs significantly from the baseline established under accurate parametrization. For instance, the steady-state command no longer attains the nominal ±500 Nm. Furthermore, the controller output exhibits increased oscillatory behavior following transient states in some test cases

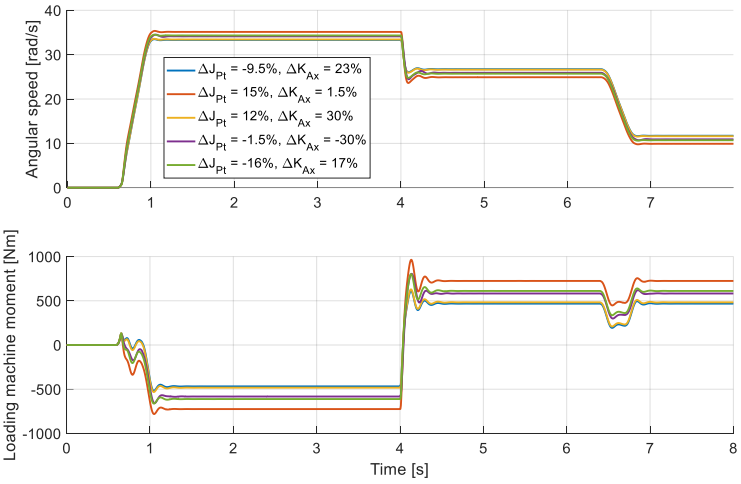

Figure 4.30: Time response of LQ-controlled system at different J_{Pt2W} and K_{Ax} values (Alhanouti & Gauterin, 2023a)

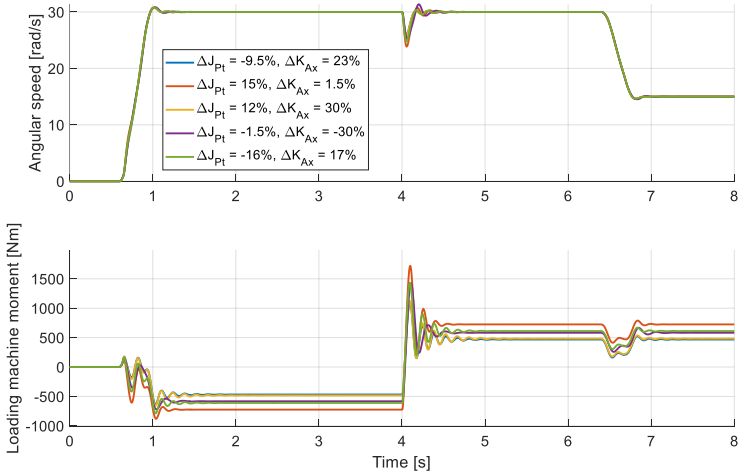

Figure 4.31: Time response of LQI-controlled system at different J_{Pt2W} and K_{Ax} values (Alhanouti & Gauterin, 2023a).

4.3.7 Proposed test maneuver for the VEL test bench

So far, the speed controller has been thoroughly investigated with a single reference angular speed. It is, however, emphasized in (Lensch-Franzen et al., 2018) that it is fundamental to reproduce realistic driving maneuvers to study the corresponding dynamic effects on the powertrain. The designed maneuvers should involve the complete system's steady-state and transient responses to get reliable results. Furthermore, the implementation of the desired maneuver necessitates a well-designed control algorithm. So, this section concerns testing the whole system with two active controllers simultaneously, i.e., for left and right driving wheels. It is desired to ensure that the two controllers work properly without imperiling the system, even with highly dynamic test maneuvers (Thomsen et al., 2011). The following test, shown in Figure 4.32, aims to inspect the performance of speed controllers when each wheel undergoes a different angular speed. As well as ensure the controllers' capacity to handle the dynamic changes in powertrain moments

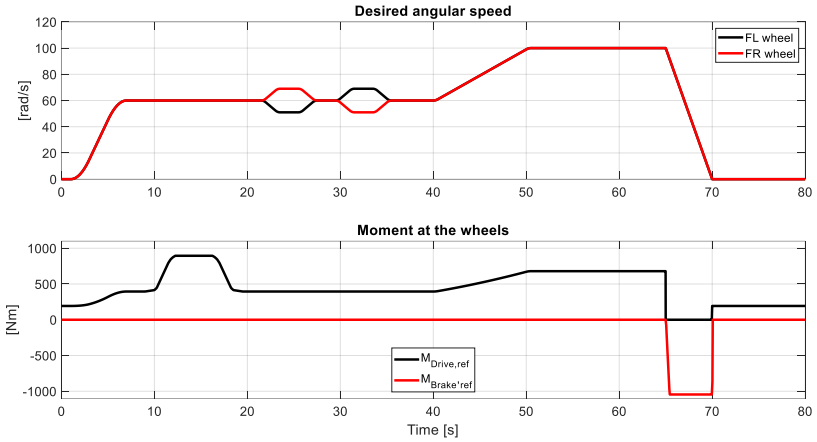

Figure 4.32: Angular reference speeds and moments for the proposed maneuver test.

In other words, the safety of having two independently controlled wheels coupled to a differential gear should be confirmed. The speed maneuver in Figure 4.32 is inspired by a similar test (Forstinger, 2017). The corresponding moment is proposed to simulate the driving resistance moment ($M_{drive,ref}$), calculated with the vehicle's estimated road load ABC factors under the test. The braking at the end of the maneuver is also introduced ($M_{brake,ref}$). This maneuver comprises several stimulating control demands. The first part of the reference angular speed signal is an acceleration from a standstill at 0 rad/s until the angular speed reaches 60 rad/s, and the driving moment is determined correspondingly. Then, the driving moment increases from 394 to 894 Nm and returns to 394 Nm, simulating uphill driving. Next, different angular speeds for the left and right wheels take place. After that, acceleration to a higher angular speed of 100 rad/s occurs. Finally, a sudden brake brings the wheels from high angular speed to a complete stop within 5 seconds. Figure 4.33 shows that the LQ controllers could not correctly track the angular reference speeds due to high driving moment demands. The error appears as a persisting offset that increases with the moment

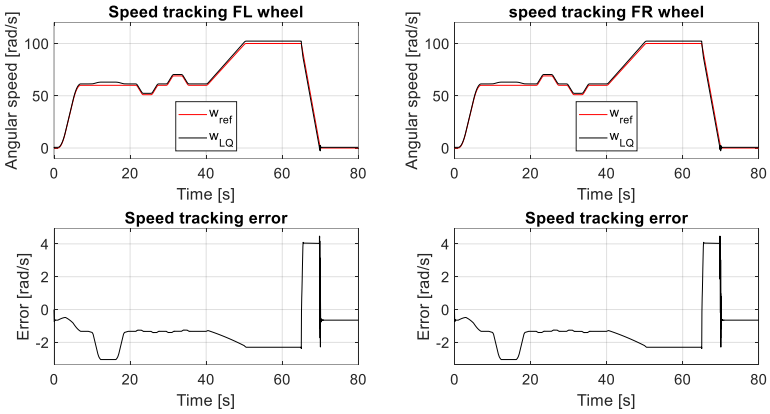

Figure 4.33: LQ controller performance in the proposed test.

In Figure 4.34, the LQI controller, otherwise, can maintain a precise trajectory, with less than an absolute error of just 0.1 rad/s in the driving mode. However, some peaks appeared due to changing the driving mode: From a standstill to accelerating, driving to braking, and decelerating to a standstill

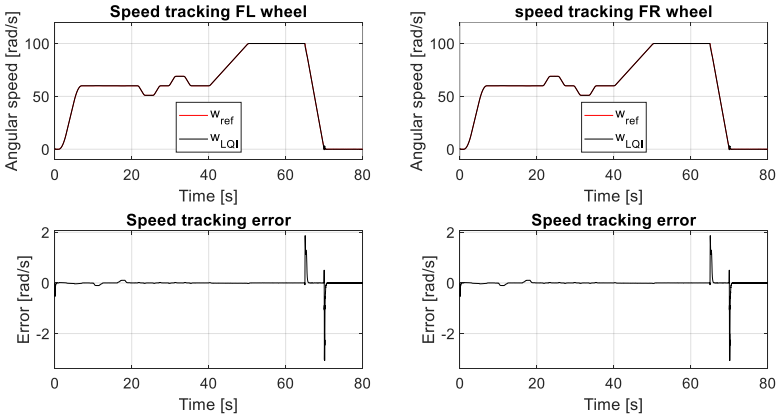

Figure 4.34: LQI controller performance in the proposed test.

The twist angle of the CV shaft and the connected axle are investigated to get a deeper insight into the impact of this excitation level on the system. Since no sensors are accessible to measure these quantities, we may benefit significantly from the observer by estimating these unmeasurable quantities. The twist angles of the CV shaft and the axle are obtained from the second and fourth estimated states, respectively. Figure 4.35 and Figure 4.36 demonstrate the dynamic changes between each shaft end when applying the LQ and LQI controllers, respectively. ($\theta_M - \theta_W$) is equal to the change in the CV shaft twist angle ($\Delta\theta_{CV}$). While ($\theta_W - \theta_{Sx}$) is equal to the change in the axle twist angle ($\Delta\theta_{Ax}$). It can be seen that the applied maneuver influences the axle multiple times more than the CV shaft because the axle has less stiffness than the CV shaft. When the maneuver is performed with LQI control, the twist angles are slightly larger than the LQ control alternative in the driving part of the maneuver. This result is a natural outcome because the LQI controller makes slightly more control effort to keep track of the reference angular speed signal. LQI controller led to minor axle deformation during the braking, though. The sum of the transmitted moments to the wheels for both LQ and LQI controllers is illustrated in Figure 4.37

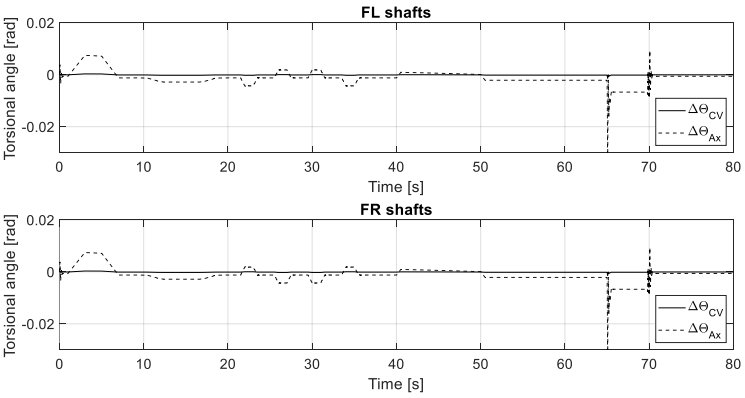

Figure 4.35: Twist angles of the CV shafts and axles for LQ control

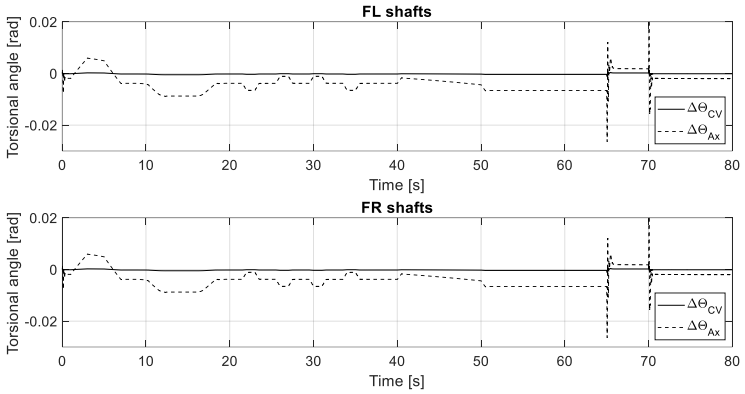

Figure 4.36: Twist angles of the CV shafts and axles for LQI control

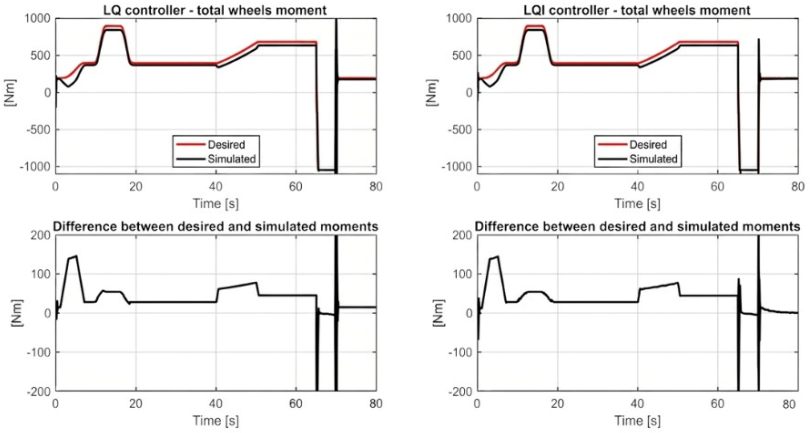

Figure 4.37: A comparison between the reference M_{drive} and the actual output moment for both LQ and LQI-controlled systems.

The difference between both control algorithms is barely recognized, making both output moments appear to be the same. However, if the peak values are investigated more perceptively, it would be realized that LQI has slightly

different moment peaks from the LQ controller. For instance, at time 0.12 s, the LQ controller led to a peak of -14.5 Nm, while it is equal to -66.5 Nm in the case of LQI, then the moments became 366.13 and 366.20 Nm for LQ and LQI controllers, respectively.

Another example, at the beginning of braking, which occurred at a time equal to 65 s and the applied braking moment was -1045 Nm, LQ produced -1057 Nm, while the corresponding peak moment in the LQI case is -1115 Nm. These values show how decisive the transient moment is, even if it takes effect for a short time. It also proves how efficient LQI is as a speed controller. LQ achieved high-quality tracking performance with minor modifications to its control moment. Nonetheless, the output moment for neither LQ nor LQI matches the expected driving moment from the driving resistance model. At the beginning of this section, it was specified that the purpose of implementing the LQ and LQI controllers is to minimize the errors in states vector $\boldsymbol{x}$ and the corresponding moment of the electrical loading machine M_M, which is the input moment to the plant. So, the difference between the reference total driving moment generated at wheels and the actual output moment at the test vehicle's wheel hubs needs an additional control algorithm.

In conclusion, as a speed controller, LQI surpasses the LQ controller in all tests, except for the robustness against time delay. In addition, a fine-tuned LQI could precisely track the reference speed, even if the assigned maneuver is highly dynamic.

4.3.8 Driving moment controller

Designing the control algorithm for the powertrain test benches is typically accomplished in two stages. Initially, the speed closed-loop control is implemented. Then, the moment controller can be designed to reach the desired moment (Bunker et al., 1997; Forstinger, 2017). Similar to the VEL test bench, the test bench studied in (Forstinger, 2017) has moment measurement sensors on the wheel hubs. The moment controller in (Forstinger, 2017) has two

parts: First, a feedforward gain (k_{FF}) for the reference powertrain moment M_{drive} that compensates a certain offset amount in the output moment. Second, an integral control with a gain parameter ($k_{I,M}$) to compensate for the remaining difference between the reference and the sum of measured moments (M_{sum}). So, the controlled driving moment (M_{drive}*) is expressed as in equation (4.30)

$$M_{drive}{}^{*} = k_{FF} M_{drive} + \frac{k_{I,M}}{s} [M_{drive} - M_{sum}] . \tag{4.30}$$

This control concept will also be employed for the VEL test bench to compensate for the moment reduction. The tuned k_{FF} and $k_{I,M}$ values are 0.2 and 8, respectively. With these relatively small gains, the resultant M_{drive}* is shown in Figure 4.38

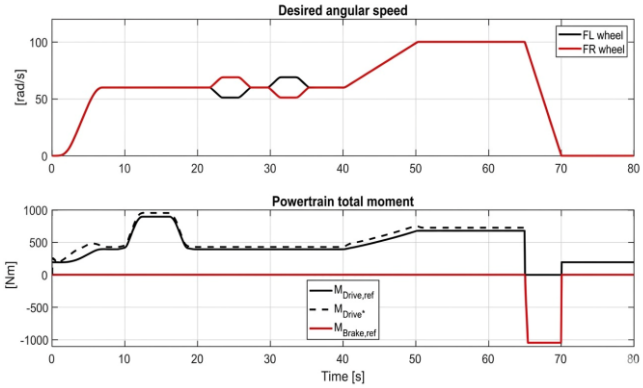

Figure 4.38: The proposed maneuver test with the controlled driving moment.

The angular speed tracking performance variation between the original LQI controller and the same LQI controller combined with the moment controller (LQI*) is insignificant, as demonstrated in Figure 4.39. Moreover, small increments in the shafts' twist angles are observed in the proposed driving maneuver segments, as illustrated in Figure 4.40. Throughout the maneuver, it is

observed that positive moments generally result in negative twist angles, while negative moments produce positive twist angles. An exception occurs at the very beginning, when the maneuver starts instantaneously with a positive driving moment at zero speed. This causes the twist angle to initially increase in the positive direction. During the first acceleration phase, i.e., from 0 to 7 seconds, the controller gradually reduces the twist angle, bringing it close to zero around the 7 second mark. Figure 4.41 shows that the implementation of the moment controller reduced the difference between the reference and actual moment to nearly zero at the steady-state. Furthermore, excluding the high peaks at the starting and braking conditions, the error of the output moment is reduced substantially, proving the system's efficiency when the proposed speed controller is implemented with a simple moment controller

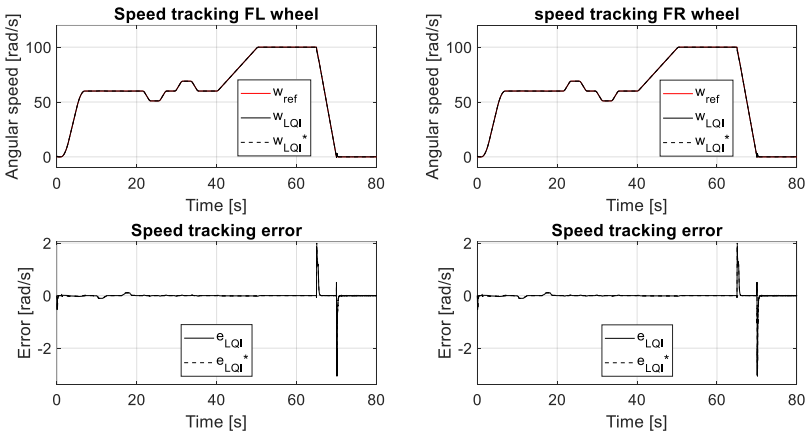

Figure 4.39: LQI* performance in the proposed test

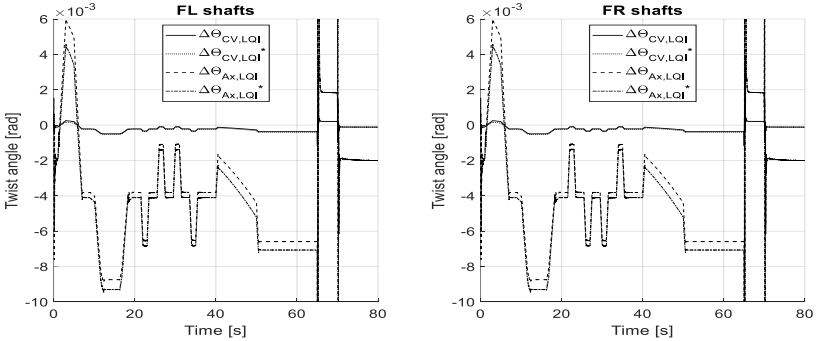

Figure 4.40: Twist angles of the CV shafts and axles for both LQI and LQI* control

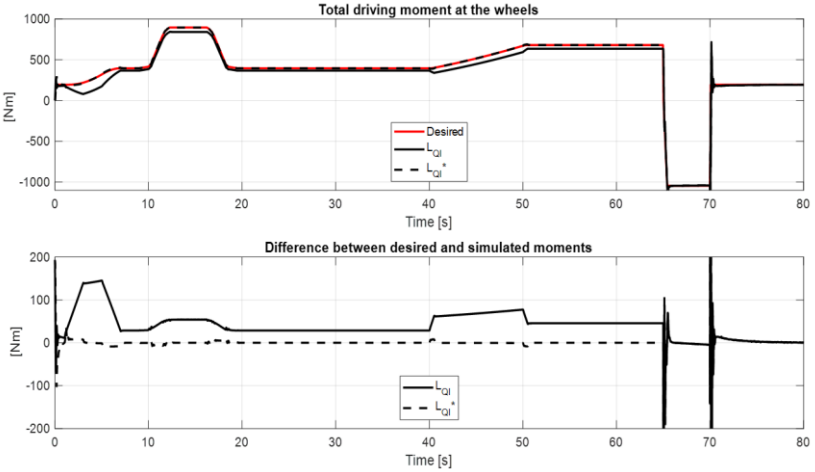

Figure 4.41: Comparison between the reference M_{drive} and the actual output moment form simulating the proposed maneuver for both LQI and LQI* controllers.

4.4 Conclusion

To bridge the gap between the testing environment and the complexity of real driving, the VEL test bench introduces greater fidelity. This test bench combines the use of physical vehicles with advanced control systems, enabling highly dynamic and maneuver-based testing. A maneuver-based approach allows systematic exploration of critical driving scenarios, while advanced controllers ensure accurate representation of powertrain dynamics and driving moments. This creates a framework where both reproducibility and realism can be achieved, providing a decisive step forward in aligning bench testing with road behavior. Building upon this, the integration of virtual environments and steerable test benches further extends the testing capability. By combining physical test setups with simulation environments and enabling additional degrees of freedom in wheel steering and vertical excitation, it becomes possible to reproduce complex real-world maneuvers within controlled laboratory conditions. This integration supports the evaluation of vehicle behavior under highly dynamic scenarios and enhances the scope of testable conditions beyond what roller dynamometers alone can provide.

From a controller design perspective, the reference adds several important insights beyond the general test-bench description. In particular, it demonstrates how the increased fidelity of maneuver-based and hybrid test environments necessitates advanced, model-based control strategies rather than classical low order controllers alone. The controller design is explicitly grounded in a reduced order but physically motivated state space representation, which preserves the dominant dynamics relevant for control while remaining tractable for synthesis. Optimal control approaches, such as LQ and LQI formulations, are shown to be especially suitable in this context, as they allow systematic shaping of closed-loop dynamics, active damping of lightly damped modes, and explicit trade-offs between performance and control effort through a quadratic cost function. Moreover, the inclusion of integral action within the optimal framework addresses steady-state errors that arise from modeling simplifications and unmeasured disturbances inherent to test-

bench operation. The reference further highlights that controller robustness to delays, actuator dynamics, and nonlinear effects must be considered already at the design stage, as these factors strongly influence stability margins in high-bandwidth test scenarios. Overall, the key takeaway for controller design is that achieving realistic and reproducible vehicle behavior on advanced test benches requires optimal, state space-based controllers that are explicitly tailored to the dominant system dynamics and validated against delay and robustness constraints, thereby ensuring reliable performance under highly dynamic maneuver-based testing conditions.

5 Implementation of real-world test maneuvers on complete vehicle test benches

The limitations of on-road testing, as outlined in the introduction chapter, highlight the necessity for controlled and reproducible alternatives in vehicle development. Complete vehicle test benches offer such an environment, enabling accurate assessments of vehicle performance while reducing the influence of uncontrollable external factors. However, to meet the increasing demands for efficiency, precision, and shorter development cycles, these platforms must evolve beyond conventional configurations toward fully integrated, automated, and maneuver-based systems.

This chapter examines the implementation of real-world driving maneuvers on complete vehicle test benches. The discussion begins with platform configuration and automation, followed by the integration of virtual vehicle components through functional mock-up techniques. Subsequently, maneuver-based simulation and the development of steerable test benches are presented as key advancements in bridging the gap between standardized testing and realistic driving conditions. Finally, attention is given to the integration of the VEL controller, the generation of representative driving maneuvers, and the application of data-driven approaches, such as deep learning and nonlinear system identification, for accurate powertrain modeling. This methodology, described in Section 5.3, was proposed in our previous study (Alhanouti & Gauterin, 2024b). Together, these topics establish a framework for enhancing test bench fidelity and supporting efficient vehicle development processes.

5.1 Test bench platform configuration and automation

Developers increasingly deal with mechatronic products, where mechanical engineering, electrical engineering, and information technology interact (Ponn & Lindemann, 2011). A test bench facility is a paradigm of an interdisciplinary mechatronic system. Figure 5.1 demonstrates an adaptable architecture of a test bench facility. It mainly consists of an information technology layer, representing the software part of the test bench, including the simulation environment, and the hardware part comprising electrical, mechanical, interfacing elements, and the unit under test (UUT) (Paulweber & Lebert, 2016)

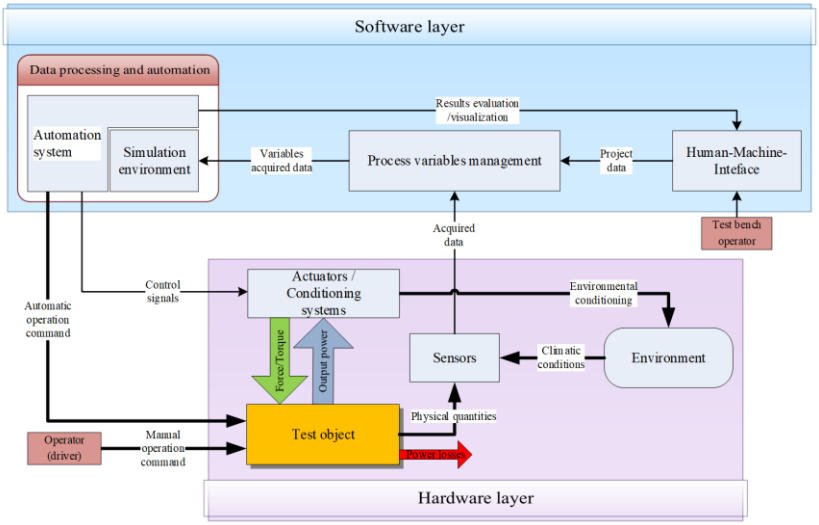

Figure 5.1: An architecture of an adaptable test facility (inspired from (Ponn & Lindemann, 2011) and (Paulweber & Lebert, 2016).

The software layer in Figure 5.1 mainly consists of the data processing algorithms, human-machine interface (HMI) modules for the test bench operator

and the automation system. Moreover, different measuring and monitoring devices within this layer must be integrated depending on the planned test tasks. These include, for instance, the detection of the operator control interventions, recognition of the UUT reactions, and an observation system for early detection of any damage to immediately stop the operational process before the destruction of the test object or the test bench itself, measurement devices for consumption and fuel gases, calibration tools for the powertrain control units, compensation models for the differences between real road tests and test bench environments, and devices for maneuver-based testing, which is represented by an environment model that runs in real-time to enable determining the operational conditions that implemented via the test bench's actuators (Paulweber & Lebert, 2016).

The connection media between the hardware and software modules is a part of the interfacing components, including measuring and computing systems. The actuators execute the test bench's demanded signals by the automation system. On the other hand, sensors are required to measure the physical quantities and convert them to data signals that are utilized to monitor these physical quantities. Therefore, different types of sensor technology and various actuators are needed on the test bench platform.

A synchronized overall system is mandatory to execute complex tasks on the test bench, enabling developers to realize activities that reproduce actual driving testing. The mechanical parts, electrical components, control algorithms, and automation systems must work together optimally to facilitate the transferability and integration of various tools. In order to provide this, detailed know-how regarding vehicle systems is required (Paulweber & Lebert, 2016). Real-time computing must process all the relevant control signals for the test bench controller and provide all sensor signals from the UUT. Therefore, the temporal behavior of the simulation must be matched to the dynamic behavior of the actual process. The correct functioning of the entire system is only provided if the simulation system responds to inputs from the actuator control signals within a specific period with the output sensor signals

(Paulweber & Lebert, 2016; Zahn et al., 2012). Figure 5.2 displays a scheme for integrating the test vehicle into a virtual environment, i.e., CarMaker in this case, via the test bench

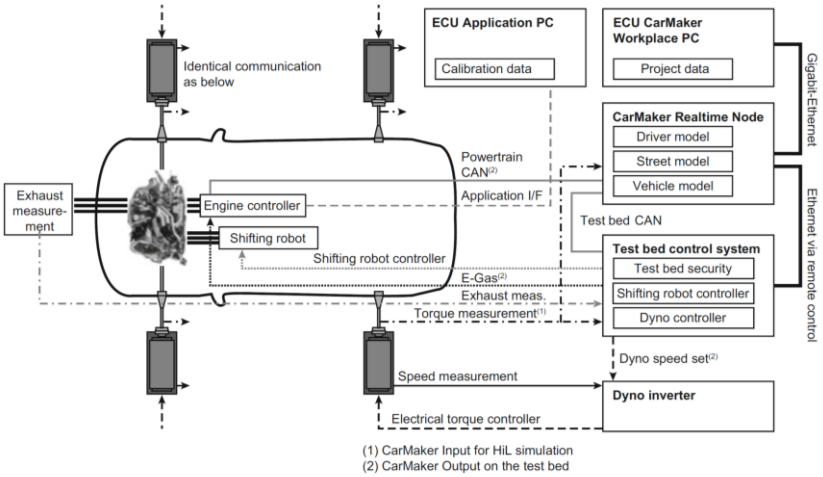

Figure 5.2: Full automated test bench platform (Paulweber & Lebert, 2016).

The figure demonstrates a variety of interfacing media between the test bench, the vehicle, and the host computers. The verified interaction of numerous models and the simulated components allow a realistic virtual conception and validation of the whole system (Paulweber & Lebert, 2016). A similar platform was developed in (Pillas, 2017; Pillas et al., 2014). The automated execution of driving maneuvers is performed with a sequential adjustment of the application parameters for every test scenario in the entire test plan. First, adjusting the application parameters relevant to the targeted powertrain components, i.e., the engine control unit (ECU). For instance, through a measuring and calibration system to realize the desired test goals. After adjusting the application parameters, the parameters of a sequence program are set within the test bench automation system. This way determines which driving maneuvers will be carried out under which boundary

conditions. After the sequence program has been completed, the process starts again until the test program is completed.

5.1.1 Integration of the virtual vehicle components (Functional Mock-Up)

All individual components of a vehicle have been and are still being further optimized by various testing facilities (Albers et al., 2014; Zehetner, Benedikt, et al., 2014). The availability of subsystems and components as detailed simulation models or actual prototypes on performance test benches is fundamental for a successful testing procedure (Schyr et al., 2012). The authors of (Schmidt et al., 2017) proposed a maneuver-based development process for substituting the test object's remaining virtual parts, which could be a part of the powertrain or the complete test vehicle. The validation process includes the simulated real route profile and the environmental conditions. This section reviews useful, practical applications to enable real-world driving for test benches. Virtual test driving enables the testing of all vehicle components. The term "system simulation" refers to an approach in which the complexity of the entire vehicle with its driving conditions, is mapped virtually in a development environment by linking one or more components to form an interactive simulation model. In other words, virtual test driving is considered as modeling of real-world tests, including the three complex interacting systems that are driver, vehicle, and environment (Albers et al., 2014; Zehetner, Stettinger, et al., 2014), see Figure 5.3.

All systems and components in the virtual vehicle could be interchangeable or expandable according to test requirements, whether as a virtual model component, software, real ECU, or mechanical components. It is essential that any components, whether real or virtual, mechanical, electrical, or from different fields, be integrated into the virtual vehicle simulation environment. This technique makes it possible to set up an adaptable simulation environment for almost all test bench types, in which a virtual driving test can be carried out for the targeted test object (Paulweber & Lebert, 2016). The so-

called Functional Mock-up Interface (FMI[1]) standard has been established in the simulation environment to integrate simulation models and tools in a standardized way. FMI defines a unified interface that enables the interaction of complex simulation models from different physics areas. In other words, FMI leads to a coupling of simulation models for various vehicle components created with different simulation tools. That can be realized with the help of a so-called *co-simulation*

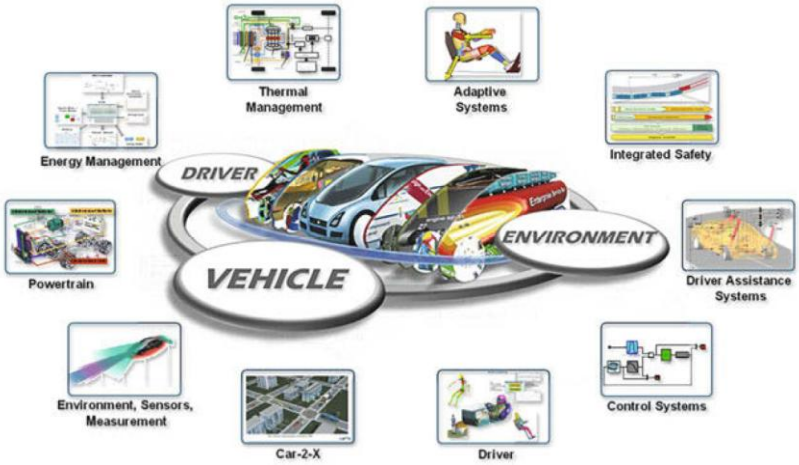

Figure 5.3: Interactive simulation model for connecting different components and domains (Zehetner, Benedikt, et al., 2014).

The co-simulation approach enables the participating domains to use the most suitable simulation tools for modeling the subsystems. It also supports the reusability of the subsystems (Zehetner, Stettinger, et al., 2014). With the introduction of co-simulation in the modern development process, developing complex mechatronic systems can be solved very efficiently. The task of a co-simulation is to enable the complex interactions of different simulation models in a suitable and, above all, reliable way (Paulweber & Lebert, 2016).

[1] https://fmi-standard.org/ , retrieved 20.11.2021

However, adding co-simulation to the real-time domain poses additional challenges; it is accompanied by some technical problems that need to be considered, such as the integration of different simulation tools, a correct data exchange, coupling of systems with different dynamic behavior, and ensuring the correctness of the simulation results (Paulweber & Lebert, 2016; Zehetner, Benedikt, et al., 2014; Zehetner, Stettinger, et al., 2014). The authors of (Rautenberg et al., 2023) presented a relevant approach for coupling the test benches virtually to represent hybrid electric vehicles through applying and extending the distributed co-simulation protocol standard. Accordingly, they provided an overview of related X-in-the-Loop applications and co-simulation scenarios. The electric machine and internal combustion test benches were connected to a virtual local area network (VLAN) within the university network. In the frame of real-time co-simulation, a distinction is commonly made between real-time and non-real-time systems. Real-time systems (RT), i.e., actual hardware systems, must satisfy the so-called *hard real-time conditions*, such as definite response time and deterministic runtime performance. On the other hand, non-real-time systems (nonRT) typically come in the form of offline simulation models that do not fulfill these conditions but might be executed faster than real-time, i.e., quasi-real-time systems. With execution time faster than in real-time, subsystems can only be applied for the real-time co-simulation platform (Zehetner, Benedikt, et al., 2014). Therefore, the offline simulation tools are coupled with the virtual vehicle via the independent co-simulation platform (ICOS2), whereby each system can run at least faster than real-time, i.e., quasi-real-time (Zehetner, Stettinger, et al., 2014). Figure 5.4 represents the integration between RT and nonRT subsystems.

The main problem of real-time co-simulation is the so-called round-trip times. Due to finite communication, computation, or data processing times, they occur in closed-loop systems. The inherent time delays and noisy measurement signals result in significant signal oscillations and, in the worst case, unstable

[2] http://www.v2c2.at/icos, retrieved 20.11.2021

closed-loop behavior. The outcome would be a distorted regeneration of the actual system

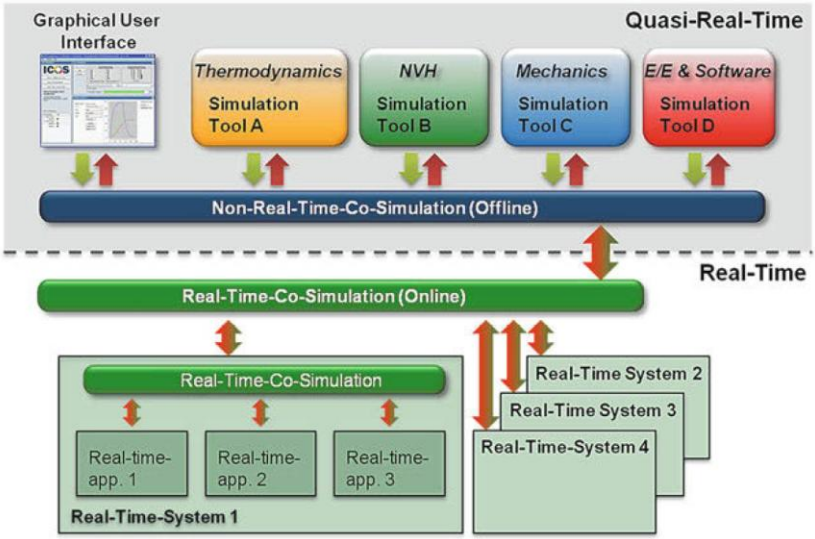

Figure 5.4: Interaction levels between real-time and non-real-time components (Zehetner et al., 2014a).

Therefore, particular connection elements must guarantee a correct time coupling between the real-time and non-time systems. The round-trip times in the overall system must be kept as small as possible to ensure the stability of existing control loops (Paulweber & Lebert, 2016). By inserting the coupling element in the outward and return branch of the closed-loop, a breakup of this loop will occur, as shown in Figure 5.5. A model-based coupling strategy can solve this problem (Zehetner, Benedikt, et al., 2014; Zehetner, Stettinger, et al., 2014), which adopts an improved extrapolation method that predicts the future quantities of the coupling signals. In addition, an error compensation is utilized to suppress the noise in the signal paths. The result was reduced response times, and thus, improved dynamics of the closed-loop system were achieved

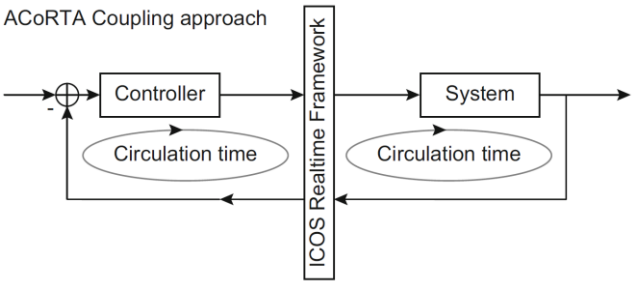

Figure 5.5: Coupling of real-time systems or real-time with non-real-time systems (Paulweber & Lebert, 2016).

As an example, this strategy is illustrated to control an engine test bench, as shown in Figure 5.6. This topic is the focus of the research project ACoRTA[3] (Advanced Co-Simulation Methods for Real-Time Applications). More details about the ACoRTA project are available in (Krammer et al., 2016).

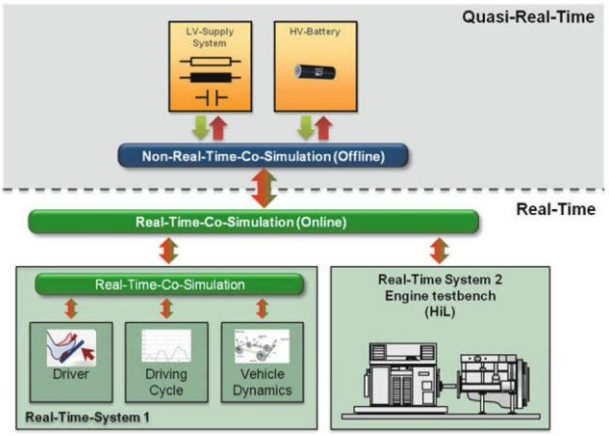

Figure 5.6: Structure and application scenario of a test bench (Zehetner, Benedikt, et al., 2014)

[3] https://www.v2c2.at/acorta-3/, retrieved 20.11.2021

5.1.2 Maneuver-based simulation

Maneuver-based testing becomes a decisive contribution to implementing an efficient development process. This maneuver-based approach allows the evaluation and optimization of the vehicle or powertrain and its interaction with the environment in all phases of the development process (Paulweber & Lebert, 2016). In particular, the maneuver-based approach makes it possible to simulate critical operating conditions and advanced driving scenarios, and vary the influencing parameters, e.g., vehicle's powertrain parameters, route landscape, and environmental conditions (Maschmeyer et al., 2016). For example, an implementation of maneuver-based testing is made in (Matros et al., 2015). As shown in Figure 5.7, simulation models were created with Matlab/Simulink to generate the driving maneuvers and the consequent driving resistances

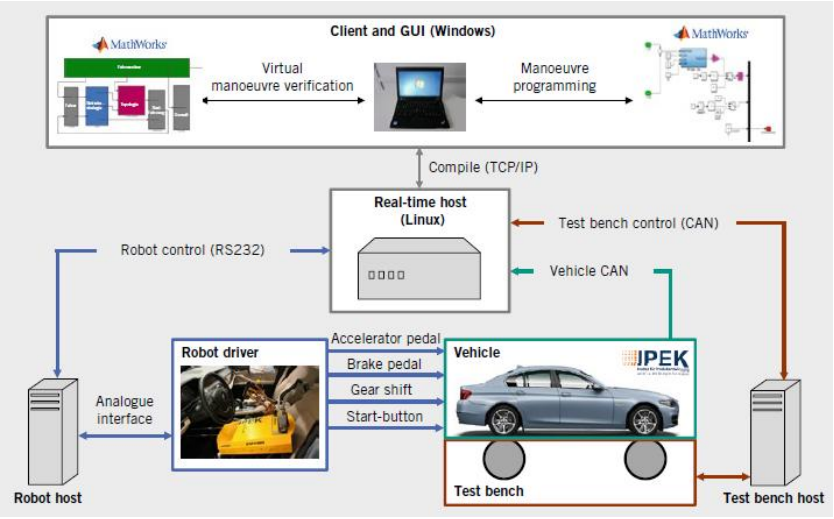

Figure 5.7: Maneuver-based testing implementation on an integrated test bench platform (Matros et al., 2015).

A driving robot, which operates the pedals and the gear lever, was employed to ensure reproducible measurements. The user controls the test bench environment via the client and graphical user interface (GUI) computer. The maneuver data are compiled on the computer and conveyed to the real-time system via a TCP/IP connection[4]. The real-time host enables the exchange of signals with the driving robot, the vehicle under test, and the test bench. Similarly, the authors of (O. Gietelink et al., 2006; O. J. Gietelink et al., 2009), employed a Vehicle-in-the-loop (ViL) simulation with other robot vehicles to reproduce the traffic environment. More to this topic, a systematic approach for model-based validation for a construction vehicle was developed in (Schyr et al., 2012). All subsystems and ECU functions were mapped virtually in the specification phase of development, and the entire vehicle was reconstructed in the form of individual FMI submodels.

Table 5.1 compares the testing features between road load simulation (RLS), maneuver-based simulation, and actual street driving. The sign (++) represents a very fitting/suitable application quality, (+) represents a decent-performing property. Poorly accomplished features are denoted by (-), and (--) means hard to accomplish. Generally, it can be said that the testing approaches reviewed in Table 5.1 have various advantages and disadvantages. For instance, although the maneuver-based offers all the options for examining the dynamic behavior of drives, it is still very complex compared to the RLS approach. Therefore, the methods and tools must be explicitly selected for the tasks in a specific development phase (Maschmeyer et al., 2016). The focus in this work would be on the maneuver-based approach.

[4] Transmission Control Protocol / Internet Protocol (TCP / IP) are a family of network protocols and is also referred to as the Internet Protocol family because of its importance for the Internet. The identification of the computers participating in the network takes place via IP addresses. A machine, or generally a device with an IP address, is called a host in TCP / IP (Fall & Stevens, 2011).

Table 5.1: Assessment for different testing approaches used in development approaches, based on (Maschmeyer et al., 2016; Paulweber & Lebert, 2016)

Testing features	**RLS**	**Maneuver-based**	**Street measurements**
Reproducibility	++	++	--
Parametrization and application effort	++	+	++
Integration effort in the testing	++	+	++
Standardizability	++	++	-
Automation capability	++	++	+
Parameter variation flexibility[5]	-	++	+
Reliability of the results	-	+	++

5.1.3 Steerable test benches

The steerable test benches are developed to allow the steering of the front wheels and even vertical excitation. These assets contribute to bridging the gap between real-world driving and ViL simulation. In addition, the steerable test benches took the ViL testing to a new level by enabling more degrees of freedom in automotive testing (Schenk, 2007). A steerable test bench that permits steering while driving was developed in (Schenk et al., 2006), which is demonstrated in Figure 5.8.

This test bench was used to develop a testing approach for improving the driver assistance functionality in accident avoidance. A concept to compensate for the disparity between conventional hardware-in-the-loop (HiL) testing and real road testing was proposed in (Schyr & Brissard, 2016). A ViL concept with an advanced simulation tool realized this method. This kind of application that requires actual steering action is beyond the testing capacities for chassis roller dynamometer and powertrain test benches

[5] Including the different options of vehicle model, driver type, and route characteristics.

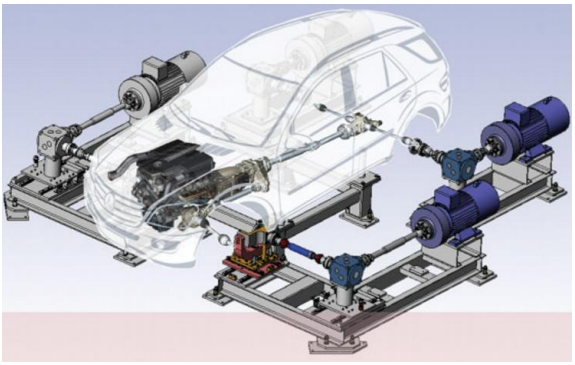

Figure 5.8: Complete test bench in SPARC[6] project (Schenk, 2007).

The authors of (Fietzek & Rinderknecht, 2015) developed a prototype for another steerable test bench. Their proposed configuration contributes to considering the vertical degree of freedom by employing a vertical hydraulic actuator. With this feature, the road inclination and unevenness can be simulated. Moreover, Noise, Vibration, and Harshness (NVH) tests can be performed. Figure 5.9 demonstrates the test bench layout developed in (Fietzek & Rinderknecht, 2015)

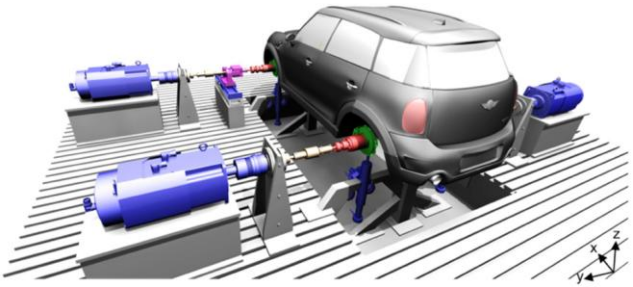

Figure 5.9: Steerable test bench with vertical actuators (Fietzek & Rinderknecht, 2015).

[6] SPARC: Secure Propulsion using Advanced Redundant Control

The flat belt test bench is a different type of the steerable test benches. With this type, there is no direct coupling between the wheel hub of the test vehicle and the corresponding loading machine; instead, the tire rolls on a flat belt. Moreover, steering action and the simulation of vertical excitations are possible in this setup. This concept can be realized through a steward platform, which supports the flat belt systems from underneath, as shown in Figure 5.10(a), or by controlling vertical actuators on the flat belt systems and the body of the test vehicle itself, as shown in Figure 5.10(b). The flat belt test bench enables a highly realistic simulation of the VUT traction performance (Ahlert et al., 2018; Fietzek & Rinderknecht, 2015). The main limitation of the flat belt test bench type is the incapability to simulate different friction coefficients between the tire and the belt. This limitation makes simulating maneuvers with sudden changes in friction, such as ABS applications or driving on a µ-split roadway, very challenging (Fietzek & Rinderknecht, 2015)

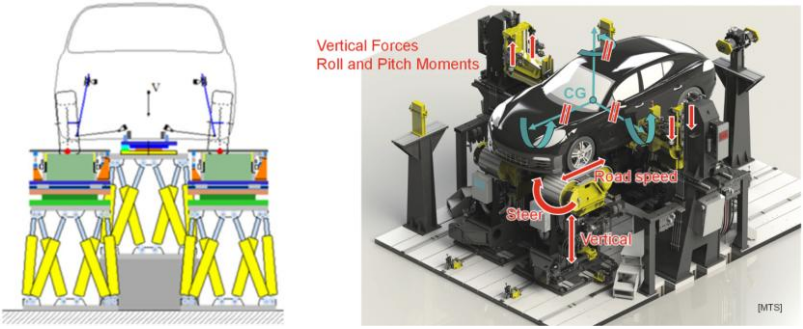

Figure 5.10: Flat belt test rig (left) with steward platform mechanisms (Fietzek & Rinderknecht, 2015) (right) with vertical actuators (Ahlert et al., 2018).

The integration of ViL concepts within the VEL further strengthens its role in the advancement in maneuver-based simulation testing. However, in comparison to the other steerable test bench concepts, the VEL remains limited in its capability to reproduce road unevenness, NVH effects, and full six-degree-of-freedom dynamics. Later developments, such as flat-belt systems supported by Stewart platforms or vertical actuators, expanded the test

space to include high-fidelity traction performance and more complex vehicle dynamics, though the flat-belt systems still face constraints in replicating variable friction conditions. Consequently, the evolution of VEL would benefit from incorporating extended vertical and multiple degrees of freedom actuation capabilities to reach the broader realism achieved in later test bench generations. Basically, the VEL can be regarded as an essential first step in the progression toward advanced 3D steerable test benches, establishing the methodological and technological groundwork for their development.

5.1.4 Integrating the VEL controller with the CarMaker simulation environment

The vehicle dynamics model developed in Section 2.1 is employed to determine the moment and rotational speed at each wheel corresponding to the applied driving maneuvers. This model also proved valuable for characterizing the dynamic behavior of the test vehicle on the roller dynamometer. Under typical driving conditions, the simulation demonstrated high accuracy in reproducing on-road vehicle dynamics, excluding extreme situations such as slippery or uneven surfaces. However, its reliability decreased when applied to highly dynamic maneuvers involving significant lateral motion. In contrast, the CarMaker model offers a more detailed and precise representation of vehicle behavior but requires more extensive parameterization data to accurately define the test vehicle dynamics. Given that CarMaker is readily available within the current testing environment, it is adopted for the subsequent sections of this work.

As the proposed controller in Section 4.3 has been validated, the combined powertrain mechanical model with the controlled VEL model, which will be labeled as the *VEL model – Level 1*, should be validated next. This combination will then be integrated with a physical powertrain model that simulates the motor's moment. This higher-level model will be called the *VEL model – Level 2*. Furthermore, the CarMaker model for the VUT will supply the required physical quantities associated with the performed maneuver to investigate

the energy consumption in the VEL test bench testing environment, as demonstrated in Figure 5.11. The vehicle dynamic model developed in Chapter 0, i.e., includes driving resistances, body dynamics, vertical load, and tire model, determined the driving resistance for the standard driving cycles and the field driving maneuver with the VUT. Nonetheless, when highly dynamic maneuvers are required, more detailed simulation models for the VUT have to be implemented. Incorporating the CarMaker model would be the sensible next step. The battery-pack, electrical motor, power electronics, gearboxes, and the powertrain losses are simulated in MATLAB/Simulink environment

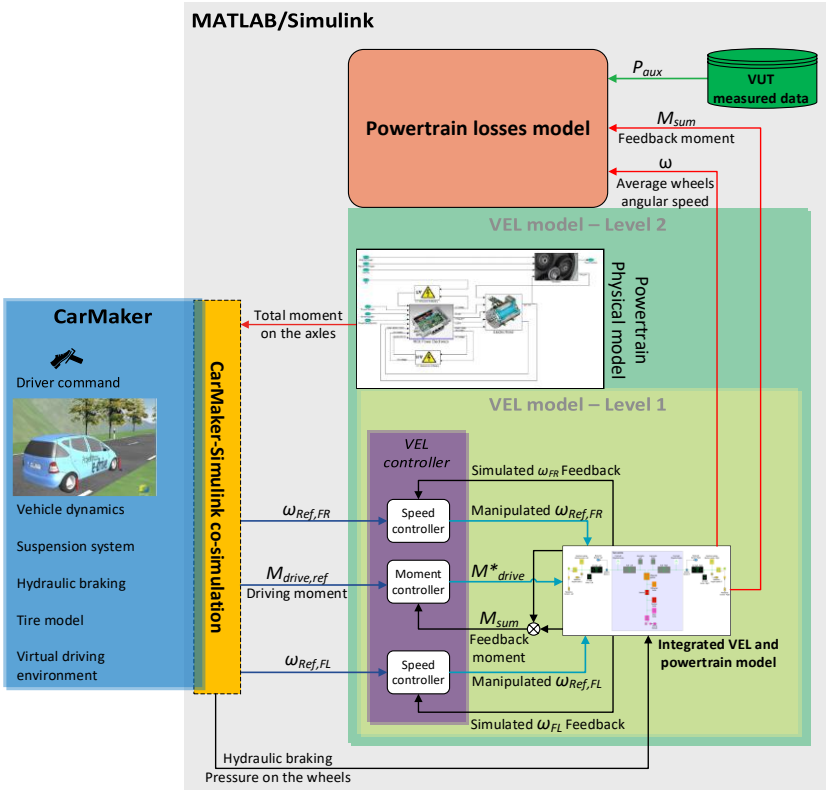

Figure 5.11: VEL model – Level 1 and Level 2.

Figure 5.11 demonstrates the co-simulation between the MATLAB/Simulink and CarMaker. A loop is formed by providing the motor's driving moment to the CarMaker model. Then, CarMaker returns the corresponding dynamic signals, which are the desired reference signals for the controller, namely, $\omega_{ref,FL}$, $\omega_{ref,FR}$, $M_{drive,ref}$, and p_{MC} for each wheel. This system will be utilized to investigate the influence of testing on the VEL test bench on energy consumption compared to the street driving case. The WLTP3 test cycle is initially performed with the system in Figure 5.11. The desired angular speed and the corresponding total moment on the driving wheels are acquired from the CarMaker model of the vehicle under test. Figure 5.12 and Figure 5.13 demonstrate the results of applying the WLTP3 driving cycle to the complete simulation model, which combines the VEL and powertrain physical model with the speed and moment controllers

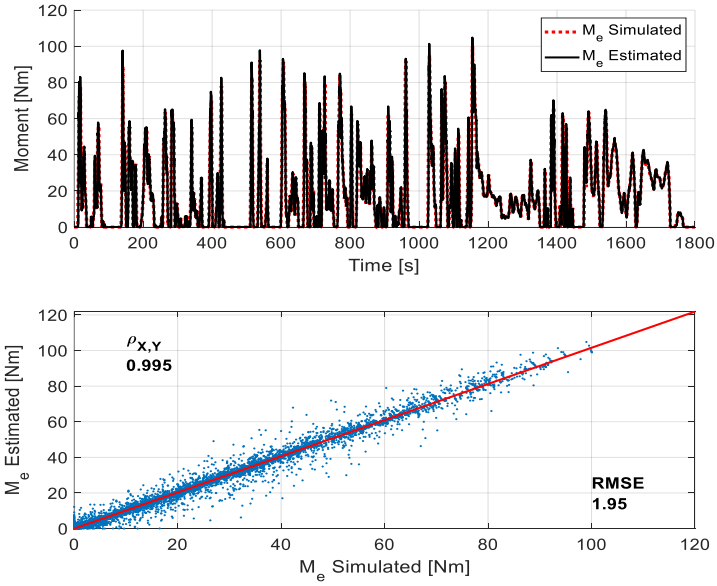

Figure 5.12: A comparison between the simulated (reference) and estimated (controlled) moment from applying the LQI* controller in the WLTP3 test simulation

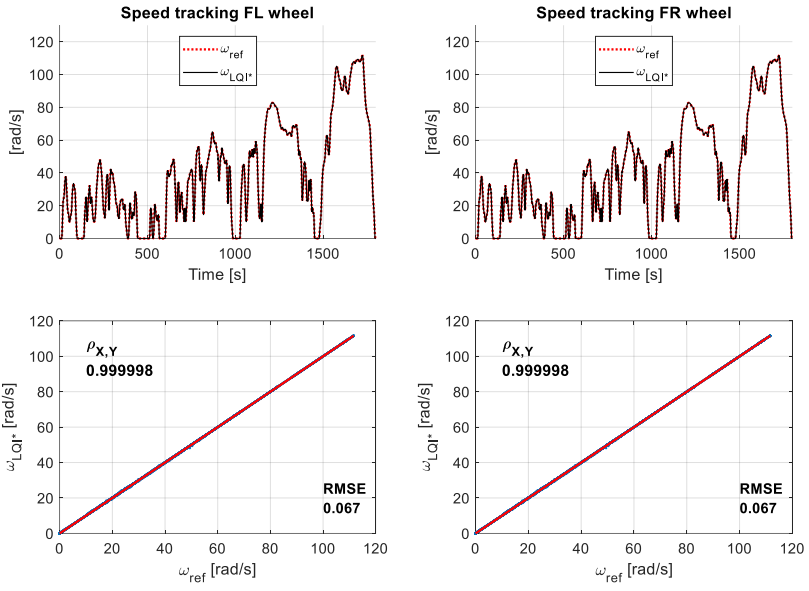

Figure 5.13: A comparison between the reference and controlled angular speed from applying the LQI* controller in the WLTP3 test simulation.

These results prove a high effectivity for angular speed and moment control. The powertrain model generates a driving moment of up to 104 Nm in this simulation test, which is about 42% of the maximum motor moment. The corresponding powertrain's moment estimation also has a high correlation accuracy of 0.999561 and RMSE of 1.95 Nm to the desired moment signal. The angular speed is estimated precisely with a correlation and RMSE values of 0.999998 and 0.067 rad/s, respectively, to the reference signal. These results are promising for accurate energy estimation on the VEL test bench.

5.2 Generation of real driving maneuvers on the test bench platform

The backward simulation model introduced in Section 2.3 demonstrated high accuracy in validating the vehicle under test (VUT) energy consumption during road testing (Section 2.4), as well as in validating the model shown in Figure 3.24, which is specifically designed for roller dynamometer testing. A key characteristic shared by both validation scenarios, and the main reason for the effectiveness of the backward simulation approach, is its ability to estimate the driving moment based on the measured vehicle speed during the maneuver. However, this condition does not hold for the VEL test bench, where the absence of physical tire–road interaction makes vehicle speed and driving moment controlled output variables. As a result, a forward simulation framework is required to determine the reference values for these parameters. In this context, the energy consumption model illustrated in Figure 2.23 is integrated within the powertrain losses model, excluding the backward vehicle dynamics component. In this configuration, the rotational speed and moment are provided by the *VEL model - Level 2*, which employs a forward simulation methodology to determine the required reference quantities.

A virtual model was developed in Figure 5.11, which comprising the vehicle, its driving environment, and the VEL test bench. So far, the driving moment has been approximated using a physical powertrain model. However, the accuracy of this estimation is influenced by the availability of model parameters and the complexity level of the powertrain representation. To overcome these limitations, it is advantageous to pursue an approach that explicitly models the powertrain driving moment. Given the objective of preparing the VEL test bench for realistic driving scenarios, this section presents a review of state-of-the-art methods for generating real-world driving maneuvers. Based on the insights gained from this review, a suitable modeling approach will be proposed in the subsequent section.

Test maneuvers may be divided into two major categories: Performance[7] and functional[8] analysis (Paulweber & Lebert, 2016). The maneuvers are executed as straight or combined driving tests, which involve longitudinal, lateral, and vertical influences. These tests can also be performed on the test bench facilities, fully or partially, according to the test requirements and the test bench's complexity level. For the practical implementation of the maneuver-based test procedure, some specifications are stipulated for the integrated test platform, according to (Paulweber & Lebert, 2016; Schyr et al., 2012):

- Consistent platform use, starting from software-in-the-loop, to hardware-in-the-loop, until the actual prototype vehicle implementation,
- efficient integration of simulation models and ECU functions from different domains and model environments. These must manage and store large amounts of data generated by various vehicle systems for different vehicles,
- efficient integration of vehicle systems and components into the test bench. Real-time and intelligent synchronization mechanisms are needed for this purpose,
- realistic reconstruction of real-use situations and driving scenarios by robust maneuver control,
- high productivity through performance and usability, such as interactive maneuver control, and efficient test automation,
- and visualization and analysis tools. In addition, the increase in the amount of data in the design of the test procedures must be taken into account, which requires efficient processes for data plausibility, evaluation, storage.

In order to generate more realistic results of actual driving maneuvers on a

[7] The performance tests involve the produced power by the UUT, which is determined over the entire working range and under specified test conditions.

[8] The functional tests are used to optimize and verify the overall system functions—for instance, the investigation of the UUT response to the variations in the test conditions.

test bench, a reference speed and the corresponding driving resistances are obtained from a real-world route simulation (Joshi, 2017b, 2017a; Paulweber & Lebert, 2016). Calibration and development of powertrain systems can import navigation map data to derive an efficient operating state. Based on these data, the reproduction of real driving maneuvers is best manifested with a simulation environment tool, such as CarMaker. The test object can be integrated as a model or actual component in a real-time simulation. Ultimately, the entire vehicle's performance may be analyzed and evaluated using data from real routes using a maneuver-based approach (Sciuto & Hellmund, 2001).

Efforts have been made to develop and implement driving simulators for traffic safety research and the advanced development of unconventional vehicle concepts. For example, data of actual 3D road courses from a navigation system, map services, or own 3D route measurements could be imported into the simulation environment, providing various roadway roughness profiles. A representative application for this functionality was made in (Geneder et al., 2014), by implementing a test bench with a GPS-based navigation system application, as shown in Figure 5.14. Prediction of the driving conditions is an essential step for real routes simulation, which can be classified into two methods, according to the availability of the driving destination information (Mei et al., 2023): First, if the destination is known, the vehicle speed and the altitude changes are evaluated based on the future route segment information. Route segment information is divided into fixed, including road speed limit and altitude data, while real-time data provides road adhesion, traffic jams, and weather conditions. Second, if the destination is unknown, stochastic models are used to predict the virtual driving conditions by employing the stored statistical data of the vehicle in the present area to estimate vehicle energy consumption. An interesting method for a stochastic model that connects the vehicle with the data cloud to predict the remaining driving range is presented in (Sun et al., 2022). The authors' concept was based on estimating the remaining discharge energy in the battery by predicting the forthcoming operating conditions. The results showed that the proposed vehicle-cloud

collaboration solution could improve the accuracy of the remaining driving range within an accuracy of 5%

Figure 5.14: Development of advanced driving concept test bench (Geneder et al., 2014).

It is essential to select the most appropriate test for specific tasks through deterministic, statistical, or experimental methods (Braess & Seiffert, 2011). It is also crucial that the maneuver test would stimulate the system to reveal its characteristics. The focus of this work will be on the energy consumption tests to investigate the integrated system of the VUT and the test bench in real-world performance test maneuvers. Based on predefined speed and road profiles.

5.3 Identification of nonlinear systems using deep-learning approaches

The control algorithm developed in Section 4.3 needs a reference moment signal, besides the reference speed signal, to achieve the related power value at every instant. However, demanding the moment directly from the vehicle control unit (VCU) is not always possible. Based on that, it is necessary to identify the powertrain moment based on the accelerator pedal position. Furthermore, developing moment demand predictive models would be a helpful approach toward accurate energy consumption estimation during real driving routes (Alhanouti & Gauterin, 2023b, 2024a, 2024b; He et al., 2021; Y. Zhang et al., 2021).

Empirical modeling methods, such as black-box model identification, contrast sharply with theoretical or physics-based modeling approaches. In empirical modeling, only system measurement data are required, eliminating the need for extensive prior knowledge of the underlying physical equations or parameters. This makes empirical methods particularly efficient for complex systems, as they enable rapid model development with significantly less effort and computational cost compared to theoretical modeling (Isermann & Münchhof, 2011). Moreover, empirical models generally require shorter computation times for model evaluation and optimization, which is advantageous for iterative design and control applications. However, a key limitation of empirical approaches is their inability to provide explicit insight into the physical relationships or design factors influencing system behavior (Pillas, 2017).

Among empirical modeling techniques, polynomial models are widely used because of their simplicity, ease of implementation, and low computational requirements (Isermann & Münchhof, 2011). These models are expressed as a linear combination of regressors and coefficients, where regressors are algebraic functions of input variables, typically represented through multiplication or exponentiation. Despite describing nonlinear system behaviors, polynomial models are referred to as linear because their coefficients entered to

the model linearly. The term “linear” relates to the relation between coefficients and the prediction space rather than between input and output variables. Based on polynomial formulations, continuously differentiable nonlinear system models can be established for more accurate dynamic representation(Alhanouti & Gauterin, 2024b; Pillas, 2017).

5.3.1 Relation between the accelerator pedal and vehicle control unit

A simplified representation of the control unit functions influencing the dynamic transmission behavior of the VUT powertrain is shown in Figure 5.15

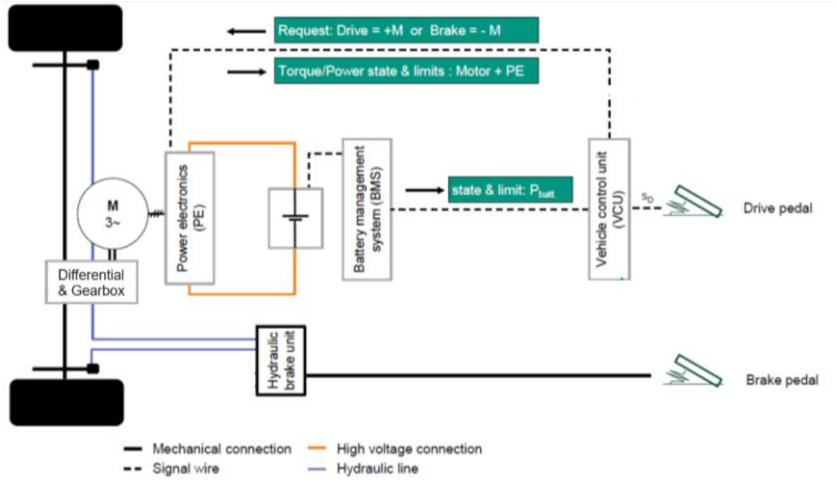

Figure 5.15: Simplified schematic for the interfacing between the accelerator pedal and the electrical motor in the VUT (Kubaisi, 2018).

The overall chain of influence in the powertrain system begins with the detection of the accelerator pedal angle by a sensor. The digitized pedal percentage signal (S_D) serves as an input variable to the Vehicle Control Unit (VCU). The VCU determines the driver’s desired torque based on current

driving conditions and system constraints, thereby defining the motor's maximum available torque output. The desired moment froms the basis for determining the final driving moment M_{drive}. In addition to the driver input, auxiliary units, vehicle dynamics controllers, and components' control unit functions also affect the VCU output. These additional functions ensure plausibility checks and coordinate the electric motor's target torque formation. Moreover, during dynamic maneuvers, comfort oriented subsystems, which are commonly known as comfort functions, are activated to enhance subjective driving smoothness and responsiveness. The exact configuration of these comfort functions varies according to the drivetrain architecture (Pillas, 2017).

5.3.2 Nonlinear autoregressive exogenous model

When linear polynomial models fail to adequately capture nonlinear system dynamics, nonlinear regression models are utilized. Recently, data-driven and machine learning methods have become increasingly prevalent in automotive system identification due to their reduced computational burden, scalability, and predictive performance (Ricci et al., 2023). Among these, artificial neural networks (ANNs) are widely adopted for modeling complex nonlinear mappings between multiple input and output variables (Nelles, 2020). ANNs are capable of performing a wide range of tasks, including function approximation, system identification, classification, regression, clustering, and optimization. However, their performance can deteriorate in systems with unknown delays or feedback dynamics. To address these limitations, the nonlinear autoregressive exogenous model (NARX) network integrates feedback connections between input and output layers, enabling accurate modeling of dynamic systems with time delays (Munagala & Jatoth, 2023). This feedback mechanism enhances the ANN's capability to capture temporal dependencies, accelerates convergence during training, reduces the required dataset size, and improves overall modeling accuracy. As a result, NARX networks have been applied extensively across industrial domains, including power system modeling, internal combustion engine control (Glass, 1999), and dynamic

prediction of electric powertrains (Munagala & Jatoth, 2023; Ricci et al., 2023; He et al., 2021; Y. Zhang et al., 2021; Togun et al., 2012).

A NARX network surpasses static neural networks in learning long-term dependencies and is particularly effective for real-time automotive applications. For example, (Zhou et al., 2019) applied a dynamic NARX-based neural network to characterize braking intensity influenced by driver actions, demonstrating the model's capacity to capture sequential behavioral dependencies. Similarly,(Grady et al., 2022) employed neural networks to model steering, acceleration, and braking systems in autonomous vehicles, observing strong tracking performance, although the NARX-based acceleration model exhibited slightly reduced accuracy. In another study, (Alghafir & Dunne, 2012) developed a computationally efficient NARX-ANN model to describe the nonlinear, thermally sensitive behavior of hydraulic dampers, enabling virtual tuning of suspension systems under high-frequency loads. Furthermore, (He et al., 2021) proposed a multivariate deep neural network with long short-term memory units to estimate dynamic brake pressure in electric vehicles, reporting that NARX approaches outperform traditional regression and support vector prediction methods (Montgomery & Runger, 2010). In an EV context, (Munagala & Jatoth, 2023) successfully identified and controlled a separately excited DC motor using NARX-based system modeling, achieving rapid and accurate response to setpoint variations. Similarly, (Forrier et al., 2020) demonstrated that NARX networks can accurately characterize torque generation in induction motors as part of electric powertrains. Although several studies validated NARX models using simulated driving cycles, few have focused on torque prediction under real-world dynamic driving conditions, which is a gap that will be addressed in this section. The autoregressive exogenous (ARX) model for the linear system is given in equations (5.1) – (5.3) (Togun et al., 2012):

$$\boldsymbol{A}(q^{-1})y(t) = \boldsymbol{B}(q^{-1})u(t) + e(t) \tag{5.1}$$

$$\boldsymbol{A}(q^{-1}) = 1 + a_1 q^{-1} + a_2 q^{-2} + \cdots + a_{na} q^{-na} \tag{5.2}$$

$$\boldsymbol{B}(q^{-1}) = b_0 + b_1 q^{-1} + b_2 q^{-2} + \cdots + b_{nb} q^{-nb} \tag{5.3}$$

where q denotes the backward shift operator, i.e., $y(t-1) = q^{-1}\, y(t)$. The linear system input and output are $u(t)$ and $y(t)$, respectively. The immeasurable noise sequence is denoted as $e(t)$. The parameters a_i and b_i are real coefficients, and n_a and n_b are the orders of the polynomials $\boldsymbol{A}$ and $\boldsymbol{B}$, respectively. The activation function used in the building nonlinear network is the sigmoid function that is shown in Figure 5.16

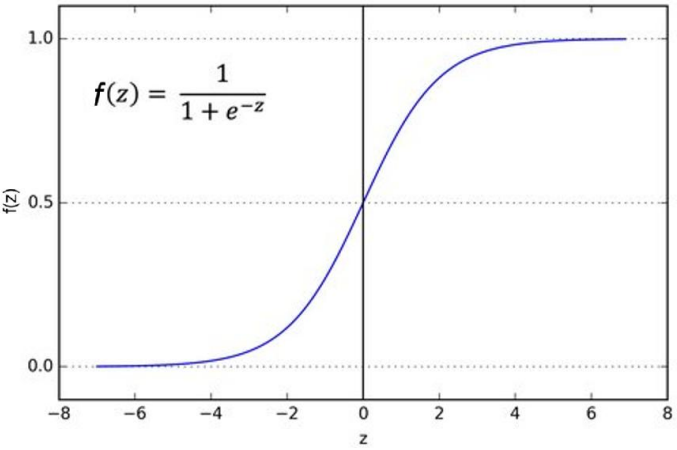

Figure 5.16: Sigmoid function[9] (Alhanouti & Gauterin, 2024b).

The sigmoid function is described by equation (5.4) (MathWorks Inc., 2023):

$$S(\boldsymbol{X}) = \sum_{i=1}^{n} s_i f(\boldsymbol{X}(t)^T \boldsymbol{Q}\, \boldsymbol{d_i} + c_i) \tag{5.4}$$

- $\boldsymbol{X}(t)$ is m-by-1 vector of regressors, i.e., $\boldsymbol{X}(t) = [\boldsymbol{x}_1(t), \boldsymbol{x}_2(t), \ldots, \boldsymbol{x}_m(t)]^T$
- $\boldsymbol{Q}$ is an m-by-p projection matrix, where $m \geq p$.
- $s_1, s_2, \ldots, s_n$ are scalar weights called *output coefficients*.

[9] https://www.researchgate.net/publication/338580890_Modeling_on_Feature_Vectors_in_Compressed_Spaces_by_the_use_of_Neural_network_techniques . Retrieved December 19, 2024.

- $d_1, d_2, \ldots, d_n$ are p-by-1 vectors called *dilation coefficients*.
- $c_1, c_2, \ldots, c_n$ are scalars called *translations*.
- $f(z) = \frac{1}{e^{-z}+1}$ is the sigmoid function, also called a unit function of the sigmoid network. Here, z is a scalar of the quantity $\boldsymbol{X}^T\boldsymbol{Q}\,\boldsymbol{d}_i + c_i$.

The sigmoid network is a mathematical function that maps m inputs to a scalar output $y(t)$ applying the relationship (5.5) (MathWorks Inc., 2023):

$$y(t) = y_0 + \boldsymbol{X}(t)^T\boldsymbol{P}\boldsymbol{L} + S\big(\boldsymbol{X}(t)\big) \tag{5.5}$$

- y_0 is a scalar output offset.
- $\boldsymbol{P}$ is m-by-p projection matrix, where m is the number of regressors and p is the number of linear weights vectors.
- $\boldsymbol{L}$ is a p-by-1 weights vector.
- $S(\boldsymbol{X}(t))$ is a sum of dilated and translated sigmoid functions. The total number of sigmoid functions is the number of units n of the network.

A NARX model contains regressors and an output function. The output function includes mapping objects; each model output has a single mapping object. The mapping function implements a combination of an offset, linear weights, and a nonlinear function to estimate the output. The nonlinear network is selected to be a sigmoid function. The block diagram illustrated in Figure 5.17 represents the arrangement of a single-output NARX model. The NARX model output y is calculated in two stages: First, regressors are constructed from current and past input values as well as past outputs. Then, these regressors are mapped to the output using an output function block comprising offset, linear, and nonlinear terms in parallel (Sjöberg et al., 1995). The linear term in equation (5.5) is denoted by $\boldsymbol{X}^T\boldsymbol{P}\boldsymbol{L}$, while $S(\boldsymbol{X}(t))$ represents the nonlinear function. The model implementation in this work follows an incremental procedure: a three-input, single-output linear torque model is first estimated, then extended to a nonlinear NARX model by incorporating a single hidden-layer sigmoid network in parallel (MathWorks Inc., 2023; Singh & Sznaier, 2021)

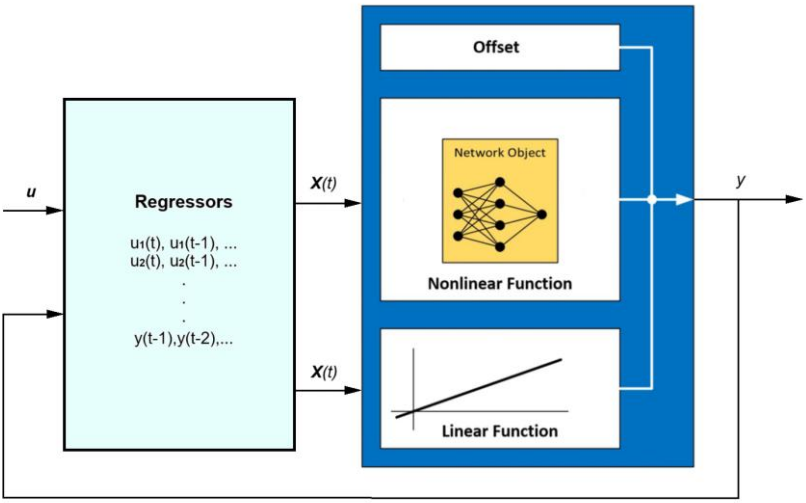

Figure 5.17: Schematic for the NARX model (Alhanouti & Gauterin, 2024b).

5.3.3 Training the NARX model using a real-world route data

The reference VUT CarMaker model will be utilized to generate the necessary data for the empirical modeling. This model represents a more detailed and physically accurate simulation compared to the model presented in Section 2.1. While such data would typically be obtained from real-world test drives, the use of the CarMaker model serves as a practical alternative to physical experimentation. This approach demonstrates the value of a validated simulation model, particularly in situations where conducting tests with the actual vehicle is challenging. For example, due to unfavorable weather conditions. Furthermore, the use of the virtual model significantly reduces the time and effort required for data collection. Therefore, simulation data will be used instead of actual measurement data for the VUT as a reference for the NARX model. Proper selecting of a test maneuver to obtain the training or validation data should consider covering as many operating points as possible, which

helps obtain sufficient information about the system's behavior with as little test effort as possible (Pillas, 2017). Based upon that, a real-world driving (RWD) scenario already created in CarMaker is implemented. The driving scenario used for model training begins from Karlsruhe city, in Germany, and follows a closed-loop route covering urban, suburban, and highway conditions. The route includes varying elevation profiles exceeding 400 m above the reference starting point and diverse dynamic resistances such as acceleration, deceleration, and curved segments. Figure 5.18 demonstrates the driving path

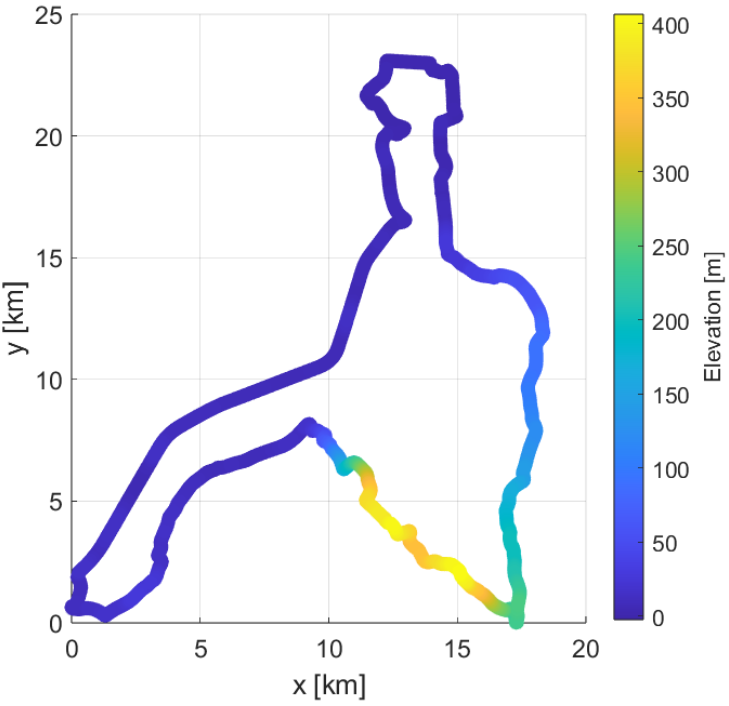

Figure 5.18: Real-world driving (RWD) route (Alhanouti & Gauterin, 2024b).

Figure 5.19 presents a surface plot of the simulated pedal position (S_D), the average angular speed of the driven wheels (ω), and the estimated motor's moment (M_e). This figure highlights the expected inverse relation between torque and speed, the full operational coverage of each variable, and the inherent nonlinearities of the electric powertrain system

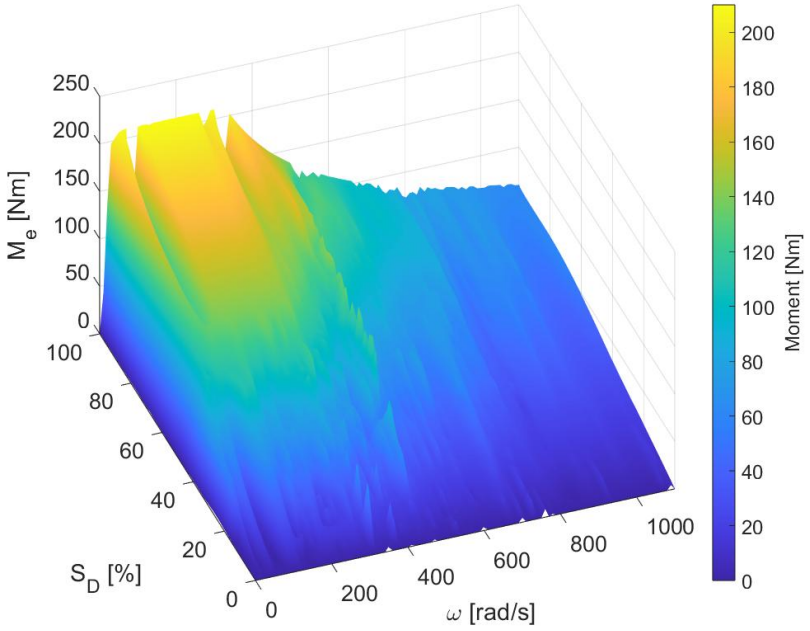

Figure 5.19: Accelerator pedal position vs. angular speed vs. motor's moment during the RWD maneuver (Alhanouti & Gauterin, 2024b).

The ICE moment model proposed by (Pillas, 2017) linked pedal position percentage, angular velocity, and vehicle speed. In this study, analogous variables are used for electric motor moment modeling via NARX, with the added challenge of a more dynamic dataset. Figure 5.20 illustrates the simulation results for the input variables V_x, S_D, and ω, and a single output M_e

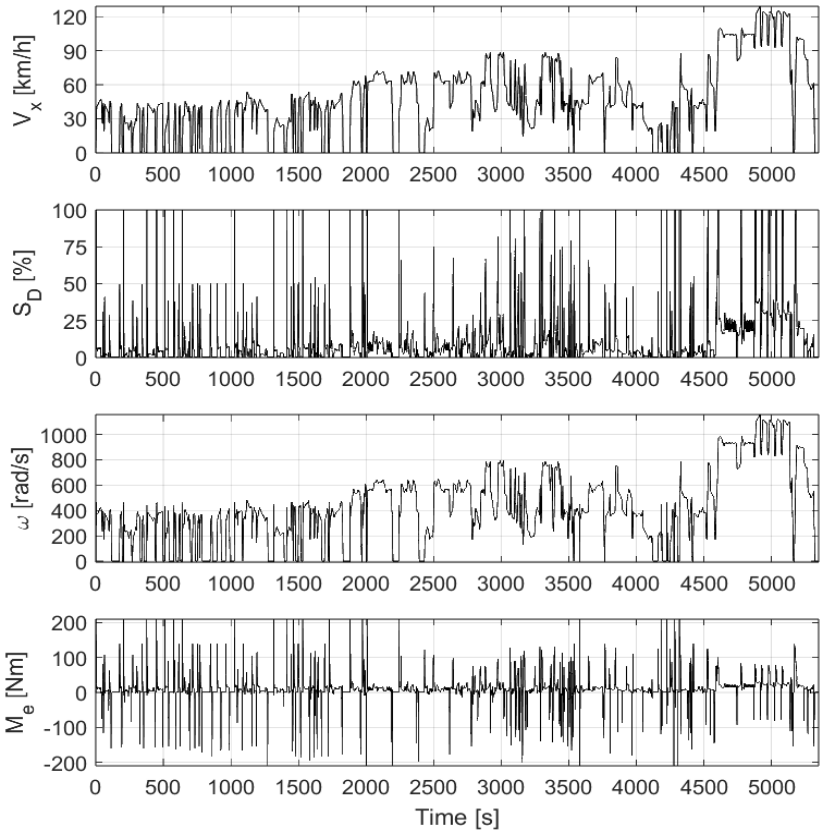

Figure 5.20: Simulated data corresponding to the RWD maneuver (Alhanouti & Gauterin, 2024b).

As depicted in Figure 5.21, the dark green regions in Figure 5.21(a) and (c) represent the intersections between S_D and M_e. The clear dissimilarity in data distribution between S_D and M_e confirms that M_e cannot be accurately predicted from pedal input S_D alone. Furthermore, the dataset collected from real-world driving (RWD) covers a broader range of operating conditions than the Artemis cycle, indicating that even highly dynamic standardized cycles may be insufficient for accurate model identification. For instance, during the

Artemis cycle, the maximum recorded pedal position and moment were 77% and 109.55 Nm, respectively, as illustrated in Figure 5.21(d). Whereas the RWD data achieved full-range excitation for both variables, as shown in Figure 5.21(b)

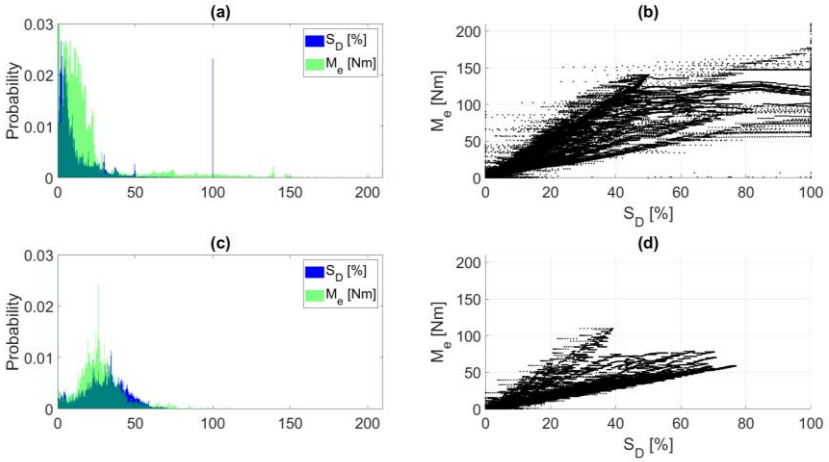

Figure 5.21: Data distribution of S_D and M_e for the training data (RWD maneuver) and the validation data (Artemis driving cycle): (a) histogram of S_D and M_e for estimation data; (b) S_D vs M_e for estimation data; (c) histogram of S_D and M_e for validation data; (d) S_D vs M_e for validation data (Alhanouti & Gauterin, 2024b).

The complete dataset is used for NARX model identification, while the Artemis highway cycle, with maximum speed of 130 km/h, serves as the validation dataset due to its high dynamic content. Figure 5.22 schematically depicts the model identification workflow. Initially, the linear portion of the NARX model is identified, as shown in Figure 5.23, using a regressor vector $X(t)$ with $n = 4$,

$$\text{i.e., } \boldsymbol{X}(t) = \begin{bmatrix} V_x(t) & \dots & V_x(t-4) \\ S_D(t) & \dots & S_D(t-4) \\ \omega(t) & \dots & \omega(t-4) \\ M_e(t-1) & \dots & M_e(t-4) \end{bmatrix}$$

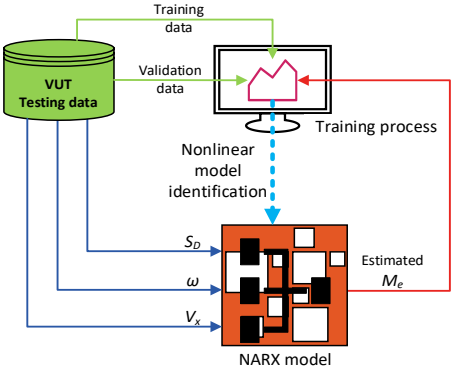

Figure 5.22: Identification of the NARX model using the RWD data (Alhanouti & Gauterin, 2024b)

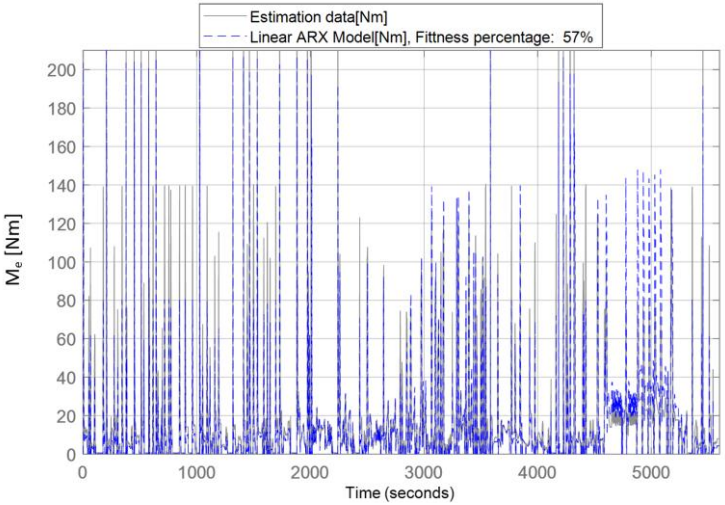

Figure 5.23: Fitness of the linear part of the NARX model to the estimation data (Alhanouti & Gauterin, 2024b).

Model accuracy is quantified using the *Normalized Root Mean Square Error* (NRMSE), as defined in equation (5.6) in terms of fitness percentage

$$fitness = (1 - \mathrm{NRMSE}) \times 100\% = \left(1 - \frac{\|\boldsymbol{y} - \hat{\boldsymbol{y}}\|}{\|\boldsymbol{y} - \mathrm{mean}(\boldsymbol{y})\|}\right) \times 100\% \quad (5.6)$$

where $\boldsymbol{y}$ represents the reference data and $\hat{\boldsymbol{y}}$ is the identified model output. The linear model achieved a fitness value of 57%, confirming the need for a nonlinear extension. After incorporating nonlinear and offset components, the final NARX model achieved excellent fitness values of 98.25% for the training data and 98.03% for the validation data, as Figure 5.24 illustrates. These results prove the model's ability to predict motor moment accurately during highly dynamic maneuvers. The Artemis driving cycle is used as a validation dataset for the NARX model

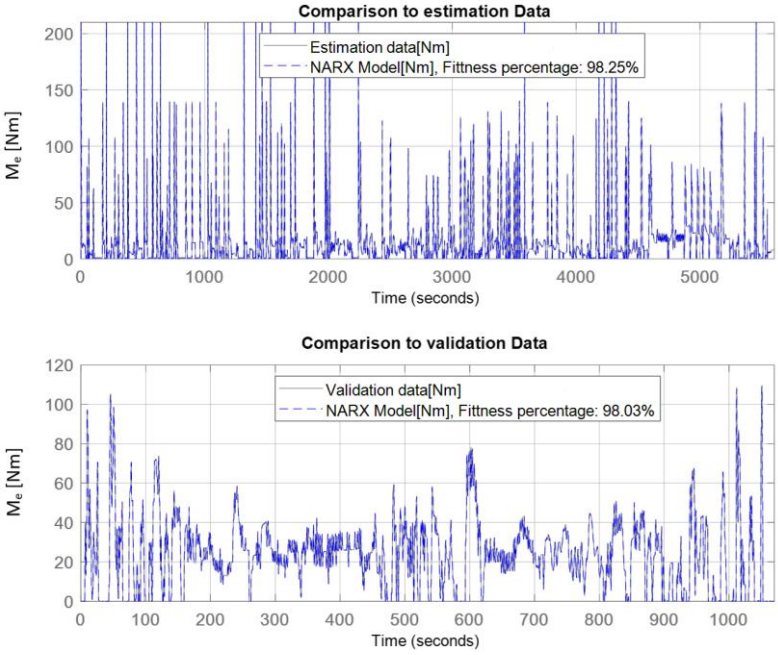

Figure 5.24: Fitness of the NARX model to the estimation and validation data (Alhanouti & Gauterin, 2024b).

5.4 Evaluating the performance of the VEL simulation model

Having the NARX model identified and validated, it can be integrated into the VEL test bench system model, as illustrated in Figure 5.25

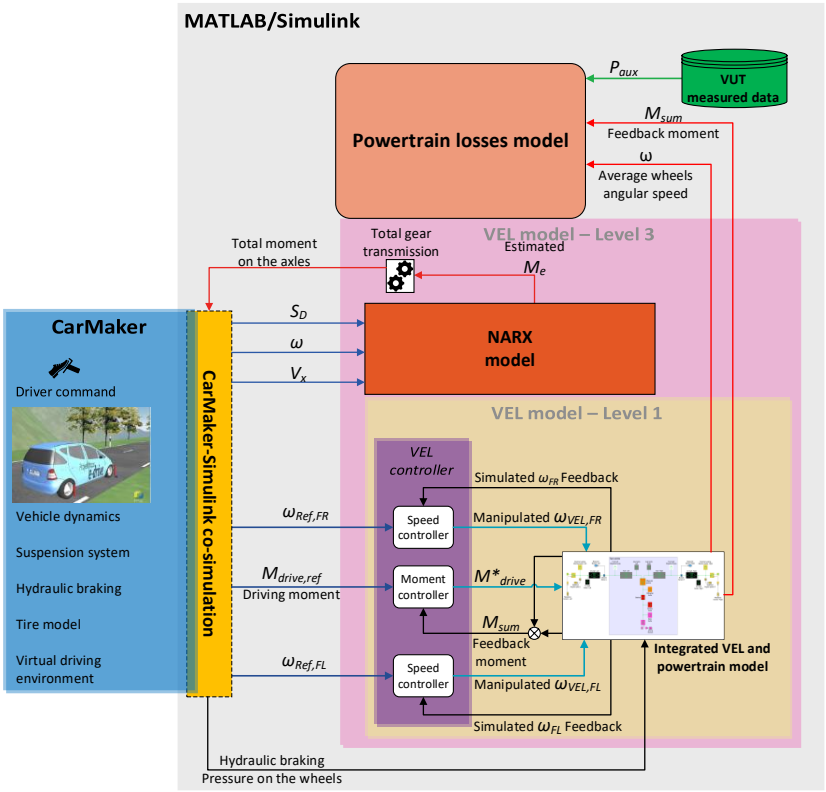

Figure 5.25: VEL model – Level 1 and Level 3.

The NARX model replaces the powertrain model in Figure 5.11 to form the *VEL model – Level 3*. It is desired to advocate that the identified driving moment model represents the actual vehicle. So, the measured data from the

same street test in Section 2.4 are used for this purpose. The results in Figure 5.26 demonstrate a high correlation of 0.994 between the estimated and measured motor's moment, and an associated RMSE value of 1.05 Nm, which approves the accuracy of the identified NARX model

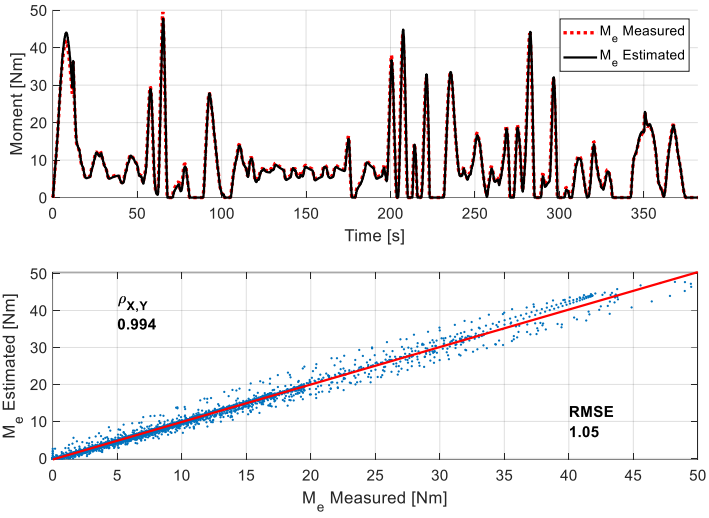

Figure 5.26: Correlation between the measured and estimated total driving moment on the wheels during the field test maneuver, using the VEL model – Level 3 (Alhanouti & Gauterin, 2024b).

At each instant, the accelerator pedal position value (S_D), along with the speed (V_x) and the average angular speed of the driving wheels (ω), are given to the NARX Simulink model to calculate the corresponding motor driving moment, which is returned as the total driving moment on the axles of the driving wheels after modified according to the total gear transmission. Then, the CarMaker model, including the tire model from CarMaker, of the test vehicle computes the reference input quantities for the LQI* controller, which are the angular speed of each wheel and the final driving moment ($M_{drive,ref}$). A further quantity needed from the CarMaker model is the hydraulic braking pressure

for each wheel, which affects the Simulink powertrain model as a braking moment on each associated wheel, as elaborated in Section 2.1.5. It is necessary to investigate the accuracy of the complete VEL test bench system model (VEL model – Level 3) shown in Figure 5.25, which incorporates the integrated VEL and powertrain Simulink model, the LQI* controller, and the NARX model. Figure 5.27 – Figure 5.28 show the accuracy of the VEL model – Level 3 performing the RWD maneuver

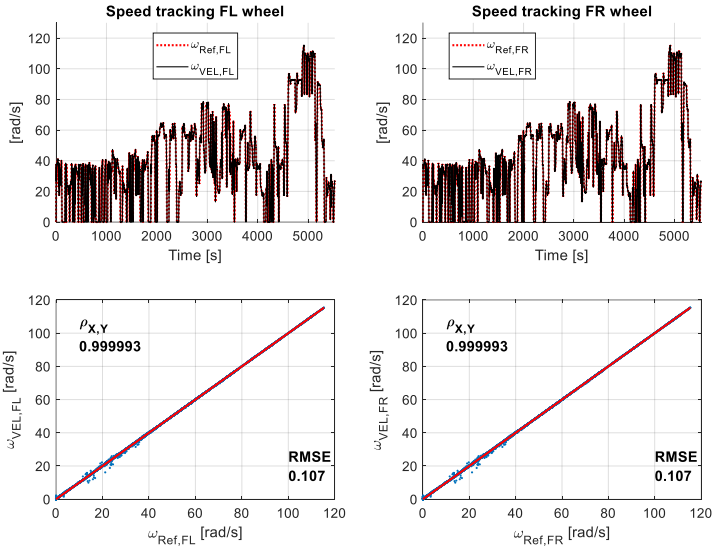

Figure 5.27: Correlation between the reference and controlled front wheels' angular speeds during the RWD maneuver, using the VEL model – Level 3.

The performance of the manipulated front left wheel angular speed ($\omega_{VEL,FL}$) and the front right wheels ($\omega_{VEL,FR}$) are both identical with correlations of 0.999 and associated RMSE of 0.107 Nm, compared to their corresponding reference signals $\omega_{Ref,FL}$ and $\omega_{Ref,FR}$, respectively. While M^*_{drive}, compared to $M_{drive,ref}$, achieved a 0.986 correlation and a RMSE equals to 4.671 Nm. The integrated model's accuracy is related to the accuracy of its contained

models, which reflects high accuracy for a system with multiple concatenated models

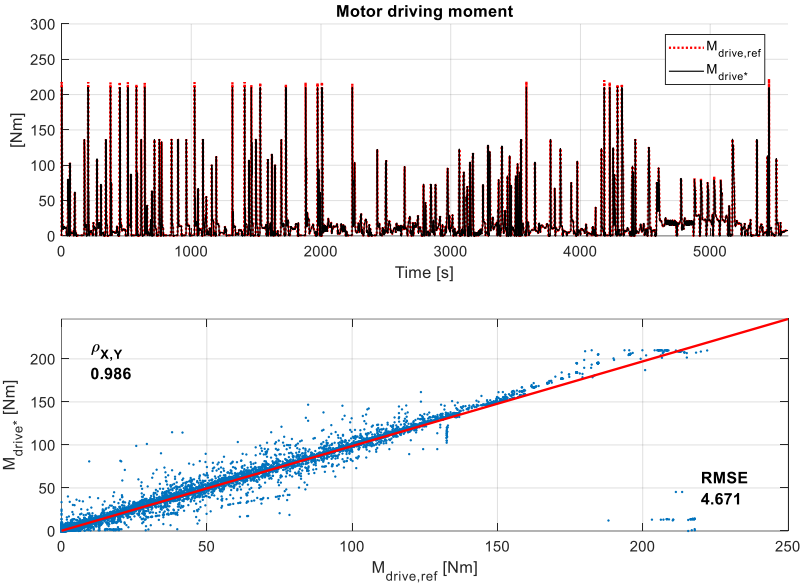

Figure 5.28: Correlation between the reference and controlled motor driving moment during the RWD maneuver, using the VEL model – Level 3.

The same RWD maneuver is used to validate the braking moment generated from the VEL model - Level 3 compared to the expected braking moment from the CarMaker model as it underwent the same maneuver. This step is necessary to confirm that the VUT model in the CarMaker simulation environment, which is used as a reference, and the physical Simulink VEL model are working equivalently. Succeeding this proves that an actual braking actuation on a vehicle mounted on the VEL test bench is achievable as desired. Figure 5.29 demonstrates the performance of NARX with the RWD maneuver simulation. The total braking moment from the VEL model - Level 3 ($M_{brake,VEL}$) matches

the expected braking moment ($M_{brake,ref}$) from the CarMaker model with a correlation of 0.942 and a RMSE of 73.664 Nm

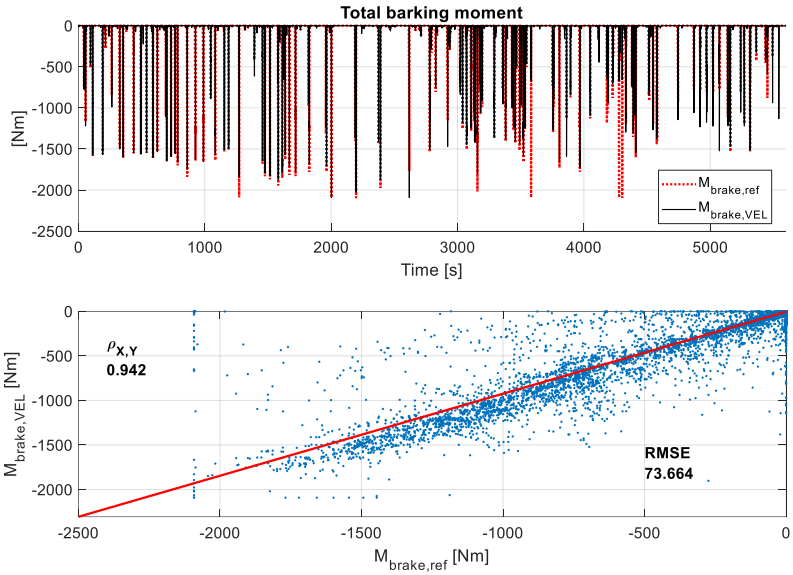

Figure 5.29: Correlation between the simulated and estimated total braking moment on the wheels during the RWD maneuver, using the VEL model – Level 3.

Since the WLTP3 driving cycle was used previously to test the performance of the proposed LQI* controller, it is also investigated again to observe the influence of the NARX model on accuracy compared to the physical powertrain model. Figure 5.30 shows an estimation precision with a correlation of 0.996 and RMSE of 1.882 Nm for the controlled driving moment, which is about 0.4% less than the RMSE value with the full powertrain model, i.e., VEL model – Level2. Also, Figure 5.31 indicates that the braking physical model accurately estimated the braking moment for this maneuver with a 0.990 correlation and 162.316 Nm RMSE

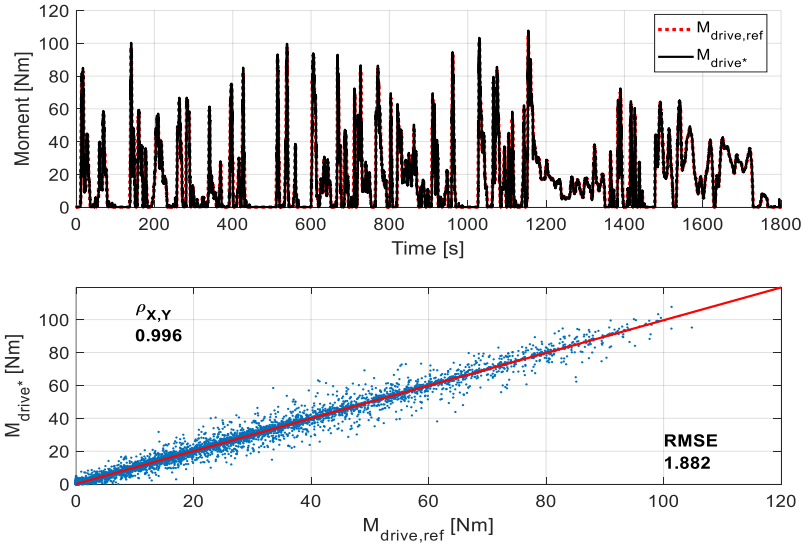

Figure 5.30: Correlation between the reference and controlled motor driving moment during the WLTP3 driving cycle, using the VEL model – Level 3.

Figure 5.32 display an outstanding performance of the VEL model – Level 3 in tracking the reference rotational speeds. The correlation values for the entire VEL model – Level 3 remain the same as for the standalone NARX model because the correlation values of the LQI* controller are also reached almost 1 for the WLTP3 test, as previously shown in Section 5.1.4. The main goal of this research, which is to establish a systematic and reproducible methodology for implementing real-world driving maneuvers on complete vehicle test benches, is successfully achieved. The developed framework integrates validated physical models, automated control strategies, and data-driven techniques to accurately simulate vehicle dynamics and estimate energy consumption without relying on costly and irreproducible on-road tests. Compared to other approaches in the literature, the proposed method significantly reduces modeling and parametrization complexity by enabling multiple modelling options, i.e. VEL model – Level 1, 2, and 3. The modeling

complexity level is determined based on the effort and the benefits. The more precisely the features of the components are depicted, the more valid the results are. However, the effort increases with accuracy. In contrast, the effort to select application parameters based on measurement data can be easily estimated and is usually lower. Therefore, this is usually preferred in practice. This progression, from vehicle modeling to the development of advanced vehicle-in-the-loop systems and data-driven modeling, establishes a comprehensive methodology for implementing real-world maneuvers on complete vehicle test benches. Each step builds upon the previous, ensuring that the resulting framework is both precise and practical. The outcome is a validated and adaptable approach to vehicle testing that bring together efficiency, accuracy, and realism. Overall, the method provides a robust yet practical solution for energy consumption evaluation and dynamic maneuver simulation in vehicle development environments

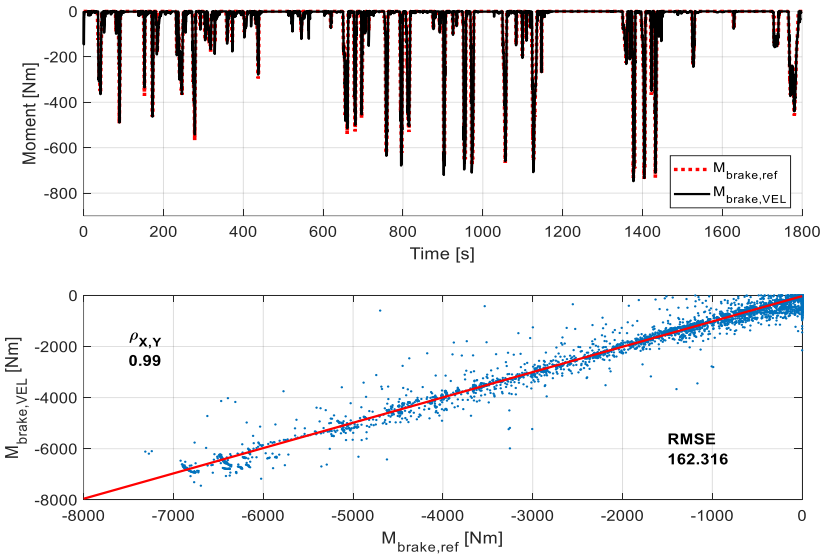

Figure 5.31: Correlation between the simulated and estimated total braking moment on the wheels during the WLTP3 driving cycle, using the VEL model – Level 3

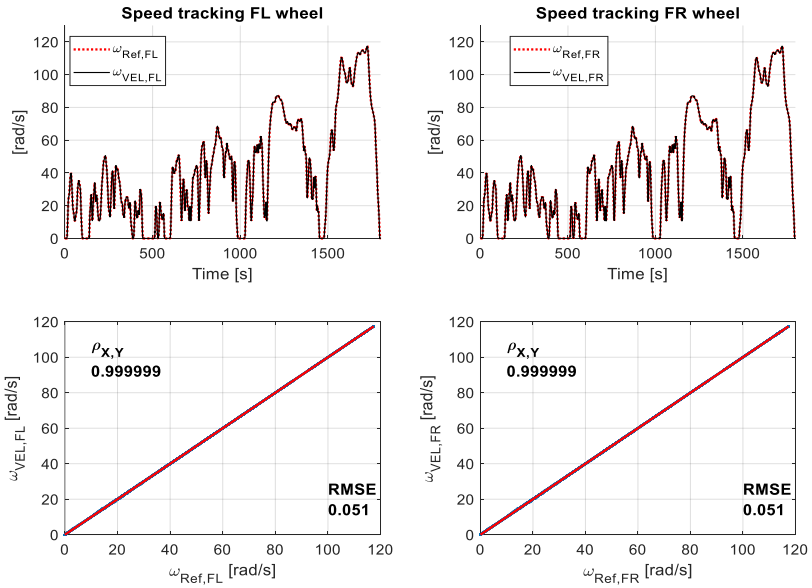

Figure 5.32: Correlation between the reference and controlled front wheels' angular speeds during the WLTP3 driving cycle, using the VEL model – Level 3.

5.5 Conclusion

Data-driven methods are introduced to address the nonlinearities inherent in real-world vehicle behavior. Empirical modeling techniques, including machine learning approaches such as NARX-based neural networks, are employed to establish predictive models that link driver inputs with vehicle responses. Trained on real-world route data, these models capture dynamic system behavior with reduced computational demands compared to fully physical models, while maintaining accuracy in energy consumption estimation and powertrain response prediction. The integration of such models into the test bench framework provides a powerful means of translating real-world driving conditions into laboratory-based testing with high fidelity.

6 Summary and outlook

The content of this dissertation is a presentation of a systematic, model-based method for reproducing dynamic driving maneuvers on test benches to determine the vehicle's energy consumption. The procedure facilitates the estimation of mechanical and electrical power quantities using simple measurement instruments, which increases the acceptance and willingness to use this model-based method in vehicle development.

The proposed adaptable simulation model for estimating the energy consumption in electric vehicles is simple to model yet provides highly accurate results. A backward model method is considered in this work for creating the complete electric vehicle since the main objective is estimating the energy consumption based on the vehicle's speed. The battery simulation model is validated in two stages. Firstly, the battery voltage estimation is validated, given the measured battery current. This step is accomplished by executing the WLTP2 drive cycle while mounting the VUT on a chassis dynamometer. The results proved high accuracy of the battery voltage estimation with a correlation of 0.981 and a RMSE equals to 0.948 compared to the measured signal. Secondly, the battery current is validated by dividing the computed total instantaneous power by the concurrent battery voltage. This validation is realized with a field driving maneuver. Comparing the measured and estimated physical quantities proves the simulation model's high reliability. Hence, the complete integrated model proved to be beneficial in evaluating the overall energy consumption of electric vehicles for a specified real driving course.

Both roller and powertrain complete vehicle test benches are examined with the help of simulation models. The analysis shows that chassis dynamometers suit dynamic driving maneuvers under certain conditions. However, the steerable test benches are the more powerful concept regarding the permissible operating range. In particular, dynamic driving maneuvers with high driving

power cannot be represented on roller test benches. In contrast, the controlled VEL test bench with the simulation of the wheel slip shows an almost exact representation of the reference powertrain dynamics. It is, therefore, more effective for dynamic driving maneuvers.

The difference between the actual and the estimated energy consumption in the roller dynamometer test benches is ascribed to the slipping of the tires on the rollers. To better simulate the tire's dynamic behavior on the roller, the implemented LuGre friction model has two different sets of equations with different parametrization: One for the driving mode and the other for the braking mode. The modifications to the uniform load LuGre friction model, which is the second central point of this work, are summarized in three key contributions: First, it was modified to be adapted to the roller dynamometer test bench by adjusting the contact patch length to the concaved roller radius according to the ETRTO-standards and optimized correction factors for roller test benches. Second, the vertical load on the axles, influenced by the restraint system, is considered. Third, the nonlinear slip estimation from the Pacejka tire model is implemented instead of the simplified slip definition in the LuGure model, considering splitting the Pacejka slip signal between driving and braking slip signals. The proposed LuGre tire model is integrated, with a larger-scale physical adaptable power consumption model. The proposed model comprises a dynamic physical model for the mounted vehicle on the chassis dynamometer, a driving resistance model, a power losses model of the electric power-train, a LuGre distributed friction tire model which considers the load distribution on the contact patch length between the tire and the ground, and a correction for the contact patch length between the wheel and the roller. Given only the measured speed of the test cycle and the corresponding auxiliary power consumption, the proposed model demonstrates high accuracy in estimating the actual measured power. Nevertheless, some different potential sources of errors still exist due to the curvature geometry of the roller, which has several influences such as increasing the tire's rolling resistance force compared to driving on a flat surface. Furthermore, inaccurately estimating the vehicle's speed leads to errors in tire slip estimation,

influencing the final power estimation results. Another source of dissimilarities in results is the slipping between the tire and the roller, which is a significant source of uncertainties that diminishes the accuracy of estimating the energy consumption in the roller dynamometer test benches.

A complete vehicle test bench is examined with the help of simulation models. The complex system from coupling the powertrain of the electric test vehicle with the mechanical part of the test bench is modeled in a three-mass system. It can be concluded that if the same weighting matrices Q and R parameters are employed with fine-tuning the integral weighting factor in the linear-quadratic optimization approach with integral LQI, both the linear-quadratic LQ, and LQI could achieve the same gain margin. However, there will be a difference in the phase margin due to the integral effect of the LQI controller. Moreover, time delay affects only the system phase in the frequency domain analysis, while it does not influence the frequency gain. In addition, the additional integration in the LQI reduces its phase margin compared to its equivalent LQ-controlled system. However, the speed error in the LQ control increases with the disturbance moment. In contrast, LQI can sustain approximately the same response regardless of the disturbance moment. Ideally, if there is no delay in the system, all controllers suppress the vibrations efficiently. Nevertheless, the PI-controlled system became vulnerable to instability as the time delay was introduced to the model. In opposition, LQ and LQI-controlled systems remained stable despite extreme operating conditions. Regarding parameter uncertainty, overestimating the powertrain inertia leads to a lower controller command moment in the transient states but slightly more oscillation in the response. On the other hand, underestimated powertrain inertia forces the controllers to generate higher moments than accurate parametrization. When the axle stiffness is the only uncertain parameter, the impact on LQ and LQI responses is minor. Despite this, LQ did not perform well with uncertainty in either the powertrain inertia or the axle stiffness. In contrast, multi parameter uncertainty did not significantly affect LQI performance. However, it did influence the controller effort response.

Analyzing the entire system's behavior between the accelerator pedal and the final motor moment is highly demanding because of the many components involved. Almost all powertrain components have nonlinear characteristics and the electronic components work discretely in time due to digital technology. A linear system can sufficiently represent the components' behavior in the best-case scenario. In the worst-case scenario, the overall system behavior is influenced by latency times between the control units. A NARX sigmoid model is also proposed in this work to interpret the driving moment from the accelerator pedal position. Supplementary quantities, besides the accelerator position value, are required to estimate the corresponding moment, which are: The electrical motor angular speed and the vehicle speed. The main finding is that the combined model from the NARX and the Sigmoid network enables modeling extremely nonlinear dynamic systems accurately.

This work can be extended in different scopes:

- The dynamic vehicle model can be upgraded from a single-track model to a full vehicle model, enabling more dynamic test maneuvers for advanced applications, such as driving comfort and ABS braking. Alternatively, simulation environments such as CarMaker may be employed if sufficient parameters are available to achieve the desired model complexity level.

- Estimating the actual energy consumption on roller test benches could be further developed by implementing the proposed approach for other types of vehicles, such as buses and trucks. Moreover, the proposed model can be extended by considering the regenerative braking system. Furthermore, this method can be implemented to estimate energy consumption for other powertrain types: Internal combustion engines, fuel cells, and hybrid powertrains. In addition, a methodology to mitigate the investigated limitations of the roller test bench, such as advanced calibration techniques or integrating additional sensors could be proposed. Also, this method could be used in real-world driving scenarios, incorporating a three-

dimensional route profile and the corresponding driving resistances on the tires. Finally, modeling the auxiliary power instead of relying on the measurements for every new test maneuver or test conditions.

- The proposed control algorithm may enable the VEL test bench to be employed in versatile applications. Moreover, the performance of nonlinear control algorithms could be compared to the proposed LQI controller. In addition, further optimal control techniques may be investigated.

7 Bibliography

Adaikkappan, M., & Sathiyamoorthy, N. (2022). Modeling, state of charge estimation, and charging of lithium-ion battery in electric vehicle: A review. International Journal of Energy Research, 46(3), 2141–2165. https://doi.org/10.1002/er.7339

Ahlert, A., Zeitvogel, D., Neubeck, J., Krantz, W., Wiedemann, J., Boone, F., & Orange, R. (2018). Next generation 3D vehicle dynamics test system – Software and control concept. In Internationales Stuttgarter Symposium (pp. 23–38). Springer Fachmedien. https://doi.org/10.1007/978-3-658-21194-3_5

Ahn, K., Rakha, H., Trani, A., & Van Aerde, M. (2002). Estimating vehicle fuel consumption and emissions based on instantaneous speed and acceleration levels. Journal of Transportation Engineering, 128(2), 182–190. https://doi.org/10.1061/(ASCE)0733-947X(2002)128:2(182)

Albers, A., Hettel, R., Behrendt, M., & Düser, T. (2013). Ohne Lenken in die Kurve - Virtuelle Kurvenfahrt auf dem 4x2 Rollenprüfstand. Proceedings. 5. Internationales Symposium für Entwicklungsmethodik, 22. und 23. Oktober 2013, Wiesbaden, 68–79.

Albers, A., You, Y., Klingler, S., Behrendt, M., Zhang, T., & Song, K. (2014). Supporting globally distributed product development with a new validation concept. Procedia CIRP, 21, 461–466. https://doi.org/10.1016/j.procir.2014.03.142

Alghafir, M. N., & Dunne, J. F. (2012). A NARX damper model for virtual tuning of automotive suspension systems with high-frequency

loading. Vehicle System Dynamics, 50(2), 167–197. https://doi.org/10.1080/00423114.2011.575946

Alhanouti, M., & Gauterin, F. (2023a). Robust Speed Control of a Multi-Mass System: Analytical Tuning and Sensitivity Analysis. Applied Sciences, 13(24), 13268. https://doi.org/10.3390/app132413268

Alhanouti, M., & Gauterin, F. (2023b). Thorough Analysis of the Reliability of Measurements on Chassis Roller Dynamometer and Accurate Energy Consumption Estimation for Electric Vehicles. Energies, 16(24), 7994. https://doi.org/10.3390/en16247994

Alhanouti, M., & Gauterin, F. (2024a). A Generic Model for Accurate Energy Estimation of Electric Vehicles. Energies, 17(2), 434. https://doi.org/10.3390/en17020434

Alhanouti, M., & Gauterin, F. (2024b). Predicting the Torque Demand of a Battery Electric Vehicle for Real-World Driving Maneuvers Using the NARX Technique. World Electric Vehicle Journal, 15(3), 103. https://doi.org/10.3390/wevj15030103

Alhanouti, M., Gießler, M., Blank, T., & Gauterin, F. (2016). New Electro-Thermal Battery Pack Model of an Electric Vehicle. Energies, 9(7), 563. https://doi.org/10.3390/en9070563

Asamer, J., Graser, A., Heilmann, B., & Ruthmair, M. (2016). Sensitivity analysis for energy demand estimation of electric vehicles. Transportation Research Part D: Transport and Environment, 46, 182–199. https://doi.org/10.1016/j.trd.2016.03.017

Astrom, K. J., & Murray, R. M. (2010). Feedback systems-an introduction for scientists and engineers. In See https://people.

duke. edu/~ hpgavin/SystemID/References/Astrom-Feedback-2006. pdf (2nd ed.). Princeton University Press.

Baker, N. D., & Presnell, K. (2006, February 1). Investigation of the effects of wheel slip on vehicle emissions and fuel economy. SAE Technical Papers. https://doi.org/10.4271/2006-01-1358

Bakker, E., Nyborg, L., & Pacejka, H. B. (1987). Tyre modelling for use in vehicle dynamics studies. SAE Technical Papers, 190–204. https://doi.org/10.4271/870421

Bauer, R. (2011a). Neues Regelkonzept für die dynamische Antriebsstrangprüfen. 17. Steirisches Seminar Über Regelungs-Technik Und Prozessautomatisierung, 104–116.

Bauer, R. (2011b). New methodology for dynamic drive train testing. SAE Technical Papers, 1–6. https://doi.org/10.4271/2011-26-0045

Bauer, S., Beidl, C., & Düser, T. (2018). Methodik zur Erzeugung RDE-relevanter Szenarien im Prüfstandsumfeld. In Simulation und Test 2017 (pp. 95–113). Springer Vieweg. https://doi.org/10.1007/978-3-658-20828-8_6

Beineke, S., Schuette, F., & Grotstollen, H. (n.d.). Comparison of methods for state estimation and on-line identification in speed and position control loops. Retrieved April 23, 2025, from https://www.semanticscholar.org/paper/COMPARISON-OF-METHODS-FOR-STATE-ESTIMATION-AND-IN-Beineke-Sch%C3%BCtte/afb1259a49ce983090adccafa53f4f1d29e86686?utm_source=direct_link

Brace, C. J., Burke, R., & Moffa, J. (2009). Increasing accuracy and repeatability of fuel consumption measurement in chassis dynamometer testing. Proceedings of the Institution of Mechanical Engineers, Part D: Journal of Automobile Engineering, 223(9), 1163–1177. https://doi.org/10.1243/09544070JAUTO1084

Braess, H.-H., & Seiffert, U. (2011). Werkstoffe und Fertigungsverfahren. In Vieweg Handbuch Kraftfahrzeugtechnik

(pp. 805–880). Vieweg+Teubner Verlag. https://doi.org/10.1007/978-3-8348-8298-1_10

Brundell-Freij, K., & Ericsson, E. (2005). Influence of street characteristics, driver category and car performance on urban driving patterns. Transportation Research Part D: Transport and Environment, 10(3), 213–229. https://doi.org/10.1016/j.trd.2005.01.001

Bunker, B. J., Franchek, M. A., & Thomason, B. E. (1997). Robust multivariable control of an engine-dynamometer system. IEEE Transactions on Control Systems Technology, 5(2), 189–199. https://doi.org/10.1109/87.556024

Canudas-de-Wit, C., Tsiotras, P., Velenis, E., Basset, M., & Gissinger, G. (2003). Dynamic friction models for road/tire longitudinal interaction. Vehicle System Dynamics, 39(3), 189–226. https://doi.org/10.1076/vesd.39.3.189.14152

Clark, S. K. (1976). Rolling resistance forces in pneumatic tires. United States. Dept. of Transportation. Office of the Secretary. https://rosap.ntl.bts.gov/view/dot/9695/dot_9695_DS1.pdf

Contestabile, M., Offer, G. J., Slade, R., Jaeger, F., & Thoennes, M. (2011). Battery electric vehicles, hydrogen fuel cells and biofuels. Which will be the winner? Energy & Environmental Science, 4(10), 3754–3772. https://doi.org/10.1039/c1ee01804c

De Cauwer, C., Van Mierlo, J., & Coosemans, T. (2015). Energy consumption prediction for electric vehicles based on real-world data. Energies, 8(8), 8573–8593. https://doi.org/10.3390/en8088573

De Cauwer, C., Verbeke, W., Coosemans, T., Faid, S., & Van Mierlo, J. (2017). A data-driven method for energy consumption prediction and energy-efficient routing of electric vehicles in real-world conditions. Energies, 10(5), 608–626. https://doi.org/10.3390/en10050608

de Wit, C. C., Lischinsky, P., Åström, K. J., & Olsson, H. (1995). A New Model for Control of Systems with Friction. IEEE Transactions on

Automatic Control, 40(3), 419–425. https://doi.org/10.1109/9.376053

de Wit, C. C., & Tsiotras, P. (1999). Dynamic tire friction models for vehicle traction control. Proceedings of the IEEE Conference on Decision and Control, 4, 3746–3751. https://doi.org/10.1109/cdc.1999.827937

Diewald, A., Kurz, C., Kannan, P. V., Gießler, M., Pauli, M., Göttel, B., Kayser, T., Gauterin, F., & Zwick, T. (2021). Radar Target Simulation for Vehicle-in-the-Loop Testing. Vehicles, 3(2), 257–271. https://doi.org/10.3390/vehicles3020016

Duarte, G. O., Gonçalves, G. A., & Farias, T. L. (2016). Analysis of fuel consumption and pollutant emissions of regulated and alternative driving cycles based on real-world measurements. Transportation Research Part D: Transport and Environment, 44, 43–54. https://doi.org/10.1016/j.trd.2016.02.009

Düser, T. (2010). X-in-the-Loop - ein durchgängiges Validierungsframework für die Fahrzeugentwicklung am Beispiel von Antriebsstrangfunktionen und Fahrerassistenzsystemen. X-in-the-Loop - an integrated validation framework for vehicle development using powertrain functions and driver assistance systems [Doctoral dissertation, Karlsruhe Institute of Technology]. https://doi.org/10.5445/IR/1000020671

Düser, T., von Gravel, R., Haase, A., Olms, H., Schmidt, C., & Schmidt, U. (2011). Fahrzeugrollenprüfstände: von der Zertifizierung bis hin zur mechatronischen Entwicklungsplattform (Vol. 341). Verlag Moderne Industrie (mi connect).

Eckert, J. J., Bertoti, E., dos Santos Costa, E., Santiciolli, F. M., Yamashita, R. Y., e Silva, L. C. de A., & Dedini, F. G. (2017). Experimental evaluation of rotational inertia and tire rolling resistance for a twin roller chassis dynamometer. SAE Technical Paper Series, Proceedings of the 26th SAE BRASIL Inernational

Congress and Display. https://doi.org/https://doi.org/10.4271/2017-36-0212

Ejsmont, J., & Owczarzak, W. (2019). Engineering method of tire rolling resistance evaluation. Measurement, 145, 144–149. https://doi.org/10.1016/j.measurement.2019.05.071

El-Haji, M. (2016). Ontologie-basierte Definition von Anforderungen an Validierungswerkzeuge in der Fahrzeugtechnik [Doctoral dissertation, Karlsruhe Institute of Technology]. https://doi.org/10.5445/KSP/1000052725

El-Sharkawy, A. E. (2007). Reliability analysis of dynamometer loading parameters during vehicle cell testing. SAE Technical Papers. https://doi.org/10.4271/2007-01-0600

Erdinc, O., Vural, B., & Uzunoglu, M. (2009). A dynamic lithium-ion battery model considering the effects of temperature and capacity fading. International Conference on Clean Electrical Power, 383–386. https://doi.org/10.1109/ICCEP.2009.5212025

Fall, K., & Stevens, R. (2011). TCP / IP Illustrated, Volume 1 : The Protocols. In Trial (2nd ed., Vol. 1). Addison-Wesley Professional.

Ficht, A., & Lienkamp, M. (2015). Rolling resistance modeling for electric vehicle consumption. In P. Pfeffer (Ed.), 6th International Munich Chassis Symposium 2015 (pp. 775–798). Springer Fachmedien Wiesbaden. https://doi.org/https://doi.org/10.1007/978-3-658-09711-0_49

Fietzek, R. (2014). Modellbildung, Regelung und Realisierung eines neuartigen Konzepts für einen Gesamtfahrzeugprüfstand (1st ed.). Shaker Verlag.

Fietzek, R., & Rinderknecht, S. (2013). Observer validation and model based control of a two mass oscillator with backlash. 2013 IEEE International Conference on Mechatronics and Automation, IEEE ICMA 2013, 318–323. https://doi.org/10.1109/ICMA.2013.6617938

Fietzek, R., & Rinderknecht, S. (2015). Car-in-the-Loop Complete Vehicle Test Rig. SAE International Journal of Passenger Cars -

Mechanical Systems, 8(2), 476–481. https://doi.org/10.4271/2015-01-0647

Fiori, C., Ahn, K., & Rakha, H. A. (2016). Power-based electric vehicle energy consumption model: Model development and validation. Applied Energy, 168, 257–268. https://doi.org/10.1016/j.apenergy.2016.01.097

Forrier, B., Loth, A., & Mollet, Y. (2020). In-Vehicle Identification of an Induction Machine Model for Operational Torque Prediction. 2020 International Conference on Electrical Machines (ICEM), 1157–1163. https://doi.org/10.1109/ICEM49940.2020.9270731

Forstinger, M. (2017). Modelling, Simulation, and Control of Power Train Test Beds [Doctoral dissertation, Graz University of Technology]. https://diglib.tugraz.at/download.php?id=5bebd9d691234&location=browse

Forstinger, M., Bauer, R., Hofer, A., & Rossegger, W. (2016). Multivariable control of a test bed for differential gears. Control Engineering Practice, 57, 18–28. https://doi.org/10.1016/j.conengprac.2016.08.010

Fritz, A., Sander, O., Müller-Glaser, K., Gießler, M., & Gauterin, F. (2012). Converted vehicle for battery electric drive: Aspects on the design of the soft-ware-driven vehicle control unit. In In Proceedings of the 2nd Energy Efficienct Vehicle Conference (EEVC 2012).

Gao, X., Xiong, Y., Liu, W., & Zhuang, Y. (2021). Modeling and experimental study of tire deformation characteristics under high-speed rolling condition. Polymer Testing, 99, 107052. https://doi.org/10.1016/j.polymertesting.2021.107052

Gao, Y., & Ehsani, M. (2009). Design and control methodology of plug-in hybrid electric vehicles. IEEE Transactions on Industrial Electronics, 57(2), 633–640.

Gao, Z., LaClair, T., Ou, S., Huff, S., Wu, G., Hao, P., Boriboonsomsin, K., & Barth, M. (2019). Evaluation of electric vehicle component

performance over eco-driving cycles. Energy, 172, 823–839. https://doi.org/10.1016/j.energy.2019.02.017

Gauterin, F. (2017). Automotive Engineering I — Lecture Notes. Karlsruhe Institute of Technology.

Geneder, S., Pfister, F., Wilhelm, C., & Arnold, A. (2014). Entwicklung vernetzter Antriebssysteme am Leistungsprüfstand. ATZ - Automobiltechnische Zeitschrift, 116(6), 28–33. https://doi.org/10.1007/s35148-014-0423-1

Genikomsakis, K. N., & Mitrentsis, G. (2017). A computationally efficient simulation model for estimating energy consumption of electric vehicles in the context of route planning applications. Transportation Research Part D: Transport and Environment, 50, 98–118. https://doi.org/10.1016/j.trd.2016.10.014

Gietelink, O. J., Ploeg, J., De Schutter, B., & Verhaegen, M. (2009). Development of a driver information and warning system with vehicle hardware-in-the-loop simulations. Mechatronics, 19(7), 1091–1104.

Gietelink, O., Ploeg, J., De Schutter, B., & Verhaegen, M. (2006). Development of advanced driver assistance systems with vehicle hardware-in-the-loop simulations. Vehicle System Dynamics, 44(7), 569–590.

Glass, J. W. (1999). NARMAX modelling and robust control of internal combustion engines. International Journal of Control, 72(4), 289–304.

Grady, H., Nauman, N., & Miah, M. S. (2022). Data-Driven Hardware-in-the-Loop Plant Modeling for Self-Driving Vehicles. 2022 IEEE

International Symposium on Robotic and Sensors Environments (ROSE), 1–8. https://doi.org/10.1109/ROSE56499.2022.9977411

Guo, K., & Ren, L. (1999). A Unified Semi-Empirical Tire Model with Higher Accuracy and Less Parameters. SAE Transactions, 108, 1513–1520. https://doi.org/10.4271/1999-01-0785

Haken, K.-L. (2018). Grundlagen der Kraftfahrzeugtechnik. In Grundlagen der Kraftfahrzeugtechnik (1st ed.). Carl Hanser Verlag. https://doi.org/10.3139/9783446455702.fm

Harnefors, L., & Nee, H. P. (1998). Model-based current control of ac machines using the internal model control method. IEEE Transactions on Industry Applications, 34(1). https://doi.org/10.1109/28.658735

He, Z., Shi, Q., Wei, Y., Zheng, J., Gao, B., & He, L. (2021). A Torque Demand Model Predictive Control Approach for Driving Energy Optimization of Battery Electric Vehicle. IEEE Transactions on Vehicular Technology, 70(4), 3232–3242. https://doi.org/10.1109/TVT.2021.3066405

Heißing, B., & Ersoy, M. (2007). Fahrwerkhandbuch. In B. Heißing & M. Ersoy (Eds.), Fahrwerkhandbuch: Grundlagen, Fahrdynamik, Komponenten, Systeme, Mechatronik, Perspektiven (1st ed.). Vieweg+Teubner Verlag. https://doi.org/10.1007/978-3-8348-9151-8_3

Hendrick, D., Vennefron, A., & Sienkiewicz, D. (2003). Vehicle retention methods for four-wheel chassis dynamometer testing. SAE Technical Papers. https://doi.org/10.4271/2003-01-1432

Horrein, L., Bouscayrol, A., Delarue, P., Verhille, J. N., & Mayet, C. (2012). Forward and Backward simulations of a power propulsion system. IFAC Proceedings Volumes, 45(21), 441–446. https://doi.org/10.3182/20120902-4-FR-2032.00078

Hu, J., Peng, T., Jia, M., Yang, Y., & Guan, Y. (2019). Study on electromechanical coupling characteristics of an integrated electric

drive system for electric vehicle. IEEE Access, 7, 166493–166508. https://doi.org/10.1109/ACCESS.2019.2953310

IEA. (2017). Global EV Outlook 2017. https://www.iea.org/reports/global-ev-outlook-2017

Ineichen, L. (2013). Konzeptvergleich zur Bekämpfung der Torsionsschwingungen im Antriebsstrang eines Kraftfahrzeugs [Doctoral dissertation, Karlsruhe Institute of Technology]. https://doi.org/10.5445/KSP/1000034947

IPG Automotive GmbH. (n.d.). CarMaker. Retrieved December 28, 2023, from https://ipg-automotive.com/en/products-solutions/software/carmaker/

Isermann, R., & Münchhof, M. (2011). Identification of dynamic systems: an introduction with applications (Vol. 85). Springer.

Jazar, R. N. (2008). Vehicle dynamics: Theory and applications. In Vehicle Dynamics: Theory and Applications (1st ed.). Springer. https://doi.org/10.1007/978-0-387-74244-1

Ji, J. K., & Sul, S. K. (1995). Kalman Filter and LQ Based Speed Controller for Torsional Vibration Suppression in a 2-Mass Motor Drive System. IEEE Transactions on Industrial Electronics, 42(6), 564–571. https://doi.org/10.1109/41.475496

Joshi, A. (2017a). Powertrain and Chassis Hardware-in-the-Loop (HIL) Simulation of Autonomous Vehicle Platform. SAE Technical Papers, Part F129886(September). https://doi.org/10.4271/2017-01-1991

Joshi, A. (2017b). Real-Time Implementation and Validation for Automated Path Following Lateral Control Using Hardware-in-the-

Loop (HIL) Simulation. SAE Technical Papers, 2017-March(March). https://doi.org/10.4271/2017-01-1683

Kohrs, C. (2017). Future challenges for commercial vehicle development. Internationales Stuttgarter Symposium, 17, 1121–1132. https://doi.org/10.1007/978-3-658-16988-6_85

Krammer, M., Marko, N., & Benedikt, M. (2016). Interfacing real-time systems for advanced co-simulation - The ACOSAR approach. CEUR Workshop Proceedings, 1675, 32–39.

Kubaisi, R. (2018). Adaptive Regenerative Braking in Electric Vehicles [Doctoral dissertation, Karlsruhe Institute of Technology]. https://doi.org/10.5445/IR/1000080341

Kurczveil, T., López, P. Ál., & Schnieder, E. (2014). Implementation of an energy model and a charging infrastructure in sumo. Lecture Notes in Computer Science (Including Subseries Lecture Notes in Artificial Intelligence and Lecture Notes in Bioinformatics), 8594, 33–43. https://doi.org/10.1007/978-3-662-45079-6_3

Lam, L., Bauer, P., & Kelder, E. (2011). A practical circuit-based model for Li-ion battery cells in electric vehicle applications. INTELEC, International Telecommunications Energy Conference (Proceedings), 1–9. https://doi.org/10.1109/INTLEC.2011.6099803

Lantos, B., & Márton, L. (2011). Nonlinear Control of Vehicles and Robots (1st ed.). Springer London. https://doi.org/10.1007/978-1-84996-122-6

Lavigne, L., Sabatier, J., Francisco, J. M., Guillemard, F., & Noury, A. (2016). Lithium-ion Open Circuit Voltage (OCV) curve modelling and its ageing adjustment. Journal of Power Sources, 324, 694–703. https://doi.org/10.1016/j.jpowsour.2016.05.121

Lensch-Franzen, C., Friedmann, M., Donn, C., & Rohrpasser, C. (2017). Mit virtuellen Prototypfahrzeugen an den Prüfstand. ATZ - Automobiltechnische Zeitschrift, 119(10), 36–43. https://doi.org/10.1007/s35148-017-0106-9

Lensch-Franzen, C., Schintzel, K., & Rosner, A. (2018). Applikationsoptimierung für aktuelle Anforderungen im

Antriebsstrang. MTZ - Motortechnische Zeitschrift, 79(5), 42–47. https://doi.org/10.1007/s35146-018-0021-y

Lourenço, M. A. de M., Eckert, J. J., Silva, F. L., Santiciolli, F. M., & Silva, L. C. A. (2023). Vehicle and twin-roller chassis dynamometer model considering slip tire interactions. Mechanics Based Design of Structures and Machines, 51(11), 6166–6183. https://doi.org/10.1080/15397734.2022.2038199

Manoharan, A., Begam, K. M., Aparow, V. R., & Sooriamoorthy, D. (2022). Artificial Neural Networks, Gradient Boosting and Support Vector Machines for electric vehicle battery state estimation: A review. Journal of Energy Storage, 55, 105384. https://doi.org/10.1016/j.est.2022.105384

Mapelli, F. L., & Tarsitano, D. (2012). Modeling of full electric and hybrid electric vehicles. In new generation of electric vehicles (pp. 207–236). IntechOpen. https://doi.org/http://dx.doi.org/10.5772/53570

Marongiu, A., Nußbaum, F. G. W., Waag, W., Garmendia, M., & Sauer, D. U. (2016). Comprehensive study of the influence of aging on the hysteresis behavior of a lithium iron phosphate cathode-based lithium ion battery–An experimental investigation of the hysteresis. Applied Energy, 171, 629–645.

Martyr, a. J., & Plint, M. a. (2012). Engine Testing: The Design, Building, Modification and Use of Powertrain Test Facilities. In Engine Testing (4th ed.). Elsevier. https://doi.org/10.1016/C2010-0-66322-X

März, M. (2010). Leistungselektronik für e-Fahrzeuge-Konzepte und Herausforderungen. DRIVE-E Akademie. https://docplayer.org/7071916-Leistungselektronik-fuer-e-fahrzeuge-konzepte-und-herausforderungen.html#download_tab_content

Maschmeyer, H., Beidl, C., Düser, T., & Schick, B. (2016). RDE-Homologation – Herausforderungen, Lösungen und Chancen. MTZ

- Motortechnische Zeitschrift, 77(10), 84–91. https://doi.org/10.1007/s35146-016-0110-8

Mathworks Inc. (2023). Simscape Reference (r2023b). https://ch.mathworks.com/help/pdf_doc/simscape/simscape_ref.pdf

MathWorks Inc. (2023). System Identification Reference (r2023b). https://ch.mathworks.com/help/pdf_doc/ident/ident_ref.pdf

Matros, K., Schille, F., Behrendt, M., & Holzer, H. (2015). Manöverbasierte Validierung von Hybridantrieben. ATZ - Automobiltechnische Zeitschrift, 117(2), 64–71. https://doi.org/10.1007/s35148-015-0384-z

Mayyas, A., Prucka, R., Pisu, P., & Haque, I. (2013). Chassis Dynamometer as a Development Platform for Vehicle Hardware In-the-Loop "VHiL." SAE International Journal of Commercial Vehicles, 6(1), 257–267. https://doi.org/10.4271/2013-01-9018

McCoy, G. A., & Douglass, J. G. (2014). Premium efficiency motor selection and application guide - A handbook for industry (No. DOE/GO-102014-4107). In Energy Efficiency & Renewable Energy (1st ed.). US Department of Energy. https://www.energy.gov/sites/default/files/2014/04/f15/amo_motors_handbook_web.pdf

Mei, P., Karimi, H. R., Huang, C., Chen, F., & Yang, S. (2023). Remaining driving range prediction for electric vehicles: Key challenges and outlook. IET Control Theory & Applications, 17(14), 1875–1893. https://doi.org/10.1049/cth2.12486

Meywerk, M. (2015). Vehicle Dynamics (1st ed.). John Wiley & Sons.

Miri, I., Fotouhi, A., & Ewin, N. (2021). Electric vehicle energy consumption modelling and estimation—A case study.

International Journal of Energy Research, 45(1), 501–520. https://doi.org/10.1002/er.5700

Mitschke, M., & Wallentowitz, H. (2004). Dynamik der Kraftfahrzeuge. In Dynamik der Kraftfahrzeuge (4th ed.). Springer. https://doi.org/10.1007/978-3-662-06802-1

Montgomery, D. C., & Runger, G. C. (2010). *Applied statistics and probability for engineers* (5th ed.). John Wiley & Sons.

Munagala, V. K., & Jatoth, R. K. (2023). A novel approach for controlling DC motor speed using NARXnet based FOPID controller. Evolving Systems, 14(1), 101–116. https://doi.org/10.1007/s12530-022-09437-1

Muszynski, R., & Deskur, J. (2010). Damping of torsional vibrations in high-dynamic industrial drives. IEEE Transactions on Industrial Electronics, 57(2), 544–552. https://doi.org/10.1109/TIE.2009.2036034

Nakajo, T., & Tsuchiya, K. (2009). Factors affecting driving force characteristics of 4WD vehicles on a 4WD chassis dynamometer. SAE Technical Papers. https://doi.org/10.4271/2009-01-1350

Nehlsen, M., Jedicke, F., Bogner, E., & Schöggl, P. (2006). Fahrbarkeitsuntersuchungen auf dem rollenprüfstand. ATZ Automobiltechnische Zeitschrift, 108(5), 376–381. https://doi.org/10.1007/BF03221788

Nelles, O. (2020). Nonlinear Dynamic System Identification. In Nonlinear System Identification (pp. 831–891). Springer International Publishing. https://doi.org/10.1007/978-3-030-47439-3_19

Nordin, M., & Gutman, P. O. (2002). Controlling mechanical systems with backlash - A survey. Automatica, 38(10), 1633–1649. https://doi.org/10.1016/S0005-1098(02)00047-X

Ogata, K. (2009). Modern Control Engineering. In IEEE Transactions on Automatic Control (5th ed., Vol. 17, Issue 3). Pearson Educaton.

O'Neill, A., Prins, J., Watts, J. F., & Gruber, P. (2022). Enhancing brush tyre model accuracy through friction measurements. Vehicle

System Dynamics, 60(6), 2075–2097. https://doi.org/10.1080/00423114.2021.1893766

Orlowska-Kowalska, T., & Szabat, K. (2007). Neural-Network application for mechanical variables estimation of a two-mass drive system. IEEE Transactions on Industrial Electronics, 54(3), 1352–1364. https://doi.org/10.1109/TIE.2007.892637

Pacejka, H. B. (2006). Tyre and Vehicle Dynamics. In Tire and Vehicle Dynamics (2nd ed.). Elsevier . https://doi.org/10.1016/B978-0-7506-6918-4.X5000-X

Paulweber, M., & Lebert, K. (2016). Powertrain Instrumentation and Test Systems (1st ed.). Springer International Publishing. https://doi.org/10.1007/978-3-319-32135-6

Pelkmans, L., & Debal, P. (2006). Comparison of on-road emissions with emissions measured on chassis dynamometer test cycles. Transportation Research Part D: Transport and Environment, 11(4), 233–241. https://doi.org/10.1016/j.trd.2006.04.001

Petersen, M. R., & Starkey, J. M. (1996). Nonlinear vehicle performance simulation with test correlation and sensitivity analysis. SAE Technical Papers, 643–653. https://doi.org/10.4271/960521

Pexa, M., Mader, D., Čedík, J., Peterka, B., Müller, M., Valášek, P., & Hloch, S. (2020). Experimental verification of small diameter rollers utilization in construction of roller test stand in evaluation of energy loss due to rolling resistance. Measurement, 152, 107287. https://doi.org/10.1016/j.measurement.2019.107287

Pfeffer, R., & Leichsenring, T. (2016). Continuous Development of Highly Automated Driving Functions with Vehicle-in-the-Loop Using the Example of Euro NCAP Scenarios. Simulation and Testing

for Vehicle Technology, 33–42. https://doi.org/10.1007/978-3-319-32345-9_4

Pfister, F., Schyr, C., & Le Rhun, F. (2009). Total energy efficiency testing. ATZ Worldwide, 111(11), 45–49. https://doi.org/10.1007/bf03225332

Pillas, J. (2017). Modellbasierte Optimierung dynamischer Fahrmanöver mittels Prüfständen [Doctoral dissertation, Darmstadt University of Technology]. https://www.shaker.de/de/content/catalogue/index.asp?lang=de&ID=8&ISBN=978-3-8440-5420-0

Pillas, J., Kirschbaum, F., Jakobi, R., Gebhardt, A., & Uphaus, F. (2014). Model-based load change reaction optimization using vehicle drivetrain test beds. Internationales Stuttgarter Symposium, 1663–1673. https://doi.org/10.1007/978-3-658-05130-3_115

Ponn, J., & Lindemann, U. (2011). Konzeptentwicklung und Gestaltung technischer Produkte: systematisch von Anforderungen zu Konzepten und Gestaltlösungen. Springer. https://doi.org/10.1007/978-3-642-20580-4

Prandtstetter, M., Straub, M., & Puchinger, J. (2013). On the way to a multi-modal energy-efficient route. IECON 2013-39th Annual Conference of the IEEE Industrial Electronics Society, 4779–4784.

Qi, X., Wu, G., Boriboonsomsin, K., & Barth, M. J. (2018). Data-driven decomposition analysis and estimation of link-level electric vehicle energy consumption under real-world traffic conditions. Transportation Research Part D: Transport and Environment, 64, 36–52. https://doi.org/10.1016/j.trd.2017.08.008

Ramsey, D., Bouscayrol, A., Boulon, L., Desreveaux, A., & Vaudrey, A. (2022). Flexible Simulation of an Electric Vehicle to Estimate the Impact of Thermal Comfort on the Energy Consumption. IEEE Transactions on Transportation Electrification, 8(2), 2288–2298. https://doi.org/10.1109/TTE.2022.3144526

Rautenberg, P., Weber, P., Degel, J. P., Hähnlein, S., Gauterin, F., Koch, T., Doppelbauer, M., & Gohl, M. (2023). Electrified Powertrain Development: Distributed Co-Simulation Protocol Extension for

Coupled Test Bench Operations. Applied Sciences, 13(4), 2657. https://doi.org/10.3390/app13042657

Reif, K. (2010). Bremsen und Bremsregelsysteme (1st ed.). Vieweg+Teubner Verlag .

Ricci, F., Petrucci, L., Mariani, F., & Grimaldi, C. N. (2023). NARX Technique to Predict Torque in Internal Combustion Engines. Information, 14(7), 417. https://doi.org/10.3390/info14070417

Saarakkala, S. E., & Hinkkanen, M. (2014). State space speed control of two-mass mechanical systems: Analytical tuning and experimental evaluation. IEEE Transactions on Industry Applications, 50(5), 3428–3437. https://doi.org/10.1109/TIA.2014.2306977

Saarakkala, S. E., Hinkkanen, M., & Zenger, K. (2012). Speed control of two-mass mechanical loads in electric drives. 2012 IEEE Energy Conversion Congress and Exposition, ECCE 2012, 1246–1253. https://doi.org/10.1109/ECCE.2012.6342673

Sato, Y., Kusakabe, T., Satonaka, T., Nakamura, S., Ogawa, Y., & Noguchi, S. (2010). An analysis of behavior for 4WD vehicle on 4WD-chassis dynamometer. SAE Technical Papers. https://doi.org/10.4271/2010-01-0926

Scamarcio, A., Metzler, M., Gruber, P., De Pinto, S., & Sorniotti, A. (2020). Comparison of Anti-Jerk Controllers for Electric Vehicles with On-Board Motors. IEEE Transactions on Vehicular Technology, 69(10), 10681–10699. https://doi.org/10.1109/TVT.2020.2997815

Schenk, J. (2007). Prüfplattform für mechatronisch ausgestattete Fahrzeuge in Entwicklung und Produktion [Doctoral dissertation, RTWH Aachen]. http://publications.rwth-aachen.de/record/49934/files/Schenk_Jan.pdf

Schenk, J., Tentrup, T., & Spiegelberg, G. (2006). Unfallvermeidendes fahrzeugkonzept SPARC und neue prüfanlage VeHil. ATZ

Automobiltechnische Zeitschrift, 108(3), 182–189. https://doi.org/10.1007/BF03221774

Schmidt, D., Maschmeyer, H., Beidl, C., & Raß, F. (2017). Neue Verfahren zur effizienten antriebsstrangspezifischen RDE-Entwicklung. 1–18. https://doi.org/10.1007/978-3-658-16754-7_1

Schramm, D., Hiller, M., & Bardini, R. (2014). Vehicle dynamics: Modeling and simulation. In Vehicle Dynamics: Modeling and Simulation (1st ed.). Springer . https://doi.org/10.1007/978-3-540-36045-2

Schyr, C., & Brissard, A. (2016). DrivingCube – A novel concept for validation of powertrain and steering systems with automated driving. International Symposium on Advanced Vehicle Control, 79–84. https://doi.org/10.1201/9781315265285-14

Schyr, C., Reiß, B., & Otto, F. (2012). Model-based Validation Applied to Off-Highway Vehicles. VDI-Fachkonferenz Elektrik Und Elektronik in Mobilen Arbeitsmaschinen, 309–329. https://www.fast.kit.edu/download/DownloadsMobima/Veroeffentlichung_ModellbasierteValidierung_Otto_08062012.pdf

Sciuto, M., & Hellmund, R. (2001). “Road to rig” - Simulationskonzept an Powertrain-Prüfständen in der Getriebeerprobung. ATZ Automobiltechnische Zeitschrift, 103(4), 298–307. https://doi.org/10.1007/BF03224372

Segovia, V. R., Hägglund, T., & Åström, K. J. (2014). Measurement noise filtering for PID controllers. Journal of Process Control, 24(4), 299–313. https://doi.org/10.1016/j.jprocont.2014.01.017

Shrivastava, P., Soon, T. K., Idris, M. Y. I. Bin, Mekhilef, S., & Adnan, S. B. R. S. (2022). Model-based state of X estimation of lithium-ion battery for electric vehicle applications. International Journal of Energy Research, 46(8), 10704–10723. https://doi.org/10.1002/er.7874

Singh, R., & Sznaier, M. (2021). On identification of nonlinear arx models with sparsity in regressors and basis functions. IFAC-

PapersOnLine, 54(7), 720–725. https://doi.org/https://doi.org/10.1016/j.ifacol.2021.08.446

Sjöberg, J., Zhang, Q., Ljung, L., Benveniste, A., Delyon, B., Glorennec, P.-Y., Hjalmarsson, H., & Juditsky, A. (1995). Nonlinear black-box modeling in system identification: a unified overview. Automatica, 31(12), 1691–1724.

Smuts, M., Scholtz, B., & Wesson, J. (2017). A critical review of factors influencing the remaining driving range of electric vehicles. 2017 1st International Conference on Next Generation Computing Applications, NextComp 2017, 196–201. https://doi.org/10.1109/NEXTCOMP.2017.8016198

Sun, T., Xu, Y., Feng, L., Xu, B., Chen, D., Zhang, F., Han, X., Zhao, L., & Zheng, Y. (2022). A vehicle-cloud collaboration strategy for remaining driving range estimation based on online traffic route information and future operation condition prediction. Energy, 248, 123608. https://doi.org/10.1016/j.energy.2022.123608

Szabat, K., & Orlowska-Kowalska, T. (2006). Adaptive control of two-mass system using nonlinear extended Kalman Filter. IECON Proceedings (Industrial Electronics Conference), 1539–1544. https://doi.org/10.1109/IECON.2006.347970

Szabat, K., & Orlowska-Kowalska, T. (2007). Vibration suppression in a two-mass drive system using PI speed controller and additional feedbacks - Comparative study. IEEE Transactions on Industrial Electronics, 54(2), 1193–1206. https://doi.org/10.1109/TIE.2007.892608

Szabat, K., & Orlowska-Kowalska, T. (2012). Application of the Kalman filters to the high-performance drive system with elastic coupling. IEEE Transactions on Industrial Electronics, 59(11), 4226–4235. https://doi.org/10.1109/TIE.2012.2183836

Thomsen, S., & Fuchs, F. W. (2009). Speed control of torsional drive systems with backlash. 13th European Conference on Power Electronics and Applications, EPE ’09, 1–10.

Thomsen, S., Hoffmann, N., & Fuchs, F. W. (2011). PI control, PI-based state space feedback, and model-based predictive control for drive

systems with elastically coupled loads-A comparative study. IEEE Transactions on Industrial Electronics, 58(8), 3647–3657. https://doi.org/10.1109/TIE.2010.2089950

Togun, N., Baysec, S., & Kara, T. (2012). Nonlinear modeling and identification of a spark ignition engine torque. Mechanical Systems and Signal Processing, 26, 294–304.

Travesset-Baro, O., Rosas-Casals, M., & Jover, E. (2015). Transport energy consumption in mountainous roads. A comparative case study for internal combustion engines and electric vehicles in Andorra. Transportation Research Part D: Transport and Environment, 34, 16–26. https://doi.org/10.1016/j.trd.2014.09.006

Tremblay, O., & Dessaint, L. A. (2009). Experimental validation of a battery dynamic model for EV applications. World Electric Vehicle Journal, 3(2), 289–298. https://doi.org/10.3390/wevj3020289

Unrau, H.-J. (2013). Der Einfluss der Fahrbahnoberflächenkrümmung auf den Rollwiderstand, die Cornering Stiffness und die Aligning Stiffness von Pkw-Reifen [Doctoral dissertation, Karlsruhe Institute of Technology]. https://doi.org/10.5445/KSP/1000032808

US Department of Energy. (2014). Determining Electric Motor Load and Efficiency. https://www.energy.gov/sites/prod/files/2014/04/f15/10097517.pdf

Valence Technology Inc. (2011). Valence Technology U-Charge® XP Rev 2 User Manual. https://www.celltech.se/fileadmin/user_upload/Celltech/Products/Litium_laddningsbara/Valence_Modules/XP_Module_Datasheet.pdf

Vögl, R., Bogner, E., Ebner, T., Dein Dias Terra, T., & Vitale, G. (2009). Innovative Use of Chassis Dynamometers for the Calibration of Driveability. ATZ Worldwide, 111(11), 51–58. https://doi.org/10.1007/bf03225334

Wang, J., Liu, K., & Yamamoto, T. (2017). Improving electricity consumption estimation for electric vehicles based on sparse GPS

observations. Energies, 10(1), 129. https://doi.org/10.3390/en10010129

Wang, R., & Lukic, S. M. (2011). Review of driving conditions prediction and driving style recognition based control algorithms for hybrid electric vehicles. IEEE Vehicle Power and Propulsion Conference, VPPC, 1–7. https://doi.org/10.1109/VPPC.2011.6043061

Weber, S., Dursun, Y., Kirschbaum, F., Jakobi, R., Bäker, B., & Fischer, J. (2017). Investigations of the process of road matching on powertrain test rigs. Internationales Stuttgarter Symposium, 1247–1261. https://doi.org/10.1007/978-3-658-16988-6_94

Weber, T., Beidl, C., Düser, T., & Gietzelt, C. (2014). The chassis dynamometer as real world driving environment. Internationales Stuttgarter Symposium, 1641–1662. https://doi.org/10.1007/978-3-658-05130-3_114

Wijewardana, S., Vepa, R., & Shaheed, M. H. (2016). Dynamic battery cell model and state of charge estimation. Journal of Power Sources, 308, 109–120. https://doi.org/10.1016/j.jpowsour.2016.01.072

Wu, X., Freese, D., Cabrera, A., & Kitch, W. A. (2015). Electric vehicles' energy consumption measurement and estimation. Transportation Research Part D: Transport and Environment, 34, 52–67. https://doi.org/10.1016/j.trd.2014.10.007

Yamashita, H., Matsutani, Y., & Sugiyama, H. (2015). Longitudinal Tire Dynamics Model for Transient Braking Analysis: ANCF-LuGre Tire Model. Journal of Computational and Nonlinear Dynamics, 10(3). https://doi.org/10.1115/1.4028335

Yao, E., Wang, M., Song, Y., & Yang, Y. (2013). State of charge estimation based on microscopic driving parameters for electric vehicle's battery. Mathematical Problems in Engineering, 2013. https://doi.org/10.1155/2013/946747

Yi, Z., & Bauer, P. H. (2017). Adaptive Multiresolution Energy Consumption Prediction for Electric Vehicles. IEEE Transactions on

Vehicular Technology, 66(11), 10515–10525. https://doi.org/10.1109/TVT.2017.2720587

Younes, Z., Boudet, L., Suard, F., Gerard, M., & Rioux, R. (2013). Analysis of the main factors influencing the energy consumption of electric vehicles. Proceedings of the 2013 IEEE International Electric Machines and Drives Conference, IEMDC 2013, 247–253. https://doi.org/10.1109/IEMDC.2013.6556260

Zahn, S., Isermann, R., & Pischinger, S. (2012). Arbeitsspielaufgelöste Modellbildung und Hardware-in-the-Loop-Simulation von Pkw-Dieselmotoren mit Abgasturboaufladung [Doctoral Dissertation, Darmstadt University of Technology]. https://tuprints.ulb.tu-darmstadt.de/id/eprint/3165

Zehetner, J., Benedikt, M., Wierse, M., Kokal, H., Paulweber, M., Stettinger, G., & Toye, B. (2014). Control of an engine test-bench via hardware-software-co-simulation. Internationales Stuttgarter Symposium, 1675–1686. https://doi.org/10.1007/978-3-658-05130-3_116

Zehetner, J., Stettinger, G., Kokal, H., & Toye, B. (2014). Echtzeit-Co-Simulation für die Regelung eines Motorprüfstands. ATZ - Automobiltechnische Zeitschrift, 116(2), 40–45. https://doi.org/10.1007/s35148-014-0042-x

Zhang, G., & Furusho, J. (2000). Speed control of two-inertia system by PI/PID control. IEEE Transactions on Industrial Electronics, 47(3), 603–609. https://doi.org/10.1109/41.847901

Zhang, R., & Tong, C. (2006). Torsional vibration control of the main drive system of a rolling mill based on an extended state observer and linear quadratic control. JVC/Journal of Vibration and Control, 12(3), 313–327. https://doi.org/10.1177/1077546306063224

Zhang, R., & Yao, E. (2015). Electric vehicles' energy consumption estimation with real driving condition data. Transportation Research Part D: Transport and Environment, 41, 177–187. https://doi.org/10.1016/j.trd.2015.10.010

Zhang, Y., Huang, Y., Chen, H., Na, X., Chen, Z., & Liu, Y. (2021). Driving behavior oriented torque demand regulation for electric vehicles

with single pedal driving. Energy, 228, 120568. https://doi.org/10.1016/j.energy.2021.120568

Zhang, Y., Wang, W., Kobayashi, Y., & Shirai, K. (2012). Remaining driving range estimation of electric vehicle. 2012 IEEE International Electric Vehicle Conference, IEVC 2012, 1–7. https://doi.org/10.1109/IEVC.2012.6183172

Zheng, Y., Ouyang, M., Han, X., Lu, L., & Li, J. (2018). Investigating the error sources of the online state of charge estimation methods for lithium-ion batteries in electric vehicles. Journal of Power Sources, 377, 161–188. https://doi.org/10.1016/j.jpowsour.2017.11.094

Zhou, J., Sun, J., He, L., Ding, Y., Cao, H., & Zhao, W. (2019). Control Oriented Prediction of Driver Brake Intention and Intensity Using a Composite Machine Learning Approach. Energies, 12(13), 2483. https://doi.org/10.3390/en12132483

Authors contributions and related publications

Muhammed Alhanouti carried out the conceptualization, modeling, simulations, data analysis, and document drafting. He was responsible for the formulation of research objectives, development of theoretical models, design and implementation of simulation frameworks, experimental setup, data acquisition, analysis, and interpretation of results.

Frank Gauterin provided general academic supervision, guidance in refining research directions, and constructive feedback on the scientific content.

Gröll reviewed the controller design algorithm, evaluated the relevant results, and contributed to improving the clarity and quality of the written work through critical review and editorial suggestions.

Martin Gießler and Thomas Blank conducted the battery open circuit voltage measurements.

This dissertation integrates the outcomes of five peer-reviewed journal publications authored during the doctoral study:

Publication 1:

Alhanouti, M., Gießler, M., Blank, T., & Gauterin, F. (2016). New Electro-Thermal Battery Pack Model of an Electric Vehicle. Energies, 9(7), 563.

Publication 2:

Alhanouti, M., & Gauterin, F. (2023a). Robust Speed Control of a Multi-Mass System: Analytical Tuning and Sensitivity Analysis. Applied Sciences, 13(24), 13268.

Publication 3:

Alhanouti, M., & Gauterin, F. (2023b). Thorough Analysis of the Reliability of Measurements on Chassis Roller Dynamometer and Accurate Energy Consumption Estimation for Electric Vehicles. Energies, 16(24), 7994.

Publication 4:

Alhanouti, M., & Gauterin, F. (2024a). A Generic Model for Accurate Energy Estimation of Electric Vehicles. Energies, 17(2), 434.

Publication 5:

Alhanouti, M., & Gauterin, F. (2024b). Predicting the Torque Demand of a Battery Electric Vehicle for Real-World Driving Maneuvers Using the NARX Technique. World Electric Vehicle Journal, 15(3), 103.